Dublin City University
Ollscoil Chathair Bhaile Átha Cliath

Stable Colloids of Magnetic Nanoparticles and Nanoparticle Assemblies with Controlled Size and Magnetic Resonance Properties

Eoin Fox, B.Sc

Thesis submitted for the Degree of
Doctor of Philosophy

Supervisor: Dr. Dermot Brougham

School of Chemical Sciences December 2013

I hereby certify that this material, which I now submit for assessment on the programme of study leading to the award of Doctor of Philosophy is entirely my own work, that I have exercised reasonable care to ensure that the work is original, and does not to the best of my knowledge breach any law of copyright, and has not been taken from the work of others save and to the extent that such work has been cited and acknowledged within the text of my work.

Signed: __________________ *ID No.:* ___________________ *Date:* _______________

This thesis is dedicated to my parents.

Acknowledgments

I would like to thank my supervisor Dr. Dermot Brougham for all his advice, patience and encouragement through my time in his group. I sincerely appreciate all the opportunities he has made available to me which has allowed me to develop my skills as a chemist.

I would like to thank all my lab colleagues past and present, Dr. Jacek Stolarczyk, Dr. Carla Meledandri, Dr. Jose Hierrezuelo, Ms. Fadwa El-Haddassi, Mr. Bing Wu, Ms Sarah Martin and all the others who have made my time in the DB group memorable. I would especially like to thank Dr. Tsedev Ninjbadgar for all the advice, suggestion and fruitful discussions.

My work has benefited from the different collaborations I was a part of, and I would like to thank Prof. Christina Wege and her group in University Stuttgart with special thanks to Dr. Sven Degenhard. I would also like to thank Dr. Teresa Pellegrino and all her group in Istituto Italiano di Tecnologia, Genova and Prof. Sanjay Mathur, University Cologne.

I would especially like to thank all the technical staff in DCU for all their expertise whom have always been on hand to answer any question. I would like to especially like to thank Mr. Vincent Hooper for all his expertise on the ICP and also Dr. Brendan Twamley for all his help on the FE-STEM.

On a personal note I would like to all my friends who listened to me talk about work over these past few years and for humouring me by listening. I would especially like to thank Vicki who was always there for support and encouragement, no matter how small the problem was. Your love and support really helped, especially down the final stretch. I will always appreciate it.

I would like to thank my family; they have always been there for me and understood the commitment this involved. Finally I would like to thank my parents who always encouraged me to do something that interested me and to do my best at it.

List of Abbreviations

Abbreviation	Description	Unit
B_{acq}	Acquisition Field	s^{-1} T^{-1}
t_{acq}	Acquisition Time	s
NP*	Activated NP	-
NPC*	Activated NPC	-
AA	Alkylamine	-
AP	Alkylphosphate	-
AC	Alternating Current	-
ΔE_{anis}	Anisotropy energy	GHz
BA	Benzyl Alcohol	-
BA-NPs	Benzyl Alcohol Nanoparticles	-
T_B	Blocking Temperature	K
k_B	Boltzman constant	$kg \cdot m^2 \cdot s^{-2} \cdot K^{-1}$
H_c	Coercivity Field	s^{-1} T^{-1}
CSD	Competitive Stabiliser Desorption	-
d_{crit}	Critical Diameter	nm
T_c	Curie Temperature	K
DHAA	Dehydro-ascorbic Acid	-
d_p	Depth of penetration	mm
d	Diameter	nm
D	Diffusion Coefficent	cm^2s^{-1}

DLS	Dynamic Light Scattering	-
EDLY	Echo Delay	ns
ELR	Echo-limiting Regime	-
EM	Elcetromagnetic	-
τ_{exp}	Exponential Time	h
FFC	Fast field cycling	-
FA	Fatty Acid	-
FE-STEM	Field Emmission- Scanning TEM	-
FID	Free Inuction Decay	-
$\Delta\omega$	frequency shift experienced by a proton at the equator of the particle	GHz
γ	gyromagnetic ratio	rad $s^{-1} \cdot T^{-1}$
HCP	Hexagonal Close Packed	-
HPPS	High Performance Particle Sizer	-
h	Hour	-
HCl	Hydrochloric Acid	-
D_{HYD}	Hydrodynamic Diameter	nm
V_{HYD}	Hydrodynamic Volume	nm^3
t_o	Induction Time	h
ICP-AES	Inductively Coupled Plasma-Atomic Emission Spectroscopy	-
γ	interfacial Tension	mN/m
K	Kelvin	-

ω_L	Larmor frequecncy	MHz
ν_{max}	Larmor Frequency Maximium	MHz
m_{lin}	Linear Slope	nm/h
$\gamma\text{-}Fe_2O_3$	Maghemite	-
H	magnetic field strength	A/m
B_0	magnetic flux density	s^{-1} T^{-1}
MPI	Magnetic Particle Imaging	-
μ_0	Magnetic permiability in vacum	$N.A^{-2}$
MRI	Magnetic Resonance Imaging	-
χ	magnetic susceptibility	$emu.Oe^{-1}\cdot g^{-1}$
M_{xy}	Magnetisation in x-y plane	-
Fe_3O_4	Magnetite	-
v_{mat}	molar volume of the magnetic material	m^3m^{-1}
MAR	Motion Averaded Regime	-
NG	Nanogel	-
NPC	Nanoparticle Cluster	-
τ_n	Neel Correlation time	ns
d_{NMR}	NMR Diameter	nm
NP	Non-polarised	-
NP/S	Non-polarised Sequence	-
NPCPMG	Non-polarized Carr–Purcell–Meiboom–Gill	-
NMRD	Nuclear Magnetic Relaxation Dispersion	-
NMR	Nuclear Magnetic Resonance	-

$R_{1,obs}$	Observed relaxation rate	s^{-1}
OA	Oleic Acid	-
B_{pol}	Polarisation Field	Tesla
t_{pol}	Polarisation Time	s
PDI	Polydispersity Index	-
PEG	Polyethylene glycol	-
PEO	Polyethylene oxide	-
PMA	Polymer Mediated Assembly	-
PPO	Polypropylene oxide	-
τ_{pow}	Power time	h
PP	Pre-polarised	-
PP/S	Pre-polarised Sequence	-
P(x)	Probability Distribution	%
S	quantised spin magnitude	-
s	quantized spin angular momentum	-
RF	Radio Frequency	-
r	Radius	nm
$\hbar$	reduced Planks constant	m^3kgs^{-1}
B_{rlx}	Relaxation Field	Tesla
$R_{1,surr}$	Relaxation rate of the surrounding liquid	s^{-1}
M_r	Remnant Magnetisation	emu/g
M_0	Sample magnetisation	emu/g
M_{NMR}	Saturation Magnetisation as extracted from NMRD	emu/g

$M_{s(0)}$	Saturation Magnetisation of the Bulk	emu/g
Mv	saturation magnetisation of the material	A/m
T_1	Spin- Latice relaxation time	s
R_1	Spin- Latice relaxation Rate	s^{-1}
R_2	Spin-Spin relaxation rate	s^{-1}
r_1	Spin-Lattice Relaxivity	$mM^{-1}\cdot s^{-1}$
r2	Spin-Spin relaxivity	$mM^{-1}\cdot s^{-1}$
T_2	Spin-Spin relaxation time	s
σ	Standard Deviation	nm
SDR	Static Domain Regime	-
SPM	superparamagnetic	-
d_{spm}	Superparamagnetic Size Limit	nm
dtem	TEM diameter	nm
V_{TEM}	TEM volume	nm^3
T	Temperature	K
THF	Tetrahydrofuran	-
φ_{intra}	the volume fraction of magnetic material	-
TGA	Thermogravametric Analysis	-
t	Thickness of the spin canted surface layer	nm
τ_D	translation diffusional time of protons relative to the diameter of the particle	s
TEM	Transmission Electron Spectroscopy	-
K_{eff}	uniaxial anisotropy constant	GHz

η	Viscoity	
V	volume	nm^3
f_V	Volume Fraction	-
f_{wt}	Weight Fraction	-
XAS	X-ray adsorption Spectroscopy	-

Table of Contents

Title page I

Declaration.. II

Dedication.. III

Acknowledgements IV

List of abbreviations VI

Table of contents XII

Abstract XVI

Chapter 1 : Introduction to Nuclear Magnetic Resonance and Magnetic Nanoparticle Suspensions.. 1

1.1. Thesis Overview 2

1.2. Nuclear Magnetic Resonance 6

1.2.1. Nuclear Magnetisation.. 6

1.2.2. Nuclear Magnetic moments under an Applied External Field 7

1.2.3. NMR Relaxation 10

1.3. Magnetisation in materials 12

1.3.1. Types of Magnetisation.. 13

1.3.2. Superparamagnetic materials.. 18

1.3.3. Relaxation Enhancement of Superparamagnetic Materials 20

1.4. Theory of Nuclear Magnetic Relaxation Dispersion (NMRD)..22

1.4.1. Appling SPM theory to simulate experimental NMRD profile 25

Chapter 2 : Experimental 30

2.1. Fast Field Cycling NMR..31

2.1.1. Theory 31

2.1.2. Experimental Set Up 31

2.1.3. Experimental Limitations 35

2.2. Transmission Electron Microscopy 35

2.2.1. Theory 35

2.2.2. Experimental Set Up 37

2.2.3. Experimental Limitations 37

2.3. Dynamic Light Scattering 38

2.3.1. Theory 38
2.3.2. Experimental Setup 43
2.3.3. Experimental Limitations 44
2.4. Inductively Coupled Plasma Atomic Emission Spectroscopy 44
2.4.1. Theory 44
2.4.2. Experimental Setup 46
2.5. ATR-IR Spectroscopy 46
2.5.1. Theory 46
2.5.2. Experimental Set up 47
2.5.3. Experimental Limitations 48
2.6. Thermogravametric Analysis 48
2.6.1. Theory 48
2.6.2. Experimental Setup 49
2.6.3. Experiment Limitations 50

Chapter 3 : Sized Controlled Synthesis of Magnetic Nanoparticles 51
3.1. Introduction 52
3.1.1. Reaction Mechanism for Nanoparticle Formation 54
3.2. Experimental 57
3.2.1. Stabilisation of Maghemite NP 58
3.2.2. Characterisation of Nanoparticle Dispersions 59
3.3. Results and Discussion 61
3.3.1. Investigation into the Effect of Polydispersity on Magnetic Resonance Properties 61
3.3.2. Effect of Reaction Time on Nanoparticle Size 65
3.3.3. Effect of Heating Temperature on Nanoparticle Size 73
3.3.4. Effect of Precursor Quantity on the Nanoparticle Size 80
3.3.5. Thermal Decomposition at Constant Volume 87
3.3.6. Magnetic Properties as Extracted from Superparamagnetic Simulations 92
3.4. Conclusion 98

Chapter 4 : Effect of Ligands on the Magnetic Resonance Properties of Nanoparticle Dispersions 99
4.1. Introduction 100
4.2. Experimental 102
4.2.1. Synthesis of Iron Oxide Nanoparticles 102
4.2.2. Stabilisation of Benzyl Alcohol Nanoparticles 102

4.2.3. Phosphorylation of Primary Alcohols 103
4.2.4. Characterisation of Nanoparticle Dispersions 106
4.3. Results and Discussion 108
4.3.1. Particle Size as determined by TEM 108
4.3.2. Phase analysis by XAS 110
4.3.3. Investigation into the Effect of Chain Length on Particle Properties 111
4.3.4. The Effect of Head Group on Magnetic Resonance Properties 124
4.4. Conclusion 130

Chapter 5 : Solvent Interface Mediated Assembly of Magnetic Nanoparticles using Competitive Stabiliser Desorption 131

5.1. Introduction 132
5.2. Experimental 136
5.2.1. Synthesis of Iron Oxide Nanoparticles 136
5.2.2. Stabilisation of Benzyl Alcohol Nanoparticles 137
5.2.3. Assembly of OA-NP using Solvent Interface Mediated Assembly 137
5.2.4. Characterisation of Nanoparticle Dispersions 138
5.3. Results & Discussion 139
5.3.1. Size and Stability of Primary Nanoparticles 139
5.3.2. Controlled Assembly of Nanoparticles 142
5.3.3. Investigation into the role of water during competitive stabiliser desorption 144
5.3.4. Morphology of Clusters 150
5.3.5. Reproducibility of the Assembly Process 151
5.3.6. Kinetics of Assembly by Competitive Stabiliser Desorption at the Solvent Interface 153
5.3.7. Effect of Oleic acid on the Kinetics of Assembly 157
5.3.8. Scale Up Of Interfacial Competitive Stabiliser Desorption 160
5.3.9. Effect of Assembly Rate on Nuclear Magnetic Resonance Properties of Nanoparticle Clusters Dispersions 163
5.4. Conclusion 168

Chapter 6 : Effects of Cluster Architecture on the Relaxation Rate Enhancement of Water Suspensions 169

6.1. Introduction 170
6.2. Experimental 173
6.2.1. Polymer Mediated Assembly of Nanoparticles 173
6.2.2. Synthesis of Dehydroascorbic Acid Stabilised Nanoparticles 174
6.2.3. Synthesis of Decorated Stimulus Responsive Polymer Nanobeads 174

6.2.4. Characterisation of Nanoparticle Clusters 175

6.3. Results and Discussion 176

6.3.1. Polymer Mediated Assembly of Nanoparticles 176

6.3.2. Dehydroascorbic Acid Stabilised Nanoparticles 184

6.3.3. Decorated Stimulus Responsive Polymer Nanobeads 189

6.3.4. Interpretation of NMR Data for Aqueous NPC Suspensions 194

6.3.5. Spin-Spin Relaxivity Values of NPC Assemblies and the Universal Scaling Law 197

6.4. Conclusion 202

Thesis Conclusions 203

Appendix 205

References 208

Abstract

Suspensions of both dispersed and clustered iron oxide nanoparticles are of interest for biomedical applications as diagnostic and therapeutic agents due to their bio-compatibility and interesting magnetic and magnetic resonance properties. Their application is critically dependent on the fact that these properties are highly size-dependant. By developing NP synthesis and assembly methods, to provide improved size control at the two levels of organisation, NP suspensions with controlled emergent magnetic properties have been prepared. The first part of this thesis presents the size-controlled synthesis of magnetic nanoparticles whose surface is functionalised with a wide range of stabilising ligands. An investigation was undertaken to elucidate the effect of the stabilising ligands on the physical properties. The second part of the thesis presents a novel method for the reproducible assembly, in suspension, of NPs to form clusters. The method can be used to produce clusters of controlled size in large quantities; it is also shown that the kinetics of assembly can be easily controlled and that this influences the emergent magnetic properties. Arising from this observation a study was undertaken to determine the role of cluster architecture on the magnetic resonance properties of their aqueous suspensions.

Chapter 1

Introduction to Nuclear Magnetic Resonance and Magnetic Nanoparticle Suspensions

1.1. **Thesis Overview**

In Chapter 1 an introduction to the theory and concepts central to this thesis is provided. The principles behind nuclear magnetisation and relaxation will be discussed. The different types of magnetic materials will be examined with emphasis on superparamagnetic materials, their unique properties and uses. The experimental theory behind fast field cycling NMR (FFC-NMR), also known as nuclear magnetic relaxation dispersion (NMRD) is examined and how this technique coupled with superparamagnetic simulations can be used to probe the magnetic properties of materials in suspensions.

In Chapter 2 the main analytical techniques used throughout this thesis are described. This includes fast field cycling-nuclear magnetic resonance (FFC-NMR), dynamic light scattering (DLS), transmission electron microscopy (TEM), inductively coupled plasma-atomic emission spectroscopy (ICP-AES), attenuated total reflectance- infrared spectroscopy (ATR-IR) and thermogravametric analysis (TGA). The physical background, experimental conditions and limitations associated with each technique are discussed.

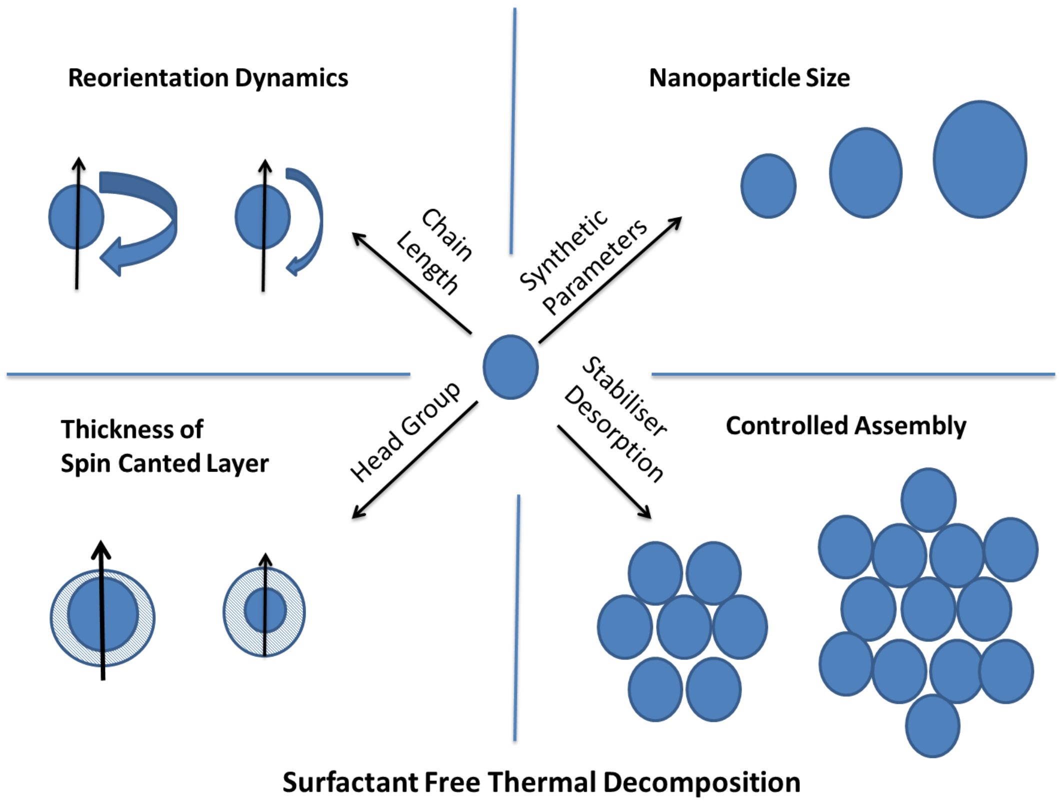

Figure 1-1 : Integrated results schematic displaying overview of outcomes of thesis

In Chapter 3 the synthesis of highly crystalline monodisperse maghemite nanoparticles (γ-Fe_2O_3) using a surfactant free thermal decomposition are presented. It is shown that through careful control over the synthetic parameters, the nanoparticle size and magnetic properties can be controlled, Figure 1-1. ^{1}H FFC-NMR allowed the estimation of the saturation magnetisation of nanoparticle dispersions in heptane and through the use of an empirical model, the thickness of the surface layer of canted spins was estimated.

In Chapter 4 the effect of the stabilising ligand on the magnetic resonance properties of magnetic nanoparticles suspensions are investigated. Using ^{1}H FFC-NMR the effect of chain length and of head group on magnetic resonance properties of nanoparticle dispersions in heptane are studied. The observed effects of chain length are attributed to ligand lateral interactions while the effects of the head group are attributed to binding strength, Figure 1-1.

In Chapter 5 a novel method for the assembly of nanoparticles into nanoparticle clusters of controlled size in chloroform is reported. The assembly method based on competitive stabiliser desorption, was shown to be extremely reproducible and was scaled up by a factor of 50. The kinetics of assembly were investigated and through control over the assembly parameters, the rate of assembly can be controlled, Figure 1-1. In the second part of Chapter 4, the effect that assembly rate on the emergent magnetic resonance properties of the suspension was investigated. It was found the magnetic resonance properties could be enhanced by controlling the assembly rate.

In Chapter 6, through a detailed ^{1}H FFC-NMR study of aqueous nanoparticle clusters suspensions, the role of cluster architecture in determining the magnetic resonance properties was investigated. In the second part of Chapter 6, using a recently developed universal scaling law which relates the magnetic volume scaled spin-spin relaxation (r_2) to cluster size and was used to estimate the volume fraction of magnetic material contained in the clusters.

Throughout this work the central focus is in improving the magnetic resonance properties of magnetic nanoparticle and understanding the principals that affect the magnetic resonance properties. This is of interest for a range of functions, particularly for biomedical applications as theranostic agents. An additional focus has been on the assembly of nanoparticles into clusters and to understand the role of architecture in determining the relaxation properties of clusters. FFC-NMRD has been central to this work and has been used advantageously to measure the relaxivities of nanoparticles dispersed in a range of solvent systems including water, heptane and chloroform.

Superparamagnetic materials, particles and their assemblies are of great scientific and technological interest due to their size dependant magnetic properties that can be controlled through colloidal synthesis [1, 2]. Their potential applications include, but are not limited to, ferrofluids, magnetic storage media [3], separations, catalyst supports and purification [4]. Perhaps the largest field of interest is for biomedical applications which range from diagnostic agents in magnetic resonance imaging, MRI, [5] and magnetic particle imaging, MPI, [6] for drug delivery agents [7, 8] and as mediators for AC-field hyperthermia [9]. This makes superparamagnetic materials true theranostic platforms. Additionally their small size is suitable for interaction within biological systems such as cells and blood vessels [10] allowing them to be conjugated to a range of biomolecules such as proteins, DNA and antibody fragments [8, 11].

When working with iron oxides, specifically maghemite, γ-Fe_2O_3, and magnetite Fe_3O_4, there are inherent advantages. Iron oxides are non-toxic; it has been shown that the particles at clinical concentration are either excreted from the body or broken down and used within the body as part of the normal metabolism[5]. Additionally, the surface chemistry of iron oxide is versatile and allows the utilisation of a wide range of surface chemicals. These surface coatings can be tailored and designed with targeting moieties [12] or simply to increase blood half-life.

It is thus important to examine the origins of magnetism and magnetism in materials and how these materials can be used to enhance the magnetic resonance relaxation rates of solvents.

1.2. **Nuclear Magnetic Resonance**

1.2.1. Nuclear Magnetisation

Nuclear spin

Nuclear magnetisation originates from the inherent spin of sub atomic particles; protons, and neutrons. This spin is a result of an intrinsic spin angular momentum which is quantised and as quantum spin. This is to say that the spin can only adopt specific discrete values. The spin angular momentums magnitude is quantised in Equation 1-1 where S is the quantised magnitude, where ħ is the reduced Planks constant and s is the quantized spin angular momentum which can only be a non-negative integer or half integer, e.g. 0, ½, 1, 3/2…..

$$S= \hbar \sqrt{s\,(s+1)}$$

Equation 1-1

Sub-atomic particles, when combined together in nuclei, can generate a possible net nuclear spin. In situations where the number of protons is equal to the number of neutrons, the quantum spin number (s) is zero. This is to say that no nuclear spin is experimentally observable; for all other cases, where s ≠ 0, there exists experimentally observable nuclear spin states. Examples of spin states are included in Table 1-1.

Table 1-1: Examples of nuclei and isotopes and their spin quantum number

Nucleus	Spin Quantum number, s
^{1}H	½
^{2}H	1
^{12}C	0
^{13}C	½
^{17}O	5/2

A particle possessing a nuclear spin will also possess an associated magnetic moment, μ. This is defined in Equation 1-2 where μ is the magnetic moment and γ is the gyromagnetic ratio (which is unique to each nucleus).

$$\mu = \hbar \gamma s$$ **Equation 1-2**

As ^{1}H nuclei are central to this study the focus of the discussion will be on a system where the spin quantum number is ½.

1.2.2. Nuclear Magnetic moments under an Applied External Field

When nuclei, with non-zero spin numbers, $s \neq 0$, are exposed to an applied external magnetic field H or magnetic flux density B_0, the number of allowed spin states, relative to the applied magnetic field, is given by Zeeman splitting, 2S+1. The relationship between magnetic field strength and magnetic flux density is defined in Equation 1-3 where μ_0 is the magnetic permeability in a vacuum and is given as $4*\pi*1x10^{-7}$ N.A^2.

$$B = \mu_0 . H$$ Equation 1-3

For the ^{1}H nuclei, where s = ½, there are only two allowed spin states. In the vector model the states correspond to spins aligned parallel or anti-parallel with B_0. When a spin is aligned parallel to B_0, this is referred to as the lower energy state (α) while when the spin is aligned anti-parallel to B_0 this is known as the higher energy state (β), Figure 1-2.

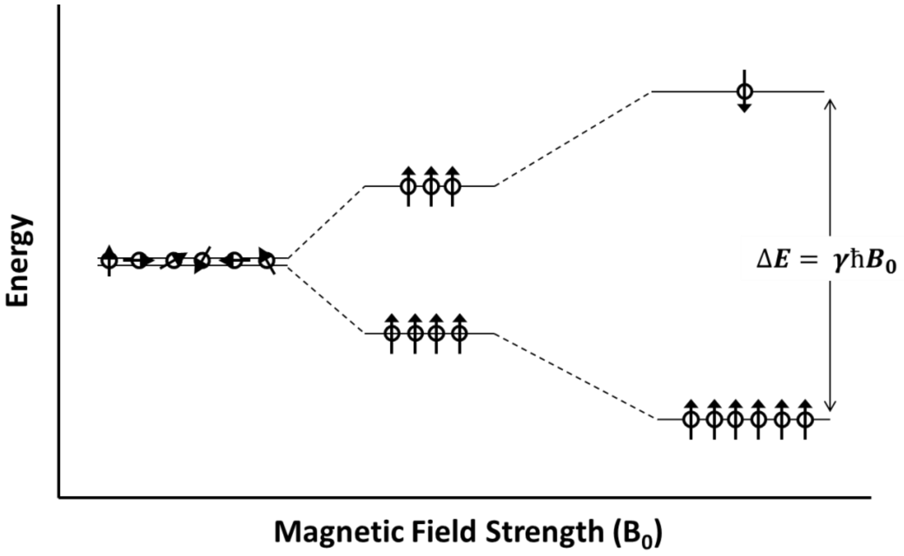

Figure 1-2 : Possible spin states for a S=1/2 system and how an external magnetic field affects the spin states

The energy difference between the two states (α, β), ΔE, is proportional to the strength of the applied magnetic field and the gyromagnetic ratio, γ, as seen in equation 3.

$$\Delta E = \gamma \hbar B_0$$

Equation 1-4

The population ratio between the number of spins in the α state (N_α) and the number of spins in the β state (N_β) follows the Boltzmann's distribution. It is determined by the energy difference (ΔE) between the states and the absolute temperature (K). The relationship is shown in Equation 1-5 where k_B is the Boltzmann's constant.

$$\frac{N\alpha}{N\beta} = e^{\frac{\Delta E}{k_B T}}$$

Equation 1-5

As ΔE is proportional to the magnetic flux density, B_0, as B_0 increases, the population ratio increases. Given the small energy level separation, Nα/Nβ is only slightly greater than 1 under normal conditions.

In the vector model, B_0 lies along the z-axis. The α spin states are displayed as vectors pointing towards the positive z-axis but quantum mechanically the z and x/y components of the moment cannot be known simultaneously, so the moments are canted with respect to the field axis. The moments therefore experience a torque due to B_0 and rotate around the positive z-axis at a fixed frequency which is known as the Larmor frequency, ω_L, which is proportional to B_0, Equation 1-6. The same holds true for the β states except they are aligned about the negative z-axis, Figure 1-3.

$$\omega_L = \gamma B_0$$

Equation 1-6

As the spins are nominally non-interacting they have random phases and are randomly distributed in the x-y plane. At equilibrium, as there is an excess of α over β states, thus the total sample ^1H magnetisation, M_0 points along the positive z-axis, Figure 1-3.

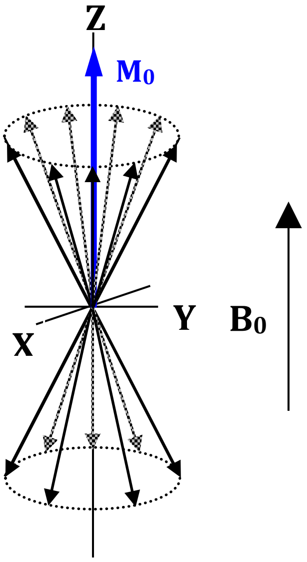

Figure 1-3: Vector model of spins under B_0 with M_0 aligned along the Z axis

The application of an on-resonance radio frequency pulse (RF) will have two effects; the pulse will create a torque thereby rotating the net magnetic moment into the xy plane, secondly the pulse will align the phase of the individual constituent spins. If a pulse is applied for a period long enough to rotate M_0 90^0, it is known as a π/2 pulse, Figure 1-4.

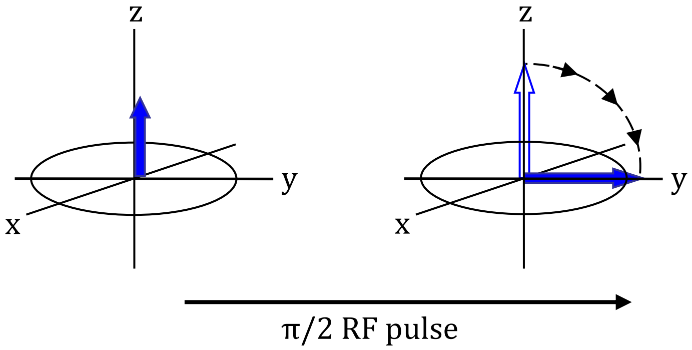

Figure 1-4: The effect on the bulk sample magnetisation, M_0 of the application of a π/2 RF pulse

1.2.3. NMR Relaxation

As previously mentioned, following a π/2 RF pulse, the magnetic moments lie along the xy plane. The spin system is now not at equilibrium. The system will relax to equilibrium by two mechanisms. Firstly the system can pass the energy of the RF pulse back to the surrounding environment. This gradually returns the magnetisation back to the z-axis and is known as longitudinal or spin-lattice relaxation, which has a characteristic time, T_1. It is a random process driven by fluctuations in the environment and hence is exponential in form. The process is shown schematically in Figure 1-5 and Equation 1-7.

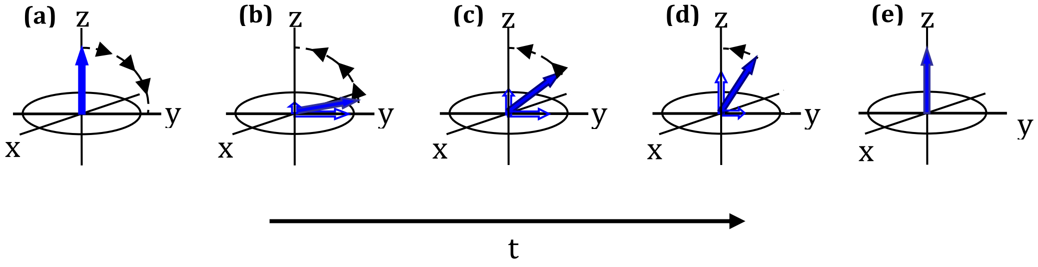

Figure 1-5: Longitudinal or spin lattice relaxation, T_1, a) π/2 pulse rotates M_0 into the xy plane, b) – c) – d) M_0 begins to relax back to the z plane, the magnetisation detectable in the xy plane dies away, while the magnetisation detectable in the z plane grows, until e) all of the magnetisation has returned to the z axis

$$M_{xy}\ (t) = M_0(1 - e^{\frac{-t}{T_1}})$$ **Equation 1-7**

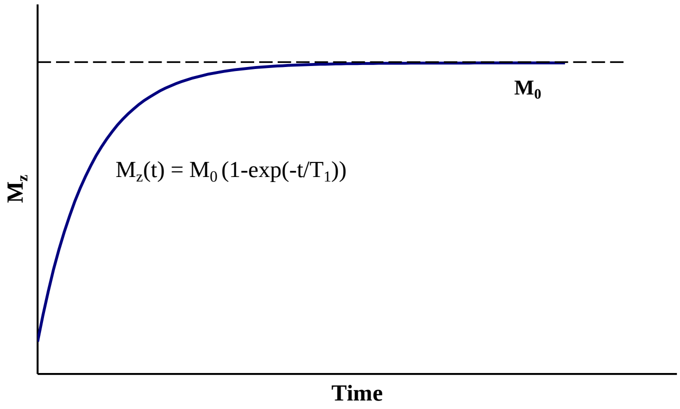

Figure 1-6: Magnetisation recovery curve of a magnetisable material, under an external applied magnetic field following the application of a π/2 RF pulse showing the exponential nature of the process

The second type of relaxation involves de-phasing of the individual spins that make up the net magnetic moment. Following the application of a π/2 RF pulse, the spins are aligned within the xy plane. The now in-phase spins start to precess and gradually loose there phase coherent. The result of this de-phasing is a loss of measurable magnetisation in the x-y plane (M_{xy}) although there is no energy transfer to the surrounding environment, Figure 1-7. This is known as transverse or spin-spin relaxation, which has a characteristic time, T_2, Equation 1-7.

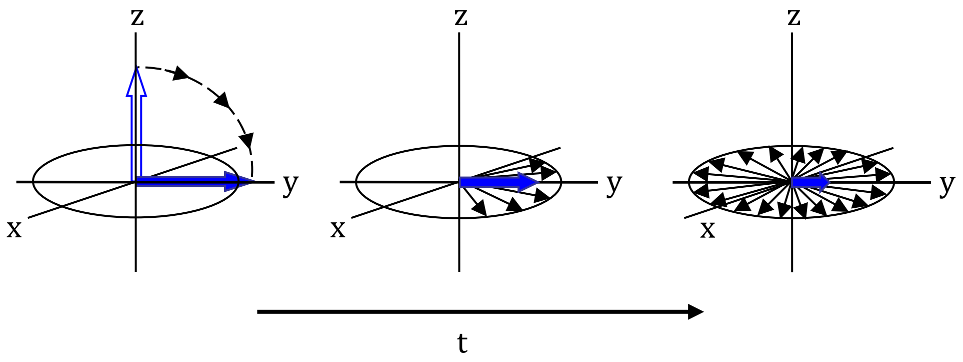

Figure 1-7: The transverse or spin-spin relaxation process, T_2, following a π/2 pulse, the aligned spins start to de-phase resulting is a loss of M_{xy}, this continues the spins are completely de-phased and there is no detectable sample magnetisation

$$M_{xy}(t) = M_0\, e^{\frac{-t}{T_2}}$$ **Equation 1-8**

There is a second cause of spin de-phasing. For real samples, magnetic field inhomogeneities exist across the sample volume. In the case of magnetic nanoparticles in suspension, there may also be local inhomogeneities due to the local changes in magnetic susceptibility arising from magnetic particles within the field. These gradients result in the rapid de-phasing of ^{1}H magnetisation of the solvent, the characteristic time for this process is T_2^*.

1.3. Magnetisation in materials

It has been established that nuclei, with spin quantum number not equal to 0, possess magnetic properties. This associated magnetic moment is directly proportional to the gyromagnetic ratio, γ, (Equation 1-2).

Table 1-2 : Gyromagnetic Ratios of sub atomic particles[13]

Sub-Atomic Particle	Gyromagnetic Ratio (rad.s^{-1} T^{-1})
Electron	1.760×10^{11}
Proton	2.675×10^{8}
Neutron	1.832×10^{8}

However, it can be seen from

Table 1-2 that electrons also possess a gyromagnetic ratio and thus when atoms/molecules have unpaired electrons it results in a net magnetic moment. Having already established that the magnetic moment is proportional to the gyromagnetic ratio (Equation 1-2), for electrons the magnetic moment is far greater in magnitude than that of the nucleus (~1000 times). Hence unpaired electrons in materials can contribute to a large magnetic moment, which gives rise to the familiar bulk magnetic properties, e.g. of ferromagnets.

1.3.1. Types of Magnetisation

The strength of the magnetic effect varies from material to material and is quantified by the magnetic susceptibility, χ. The relationship between a material's magnetisation and the applied field strength, H, is given in Equation 1-9.

$$\chi = \frac{M_s}{H} \qquad \textbf{Equation 1-9}$$

Diamagnetic Materials

Typically, when an external magnetic field is applied to an electron, the electron experiences a torque, resulting in a Larmor precession. For paired electrons, this rotation creates a magnetic moment in opposition to the applied field, Figure 1-8. Diamagnetic materials possess no unpaired electrons in orbitals. Diamagnetic materials are characterised by a weak and negative magnetic susceptibility, χ which results in weak magnetisation opposing an applied field [14].

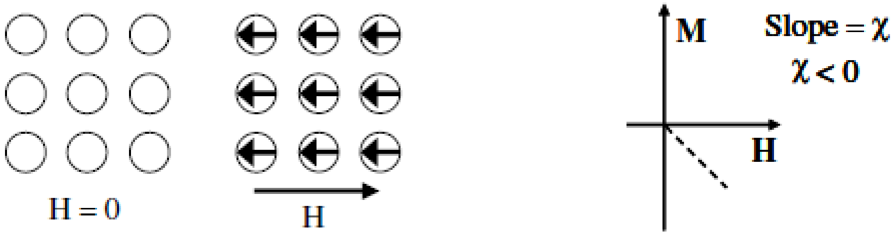

Figure 1-8: Schematic representation of the spin ordering of diamagnetic materials and the negative magnetic susceptibility

Paramagnetic materials

Paramagnetic materials contain unpaired electrons in partially filled orbitals, for which there is no coupling between neighbouring magnetic moments. In the absence of an applied external field, the magnetic moments are orientated randomly due to thermal fluctuations. In the presence of an applied external field the magnetic moments align parallel to the field and a bulk magnetisation is induced. Paramagnetic materials typically are weakly attracted to an applied field and so are characterised by a positive magnetic susceptibility, χ. Upon removal of the magnetic field, any ordering of the moments is lost[14].

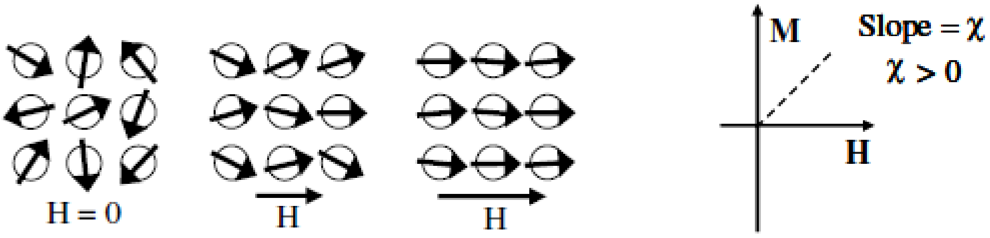

Figure 1-9: Schematic representation of the dipole ordering in paramagnetic materials and the positive magnetic susceptibility typically associated with these materials

Ferromagnetic materials

Ferromagnetic materials possess unpaired electrons in partially filled orbitals. Ferromagnetic materials differ from paramagnetic materials as coupling between neighbouring moments result in an inherent or permanent magnetisation. In ferromagnetic materials, orbitals containing unpaired electrons from different nuclei overlap which results in the coupling of the moments in a parallel fashion. The overlap allows electrons to be located further apart while retaining the same spin and is known as the exchange interaction. This configuration is favoured as it reduces the energy of the system. The energy difference between an anti-parallel aligned spin system and an exchange interaction parallel aligned spin system is referred to as the exchange energy. When an external magnetic field is applied to a ferromagnetic material, the exchange interaction will drive the magnetic moments to align parallel to the field, inducing a strong magnetisation. Ferromagnetic materials are characterised by a large positive magnetic susceptibility, χ.

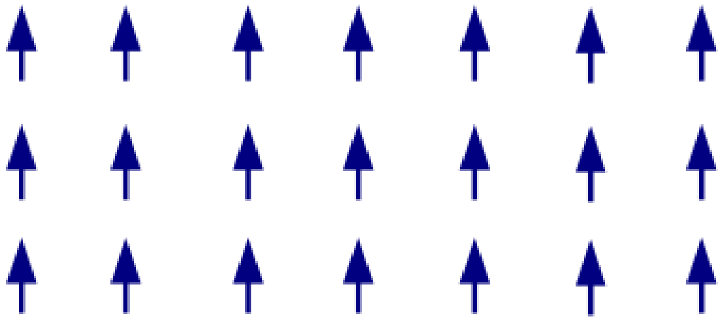

Figure 1-10: Representation of the parallel spin coupling found in of ferromagnetic materials

The magnetic properties of a sample can be studied experimentally by magnetometry; a schematic of the response of a ferromagnetic material is shown in Figure 1-11. Starting at zero magnetic field, initially there is no magnetisation. On application of a magnetic field, the sample magnetisation builds according to χ. Eventually, the magnetisation does not increase further as all the moments are aligned; this is known as the saturation magnetisation, M_s, and it occurs at the saturation field, B_s. As the applied field is reduced; the sample magnetisation decreases. If at zero applied field, there is still remnant magnetisation in the sample, M_r, the sample is said to be ferromagnetic. As the applied field is reversed, the field at which the sample magnetisation reaches zero is known as the of the coercivity field (H_c).

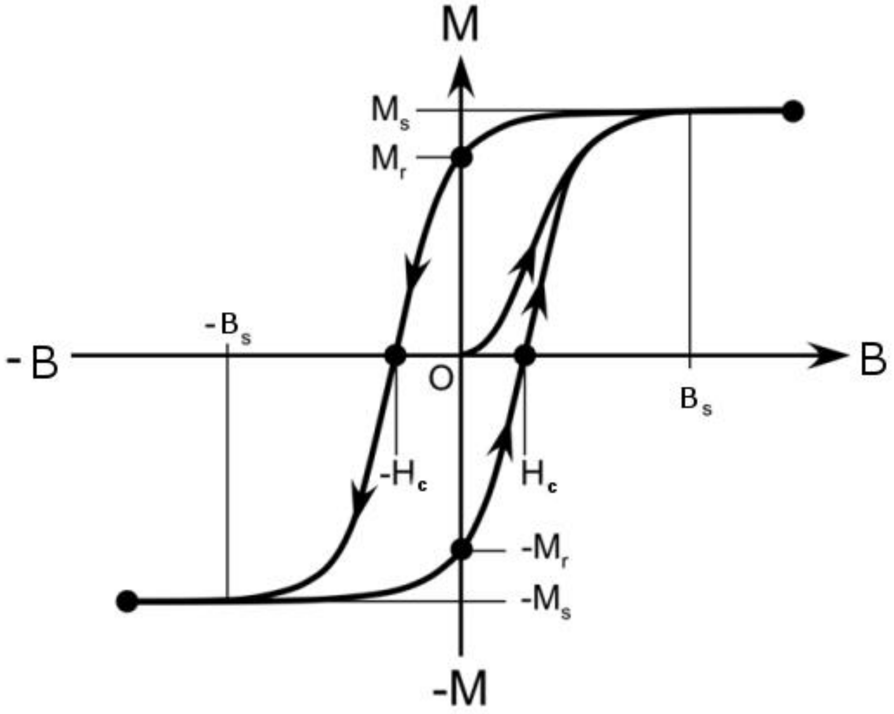

Figure 1-11: Magnetometry curve showing the evolution of magnetisation along with important magnetic parameters; saturation magnetisation, M_S , the Coercivity, H_c and the remnant magnetisation, M_r adapted from Furlani et al [15]

When a ferromagnetic material is heated above a critical temperature, the thermal energy is sufficient to overcome the exchange interaction. The thermally disruption of the coupling between the magnetic moments results in a loss of magnetisation. This is known as the Curie temperature, T_c. The Curie temperature is a characteristic property of the material and is a measure of the strength of the coupling.

Antiferromagnetic Materials

Antiferromagnetic materials share similar properties to ferromagnetic materials, they have unpaired electrons in partially filled orbitals. In ferromagnetic materials, the structure promotes neighbouring magnetic moments to align parallel however, in antiferromagnetic materials the neighbouring magnetic moments are aligned in an anti-parallel alignment. The exchange interaction has a negative value. This results in a net magnetic moment of zero.

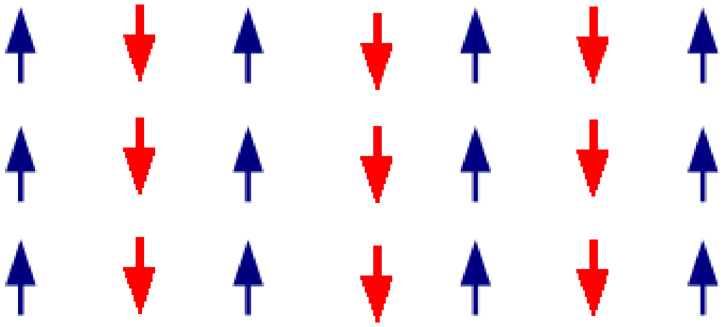

Figure 1-12 : Anti-parallel spin ordering of anti-ferromagnetic materials

Ferrimagnetism

Ferrimagnetic materials share similar properties to antiferromagnetic materials. Ferrimagnetic materials possess unpaired electrons in partially filled orbitals whose structure promotes neighbouring magnetic moments to align anti-parallel. Unlike antiferromagnetic materials, in ferrimagnetic materials the opposing spins (usually in different crystal sub lattices) are not of equal magnitude. In an applied external field, magnetisation is induced. Ferrimagnetic materials retain their magnetism in the absence of an external magnetic field and behave like weak ferromagnets. Ferrimagnetism is common in iron oxides and is the type of magnetisation present in magnetite (Fe_3O_4) and maghemite (γ-Fe_2O_3).

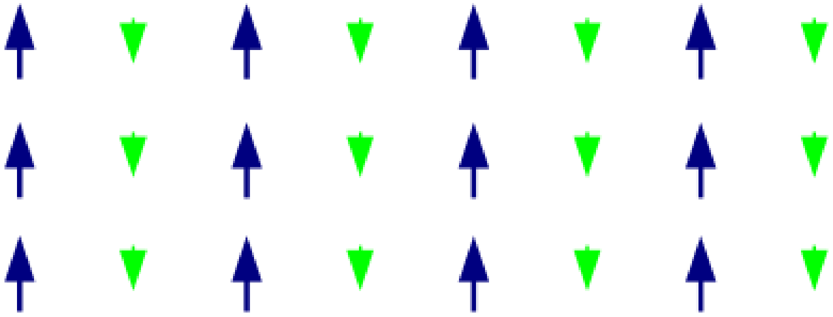

Figure 1-13 : Unequal anti-parallel spin ordering of ferrimagnetic materials

1.3.2. Superparamagnetic materials

Superparamagnetism is a type of magnetism that arises in ferromagnetic and ferrimagnetic materials as the size of the materials is reduced. In both ferromagnetic materials and ferrimagnetic materials discreet crystallites known as Weiss domains are thermodynamically favoured[14]. A Weiss domain is one within which the individual magnetic moments are coupled, and so they behave as a one larger magnetic moment. In the case of larger ferromagnetic and ferrimagnetic objects, multiple domains are present and these domains are separated by grain boundaries. These domains (depending on the nature of the interface) are coupled by exchange interaction and/or by dipole-dipole interactions. As ferromagnetic materials and ferrimagnetic materials approach smaller sizes, the materials reach a size known as the critical diameter, d_{crit}. Below d_{crit}, the surface area to volume relationship makes it thermodynamically disfavoured for grain boundaries to exist, resulting in single domain materials. The d_{crit} value is related to the exchange constant, A, the uniaxial anisotropy constant, K_{eff} and is inversely related to the permeability, μ_0, Equation 1-10. Some examples of d_{crit} are listed below in Table 1-3.

Equation 1-10

$$d_{crit} \approx 18 \frac{(A\, K_{eff})^{\frac{1}{2}}}{\mu_0\, M_s^2}$$

Table 1-3 : Typical d_{crit} and d_{spm} values for a range of common magnetic materials [16]

Material	d_{crit} (nm)	d_{spm} (nm)
Fe_3O_4	128-85	25
γ-Fe_2O_3	166-90	30
$CoFe_2O_4$	100	10
Fe	15	12

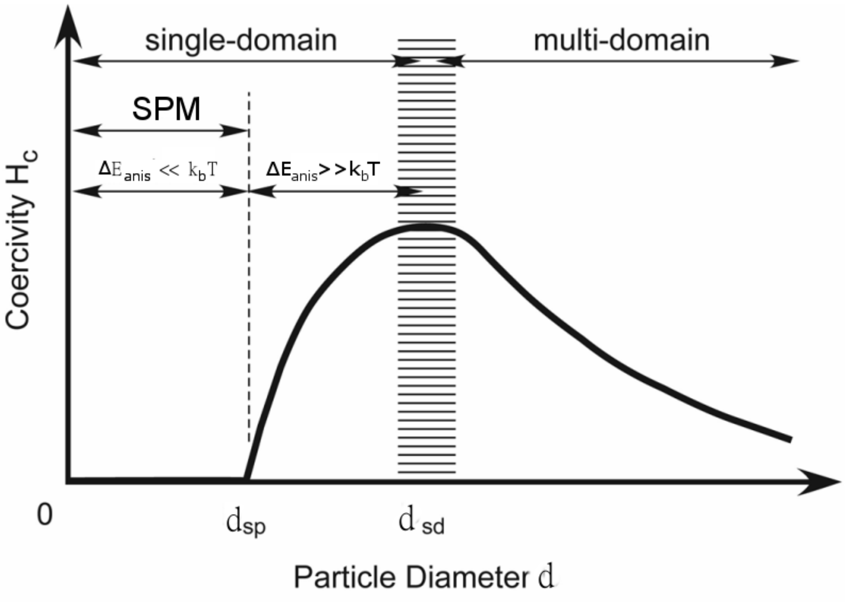

Figure 1-14: Schematic overview of the affect size of a magnetic particle has on coercivity (H_c); identifying the relationship between ΔE_{anis} and the superparamagnetic size limit, d_{spm}, and the single domain limit, d_{sd} adapted from Furlani et al. [15]

As the particle size of ferrimagnetic and ferromagnetic materials decreases below d_{crit}, the particle approaches a size known as the superparamagnetic diameter, d_{spm}. Below d_{spm} , the thermal energy, k_BT, available in the system at that temperature is comparable to the energy required to reverse the magnetic orientation of the domain, ΔE_{anis} (surface anisotropy energy) which is proportional to the volume of the particle, V, and k_{eff}, Equation 1-11 [15]. This results in a spontaneous flipping of the magnetic moment about the preferred axis of magnetisation, known as the easy axis. Superparamagnetic materials are characterised by a near zero remnant magnetisation.

$$\Delta E_{\text{anis}} = \mathrm{k}_{\text{eff}}\mathrm{V} \qquad \textbf{Equation 1-11}$$

The characteristic time scale for flipping of a magnetic moment for superparamagnetic materials is known as the Néel correlation time, τ_n. The correlation time is related to the ΔE_{anis} in a Arrhenius manner, shown in Equation 1-12[17], where τ_0 is usually in the order of 10^{-9}s.

$$\tau_n = \tau_0 e^{\frac{\Delta E_{\mathrm{anis}}}{k_B T}}$$ **Equation 1-12**

Upon decreasing the temperate the reorientation rate decreases to a point where the magnetic moment appears static for the time scale of the measurement and the moment is said to be blocked. This characteristic temperature is known as the blocking temperature, T_B, the phenomenological equation for a measurement time of 100s and τ of 1 ns is given in Equation 1-13. T_B can be measured using field cooled magnetometry/zero-field cooled magnetometry and is a commonly used measure of superparamagnetism.

$$T_B = \frac{\Delta E_{\mathrm{anis}}}{25 k_B}$$ **Equation 1-13**

1.3.3. Relaxation Enhancement of Superparamagnetic Materials

As discussed above, superparamagnetic materials enhance the ^1H NMR relaxation of fluids. This effect makes superparamagnetic particles very interesting with regards to MRI for use as contrast agents, which is a particular focus of this work.

Superparamagnetic nanoparticles or magnetic nanoparticles (NPs) have can be used as Magnetic Resonance Image (MRI) contrast agents. NPs reduce both the longitudinal (T_1) and transverse (T_2) of ^1H relaxation the surrounding fluid. NPs are classified as T_1 or T_2 acting agents. T_1 agents brighten MRI images while T_2 agents darken MRI images. In particular, individual NPs have a greater capacity to act as T_1 acting agents. However, clusters of NPs, due to their larger size have a greater capacity to act as T_2 agents [18, 19]. These unique aspects expand the potential and sensitivity for iron oxide NP for use in MRI for both tissue diagnostics and for angiography.

It is necessary to evaluate the efficiency of contrast agents by taking the relaxation times or relaxation rates ($1/T_{1,2} = R_{1,2}$) and normalising by the iron concentration, Equation 1-14 and Equation 1-15, where $R_{1,obs}$ is the observed relaxation rate and $R_{1,surr}$ is the relaxation rate of the surroundings. This is known as the concentration independent relaxivity whose units are s^{-1} mM^{-1}.

$$r_1 = \frac{R_{1,obs} - R_{1,surr}}{[Fe]}$$

Equation 1-14

$$r_2 = \frac{R_{2,obs} - R_{2,surr}}{[Fe]}$$

Equation 1-15

To establish if a contrast agent will be a predominantly T_2 or a T_1 acting agent the ratio between r_2 and r_1 is calculated. Contrast agents with a low ratio, typically >2, indicate a greater capacity to be a T_1 acting agent under T_1 weighted conditions, while ratios above 2 indicate a greater capacity to be a T_2 acting agent under T_2 weighted conditions. Alternatively, this can be demonstrated using a phenomenological equation derived from the original equations developed by Bloch [20] where S is the intensity of the MRI signal, ρ_H being the density of ^1H, TE being the echo delay between successive spins and TR experiment repetition time as shown in Equation 1-16.

$$S \propto \rho_{\,^1H}\left(1 - e^{-\frac{TE}{T_1}}\right) * e^{-\frac{TR}{T_2}}$$

Equation 1-16

Table 1-4: Examples of some iron oxide based contrast agents [21], the relevant coating and the clinical application

Agent Name	r_2, r_1 @ 61 MHz (s^{-1} mM^{-1})	r_2/r_1 @ 61 MHz	Coating	Applications
Resovist	190, 10.9	17.4	Carboxydextran	clinical T_2 agent (liver) T_1 possible
Ferumoxytol (Combidex)	89, 15	5.9	Carboxymethyl-dextran	clinical T_1 and T_2 agent, blood pool
Sinerem	65, 9.9	6.6	Dextran	Clinical T_1 and T_2 agent, blood pool
VSOP-C184	33.4, 14	2.4	Citrate	preclinical T_1 agent, blood pool

1.4. Theory of Nuclear Magnetic Relaxation Dispersion (NMRD)

NMRD or fast field cycling NMR relaxometry is a pulsed NMR technique which uses fast cycling electromagnets to measure the relaxation rate of a sample over a wide range of applied fields, corresponding to ^1H Larmor frequencies between 0.01 MHz to 40 MHz. NMRD is a very versatile method which allows probing of the magnetic properties that drive molecular relaxation.

For superparamagnetic nanoparticles, at low B_0, ^1H relaxation is driven by the rapid motion of the magnetic moment about the easy axis, Equation 1-12, this is known as the Néel relaxation process which result in the spontaneous reorientation of the magnetic moments results in a time averaged magnetic moment of zero. The capacity for a moment's reorientation to relax diffusing ^1H atoms depends whether its correlation time is longer or shorter than the ^1H spins precession within an external field. Therefore for a Néel driven relaxation process the reorientation of the moment, τ_n is fast, when compared to the translational diffusion coefficient of the solvent, relative to the particle diameter, τ_D and so this mechanism dominated the relaxation process. Thus for low frequencies, the Néel relaxation process is the dominant process and gives rise to the Néel relaxation curve in Figure 1-15.

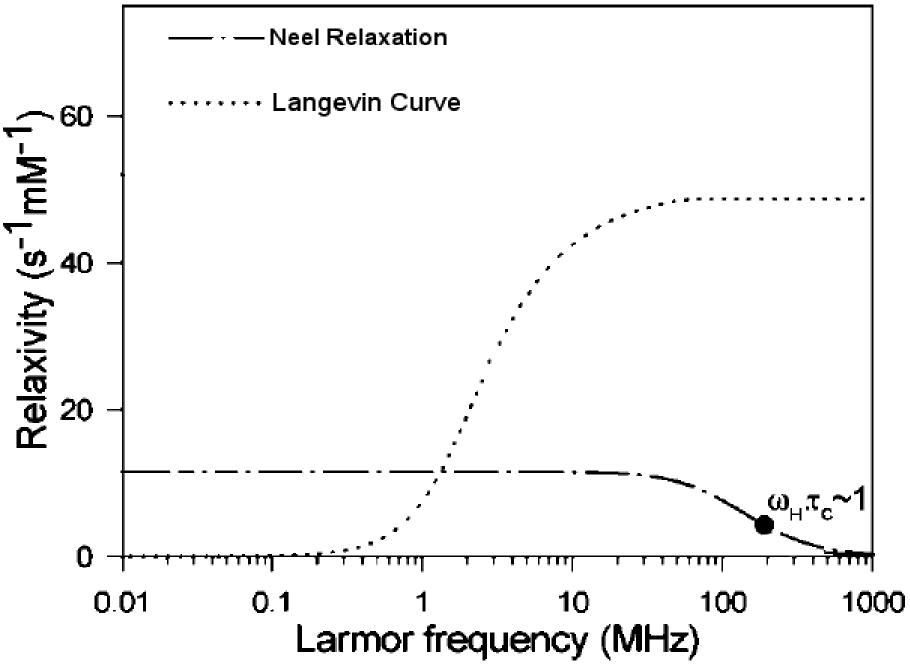

Figure 1-15 : Néel relaxation evolving with applied frequency, overlaid is the Langevin curve which shows the proportion of the magnetic moments that are locked adapted from Laurent at al [22]

The second mechanism which contributes to relaxation is Brownian motion. When the magnetic moments are locked, there is no precession of the magnetic moment relative to the diffusion of the solvent molecules. The translational diffusion of the water molecules through the magnetic moment of the nanoparticle drives the relaxation. This mechanism operates at higher frequencies, when the magnetic moments become locked, Figure 1-16; the fraction of spins locked at a given field is given by the Langevin curve.

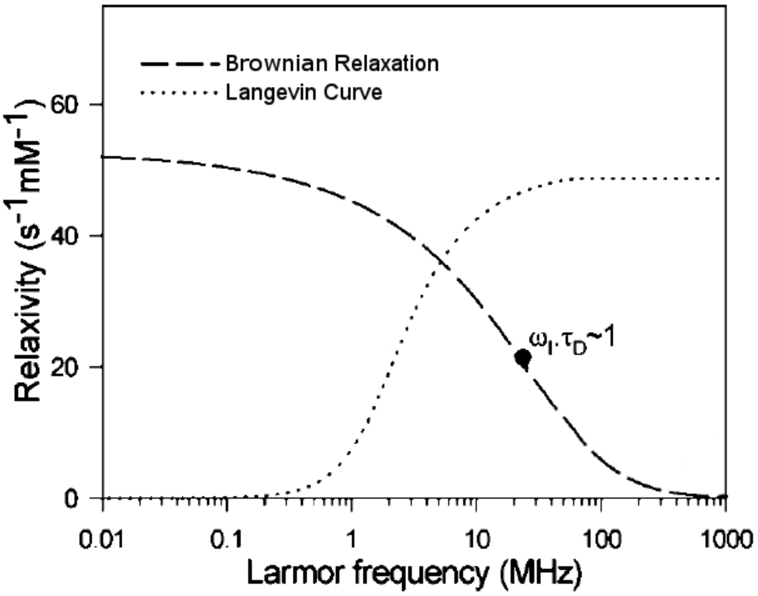

Figure 1-16 : Brownian relaxation evolving with frequency and the Langevain function which shows the proportion of the magnetic moments that are locked adapted from Laurent et al[22]

At intermediate frequencies, both relaxation processes contribute. The frequency dependence can be thought of as the Néel and Brownian contribution weighted by the Langevin function. This results in the characteristic relaxation curve of superparamagnetic materials shown in Figure 1-17.

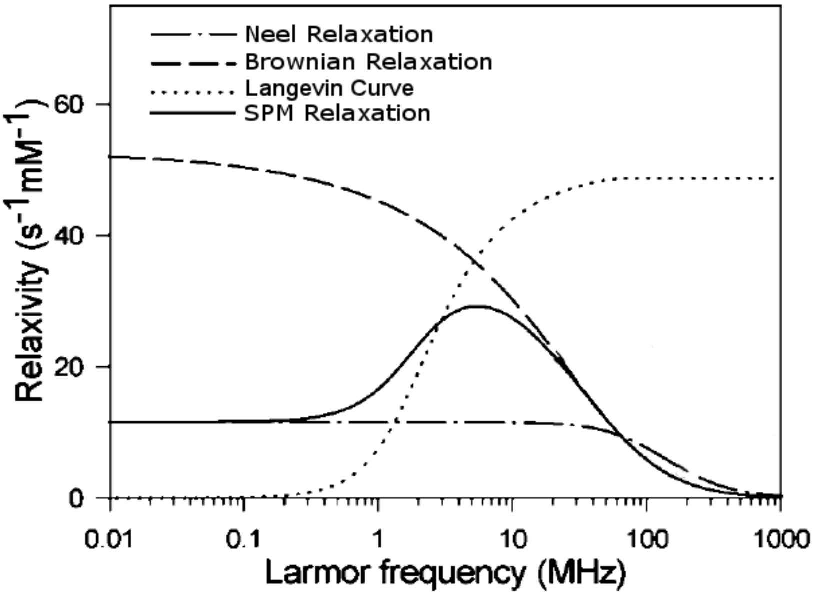

Figure 1-17: Superparamagnetic relaxation curve and the two contributing relaxation curves, Néel and Brownian relaxation adapted from Laurent at al[22]

1.4.1. Appling SPM theory to simulate experimental NMRD profile

The NMRD profile is dependent on numerous parameters arising from the two mechanisms, namely ΔE_{anis}, τ_n, the particle radius, r, and the saturation magnetisation, M_S. Muller et al have developed a mathematical model to simulate the effect of the magnetic properties on the NMRD profile [18, 22, 23]. This has led to the development of simulation software which can be used to extract, subject to the limitations of the model, the magnetic properties of the particles.

At high fields the dominant correlation time is τ_D, the diffusion of solvent past the particle. For larger particles τ_D increases (τ_D^{-1} decreases) so the inflection point for the Brownian spectral density contribution shifts to lower frequency. This is the major reason why the r_1 maximum moves to lower frequencies with increasing size [22, 23]. This effect is shown in Figure 1-18.

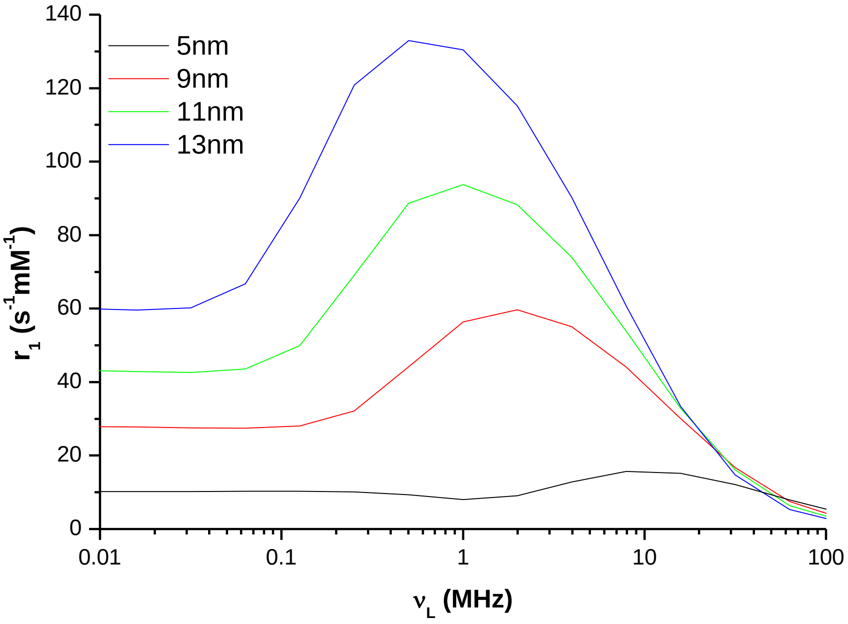

Figure 1-18 : NMRD profiles simulated using the SPM theory developed by Muller et al showing the effect of particle size on profile shape; with ΔE_{anis} = 2 GHz, τ_n = 9 ns and M_{NMR} = 40 emu/g.

The r_1 value at all frequencies is strongly dependent on the saturation magnetisation. This arises as a larger magnetic moment will create a greater field gradient around the nanoparticles. The effect is schematically shown in Figure 1-19.

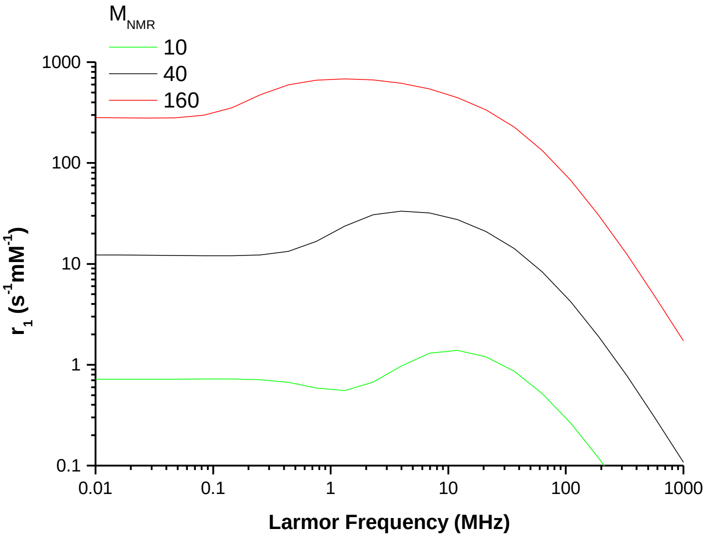

Figure 1-19 : NMRD profiles simulated using the SPM theory developed by Muller et al showing the effect of M_s on profile shape; ΔE_{anis} = 2 GHz, τ_n = 9 ns and r = 3.5 nm

The low-frequency relaxation is primarily due to the Néel relaxation mechanism. The magnetic field is not strong enough to align the particles, and rapid precession of the magnetic moments drives relaxation. The Néel correlation time is shown to be proportional to tau_0, but varies with ΔE_{anis} through a Boltzmann relationship, Equation 1-12. Thus the low-frequency portion of the curve is driven by τ_n and ΔE_{anis}, as shown in Figure 1-20.

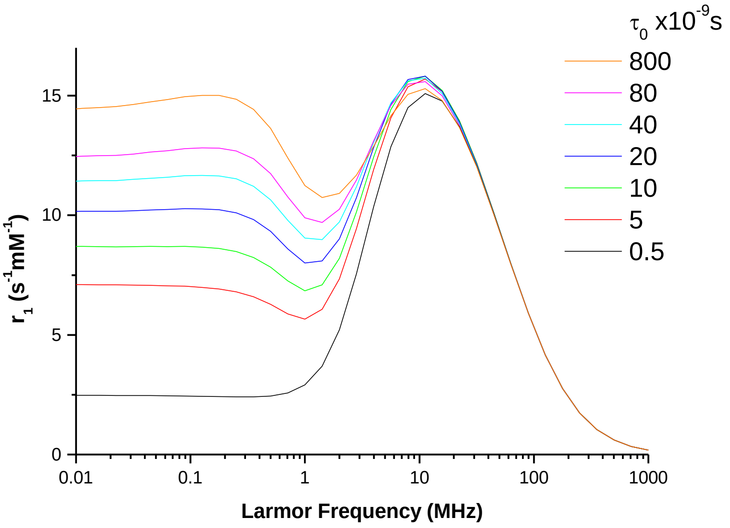

Figure 1-20 : NMRD profiles simulated using the SPM theory developed by Muller et al showing the effect of τ_0 on profile shape; ΔE_{anis} = 2 GHz, r = 2.5 nm and M_{NMR} = 40 emu/g

The appearance and shape of the mid-frequency response is dependent on a number of factors. We can see in Figure 1-18 and Figure 1-20 that particle size and Néel correlation time affect this mid-frequency minimum. Furthermore it can be seen from Figure 1-21 that ΔE_{anis} also plays a large role in determining the low-frequency portion and the mid-frequency minimum. In this frequency range an interpolation between the two relaxation mechanisms is performed. In principle, the interpolation could be re-parameterised for each sample to improve the agreement with experimental data. However, the high and the low frequency parts are key in determining the parameters of interest, so the approach adopted in this thesis has been to accept a mid-frequency discrepancy, to avoid over fitting

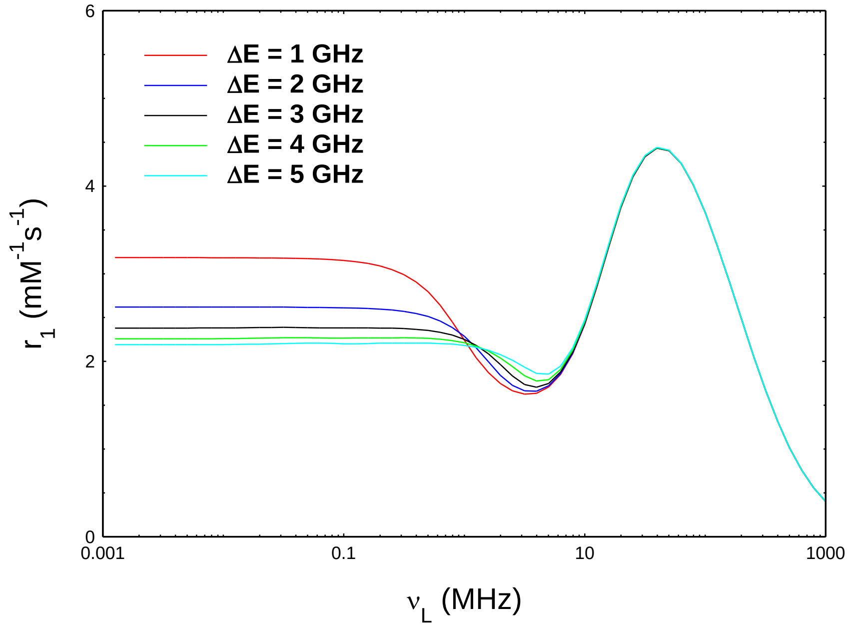

Figure 1-21 : NMRD profiles simulated using the SPM theory developed by Muller et al showing the effect of ΔE_{anis} on profile shape; r = 2.5 nm, τ_0 = 9 ns and M_{NMR} = 40 emu/g

It is clear that SPM simulations have potential to be applied to interpretation of NMRD profiles in order to extract some of the magnetic parameters of the suspensions. This approach has been established for aqueous [24] and organic suspensions[1]. In this thesis a common thread is to exploit the potential the approach offers for a wide range of particle and cluster types in many different solvents.

For primary nanoparticles, the effects of particle size on the magnetic resonance properties are well understood [18, 22-26]. There are methods that allow for the synthesis of nanoparticles of a controlled size [1, 2], however these methods are limited in terms available surface chemistries and modification post synthesis. As a result, there is a need for size controlled synthesis of iron oxide nanoparticles that are amenable to a range of surface chemistries. Furthermore, with the growing trend towards higher sensitivity MRI, there is a need to understand the affect surface coating has on the magnetic resonance properties and how these effects can be utilised to optimise magnetic resonance properties. Hence the first part of this thesis focuses on this potential. A detailed analysis of the relevant literature is provided in Chapters 3 and 4.

Furthermore, there has been much recent development in the controlled assembly of nanoparticles [27-29], for uses including separation science and MRI imaging as r_2, or negative contrast agents. However, there is a need for assembly methods that can produce nanoparticle clusters reproducibly and on a bulk scale, so that the effect of internal organisation of the assemblies on the magnetic resonance properties can be assessed. Additionally, there has been much development in generation of hybrid nano-materials [30-34] for drug delivery applications. So the ability to maximise one property, e.g. the relaxivity, while adding additional function is emerging as an important consideration. The second part of this thesis focuses on the formation and physiochemical properties of assemblies of magnetic nanoparticle in suspension. A detailed analysis of the relevant literature is provides in Chapter 5 and 6.

Chapter 2

Experimental Section

2.1. **Fast Field Cycling NMR**

2.1.1. Theory

A common experimental method used to measure the field dependence relaxation properties of materials is Fast Field Cycling NMR (FFC-NMR)[26, 35], this method is also known as FFC-NMR, or NMR Dispersion (NMRD) uses a rapidly changing B_o to probe the relaxation rate of liquids, solids and colloidal dispersions. NMRD allows the measurement of the relaxation enhancement effect of SPM nanoparticles on solvent systems such as water which makes NMRD a suitable method to probe the relaxation mechanisms of materials.

2.1.2. Experimental Set Up

Typically 0.5 to 1.5 mL of solution is placed inside a standard 10 mm NMR tube. Between the fields of 0.01MHz to 40MHz, the samples relaxation properties are measured using a Spinmaster FFC-2000 Fast Field Cycling NMR Relaxometer (Stelar, Mede, Italy). For fields above 40MHz, the sample is measured using a reconditioned WP80 NMR Spectrometer (Brucker, Massachusetts, USA). The RF pulses were controlled using a Spinmaster RF Console (Stelar, Mede, Italy). The temperature was controlled using a Spinmaster Variable Temperature Controller (Stelar, Mede, Italy). The temperature was set to 25 ±0.1 ^{0}C unless otherwise stated and allowed to thermally equilibrate at temperature for 10 min prior to measurement. During this thesis two pulse sequences were used to measure T_1; for frequencies higher than 10 MHz, a non-polarised (NP) sequence is used while for frequencies below 10 MHz a pre-polarised (PP) sequence was used. For T_2 measurements, the Non-polarized Carr–Purcell–Meiboom–Gill (NPCPMG) was used with an initial echo delay of 10 times the pulse width 90.

Non-polarised scan (NP/S)

Shown in Figure 2-1 is a typical NP sequence. Initially there is no external field so the sample has no magnetisation; B_0 is rapidly switched to the relaxation field (B_{rlx}). This time needed for the field to stabilise from one field to the next is known as the switching time (SWT), this is in the order of 1.5ms. Once at B_{rlx} the magnetisation of the sample will begin to build for a time, τ, at a rate related to the T_1 for the B_{rlx}. The field is switched to the acquisition field (B_{acq}) and once the field has stabilised, the magnetisation is rotated into the XY plane with a π/2 RF pulse. The receiver coil then measures the decay in magnetisation as the B_{xy} returns to the Z-axis/B_0 over a time (t_{acq}), Figure 2-1.

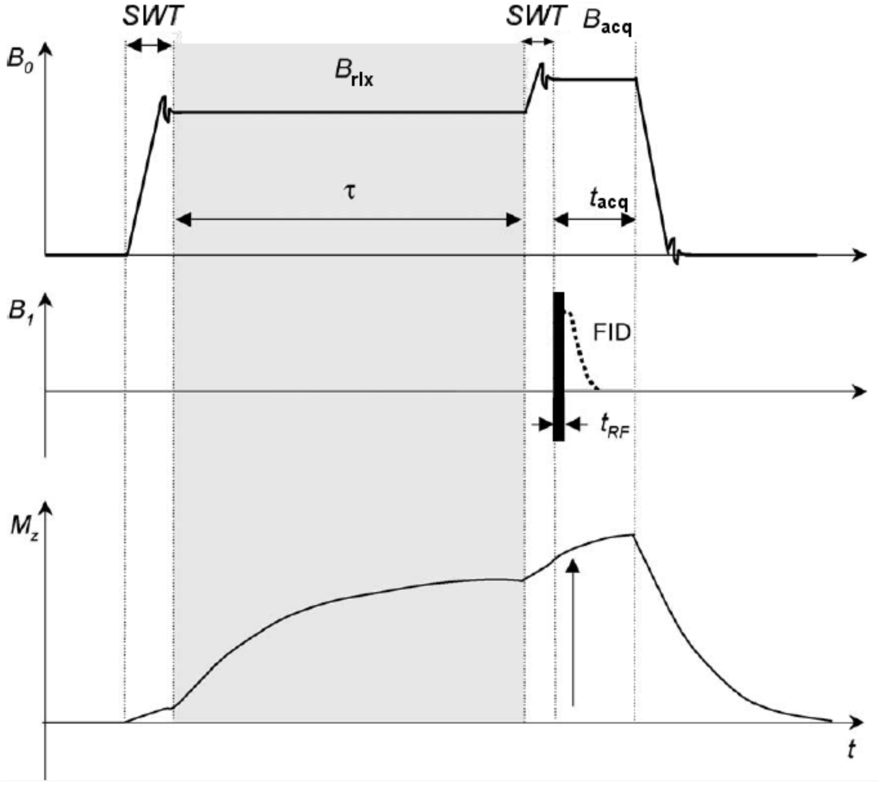

Figure 2-1 : Development of B_0, the B_1 and the M_Z throughout a typical FFC NP Sequence. t_{RF} is the π/2 pulse needed to detect the FID. τ is varied in the case of a NP/S sequence, adapted from Kimmich et al [35]

This signal is known as a free induction decay (FID). As τ increases, M_z and thus M_{xy} increases until it reaches the equilibrium magnetisation at B_{rlx}. The plot of τ versus M_{xy} will yield a magnetisation recovery curve and T_1 can be determined by fitting for a given field. This is known as a NP scan, NP/S.

Pre-polarised Scan (PP/S)

As B_{rlx} is reduced, M_{xy} decreases. Typically below a B_{rlx} of 7 MHz the M_{xy} will become more difficult to measure due to a poor signal to noise ratio. To overcome this, it is necessary to pre-polarise the sample at a high B_0, this is known as the polarisation field (B_{pol}).

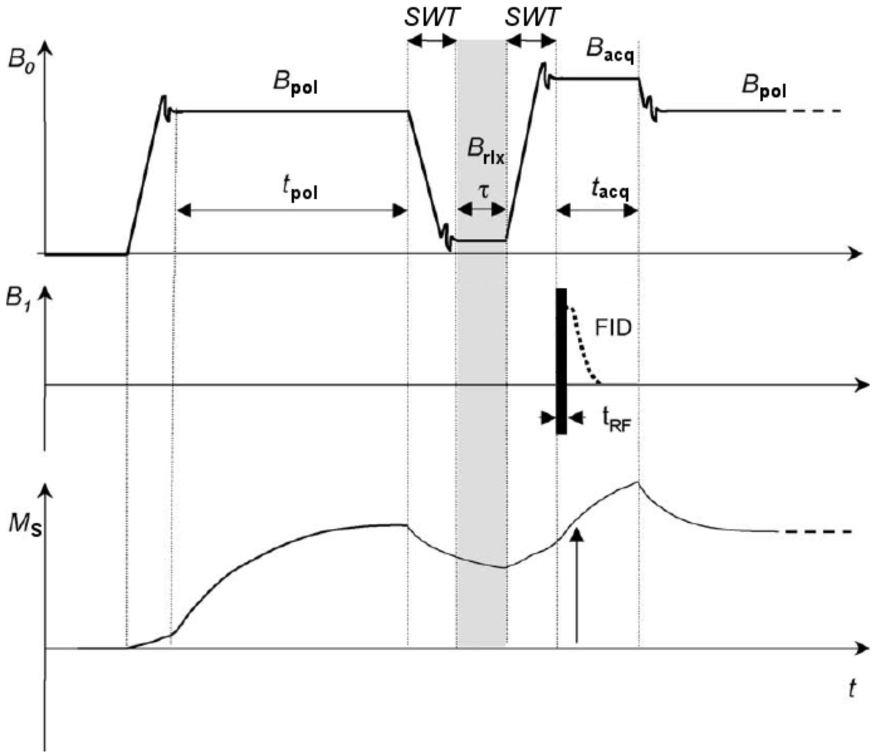

Figure 2-2: Development of B_0, the B_1 and the M_z throughout a typical FFC PP Sequence. t_{RF} is the π/2 pulse needed to detect the FID. τ is varied in the case of a PP/S sequence, adapted from Kimmich et al [35]

This sample is polarised at a higher field for a time long enough (t_{pol}) to achieve equilibrium M_z at B_{pol}. Following this, the field is switched to B_{rlx} and the magnetisation is allowed to relax for a time, τ. Following τ, the field is switched to B_{acq} and the magnetisation is rotated into the xy plane with a π/2 RF pulse and the FID is measured. As τ increases, the pre-polarised magnetisation will have relaxed further resulting in a decreased M_{xy}. Plotting τ versus M_{xy} will yield a magnetisation decay curve and T_1 can be determined by fitting. This is known as PP scan, PP/S.

Non-polarized Carr–Purcell–Meiboom–Gill (NPCPMG)

To measure T_2, we must use a different sequence where a fixed field is used. The CPMG sequence is the main sequence used to measure T_2 throughout this study. The CPMG is a variation on a spin echo delay sequence. First the magnetisation is rotated to the X-Y plane using a $\pi/2$ pulse. The spins will diphase by two processes, T_2 and T_2^*. After a time, τ, a π pulse is applied. This will invert the magnetisation and also reverse any dephasing due to T_2^*, which are systematic, but will not reverse any genuine T_2 effects as these are random in nature. This is known as an echo delay, and is characterised by the time between pulses (EDLY). As this echo delay is repeated, the magnetisation is lost due to true T_2 processes rather than T_2^* processes. This is shown in Figure 2-3.

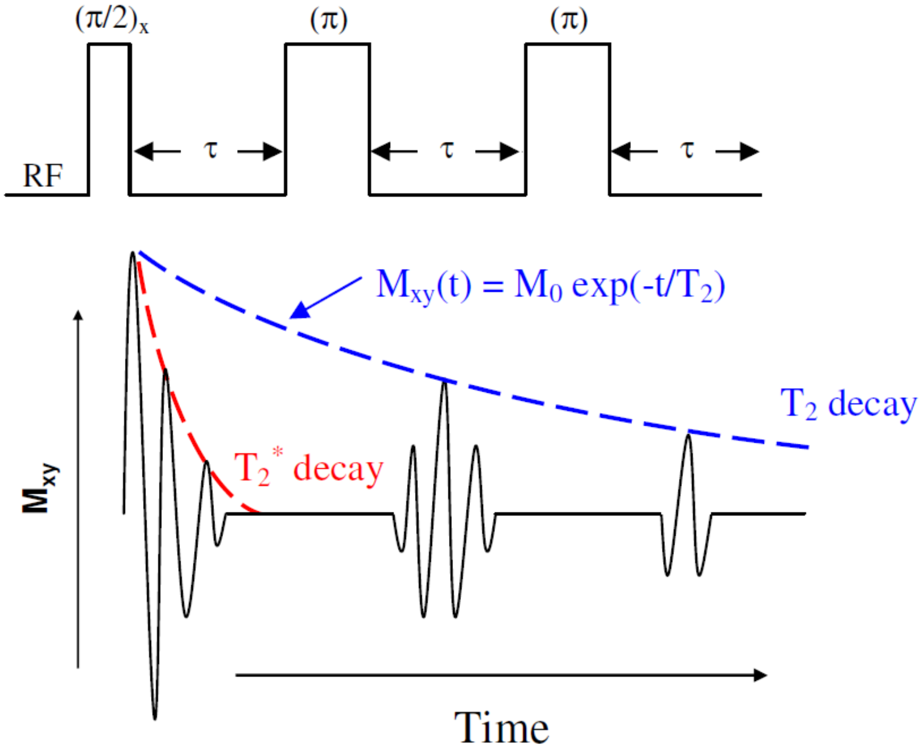

Figure 2-3: Schematic representation of a CPMG sequence performed at a fixed B_0; top graph shows RF pulse sequence with the echo delay constant (τ); bottom shows the free induction delay and the resultant T_2 delay

2.1.3. Experimental Limitations

There are a number of limitations associated with NMRD; most of these involve physical limitations of the hardware. The main limitation is associated with the magnet. The electromagnet generates heat during the switching of fields and while at field. The heat generated is proportional to the current and thus to field. Repeated excessive temperature will degrade the electromagnet. As a result for higher fields, the maximum time for τ is limited which defines the upper measurable limits of T_1. For NP suspensions this can be simply overcome by increasing the concentration of the sample thus shortens T_1. The second limitation is associated with the switching time. The switching time is 1.5 ms which means it takes 1.5ms for the field to adjust from B_{acq} to B_{rlx} and stabilise. T_1 must be at least several times longer than this or significant relaxation will occur during the time that the field is stabilising. This defines the lower limit for a measurable T_1. For NP suspensions, this problem can be simply overcome by diluting the sample thus reducing the relaxation rate.

2.2. Transmission Electron Microscopy

2.2.1. Theory

Transmission Electron Microscopy (TEM) is a microscopy technique. Typically a dispersion of nanoparticles is dried onto a Copper grid coated in Formvar which forms a very thin layer of nanoparticles on the grid. The grid is then placed inside a vacuum, where a beam of high voltage electrons (~kV) is passed through the sample. The electrons interact with the sample and some electrons are deflected or scattered by sample while most electrons pass through the sample, these transmitted electrons are focused and form an image capable of being recorded or viewed.

Traditional light microscopy can be very limited. The resolving power is limited by the wavelength of light source and as a result, as materials and particles become smaller; sub micrometer range, light microscopy cannot be used. In TEM electrons are used as the illumination source. The de Broglie relation, Equation 2-1, shows that the wavelength, λ, is inversely proportional to the momentum, p, of a particle/electron and h is planks constant. This relationship allows for the wavelength of the electron to be changed by increasing the momentum of the electron. This allows the imaging of very small (sub nm) features.

$$\lambda = \frac{h}{p}$$

Equation 2-1

In Figure 2-4 a schematic representation of a TEM. Positioned along the TEM are a series of lenses which act to focus the beam of electrons onto the sample. The electrons that are focused onto the sample interact with the sample, a number of electrons are deflected by the sample. The scattering intensity is approximately proportional to the square of the atomic number, so larger atoms such as heavy metals will deflect more electrons thus appearing darker then lower atomic numbered elements. Hence we can obtain real information with regards to size and shape of particles. This is especially useful in our case as we can physically see the size and shape of the metal oxide nanoparticle cores.

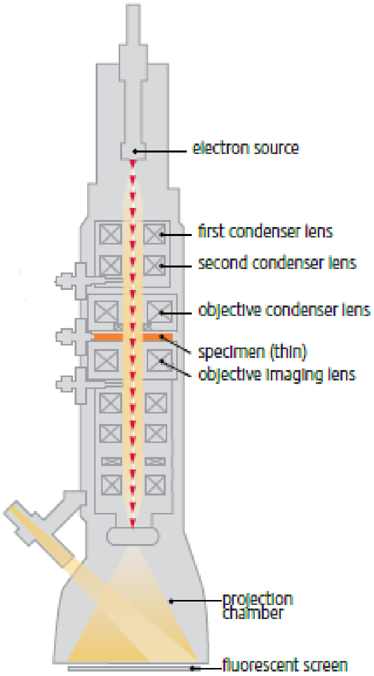

Figure 2-4 : Schematic representation of a TEM with the typical bean focusing lenses identified

2.2.2. Experimental Set Up

Typically NP dispersions are diluted to a range appropriate with TEM (0.2 – 1mM). One drop of diluted dispersion was spotted on 3.05mm diameter copper grid. This grid comprised of a 400 square mesh coated in formvar with a thin layer of carbon evaporated onto the grid for extra stability and to render the sample conductive for the generation of electrons. The grids were supplied by Agar scientific and used as supplied. The machines used were a Tecnai G^2 12 BioTwin (FEI, Oregon, USA), acceleration voltage 120kV equipped with a Megaview III camera (Olympus, SIS, Münster, Germany) and a Tecnai G^2 20 (FEI, Oregon, USA), acceleration voltage 200kV equipped with an Eagle 4k CCD camera (FEI, Oregon, USA). The grids were placed in a topography grid holder and measured at an angle of 0^o tilt with respect to the beam.

2.2.3. Experimental Limitations

There are some limitations to TEM; the first arises due to the sampling method. For TEM a volume of dispersed sample is spotted and evaporated onto a TEM grid, leaving behind deposited NP. The particles dry as a thin flat film on the grid which can disrupt the structure the particle adopts in solution. The second limitation arises from the materials themselves and their interaction with the electrons. As mentioned in the theory, larger nuclei appear darker while smaller nuclei appear lighter. This raises two issues; if two nuclei have similar atomic numbers, it may be hard to distinguish between the two nuclei. Furthermore, there is a limit to the different in contrast that can be recorded. For examples when analysing molecules with large Z-numbers (such as metals) and molecules with a small Z-number (such as carbon coatings), it can be hard to distinguish between the two nuclei. Finally, TEM relies of the transmission of electrons through a sample to form an image, this limits the thickness of a sample.

2.3. **Dynamic Light Scattering**

As mentioned in Chapter 1, the volume or size of the magnetic core plays a major role in determining the magnet properties. TEM allows you to measure the size and shape of the particles metal oxide core, it is a limited technique when it comes to yielding information such as size and dispersion of particles in solution. This information is vital in understanding and comparing results of different dispersions. Therefore it is crucial to be able to measure the actual size of the particle in solution and measure the dispersity of the particles while they are in solution. These can be measured using Dynamic light scattering (DLS).

2.3.1. Theory

DLS is a non-destructive analytical technique which measures the intensity of light scattered by suspended particles over time. Figure 2-5 shows a typical arrangement of a DLS instrument, the DLS comprises of 3 parts; a monochromatic light source which produces very uniform light, the sample (placed inside a cuvette) and a detector which consists of a photodiode array which counts the photons scattered. The light hits the dispersed particles, scattering the light. The DLS measures how the scattering of light varies with the time.

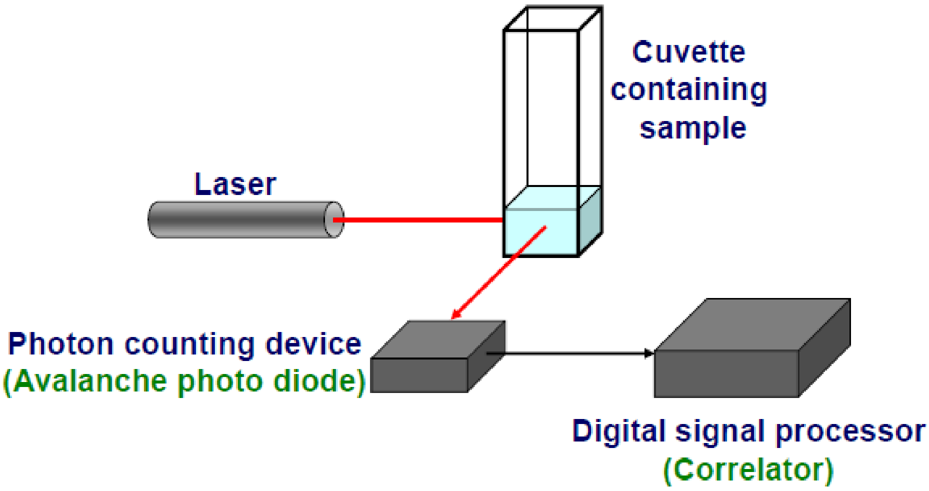

Figure 2-5 : Schematic representation of a dynamic light scattering instrument set up adopted from ,adapted from Malvern technical notes [36]

In order to fully understand the scattering of light by suspended particles, we must examine a system of dispersed nanoparticles. Particles dispersed in solution undergo Brownian motion which is a random motion of particles caused by the collision of fast moving solvent particles with particles. These range of motions, in a DLS experiment, result in fluctuations in the light. These fluctuations are related to the velocity of the Brownian motion. Simply smaller particles will diffuse faster and thus will have cause faster fluctuations of light; conversely larger particles diffuse slower and will cause slower fluctuations of the scattered light, Figure 2-6.

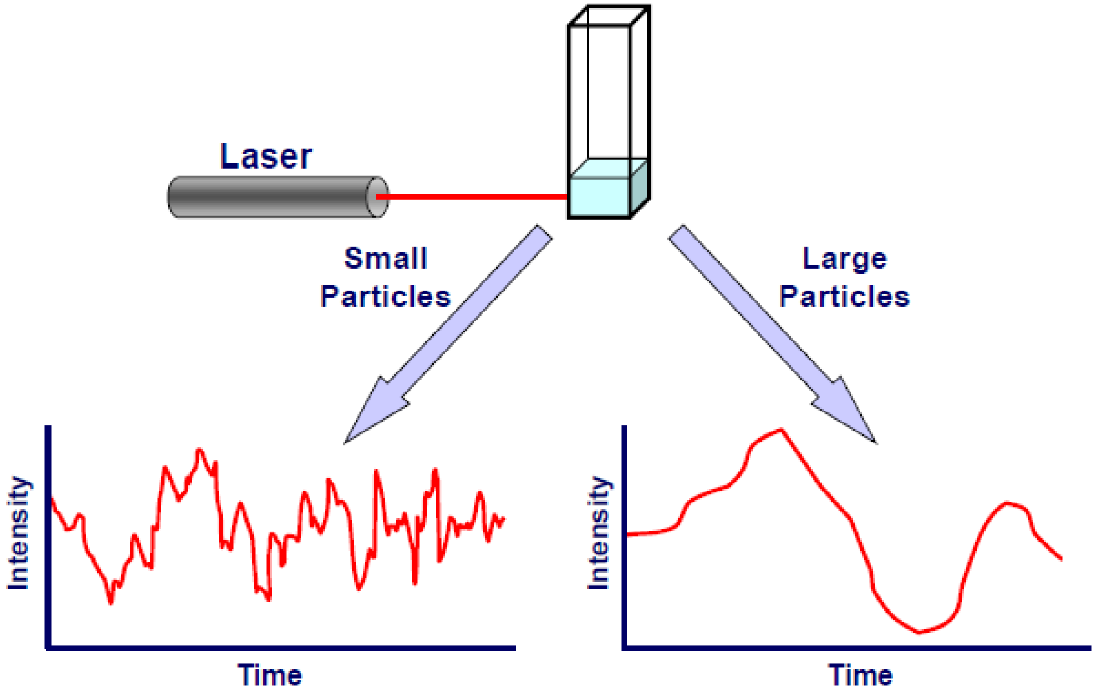

Figure 2-6 : Schematic representation of the effect particle size has on the fluctuations of scattered light, adapted from Malvern technical notes

These fluctuations are related to the translational Diffusion coefficient (D) of the particles which is related to the hydrodynamic size (d_{HYD}), Equation 2-2 where η is the viscosity of the solvent, T is the temperature (K) and k is Boltzman constant.

$$d_{HYD} = \frac{kT}{3\pi\eta D}$$

Equation 2-2

If we have a truly random fluctuation due to one size of dispersed particles, the intensity of a signal, compared with itself at a later time interval will have no relation/correlation. However if we compare it with itself at a very small interval, τ, there will be a strong correlation. If we take a slightly larger time interval, the signal will still correlate, but will correlate less, Figure 2-7. Thus with increasing time, the fluctuations will correlate less until such a time as the signal is no way related to itself. The speed at which the correlation decays from 1 (perfect correlation) to 0 (no correlation) is related to the translational diffusion coefficient (D). For smaller particles, the correlation will decay over a short time scale, in the order of micro/nanoseconds. For larger particles, the correlation, G(τ) will be longer lived and is proportional to the intensity of light at a time t. Examples of correlograms are shown in Figure 2-8.

$$\boldsymbol{G(\tau)} = \langle \frac{\boldsymbol{I(t) * I(t + \tau)}}{\boldsymbol{I\,(t)^2}} \rangle$$

Equation 2-3

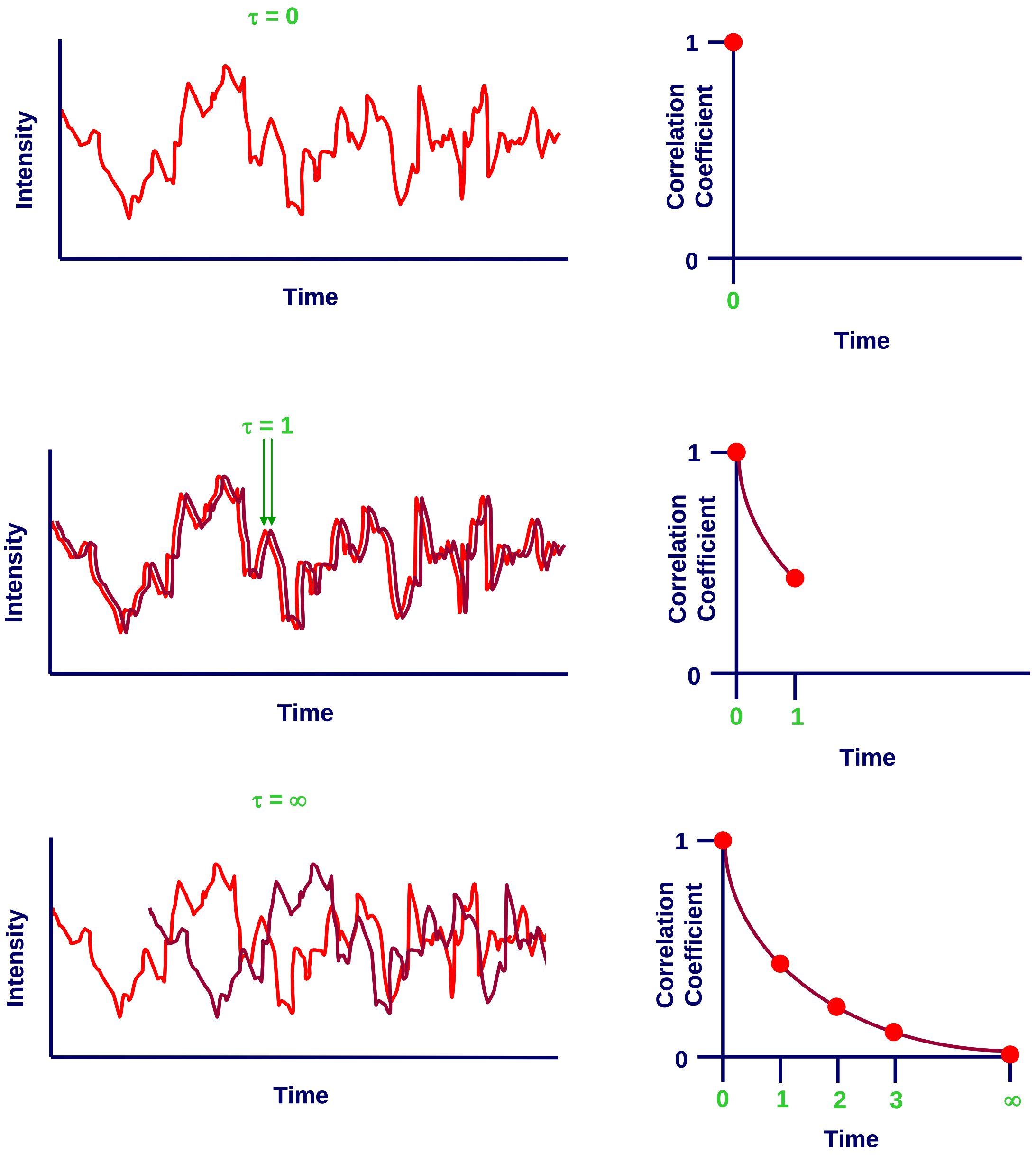

Figure 2-7 : Schematic representation showing how the correlation function is constructed, adapted from Kazuba et al[37]

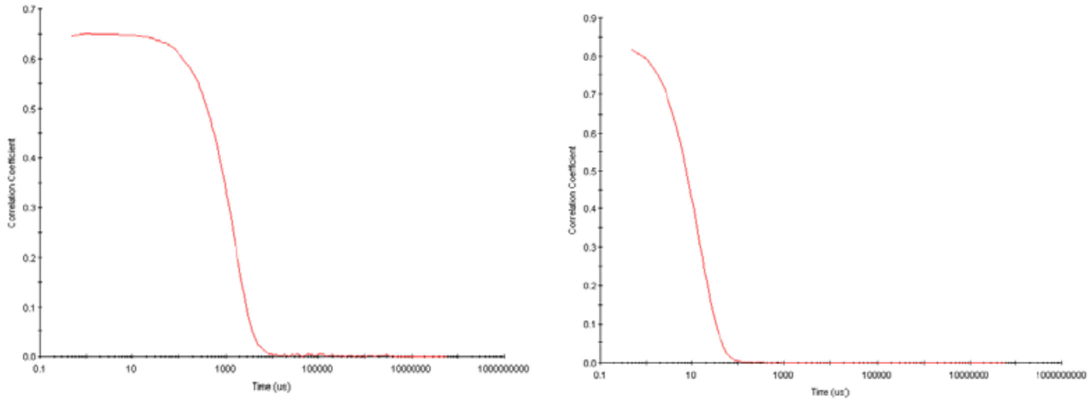

Figure 2-8 : Left diagram showing a sample correlation diagram for large particle (>100 nm); Right graphs shown a sample correlation diagram for small particles (~20 nm)

Using this correlogram, there are two methods by which we can extract the translational diffusion coefficient; the cumulants analysis and the distribution analysis. The first method; cumulants analysis, is defined in international standards ISO13321 and ISO22412 where a natural log is applied to the correlation coefficient (y value) and a three term polynomial is fit to the curve.

$$Ln(G)=a+b\tau+c\tau^2$$

Equation 2-4

From Equation 2-4; b is the z-average which is an intensity weighted mean particle size. The dispersity of the solution is measured by the poly dispersity index (PDI). This is an arbitrary number which is a measure of the broadness of a size distribution. It ranges from 0-1, where 0 is truly monodisperse, and 1 being fully poly disperse and is calculated from Equation 2-4, PDI equals $2c/b^2$.

The alternative method of generating the translational Diffusion coefficient is by fitting an exponential model to the data shown in Equation 2-5, where B is the baseline, A is the intercept and q is the scattering vector calculated by $q=\left(\frac{4\pi n}{\lambda_0}\right).\sin\left(\frac{\theta}{2}\right)$, where n is the dispersant refractive index, θ is the measurement angle and λ_0 is the laser wavelength. From the diffusional coefficient, the hydrodynamic size can calculated using the Stokes-Einstein equation, Equation 2-2.

$$G(\tau) = B + \sum e^{-2q^2D\tau}$$

Equation 2-5

The size measured by DLS is different to the size measured by TEM. This is because every particle is stabilised in solution using a stabilising ligand. This ligand in solution becomes hydrated and extends/swells. The DLS measures the entire size of the particle and the associated solvent molecules while, on the other hand, TEM only measures the size of the core of the particles. Thus there is a systematic difference between the DLS and TEM size, which will be referred to as d_{HYD} or d_{TEM}. In addition, the intensity weighted size distribution as measured by DLS is shifted towards larger sizes because the contribution of NPs in the intensity-weighted size distribution scales with the 6th power of diameter.

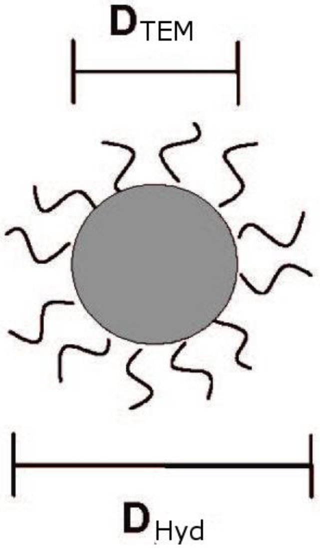

Figure 2-9 : Schematic representation showing the difference in size extracted from DLS and TEM

2.3.2. Experimental Setup

DLS measurements are carried out on either a High Performance Particle Sizer (HPPS) or a NanosizerZS (Malvern Instruments; Worcestershire UK). Typically organic solutions are placed in a 1cm by 1cm (internal dimensions,i.d)glass or quartz cuvette. Aqueous solutions are placed in disposable 1cm by 1cm (i.d) cuvettes. For low volumes of solutions, low volume glass or plastic cuvette are used. The measurement takes place at 25°C unless otherwise stated and allowed to thermally equilibrate for 3 minutes prior to the measurement. A He-Ne 5mW laser operating at 632.8nm is used as the light source. For back scattering the detector angle is set to 7° with respect to the incident beam. For forward scattering, an angle of 180° is used with respect to the incident beam. Unless otherwise stated the back-scattering angle was used. This results in an eight fold increase in intensity [38] over forward scattering which allows for greater sensitivity during measurements due to improved signal to noise ratio.

2.3.3. Experimental Limitations

In theory, there is no limit in the size range DLS can measure. Once we measure the scattered light, with a very high sampling rate (in the order or MHz), we can measure the smaller fluctuations of the smaller particles. In practice this isn't the case. According to Rayleigh scattering theory, if a particle is sufficiently smaller than the wavelength source ($d < \lambda/10$) then light is scattered in an isotropic fashion. Rayleigh theory approximates that the intensity of scattered light is proportional to the sixth power of diameter of the particle i.e. $I = d^6$ .In essence, the larger the particle, the more light that will scattered. Thus as the particle size drops, the intensity of the scattered light also drops the measurement is limited by sensitivity of the detector and the stability of the measurement. According to Rayleigh approximation, intensity of scattered light is proportional to the d^6. For bimodal or polydisperse, it is a concern that the smaller particles are masked or hidden by the scattering of the large particles.

Another limitation of DLS is the concentration range of the sample. As the concentration drops, so does the intensity of scattered light. If the concentration becomes too great, the scattered light on its path back to the detector may be scattered by further particles. This is referred to as multiple scattering. This results in an underestimation of the size. For this work the working concentration range was between 0.5 mM to 5 mM [Fe].

2.4. Inductively Coupled Plasma Atomic Emission Spectroscopy

2.4.1. Theory

Inductively Coupled Plasma Atomic Emission Spectroscopy (ICP-AES) is a qualitative and quantitative analytical technique designed to detect trace amounts of elements suspended in solution. It consists of two parts, the ICP and the optical AES detector. The ICP produces excited atoms and ions that emit EM radiation. This radiation is specific to each element and the AES detects and records the EM radiation. In ICP the torch head consists of concentric quartz tubes, surrounded by a radio frequency (RF) coil, Figure 2-10.

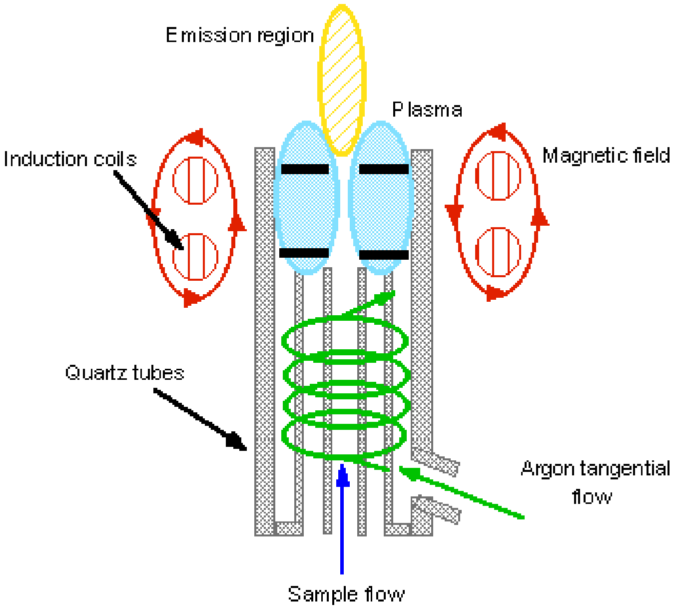

Figure 2-10: Schematic representation of the torch head of an ICP-AES, used under the Creative Commons sharing License [39]

Argon gas flows through the quartz tubes which is surrounded by RF coils that produce a high powered (~kW) RF signal. This high powered RF signal creates a very intense magnetic field inside the coil. The argon gas flows in a rotational manor towards the magnetic field that then ionises the argon and the rotational flow creates inelastic collisions between the ions and the neutral atoms. This results in a stable, high temperature plasma torch of ~7000K. Meanwhile the dissolved sample is pushed through a nebuliser using a peristaltic pump and the resultant fine mist wets the argon gas and is carried into the torch assembly. Once inside the plasma, the intense collisions with electrons and ions result in the molecules breaking up into their individual atoms when the outer shell of electrons of the elements are thermally excited jumping to an elevated energy state. As the electrons fall back to their ground state, they release a photon of light at particular wavelength which is then measured by the detector. This emitted light is then focused onto a diffraction grating which separates the light into its individual wavelength components, thus producing an emission spectrum specific to each element.

It is necessary to plot an external calibration curve with a range of known concentrations of the analyte. A 998±2mg/L iron standard (Fe $(NO_3)_3$ in 1M Nitric, Merck Chemicals, Darmstadt, Germany) was used to make up the curve. The curve ranged from 0.05mg/L to 10mg/L ($8.9x10^{-7}$ to $1.7x10^{-4}$ M) Fe. A linear fit was used to calculate the iron concentration.

2.4.2. Experimental Setup

The Fe concentrations of the different dispersions were measured using ICP-AES, as described in Chapter 2. To digest the NPs, a standard acid digestion method was followed [1]. Typically 100 to 200 µL of the dispersion was placed into a conical flask and covered. Over time the solvent will evaporate leaving behind the NPs. 1 mL of concentrated HCl (36% reagent grade) was added to the flask. This was heated until the volume of the solution was reduced to ~100 µL. 3 mL of deionised water was added to the flask and the solution was heated to boiling. This solution was allowed to cool and was quantitatively transferred to a volumetric flask and made up to the mark using 1 M nitric acid (dilution of min 65% reagent grade). The calibration curve was linear in the range 0.01 ppm to 10 ppm, in all cases $R^2 > 0.995$. The solutions were then analysed using a Liberty 220 ICP Emission Spectrometer (Varian Inc, Agilent Technologies, Santa Clara, USA). A RF power of 1.1kW was used and premium Argon (Air products, Dublin Ireland) was used as the plasma gas.

2.5. ATR-IR Spectroscopy

2.5.1. Theory

Attenuated Total Reflectance Infra-red (ATR-IR) Spectroscopy is a variant of IR Spectroscopy. It is a non-destructive analytical method where a sample (liquid or solid) is placed onto a crystal. In the case of a solid, it is pressed onto the crystal to increase surface contact. This variation of IR spectroscopy relies on total internal reflection. This occurs when two mediums of differing refractive indices are in contact and a light is focused through them. In the case of ATR-IR, the IR beam is transmitted through a transparent crystal; this crystal has a higher refractive index than the sample placed on the crystal. If the angle of the transmitted beam is greater than the critical angle, the beam will be internally reflected. At the boundary between the crystal and the sample, the IR beam will penetrate into the sample. This is known as an evanescent wave which is the same frequency as the incident light but the intensity decays exponentially with distance from the crystal surface (z), $E = E_0 . e^{-z/d_p}$ where d_p is the depth of penetration which is proportional to wavelength, λ , the incident angle, θ and the refractive index of the material, η , Equation 2-6.

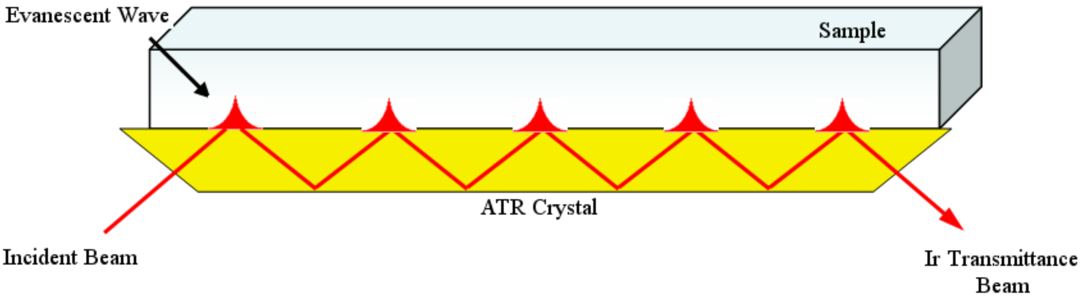

Figure 2-11 : Schematic representation of total internal reflectance and the evanescant waze of ATR-IR, adapted under, used under the Creative Commons Sharing Lisence[40]

$$d_p = \frac{\lambda}{2\pi\eta_{crystal}\left(\sin^2\theta - \left(\frac{\eta_{sample}}{\eta_{crystal}}\right)^2\right)^{\frac{1}{2}}}$$

Equation 2-6

2.5.2. Experimental Set up

The instrument used was a Spectrum100 FT-IR equipped with a ZnSe crystal Universal ATR attachment (PelkinElmer, Massachusetts, USA). For solid samples, a spatula tip of material was placed on the crystal, and the pressure arm was tightened until the pressure gauge read ~90. For liquids, a drop of the analyte was placed on the crystal and the spectrum measured.

2.5.3. Experimental Limitations

For this experimental set up the main limitation with this technique as opposed to traditional IR is the analyte must be compatible with the ATR ZnSe crystal. ZnSe has a limited working pH range of 5-9. However, a diamond equipped ATR crystal can be used to overcome this. In traditional IR spectroscopy, path length of the EM wave is dependent on the thickness of the sample. In ATR-IR there is also a dependence on the wavelength of the light, Equation 2-6. Thus the spectrum must be corrected accordingly. This is done, post analysis using an ATR correction algorithm provided within the analysis software.

2.6. Thermogravametric Analysis

2.6.1. Theory

Thermogravametric Analysis (TGA) is a destructive form of thermal analysis. A sample is heated and the weight change is measured throughout the heating process. The precision balance is made up of a pan balance with an empty platinum pan acting as a counterweight. The rotation of this arm when loaded is measured electronically and this is correlated to weight. The pan is lowered into a furnace, which is purged using an inert gas. The gas ensures no unintended oxidation occurs due to O_2 present in the furnace. The furnace and pan are heated to a user defined temperature (up to 1000^{O}C), with a user defined heating ramp. The weight is constantly measured during the heating profile and weight loss versus temperature is plotted.

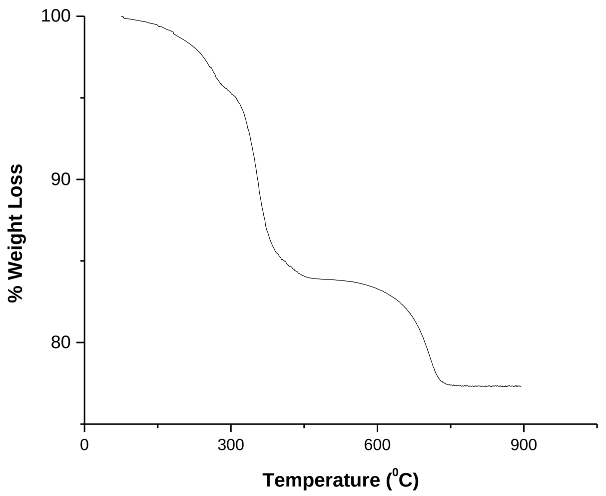

Figure 2-12 : Example TGA % weight loss curve showing different weight loss features

2.6.2. Experimental Setup

For particles dispersed in organic solvents, initially the samples were dried under N_2 gas. Next the samples were further dried in a Weiss-Gallencamp vacuum oven (Loughborough, United Kingdom), set to ~75^{0}C using bench top vacuum. For aqueous dispersions or for synthesised surfactants, these were freeze dried overnight. For a typical measurement ~5-40mg of analyte was loaded into a platinum pan and placed inside a Q series™ Q-50 Thermogravametric Anaylser (Ta Instr-uments, Delaware, USA). N_2 gas pumped in at 50ml/min was used to ensure an inert atmosphere throughout the measurement.

To help in the identification of weight loss features, the data is often differentiated. This allows identification of the peeks by showing areas of greatest change with respect to weight, Figure 2-13.

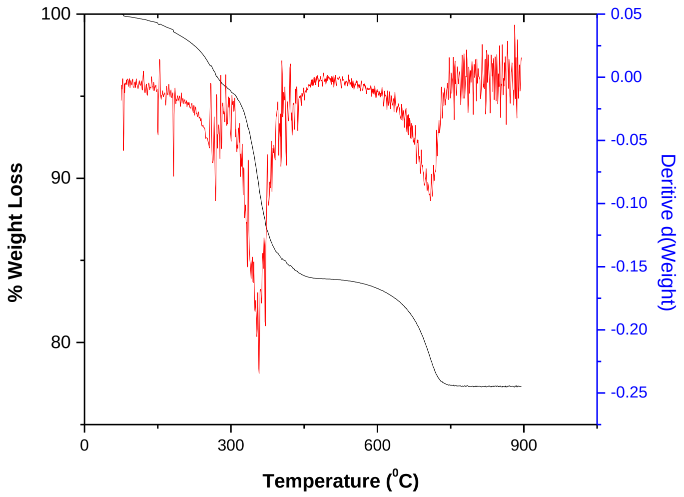

Figure 2-13 : Example of a TGA % weight loss curve (—) overlaid with a deritive weight loss curve (—)

2.6.3. Experiment Limitations

The TGA uses a high precision balance. This balance is capable of measuring sub-mg weight ranges. Within this weight range environmental factors can play a significant role; such as vibrations in close proximity to the machine, quality in regulation of flow for the inert gas into the furnace and how level the machine is. To overcome these external factors it is necessary to use a larger weight so the measured weight change is maximised. This reduces the relative effects of external factors. Secondly as the instrument is measuring two variables; temperature and time it is necessary to insure that the machine is properly calibrated.

Chapter 3

Sized Controlled Synthesis of Magnetic Nanoparticles

3.1. **Introduction**

Magnetic nanoparticles (NPs) due to their size dependant properties are a versatile material which can be used for a wide range of application, including biomedical applications, water purification, catalytic supports[4], data storage[3] and ferrofluids among others. The biomedical application of magnetic NPs range from diagnostics; Magnetic Particle Imaging (MPI)[6] and as contrast agents for Magnetic Resonance Imaging (MRI)[5] to therapeutics; for intelligent drug delivery[7, 8] and as hyperthermia mediators[41] for cancer treatment. NPs size dependant magnetic properties arise from surface area and volume considerations. Control over NP size is therefore essential in determining the emergent magnetic properties.

Currently there are two main protocols for synthesising iron-oxide NPs; surfactant assisted thermal decomposition of an organic iron precursor [1, 2, 42, 43], and alkaline co-precipitation of iron salts [44, 45]. These methods are not without their short comings. The surfactant assisted thermal decomposition of an organic iron precursor yields crystalline NPs of controlled size with good mono dispersity. The surfactants also act as the stabilising ligands and, typically are present in a huge excess[2]. Hence, the resultant NPs are fully soluble in organic media. However, for biomedical applications, the particles must be soluble in aqueous media so there have been several phase transfer and ligand exchange methodologies developed [42, 43, 46, 47]. These methods often fail to maintain the mono-dispersity and dispersion of the original organic suspension and can lead to significant NP aggregation. The alternative method involves the alkaline co-precipitation of iron salts. This method produces NPs with good M_S values (50 – 60 emu/g)[44, 45] that are hydroxyl functionalised and can be easily phase transferred into water. However, the NPs have poorly defined crystal shape when compared to particles synthesised using thermal decomposition and the resulting dispersions have a relatively poor mono-dispersity. On the contrary, certain thermal decomposition protocols, like the "seed mediated growth", produce spherical and monodisperse

NP but have poor magnetic properties due to internal crystal defects [48]. These limitations present the need for an alternative method for synthesising NP.

Turning to the issue of size control, previously the size controlled synthesis of iron oxide nanoparticles was published by Sun et al. [2]. This used a method known as surfactant assisted thermal decomposition of an organic iron precursor to synthesise NP seeds, and by adding further precursor to these, the NPs could be grown to a larger size. Unfortunately this method has the limitations associated with the surfactant assisted thermal decomposition discussed above and it usually results in imperfect crystals, with potential for magnetic frustration at grain boundaries arising from the sequential nature of the synthesis. Another approach is to use a single step reaction but to modify the surfactant to precursor ratio [1, 49]; control of size from 3 to 15 nm was achieved. Once again this method has the usual limitations associated with surfactant assisted thermal decomposition.

In this Chapter a synthetic method published by Pinna et al.[50-52] has been used to prepare monodisperse suspensions of maghemite NPs and by varying the synthetic conditions, i.e. reaction time, reaction temperature, or by varying the ratio of precursor to solvent, we have achieved control over the size of the NPs. The results were confirmed using both transmission electron microscopy (TEM, FE-STEM) and light scattering (DLS). The magnetic resonance properties of heptane dispersions was measured using fast field cycling nuclear magnetic resonance dispersion (NMRD) and by using the SPM model developed by Muller et al.[18, 23], size dependant magnetic properties were confirmed. This method produced NPs with a higher saturation magnetisation (M_S) than other previously reported nanoparticles of the similar composition and size. Additionally the effect of the width of the size distribution on the magnetic resonance properties was investigated using NMR. For the first time it was found that the width of the size dispersion has a large effect in the magnetic resonance properties and the magnetic resonance properties can be dramatically increased by reducing the size dispersion width. An important advantage of the method is the stabilising ligand is added in a second step and therefore the type and surface excess can be controlled. This is a key point for the work persistent throughout this thesis.

3.1.1. Reaction Mechanism for Nanoparticle Formation

Before we examine the results we must examine the synthetic mechanism for the formation of NPs in solution. The mechanism can be separated into three separate phases, saturation, nucleation and growth. This model was first proposed by LaMer and Dineger[53] for disulphide (S_2) systems. The first stage deals with the increase in concentration of, in our case, Fe-OH. The concentration increases to a critical concentration, known as supersaturation (Figure 3-1-I), where we have a burst of nucleation, where nucleation sites are spontaneously created, Figure 3-1-II. The NP nucleation sites then undergo growth by diffusion of Fe (the monomer) from solution onto the nucleus, thus lowering the concentration of the monomer. Thermodynamic forces drive this process; atoms at the surface have a higher energy than atoms in the bulk [54], by forming larger NPs which have a lower surface area to volume ratio the global energy of the system is reduced. This diffusion growth continues until the Fe-OH concentration diminishes (Figure 3-1-III).

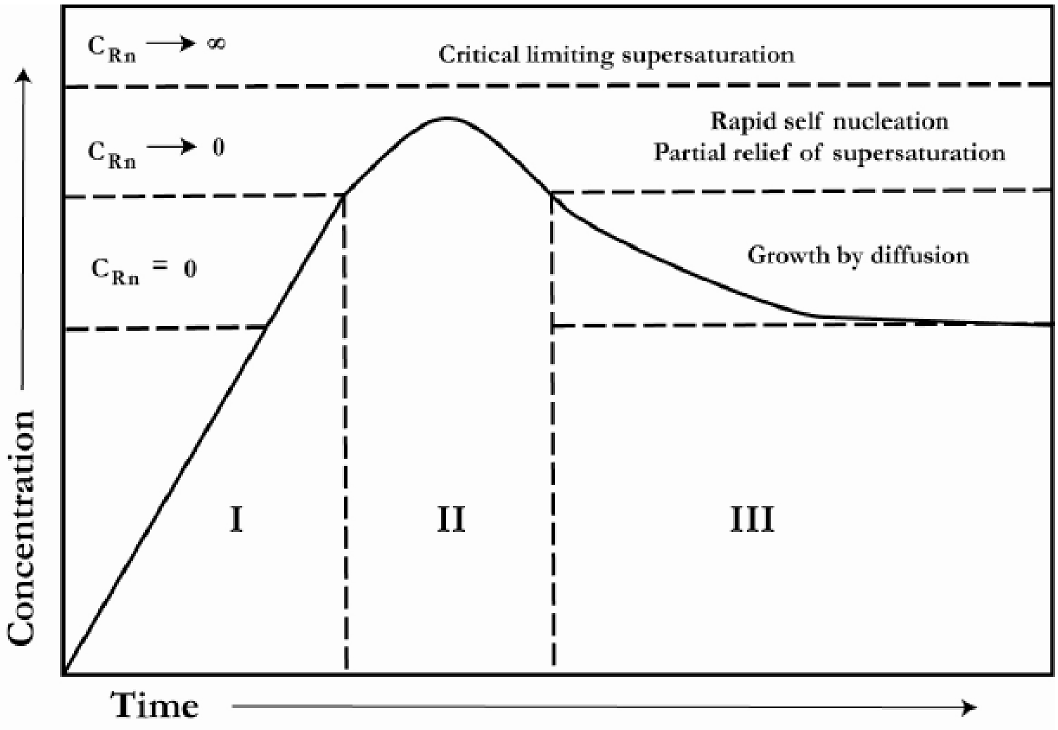

Figure 3-1 : Schematic representation of the evolution of the monomer concentration (y-axis) during a nanoparticle synthesis, adopted from LaMer et al [53], identifying the role of supersaturation of monomer concentration in the nanoparticle nucleation event

Monodisperse NPs can be created by ensuring a rapid or a burst of nucleation and also by temporal separation of the nucleation and growth stages. This ensures that all nucleation sites are formed before any growth starts, which allows all nuclei to grow from the same time. This theory has been further developed to include two further mechanisms, coalescence and Ostwald ripening. Coalescence is the mechanism by which two NP collide due to Brownian motion at an appropriate geometry for the particles to merge [55, 56] as shown in Figure 3-2-IV. Ostwald ripening was originally proposed by Wilhelm Ostwald to describe the recombination of droplets in oil in water emulsions, it has been commonly applied to NP synthesis [57]. Over time, smaller NPs will give up material to larger particles to increase the size of these NPs (Figure 3-2-V).

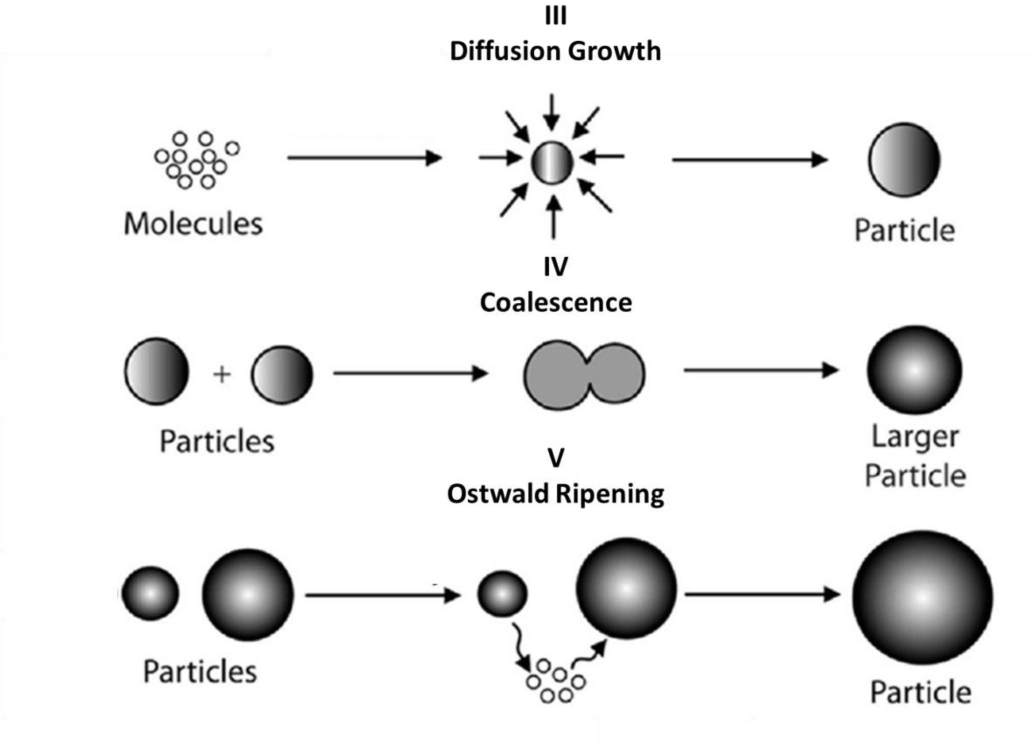

Figure 3-2 : Schematic representation of the different mechanisms of nanoparticle growth, recreated from Layek et al [58]

The reaction used throughout this thesis involves the thermal decomposition of iron (III) acetylacetonate in benzyl alcohol in the absent of surfactants. The reaction mechanism has been elucidated by Pinna et al [50, 51] using analysis of the organic by products. Initially a carbonyl of the acetylacetonate undergoes nucleophilic attack from benzyl alcohol (Figure 3-3-1); this complex then undergoes alcoholysis forming an enolate and elimination of benzyl acetate (Figure 3-3-2). The Fe centre is then attacked by a benzyl alcohol forming an alkoxide (Figure 3-3-3) which is attacked by the enolate leading to the release of 4-phenyl-2-butanone (Figure 3-3-4) and the formation of the Fe-OH source (Figure 3-3-5).

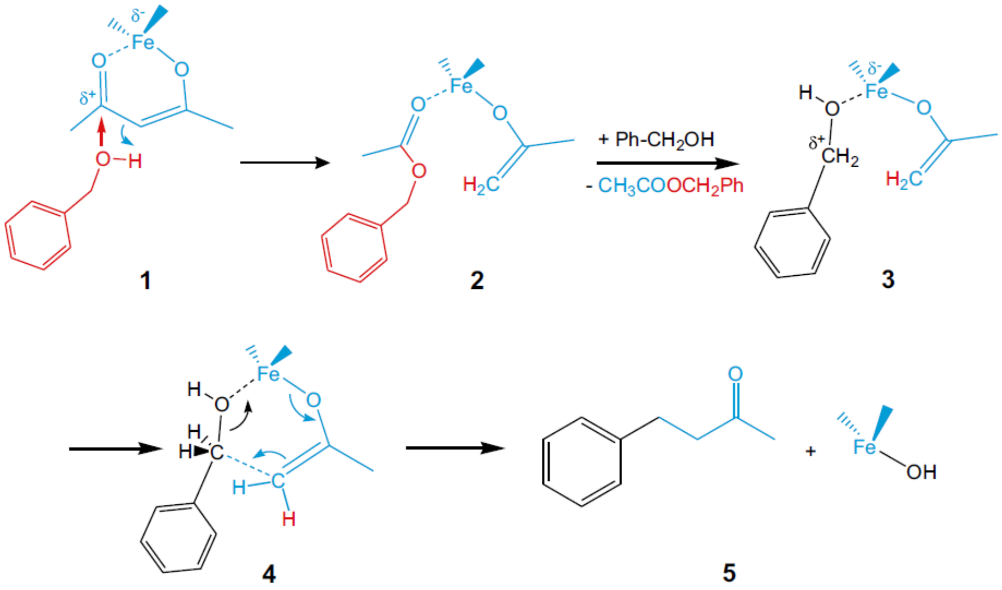

Figure 3-3 : Reaction mechanism of benzyl alcohol and iron (III) acetylacetonate, reproduced from Niederberger et al [50]

This chapter describes size controlled synthesis of iron oxide NP, which is achieved by modifying the particle nucleation and growth phases, through precise control over the reaction conditions.

3.2. **Experimental**

Iron (III) acetylacetonate, Fe (III) acac3 (purity ≥99.9%), oleic acid (≥99.0%) and benzyl alcohol, BA (purity ≥99.0%) were purchased from Sigma Aldrich. All reagents were used without further purification. Puriss heptane was purchased from Sigma Aldrich and used with any further purification. Reagent grade acetone was purchased from Labscan and was used without any further purification. De-ionised water was obtained from a Millipore MilliQ system and had a resistivity of < 16 MΩ.cm, prior to use.

The protocol used to synthesis the NPs in this chapter is a modified protocol similar to the one first developed by Pinna et al [50-52]. In a typical synthesis 1 g (2.832 mmol) of Fe (III) acac3 was weighed into a glass vial and then transferred to a three neck round bottom flask. 20 mL (0.193 mol) of benzyl alcohol was transferred to the round bottom flask. A N_2 flow system, a water cooled condenser and a high temperature thermometer (>300^{0}C) were attached to the three neck round bottom. The mixture was de-oxygenated at room temperature by purging with N_2 for 15 minutes and a N_2 atmosphere was maintained for the duration of the reaction. The heating mantle was turned to its highest settling and in all cases the reaction reached reflux at ~200^{0}C within 15 minutes. The reaction was allowed to reflux for 7 hours without stirring.

During the reaction, a colour change from red to dark brown/black was observed. This suggests the formation of iron oxide NPs[59]. Following the reaction, the heating mantle was turned off and the reaction vessel was allowed to cool to room temperature gradually, while still under a N_2 atmosphere. The synthesised particles are known as benzyl alcohol stabilised iron oxide nanoparticles and hereby referred to as BA-NPs. Thereafter the suspensions were stored in a sealed container under N_2.

For this study the reaction parameters of the synthesis were modified and the resultant nanoparticles were characterised as mentioned below. The parameters studies included reaction time, reaction temperature and the molar ratio of reaction solvent to iron precursor as shown in (Table 3-1). Additional the synthesis was performed under constant volume using an acid digestion bomb.

Table 3-1 : Sample identification scheme for the different samples including the different reaction parameters

Sample Name	Reaction Time (h)	Reaction Temperature (^{O}C)	Precursor Quantity (g)	Solvent : Precursor (mol : mol)
BA-0.5h	0.5	200	1	68.3 : 1
BA-3h	3	200	1	68.3 : 1
BA-7h	7	200	1	68.3 : 1
BA-24h	24	200	1	68.3 : 1
BA-130	7	130	1	68.3 : 1
BA-150	7	150	1	68.3 : 1
BA-170	7	170	1	68.3 : 1
BA-180	7	180	1	68.3 : 1
BA-205	7	200	1	68.3 : 1
BA-0.66g	7	200	0.66	103.4 : 1
BA-1g	7	200	1	68.3 : 1
BA-2g	7	200	2	34.1 : 1
BA-4g	7	200	4	17.1 : 1
BA-8g	7	200	8	8.5 : 1
BA-12g	7	200	12	5.7 : 1
BA-16g	7	200	16	4.3 : 1

3.2.1. Stabilisation of Maghemite NP

Over time the BA-NPs fall out of the mother liquor. They are present as a black/brown precipitate. The mother liquor was shaken using a vortex mixer until the precipitate was homogenously distributed throughout the solvent (~ 60 s). Typically, 1.5 mL of the mother liquor was washed by placing it into a 1.5 mL

Eppendorf™ centrifuge tube and centrifuging at 13200 rpm for 5 minutes using a table top Eppendorf Centrifuge 5415D. The BA-NPs sediment at the bottom of the flask and the resultant supernatant was removed. The centrifuge tube was filled with 1.5 mL of acetone and was mixed using a vortex mixer for 60 s. The mixture was centrifuged at 13200 rpm (16,100 rcf) for 5 minutes again to sediment the BA-NPs. The supernatant was removed and the above step was repeated once more. The aim of this process is to remove all free benzyl alcohol and reactant bi-products, allowing for stabilisation of the particles.

Oleic acid (OA) was solubilised in heptane at a concentration of 10 mg/mL. A pre-calculated quantity of this stock solution was added to the washed BA-NPs. This quantity is equivalent to a 3 fold excess of ligand needed to form a monolayer on the surface of the NPs (using a core size obtained from TEM of 8.2 nm (assuming spherical NPs) and an OA footprint of 38Å^2 [60]. This mixture was shaken using the vortex mixer, transferred to a glass vial and the final volume was made up to 1.5 mL using heptane. The vial was shaken overnight to allow complete surface coating of the NPs. The stabilised NPs were centrifuged for 10 minutes at 13,200 rpm in order to remove aggregates. This material is known as the concentrated stabilised NP solution and was dark brown in colour suggesting the formation of maghemite (γ-Fe_2O_3) and it is typically in the concentration range of 142 mM of Fe and is stable for extended periods (years).

3.2.2. Characterisation of Nanoparticle Dispersions

DLS measurements were performed at a stable temperature of 25^{0}C ± 0.1^{0}C. The concentration range used for DLS was between 1 – 5 mM. Each sample measurement consisted of an average of 3 measurements, each measurement was an average at least 10 sub runs of 10 seconds in length with the average being reported and in all cases, the %RSD was below 1%. All sizes reported in this chapter are the z-average, derived from the cumulants analysis, and will be referred to as d_{HYD} unless stated otherwise. All size intensity distributions presented are derived from the intensity weighted distribution analysis. In section

3.3.1 the inter-sample reproducibility is examined and it was found that the error is negligible (0.6%) once the PDI of the suspension is <0.1.

The particles size and morphology of the particles were characterised as described in Chapter 2 using TEM and FE-STEM. The solutions were diluted to approximately 0.2 – 1 mM with heptane. 5 μL of this solution was dropped onto a Formvar coated 400 mesh Copper grid or a Holey Carbon coated 400 mesh copper grid (Agar Scientific, Essex, UK.) and allowed to evaporate prior to imaging.

The magnetic resonance properties of the suspensions were measured as described in Chapter 1 using NMRD. NMRD was carried out at 25°C ± 0.1°C. Each frequency reported consisted of an accumulation of at least 12 scans. In all cases the measurements at different frequencies were successfully fitted to a mono exponential function. The error of the exponential fits was always below 2%, with the vast majority being below 1%. This confirms that these dispersions have only a single T_1 and a single T_2 process. DLS measurements were performed before and after NMRD to assess whether there is any aggregation due to exposure to the magnetic field. In all cases, following NMRD measurements, no aggregation was observed confirming colloidal stability during the NMRD measurement. In section 3.3.1 the inter-sample reproducibility is examined and it was found that the error is small (<3%) once the PDI of the suspension is <0.1.

The Fe concentrations of the different dispersions were measured using ICP-AES, as described in Chapter 2. To digest the NPs, a standard acid digestion method was followed [1]. Typically 100 to 200 μL of the dispersion was placed into a 50 mL conical flask and covered. Over time the solvent will evaporate leaving behind the NPs. 1 mL of concentrated HCl (36% reagent grade) was added to the flask. This was heated until the volume of the solution was reduced to ~100 μL. 3 mL of deionised water was added to the flask and the solution was heated to boiling. This solution was allowed to cool and was quantitatively transferred to a volumetric flask and made up to the mark using 1 M nitric acid (dilution of min 65% reagent grade). The calibration curve was linear in the range 0.01 ppm to 10 ppm, in all cases $R^2 > 0.995$. The inter-sample reproducibility was measured to be ~1.4%.

Selected samples were characterised by x-ray absorption spectroscopy (XAS) as performed in collaboration with Miguel Angel Garcia, Instituto de Cerámica y Vidrio, Madrid by x-ray absorption spectroscopy (XAS). These measurements confirm the phase is γ-Fe_2O_3 details are provided in Chapter 4.

3.3. Results and Discussion

Throughout this thesis NMRD was used as the primary method to probe the magnetic resonance properties of different NP suspensions. As a result it was necessary to carry out a control study into the effect that polydispersity, as measured by the PDI parameter had on the magnetic properties, as this may vary from sample to sample.

3.3.1. Investigation into the Effect of Polydispersity on Magnetic Resonance Properties

Oleic acid (OA), a fatty acid was used to stabilise the NP as oleic acid stabilised iron-oxide NPs (OA-NP) are particularly well characterised [1, 2, 27, 28]. It should be emphasised that all the suspensions described in this Chapter are in heptane. NPs were stabilised using oleic acid to yield multiple preparations of OA-NP (C18:1A/B/C/D). The preparations were centrifuged until each suspension had a unimodal distribution as measured by DLS. Some preparations required repeated centrifugation to achieve this. It was found that longer centrifugation time results in a lower PDI and d_{HYD}. This is attributed to the progressive centrifugation removing larger aggregates of nanoparticles present in the sample or removing larger nanoparticles from the size distribution, or a combination of both. The DLS intensity distributions of the different preparations are shown in Figure 3-4. Note that for the sample with the lower d_{HYD} the core size, d_{TEM} was found to be 8.2 nm. This corresponds to a difference of 3.3 nm between the measurements.

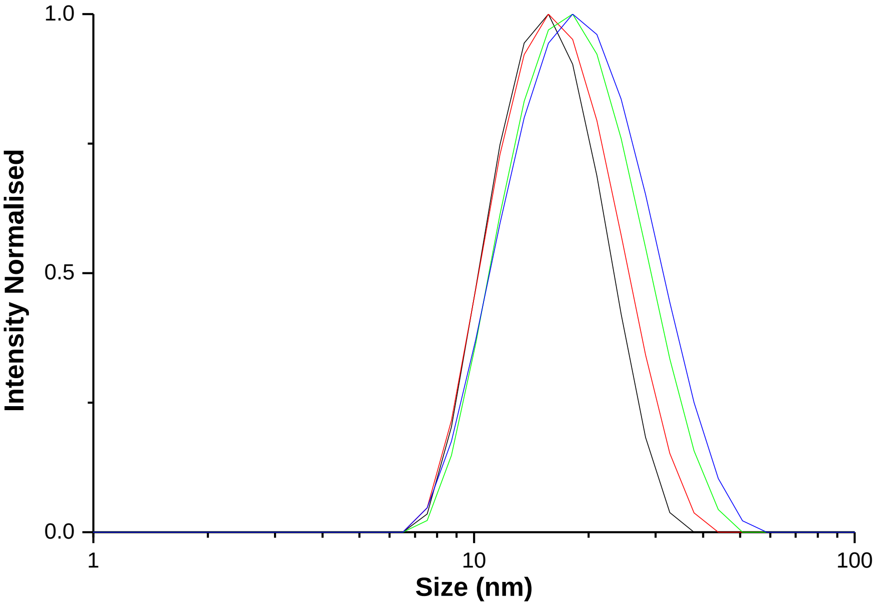

Figure 3-4: DLS intensity weighted size distributions for repeat preparations of OA- NP each with a different size and PDI, — C18:1 D (14.8 nm, PDI – 0.09), — C18:1 C (15.5 nm, PDI – 0.11), — C18:1 A (17.0 nm, PDI – 0.12) and — C18:1 B (17.5 nm, PDI – 0.13)

The NMRD profiles of the repeat suspensions of OA-NPs are shown in Figure 3-5.It should be noted that there is little change in d_{HYD} following NMRD, confirming that the preparations are stable to the magnetic fields used. The presence of a mid-frequency dip shows that the different samples are superparamagnetic in nature. There is a clear trend evident, as the size decreases and thus the PDI reduces, the relaxation enhancement increases. The shape of the profiles does not vary significantly. The SPM model developed by Muller [26] as described in Chapter 1 was used to simulate NMRD profiles of dispersed NP suspensions. In Figure 3-5 NMRD profiles of different preparations of OA-NPs are shown, overlaid with simulations using SPM theory. The simulations agree well with the data at low frequency and higher frequency, with a discrepancy in the mid frequency range. This is expected as in this range the simulation provides an interpolation between the two different relaxation processes.

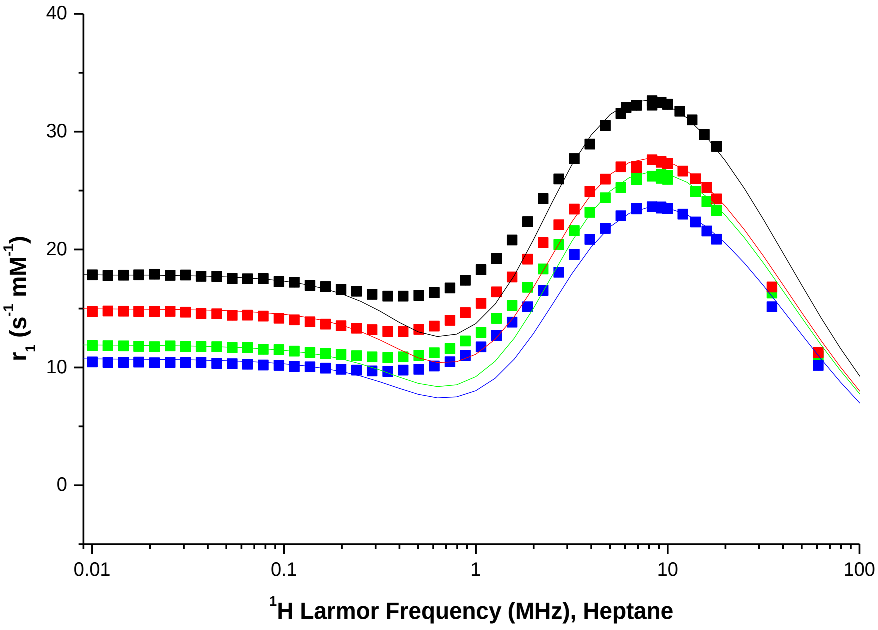

Figure 3-5: Experimental and simulated profiles of OA-NP of varying sizes and PDI, ■ 14.8 nm 0.08 PDI, 🟥 15.5 nm 0.11 PDI, 🟩 17.0 nm 0.12 PDI and 🟦 17.5 nm 0.13 PDI

Table 3-2: The parameters used in the simulated profiles of different preparations of OA-NP in heptane, each with a d_{TEM} of 8.2 nm

	d_{HYD} (nm)	PDI	d_{NMRD} (nm)	M_{NMR} (emu/g)	ΔE_{anis} (GHz)	τ_0 (s)
■	14.8	0.08	10.4	53	0.5	10E-9
🟥	15.5	0.11	10.4	49.3	0.5	8E-9
🟩	17	0.12	10.4	48.5	0.6	5E-9
🟦	17.5	0.13	10.4	46	0.625	5E-9

The key parameters extracted from the SPM fits to the NMRD curves are shown in Table 3-2 with d_{NMR} the size of the magnetic core as sensed by the diffusing solvent molecules, M_{NMR} the saturation magnetisation of the material, ΔE_{anis} the surface anisotropy energy and τ_n, the Néel correlation time. From the extracted parameters it is interesting to note that despite d_{HYD} changing by 21%, the ν_{max} and the extracted d_{NMRD} does not change. This suggests that the cores are all the same size and that NMRD is not sensitive to the effects responsible for the changes in d_{HYD}. From Table 3-2 the suspensions with lower overall r_1 and lower extracted M_{NMR} had a higher average hydrodynamic size and a higher PDI. This suggests that the larger particles contained within the broader size distributions contribute less to the ^{1}H relaxation of the solvent. This is surprising considering r_1 is expected to increase with particle size, as M_{NMR} is proportional to volume, which suggests that the larger particles in the wider distributions are aggregates or more likely, multi-domain particles of lower magnetisation.

In a different experiment centrifugation was used to produce four different preparations each with PDI values below 0.1 (C18:1D1/D2/D3/C2). Below this threshold, there was no discernible difference in the size distribution within the limits of detection of DLS, Figure 3-6.

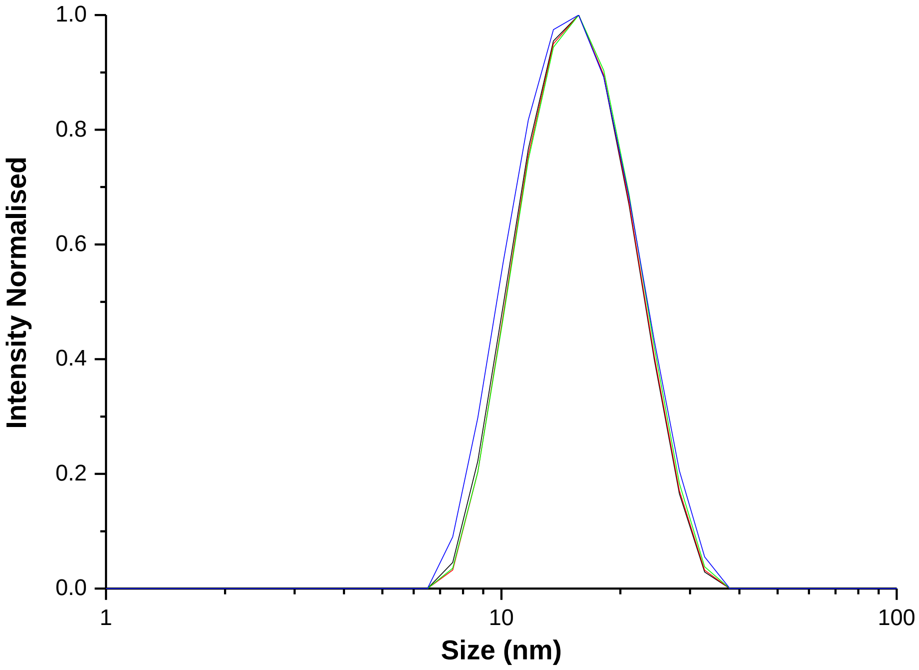

Figure 3-6: DLS intensity weighted size distributions for repeat preparations of OA- NP each with a similar size and PDI, — C18:1 D2 (14.7 nm, PDI – 0.07), — C18:1 D3 (14.8 nm, PDI – 0.08), — C18:1 D1 (14.8 nm, PDI – 0.08) and — C18:1 C2 (14.7 nm, PDI – 0.8)

In Figure 3-7, the NMRD profiles of the OA-NP suspensions are shown. There is little change in d_{HYD} before and after NMRD showing the suspensions are stable to the magnetic fields used. Again the presence of a mid-frequency dip shows that the different samples are superparamagnetic. It is evident that for repeat preparations where the PDI value is <0.1, the d_{HYD} are very similar and there is little discernible difference in NMRD profile with little change in the r_1 max. The variability at low fields is < 5% while at high fields the deviation is 3%.

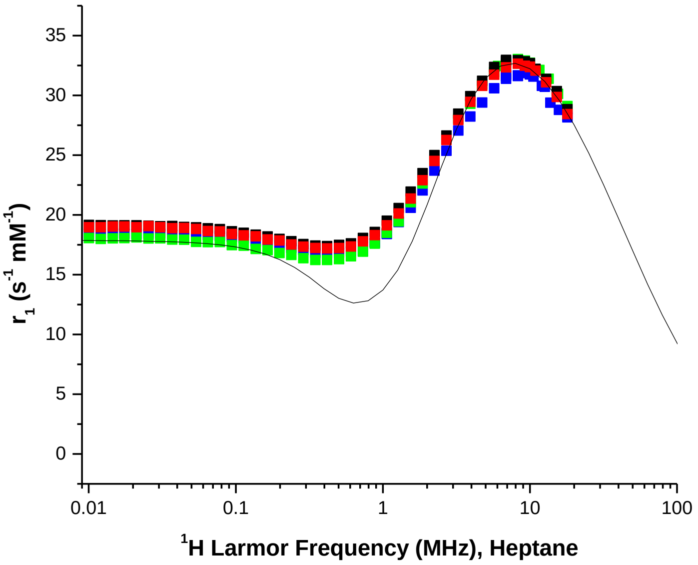

Figure 3-7: NMRD results of different preparations of OA-NP, ■ C18:1 D2 (14.7 nm, PDI – 0.07), 🟥 C18:1 D3 (14.8 nm, PDI – 0.08), 🟩 C18:1 D1 (14.8 nm, PDI – 0.08) and 🟦 C18:1 C2 (14.7 nm, PDI – 0.8) overlaid with a sample SPM simulation

From the observed results in order for valid systematic comparisons of r_1, the PDI must be <0.1. This criterion was adopted for the rest of the study.

3.3.2. Effect of Reaction Time on Nanoparticle Size

The TEM micrographs of different samples, each with a different reaction time are shown below. Each micrograph is accompanied by the statistical numerical analysis and an overlaid log-normal fit.

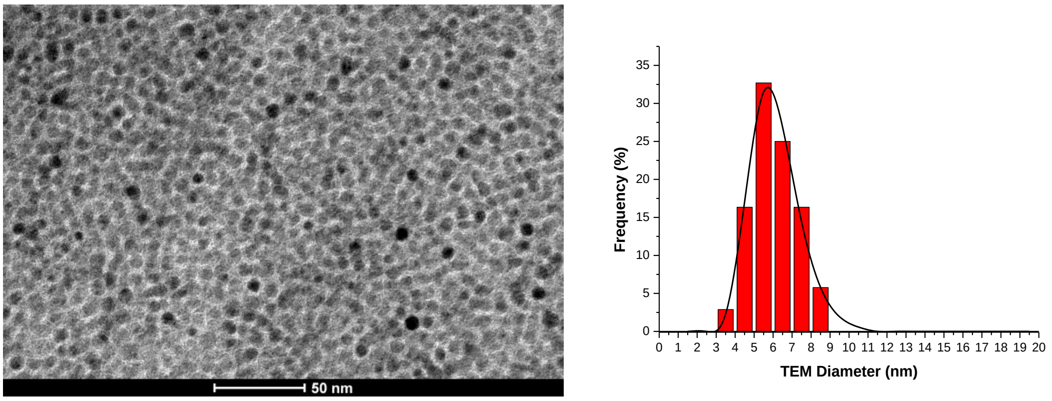

Figure 3-8: Left- TEM micrograph of OA stabilised BA-NP from a 1 hour reflux (BA-0.5H); Right- Experimental particle size distribution and log-normal fit to the experimental distribution

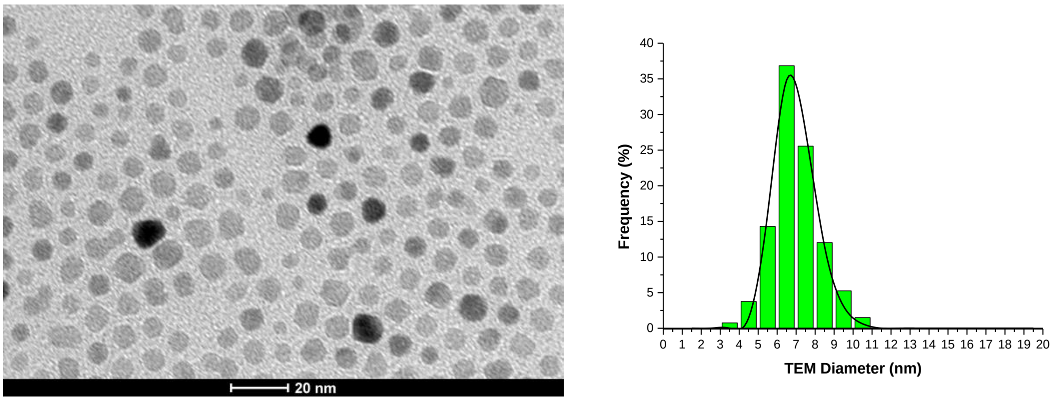

Figure 3-9: Left- TEM micrograph of OA stabilised BA-NP from a 3 hour reflux (BA-3H); Right- Experimental particle size distribution and log-normal fit to the experimental distribution

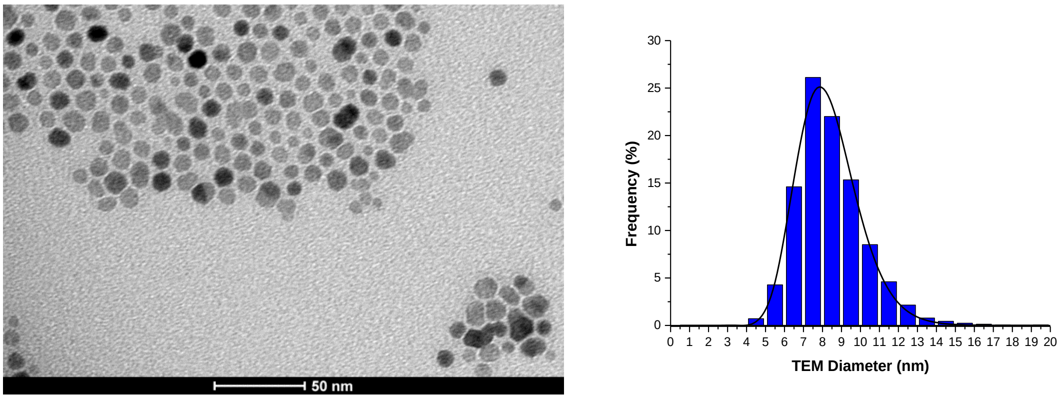

Figure 3-10: Left - TEM micrograph of OA stabilised BA-NP from a 7 hour reflux (BA-7H); Right - Experimental Particle Size distribution and log-normal fit to the experimental distribution

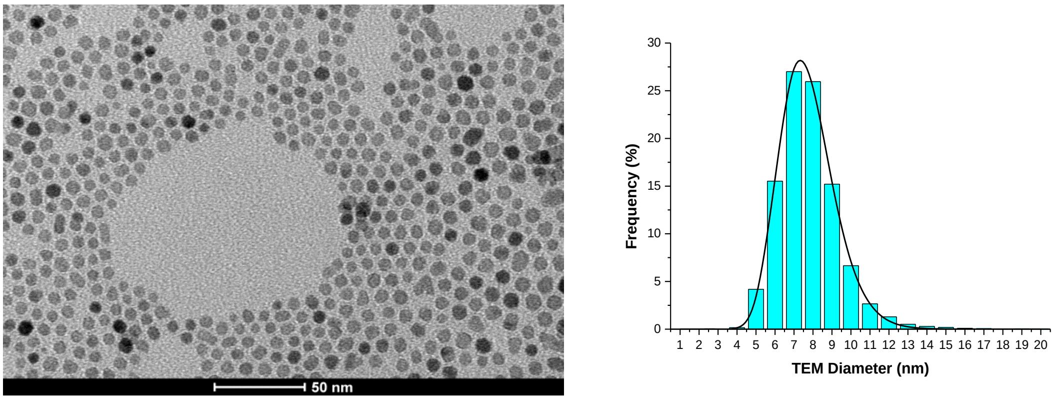

Figure 3-11: Left - TEM micrograph of OA stabilised BA-NP from a 24 hour reflux (BA-24H); Right - Experimental particle size distribution and log-normal fit to the experimental distribution

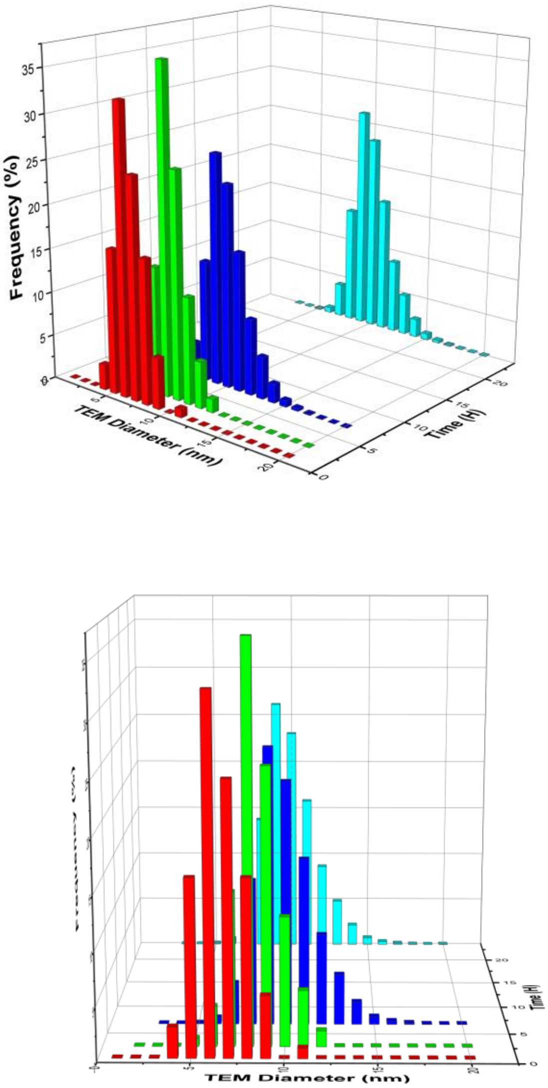

Figure 3-12 : 3D Frequency histogram for OA stabilised BA-NP with differing reaction time, 🟥 0.5 hour (BA-0.5H), 🟩 3 hour (BA-3H), 🟦 7 hour (BA-7H) and 🟦 24 hour (BA-24H)

Statistical analysis was performed on each image using ImageJ (National Institute of Health, US government) or manual counting and for all sample, histograms were constructed. Previously it was confirmed there was no statistical difference between manual counting and automatic analysis within 1σ[61]. The distributions were fitted to a log-normal particle size distribution with the probability density function (P(x)) of where d is the diameter and μ and σ are the mean and standard deviation of the ln (x) respectively. This model is shown in Equation 3-1 [1, 44, 62, 63].

$$P(x) = \frac{A}{\sqrt{2\pi}\sigma x} e^{\frac{-(lnx-\mu)^2}{2\sigma^2}}$$

Equation 3-1

Following the successful fitting of this model the particle mean, the particle mode and the standard deviation were calculated using Equation 3-2, Equation 3-4 and Equation 3-5 respectively.

$$d_{TEM(Mean)} = e^{\mu+\frac{\sigma^2}{2}}$$

Equation 3-2

$$d_{TEM(Median)} = e^{\mu}$$

Equation 3-3

$$d_{TEM(Mode)} = \left(e^{\mu-\sigma^2}\right)$$

Equation 3-4

$$\sigma_{TEM} = d_{TEM(Mean)} * \sqrt{\left(e^{\sigma^2}-1\right)}$$

Equation 3-5

Table 3-3 : The statistical analysis of TEM images calculated using the log-normal model for OA stabilised BA-NP synthesised using 1g of precursor refluxed for varying time

Reaction Time (h)	# Particles Counted	d_{TEM}, Mean (nm)	d_{TEM}, Mode (nm)	σ (nm)	σ (%)
0.5	103	6.6	6.2	1.35	20.5
3	132	7.3	7.2	0.96	13.2
7	5518	8.8	8.4	1.62	18.4
24	6950	7.7	7.4	1.45	18.8

In all cases, monodisperse quasi-spherical NPs were synthesised which fit a log normal model. BA-0.5H and BA-3H statistics were gathered manually as a result the number of particles counted is smaller. Each size distribution has a %σ of ~ 19% which is similar to NPs synthesised via other preparations, values of ~20% are typically quoted [1, 24]. Considering the NP formation mechanism discussed above (Figure 3-1, Figure 3-2), as reaction time is increased the growth phase will be extended. From Table 3-3 it can be seen that the size increases as the reaction time increases. However for BA-24H the size decreases, it should be noted that during the centrifugation steps for BA-24H, there was a large amount of magnetic material removed by centrifugation, in this case. We attribute this to the removal of very large particles, perhaps formed by Ostwald ripening during the extended synthesis, at the expense of the remaining NP. The remaining dispersible NPs are smaller in size as measured by TEM. We see the same trend when the NP are analysed by DLS as seen in Figure 3-13 and Table 3-4.

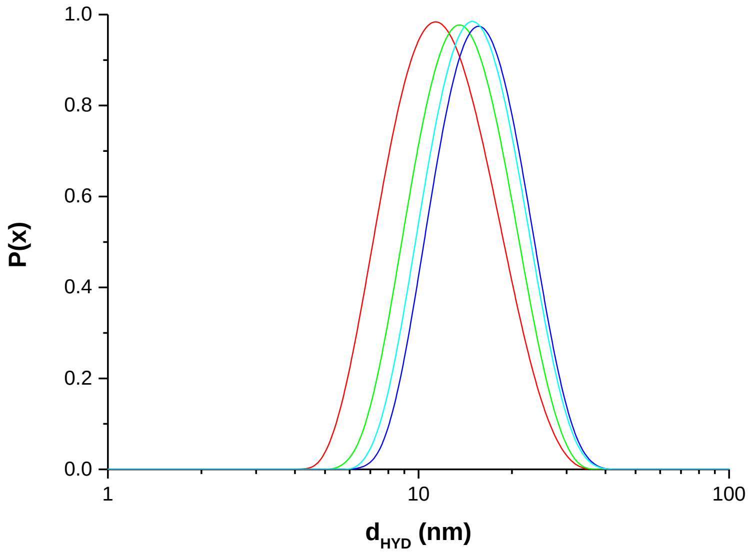

Figure 3-13 : Hydrodynamic size distribution of OA stabilised BA-NP with varying reaction time, — 0.5 hour (BA-0.5H), — 3 Hour (BA-3H), — 7 hour (BA-7H) and — 24 hour (BA-24H)

Table 3-4 : The hydrodynamic size and polydispersity index (PDI) obtained from DLS analysis of OA stabilised BA-NP in heptane synthesised using 1g of precursor refluxed for varying time

Reaction Time (h)	d_{HYD} (nm)	PDI
1	11.0	0.13
3	13.0	0.09
7	14.8	0.06
24	14.7	0.08

The NMRD data for the dispersions is shown in Figure 3-14; it is found that there is little change in the d_{HYD} following the NMRD measurements confirming the dispersions are stable to the measurement. For all samples the superparamagnetic response is confirmed by the presence of the mid-frequency dip, including BA-0.5H. The frequency of the maximum (ν_{max}), which is very sensitive to particle size, shifts to lower fields i.e. from >60 to 10.6 to 8.2 MHz as the reaction time is increased from 0.5 to 3 to 7 hours, respectively, which indicates the size of the particles as measured by NMRD increases. The NMRD profiles were modelled using simulation by Muller et al and are over laid with the NMRD profile as shown in Figure 3-14. In all cases the simulations fit the NMRD profile well; there is, as expected, a discrepancy in the mid-frequency range as the SPM model interpolates between the two relaxation mechanisms. For BA-0.5H, the size of the particle is so small; the ν_{max} cannot be measured as it lies beyond our range and this was an unusual case with a PDI value of >0.1. For this sample particular care was taken during the fitting, and a conservative approach was taken by simulating using the largest size possible.

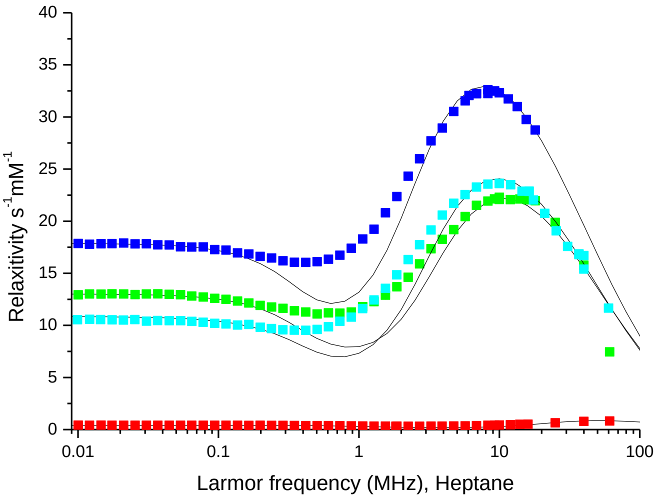

Figure 3-14: NMRD profiles of OA stabilised BA-NP each synthesised with a different reaction time, with relaxivity (expressed as solid blocks) on the X_1 axis and ratio (expressed as a solid line) on the X_2 axis, 🟥 0.5 hour (BA-0.5H), 🟩 3 hour (BA-3H), 🟦 7 hour (BA-7H) and 🟦 24 hour (BA-24H)

Table 3-5 : The d_{NMRD}, the M_{NMR}, ΔE and τ_0 obtained from NMRD profile simulations developed by Muller et al [22, 23, 26] for OA stabilised BA-NP in heptane synthesised using 1g of precursor refluxed for varying time

Reaction Time (h)	d_{NMRD} (nm)	M_{NMR} (emu/g)	ΔE (GHz)	τ_0 (s)
0.5	6.9	16.5	1.00	5.0E-10
3	9.3	48.5	0.45	6.0E-09
7	10.3	52.3	0.45	8.0E-09
24	9.8	48.0	0.45	3.0E-09

From the parameters extracted from the SPM models shown in Table 3-5 we can see a similar trend in the size extracted using the model. The d_{NMRD} value increases with reaction time except for BA-24H; in this case we see a decrease in size which is of similar magnitude for both d_{TEM} and d_{HYD}. BA-24H was re-stabilised from the same mother liquor and reanalysed by NMRD. The profile is shown in Figure 3-15 and it displays very similar results to the original preparation, the difference is ~ 4% confirming our initial observations. This also goes to demonstrate the reproducibility of the NMRD measurements.

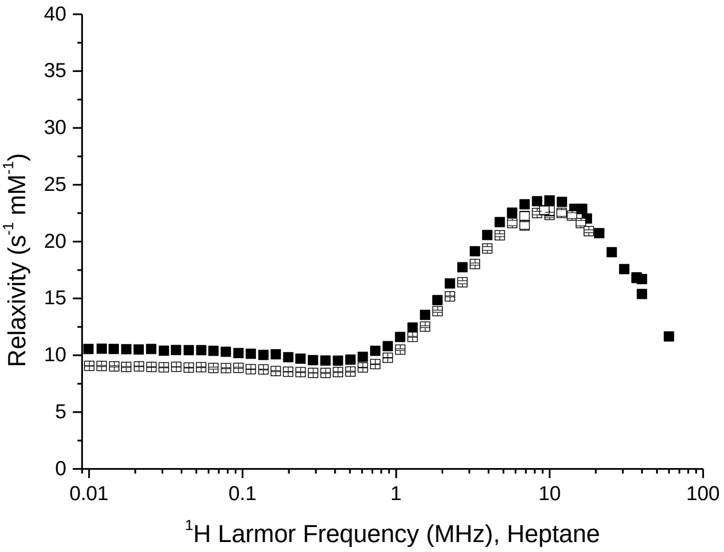

Figure 3-15 : NMRD profiles for two subsequent stabilisations of BA-24H with OA

The magnetic parameters as extracted using SPM simulations of NMRD profiles will be discussed in detail below.

3.3.3. Effect of Heating Temperature on Nanoparticle Size

The TEM and FE-STEM micrographs for the different reaction temperatures are shown below. Each image is accompanied with a frequency histogram and a numerical analysis as described above.

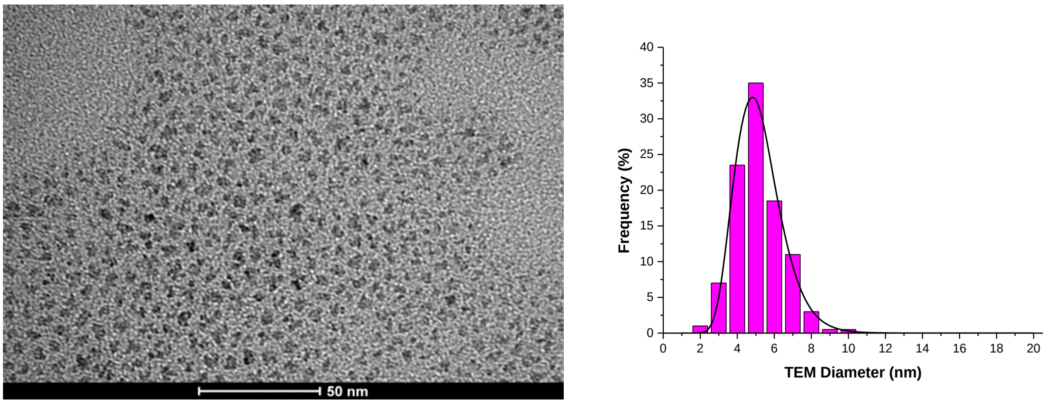

Figure 3-16: Left - TEM micrograph of OA stabilised BA-NP from a 7 hour reflux heated to 130⁰C (BA-130); Right - Experimental Particle Size distribution and log-normal fit to the experimental distribution

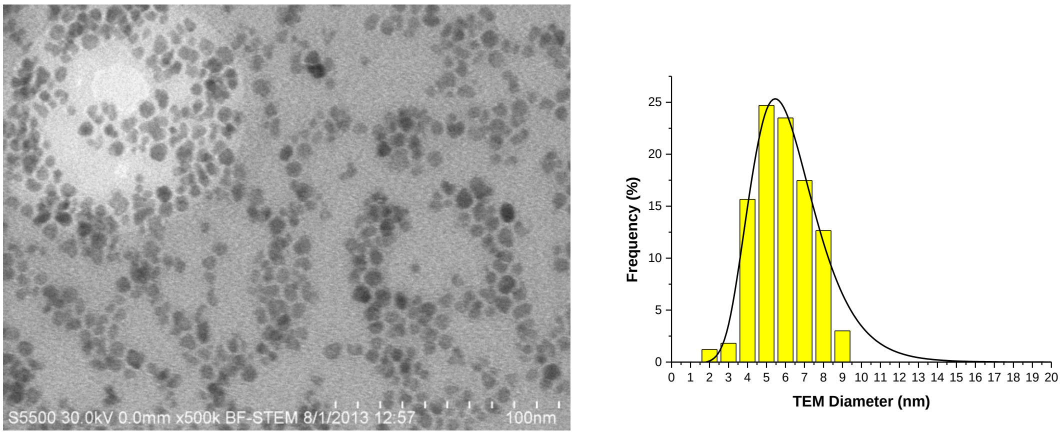

Figure 3-17: Left - STEM micrograph of OA stabilised BA-NP from a 7 hour reflux heated to 150⁰C (BA-150); Right - Experimental Particle Size distribution and log-normal fit to the experimental distribution

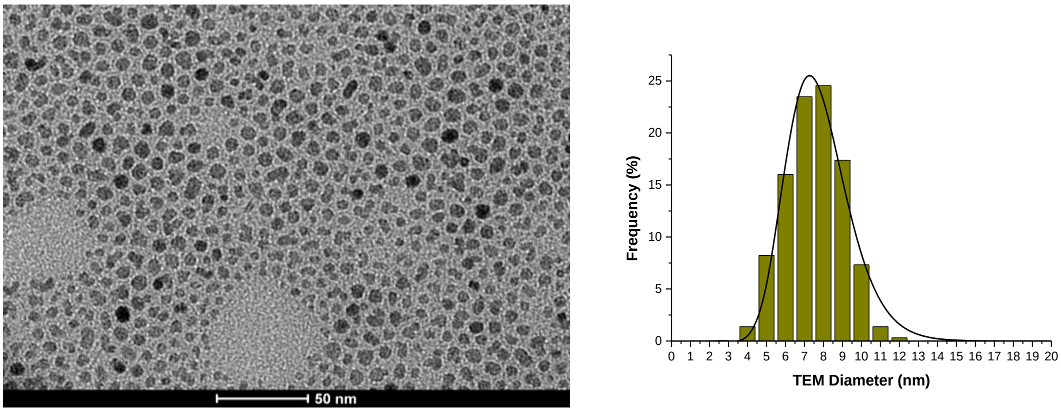

Figure 3-18: Left - TEM micrograph of OA stabilised BA-NP from a 7 hour reflux heated to 170⁰C (BA-170); Right - Experimental Particle Size distribution and log-normal fit to the experimental distribution

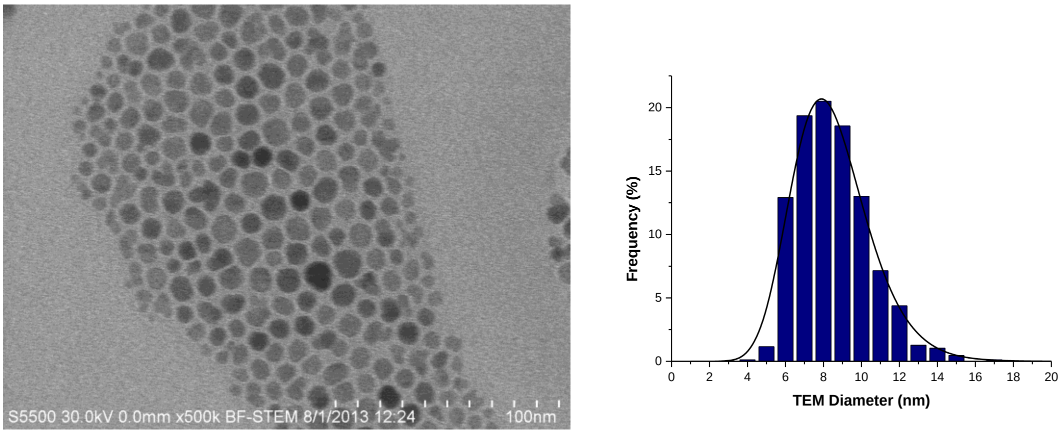

Figure 3-19: Left - TEM micrograph of OA stabilised BA-NP from a 7 hour reflux heated to 180⁰C (BA-180); Right - Experimental Particle Size distribution and log-normal fit to the experimental distribution

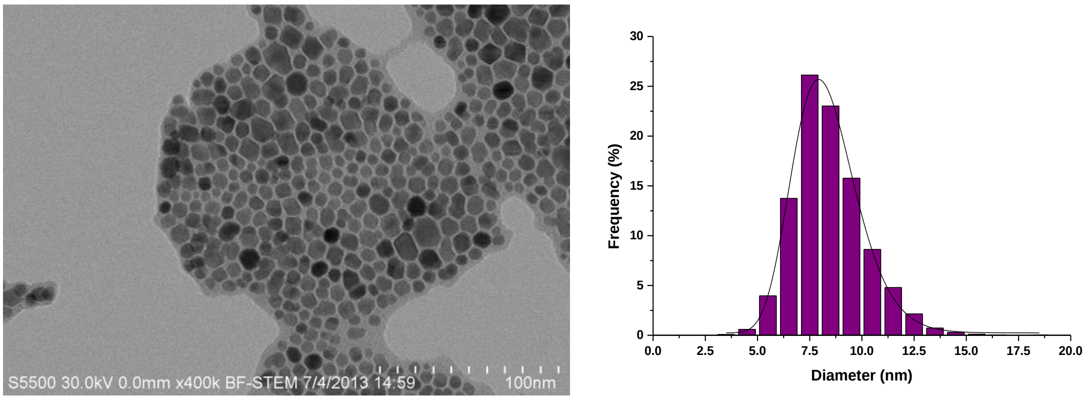

Figure 3-20: Left - TEM micrograph of OA stabilised BA-NP from a 7 hour reflux heated to 205⁰C (BA-205); Right - Experimental Particle Size distribution and log-normal fit to the experimental distribution

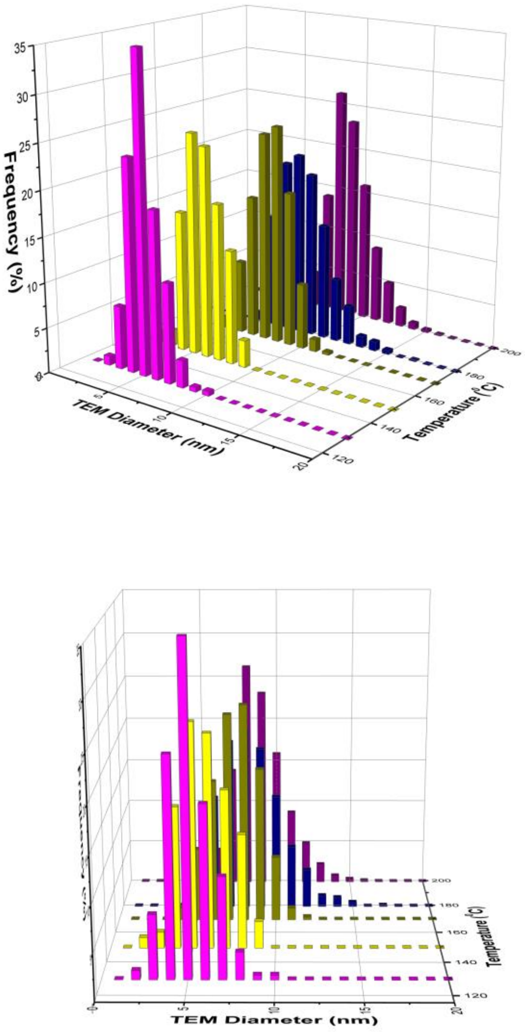

Figure 3-21: Frequency Histograms for OA stabilised BA-NP with differing reaction temperature, ■ 130 ^{0}C (BA-130), ■ 150 ^{0}C (BA-150), ■ 170 ^{0}C (BA-170), ■ 180 ^{0}C (BA-180) and ■ 205 ^{0}C (BA-205)

Table 3-6 : The Statistical analysis of TEM images calculated using the log-normal model for OA stabilised BA-NP synthesised using 1g of precursor heated for 7 hours at varying temperature

Reaction Temperature (^{0}C)	# Particles Counted	d_{TEM}, Mean (nm)	d_{TEM}, Mode (nm)	σ (nm)	% σ (%)
130	199	5.2	4.8	1.5	29.0
150	165	6.3	5.6	1.9	30.2
170	657	7.8	7.3	1.7	21.8
180	867	8.5	7.8	2.0	23.5
200	5407	8.9	8.5	1.6	18.1

The images show that the quality of the particles increases with temperature, in that they show sphericality, uniformity and narrow size distributions. The lower temperature synthesises, especially BA-130 and BA-150, produce non-uniform and

NP that are irregular in both shape and size. The uniformity and sphericality improves as the reaction temperature increased with both BA-180 and BA-200 having a very uniform and spherical shape. These observations suggest an increase in crystallinity with increased temperature. In all cases the histograms were successfully fitted using a log-normal model described above,

Table 3-6. The d_{TEM} values are found to increase and %σ to decrease with increasing reaction temperature. These observations are consistent with an extended growth phase with some size focusing. Similar trends are seen in size with the DLS measurements; we see an increase in d_{HYD} as the reaction temperature is increase, Figure 3-22 and Table 3-7.

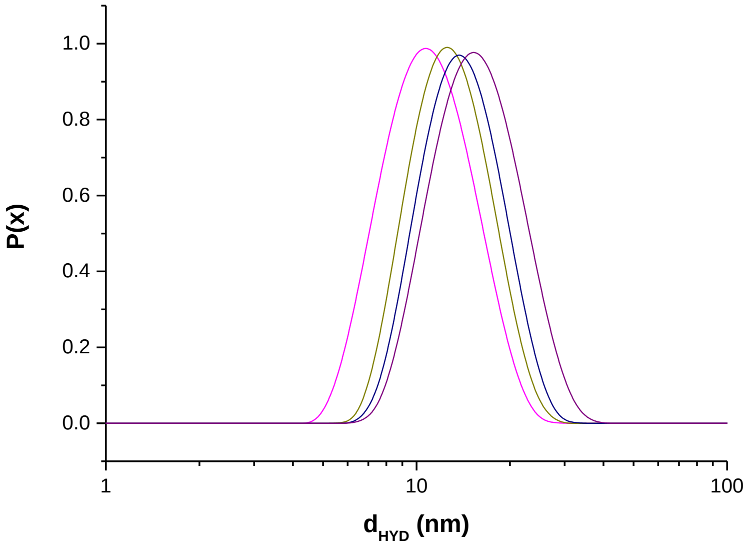

Figure 3-22 : Hydrodynamic size distribution of OA stabilised BA-NP with varying reaction time, ■ 130 ⁰C (BA-130), ■ 150 ⁰C (BA-150), ■ 170 ⁰C (BA-170), ■ 180 ⁰C (BA-180) and ■ 205 ⁰C (BA-205)

Table 3-7 : The hydrodynamic size and polydispersity index (PDI) obtained from DLS analysis of OA stabilised BA-NP in heptane synthesised using 1g of precursor heated for 7 hours at varying temperature

Reaction Temperature (^{0}C)	d_{HYD} (nm)	PDI
130	10.5	0.08
170	12.2	0.09
185	13.2	0.09
200	14.4	0.07

Considering the NMRD data shown in Figure 3-23, the presence of a mid-frequency dip confirms the superparamagnetic behaviour of the dispersions. Colloidal stability was confirmed by a minimal size change as measured by DLS following NMRD. The ν_{max} value, which is very sensitive to NP size, shifts to lower fields i.e. from >18 to 12 to 9 to 8.1 MHz on increasing reaction temperature from 130 to 170 to 180 to 200^{0}C, respectively. This suggests that the magnetic core of the NP is increasing in size with reaction temperature. The NMRD profiles were simulated using the SPM model and are overlaid in the figure below. The SPM simulations are consistent with the experiments with the expected discrepancy in the mid-frequency portion. For BA-130, the ν_{max} value is above the measured range, so the simulation must be treated with caution. However, we can suggest that the size is no larger and the M_{NMR}, as extracted from the SPM model, is no smaller than the numbers reported in Table 3-8.

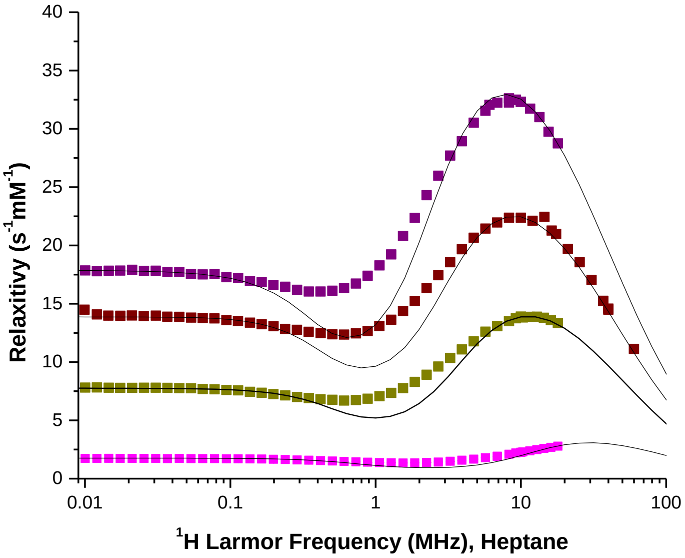

Figure 3-23 : NMRD profiles of OA stabilised BA-NP each synthesised with a different reaction temperature, ■ 130 ^{0}C (BA-130), ■ 170 ^{0}C (BA-170), ■ 180 ^{0}C (BA-180) and ■ 200 ^{0}C (BA-200)

Table 3-8: The d_{NMRD}, the M_{NMR}, ΔE and τ_0 values obtained from SPM simulations developed by Muller et al [22, 23, 26] for OA stabilised BA-NP in heptane synthesised using 1g of precursor heated for 7 hours at varying temperature

Reaction Temperature (^{0}C)	d_{NMRD} (nm)	M_{NMR} (emu/g)	ΔE (GHz)	τ_0 (s)
130	7.6	25.5	0.85	1.8E-09
170	9.4	37.8	0.65	7.0E-09
185	10.0	45.0	0.55	1.3E-08
200	10.5	52.3	0.45	8.0E-09

It can be seen that the d_{NMRD} value increases with increasing reaction temperature, Table 3-8. This is a similar trend to that observed for the d_{TEM} and the d_{HYD} values. The M_{NMR} value also increases with size and reaction temperature. Again, the M_{NMR} results will be discussed fully below.

When the three sizes obtained by the different sizing techniques are compared (Figure 3-24), it is clear there is a linear correlation between size and precursor quantity. In all cases there is good correlation ($R^2>0.98$) demonstrating a linear dependence. The slopes are 0.054 ±0.006, 0.042 ±0.002 and 0.057 ±0.05 nm/^{0}C for the sizes as determined by d_{HYD}, d_{NMRD} and d_{TEM} respectively. The difference in the slopes between the d_{TEM} and the d_{HYD} is less than the standard errors of the fit, indicating there is not a significant difference between these two slopes. Interestingly this observation does not hold for the d_{NMRD} value. It is expected that $d_{TEM} < d_{NMRD} < d_{DLS}$ since TEM shows only the core while NMRD includes any organic or inorganic surface layers impermeable to solvent molecules and DLS is always shifted towards larger values by its strong dependence on size-dispersity.

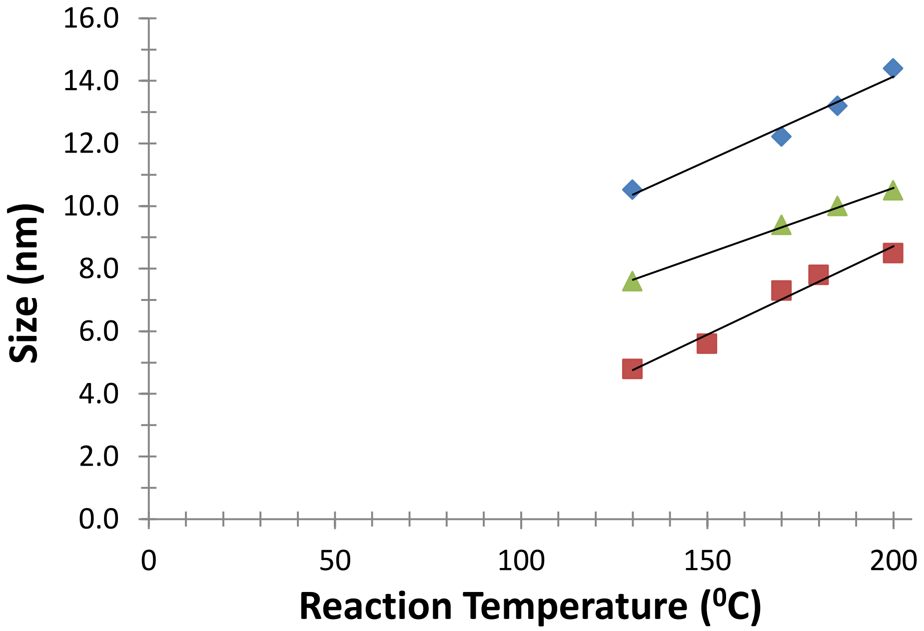

Figure 3-24 : Size as measured by the different techniques, each data set fitted to a straight line, 🟥 d_{TEM} ($y=0.0565x - 2.5801$; $R^2 = 0.973$), ▲d_{NMRD} ($y=0.042x + 2.1864$; $R^2 = 0.997$) and ♦ d_{HYD} ($y=0.0538x + 3.3714$; $R^2 = 0.975$)

3.3.4. Effect of Precursor Quantity on the Nanoparticle Size

TEM and FE-STEM micrographs for particles synthesised using different quantities of precursor, at 200^{0}C for 7 hours, are shown below. Each is accompanied with a frequency histogram and a numerical analysis, described above.

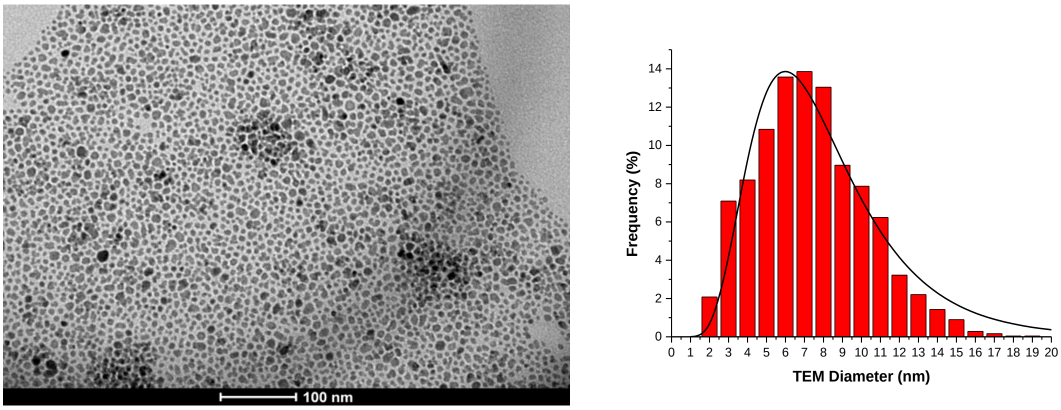

Figure 3-25 : Left - TEM micrograph of OA stabilised BA-NP synthesised using a 7 hour reflux and 0.66 g of precursor (BA-0.66g); Right - Experimental Particle Size distribution and log-normal fit to the experimental distribution

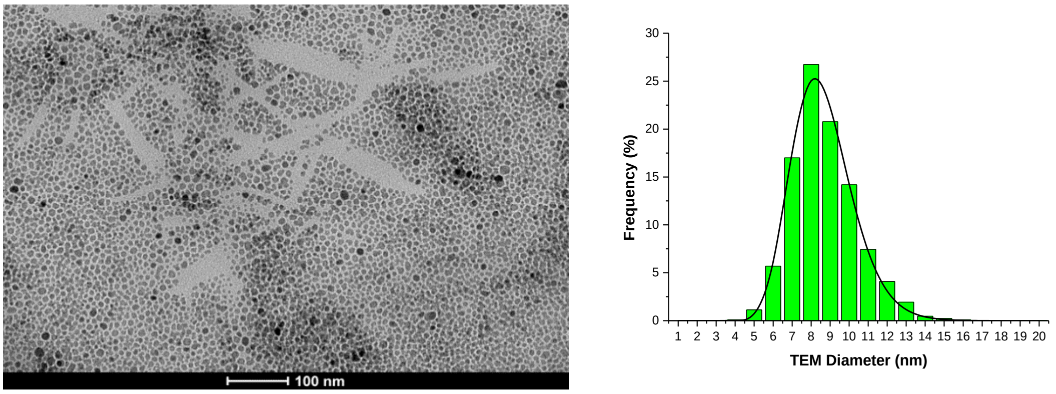

Figure 3-26 : Left - TEM micrograph of OA stabilised BA-NP synthesised using a 7 hour reflux and 1 g of precursor (BA-1g) ; Right - Experimental Particle Size distribution and log-normal fit to the experimental distribution

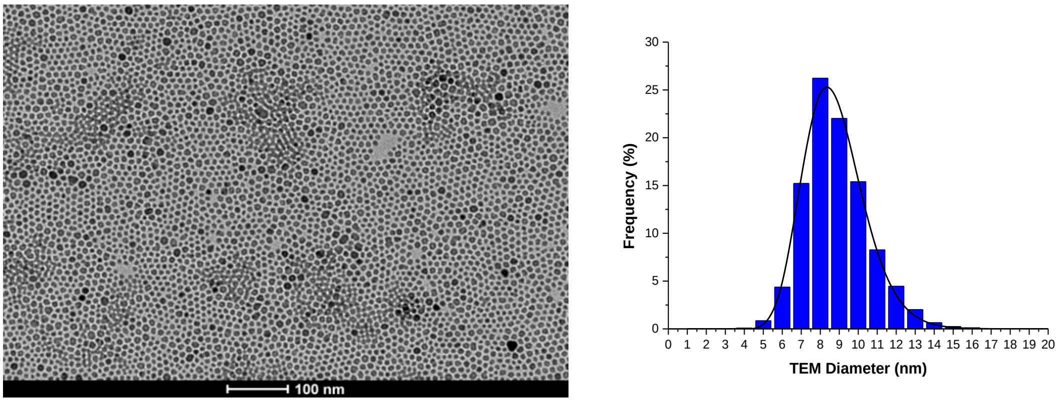

Figure 3-27 : Left - TEM micrograph of OA stabilised BA-NP synthesised using a 7 hour reflux and 2 g of precursor (BA-2g) ; Right - Experimental Particle Size distribution and log-normal fit to the experimental distribution

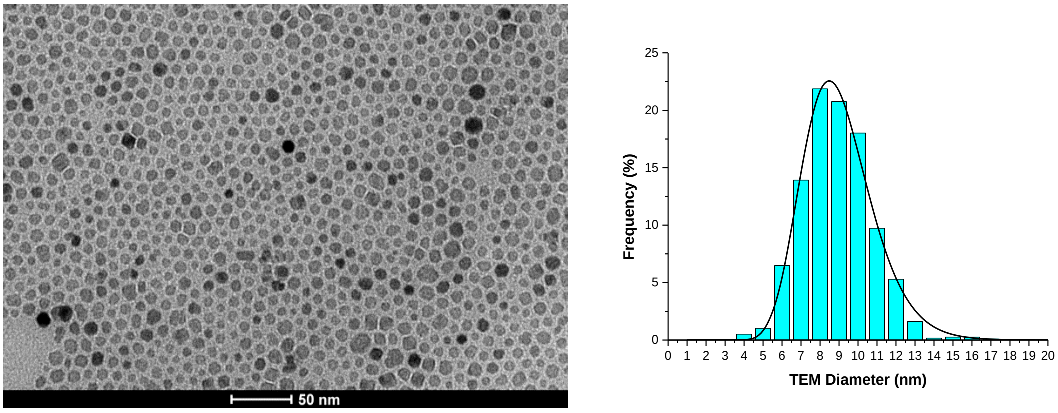

Figure 3-28 Left - TEM micrograph of OA stabilised BA-NP synthesised using a 7 hour reflux and 4 g of precursor (BA-4g) ; Right - Experimental Particle Size distribution and log-normal fit to the experimental distribution

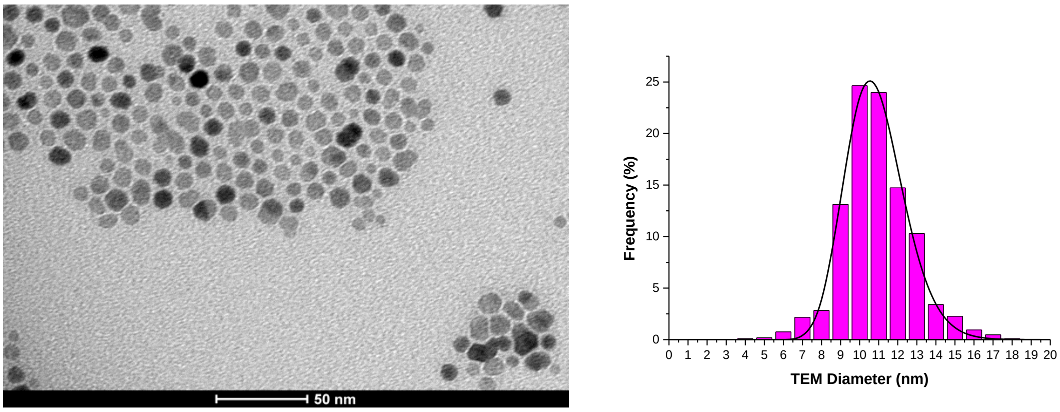

Figure 3-29 : Left - TEM micrograph of OA stabilised BA-NP synthesised using a 7 hour reflux and 8 g of precursor (BA-8g) ; Right - Experimental Particle Size distribution and log-normal fit to the experimental distribution

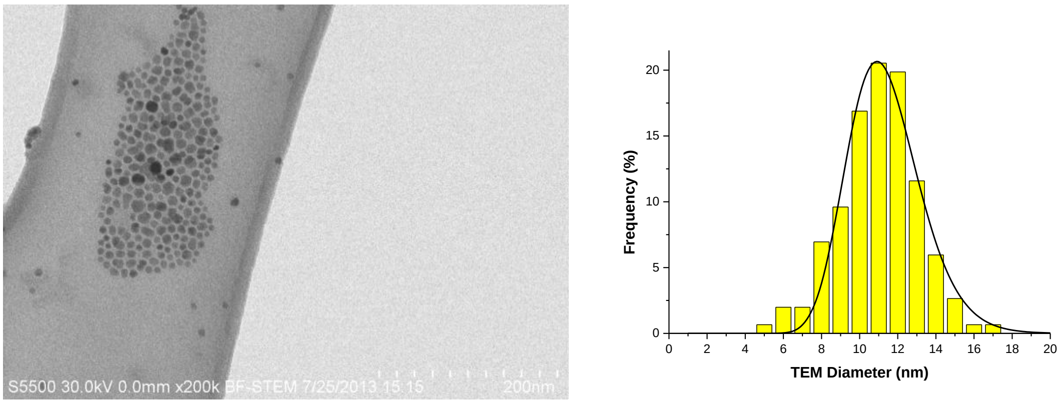

Figure 3-30 : Left - TEM micrograph of OA stabilised BA-NP synthesised using a 7 hour reflux and 12 g of precursor (BA-12g) ; Right - Experimental Particle Size distribution and log-normal fit to the experimental distribution

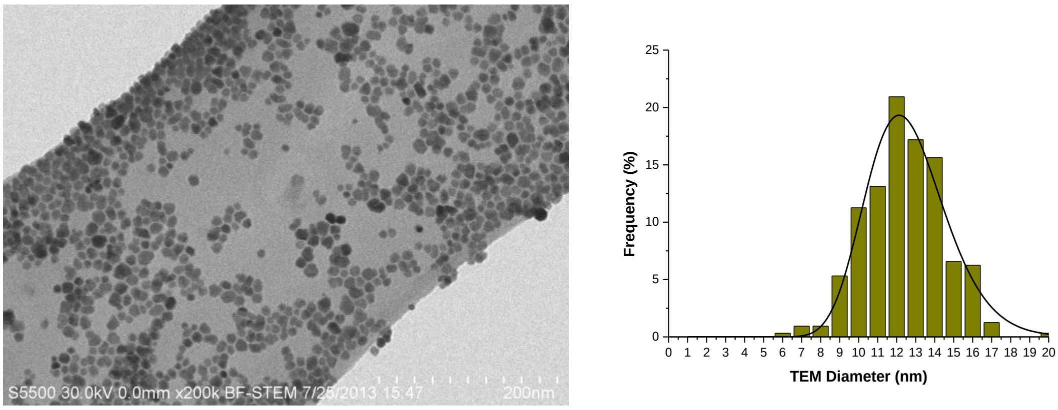

Figure 3-31 :Left - TEM micrograph of OA stabilised BA-NP synthesised using a 7 hour reflux and 16 g of precursor (BA-16g) ; Right - Experimental Particle Size distribution and log-normal fit to the experimental distribution

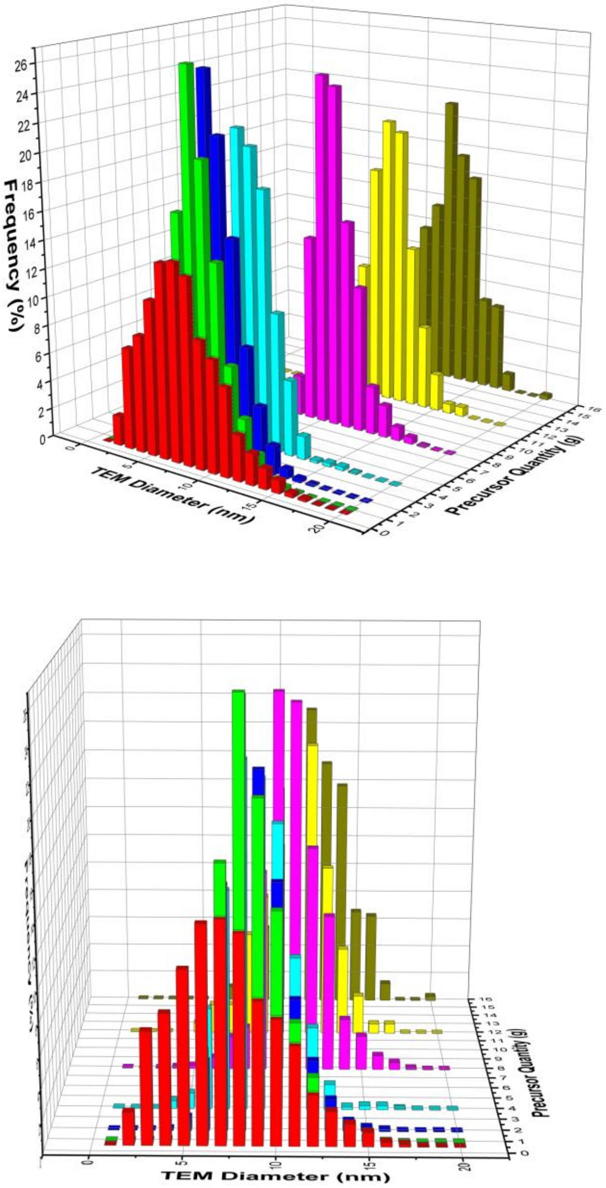

Figure 3-32 : Frequency Histograms for OA stabilised BA-NP synthesised using a 7 hour reflux with differing quantities of precursor, 🟥 0.66 g (BA-0.6g), 🟩 1 g (BA-1g), 🟦 2 g (BA-2g), 🟦 4 g (BA-4g) 🟪 8 g (BA-8g), 🟨 12 g (BA-12g) and 🟧 16 g (BA-16g)

Table 3-9 : The statistical analysis of TEM images calculated using the log-normal model for OA stabilised BA-NP synthesised by refluxing for 7 hours using varying amounts of precursor

Precursor quantity (g)	# Particles Counted	d_{TEM}, Mean (nm)	d_{TEM}, Mode (nm)	σ (nm)	% σ (%)
0.66	2453	8.1	6.0	3.8	63.6
1	5460	8.6	8.2	1.6	19.8
2	5409	8.8	8.4	1.6	19.2
4	1319	9.0	8.5	1.9	22.0
8	1058	10.9	10.5	1.6	14.7
12	278	11.4	10.9	1.9	17.4
16	319	12.7	12.1	2.1	17.6

From the TEM and STEM micrographs show that, with the exception of BA-0.66g, all the preparations are uniform in both size and shape and all particles are quasi-spherical. In Figure 3-32 and Table 3-9 a summary of the microscopy results is presented. It is apparent that as the amount of precursor is increased, the particle size increases, from 8.1 to 12.7 nm. Assuming the nucleation and growth phases are temporally separated, this result is consistent with the amount of precursor having no effect on the nucleation process but resulting in a higher growth rate (Figure 3-1, Figure 3-2).

It should be noted that in the BA-12G and BA-16G preparations, the precursor could not completely dissolved during the preparation of the reaction mixture. Furthermore, during the washing stage of the mother liquor, it was evident from the colour that there was still some unreacted Fe-OH in solution. Quantitative analysis by ICP-AES gave values of 2.8 mg for BA-12g and 478.1 mg for BA-16g for unreacted Fe per synthesis, suggesting the reaction had not gone to completion. For future experiments, the reaction time could be extended to rectify this.

However, a trend is still apparent; d_{TEM} was found to increase with increasing precursor quantity. We see a similar trend in the DLS data, Figure 3-6 and Table 3-10, with an increase in d_{HYD} with an increase in precursor quantity. It is interesting that despite the presence of unreacted precursor, BA-12g and BA-16g fit the observed trend.

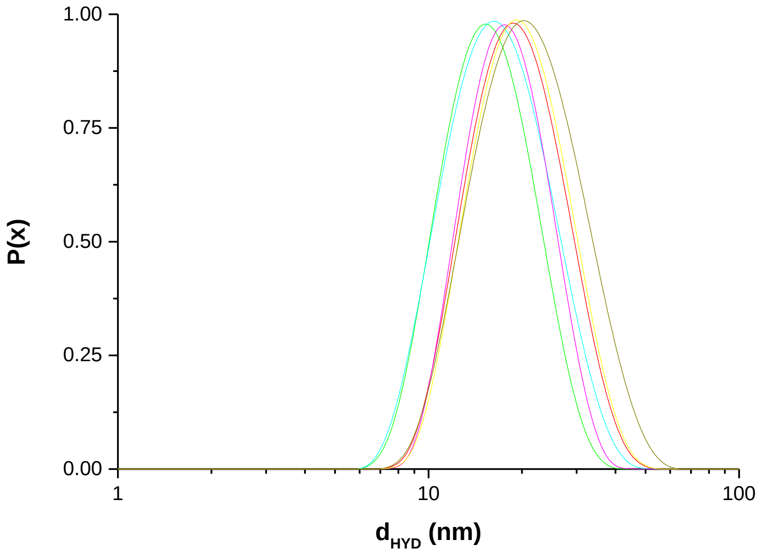

Figure 3-33 : Probability hydrodynamic size distributions of for OA stabilised BA-NP synthesised using a 7 hour reflux with differing quantities of precursor, — 0.66 g (BA-0.6g), — 1 g (BA-1g), — 4 g (BA-4g), — 8 g (BA-8g), — 12 g (BA-12g) and — 16 g (BA-16g)

Table 3-10 : d_{HYD} size and poly-dispersity index (PDI) obtained from DLS analysis of OA stabilised BA-NP in heptane synthesised by refluxing for 7 hours using varying amounts of precursor

Precursor quantity (g)	d_{HYD} (nm)	PDI
0.66	18.2	0.12
1	14.8	0.06
4	15.6	0.09
8	17.1	0.08
12	18.5	0.09
16	19.5	0.10

The NMRD data for OA stabilised BA-NP synthesised by refluxing (200^0C) for 7 hours is shown in Figure 3-34. These profiles are overlaid with SPM simulations which are consistent with the experiments with the expected mid-frequency discrepancy. In all cases, the samples were shown to be stable by DLS, confirming colloidal stability throughout the measurement. It is interesting to note that the ν_{max} shifts to lower frequencies as the precursor quantity is increased suggesting an increase in the size. It should be noted that for larger particles it is expected that the relaxivity would be higher. However, we do not see a uniform trend in the r_1 values. At ν_{max} r_1 is found to increase sequentially from 16 – 85 s^{-1} mM^{-1} as the precursor quantity increases from 0.66 – 8 g. For BA-12g and BA-16g we see a lower relaxivity when compared to BA-8g. Furthermore there is a smaller than expected midfield dip, associated with superparamagnetic behaviour. This cannot be related to parts of the size distributions lying above the critical diameter associated with superparamagnetic behaviour (d_{SPM}) as by TEM, this fraction is estimated to be ~<1% for both BA-12g and BA-16g. It is likely that either this change in expected relaxivity is a result of free Fe contributing to the concentration used in the normalisation of the relaxation rates, or the particles have reduced crystallinity.

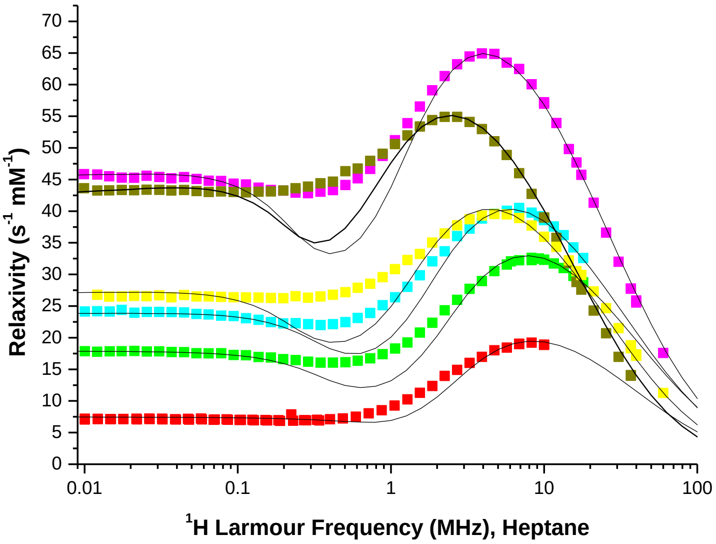

Figure 3-34 : NMRD profiles for OA stabilised BA-NP synthesised using a 7 hour reflux with differing quantities of precursor overlaid with SPM simulations, 🟥 0.66 g (BA-0.6g), 🟩 1 g (BA-1g), 🟦 4 g (BA-4g), 🟪 8 g (BA-8g), 🟨 12 g (BA-12g) and 🟫 16 g (BA-16g)

Table 3-11 : d_{NMRD}, the M_{NMR}, ΔE and τ_0 values obtained from SPM simulations developed by Muller et al [22, 23, 26] for OA stabilised BA-NP in heptane synthesised by refluxing (200^{0}C) for 7 hours using varying quantities of precursor

Precursor Quantity (g)	d_{NMRD} (nm)	M_{NMR} (emu/g)	ΔE (GHz)	τ_0 (s)
0.66	10.8	39.5	1.00	4.50E-09
1	10.3	52.3	0.45	8.00E-09
4	11.2	53.5	0.45	1.80E-08
8	12.6	58.0	0.30	6.50E-08
12	13.0	45.3	0.30	4.30E-08
16	16.5	41.3	0.30	3.5E-07

To rule out the presence of any unreacted iron in BA-12g or BA-16g, the particles were stabilised again and extra washing steps were undertaken. In Figure 3-35 it can be seen that following the repeat there is no significant difference in relaxivity, the two profiles differ by ~6%. It can be said that at the time of NMRD experiment, there was no significant quantities of free Fe in solution.

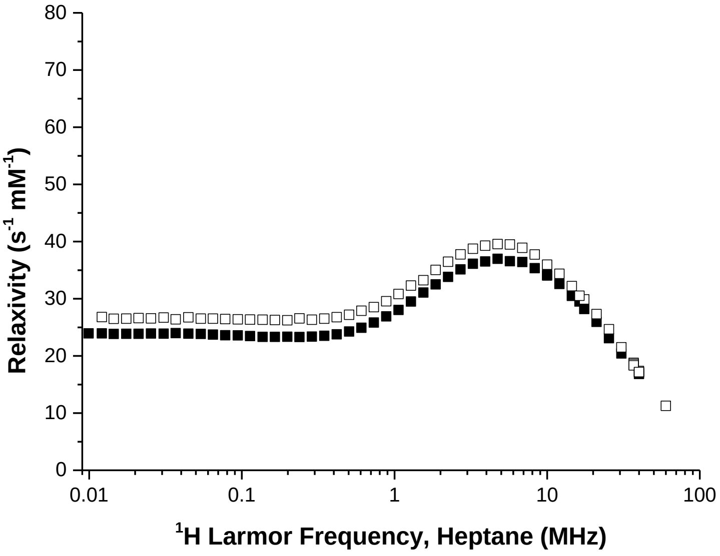

Figure 3-35: NMRD profiles of BA-12g and a repeat involving further washing steps

As expected from the preliminary analysis of the profiles in Figure 3-34, we can see in Table 3-11 there is a similar trend in the NMRD size, to that observed previously by TEM and DLS. As the amount of precursor is increased, the d_{NMR} value increases. When the sizes obtained by the three different sizing techniques are compared (Figure 3-36) it is clear there is a linear correlation between size and precursor quantity. In all cases there is a good correlation ($R^2>0.95$) demonstrating a linear relationship. The slopes are 0.32 ±0.02, 0.26 ±0.37 and 0.28 ±0.02 for the sizes as determined by d_{HYD}, d_{NMRD} and d_{TEM}, respectively. The difference in the slopes is less than the standard errors of the fit, indicating there is no significant difference between the slopes in this case. It is found that, as expected, $d_{TEM} < d_{NMRD} < d_{DLS}$ due to differences in the measurement techniques, as discussed above.

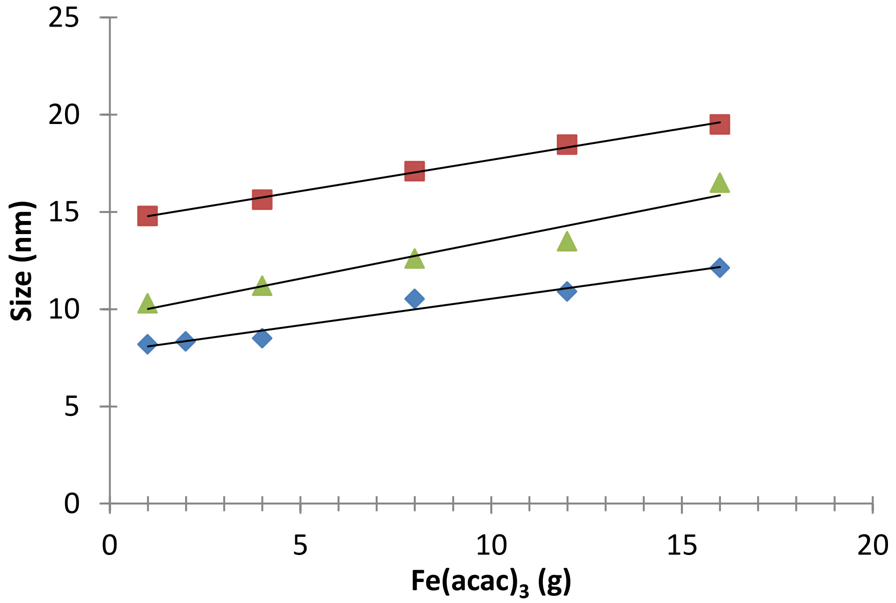

Figure 3-36 : Size as measured by the different techniques, each data set fitted to a straight line, ■ d_{HYD} (y=0.32x +14.46; R^2 = 0.99), ▲d_{NMRD} (y=0.38x +9.6; R^2 = 0.94) and ♦ d_{TEM} (y=0.27x + 7.82; R^2 = 0.97)

3.3.5. Thermal Decomposition at Constant Volume

In the initial report of surfactant free thermal decomposition, the reactions were performed at constant volume inside a Teflon lined acid digestion bomb. The reactions reported to date in this Chapter were performed in a normal reflux set up (constant pressure). In a typical synthesis, 1 g of the precursor was heated to reflux (200^0C) in 20 mL of benzyl alcohol for 7 hours at constant pressure. In order to investigate the effects of reacting at constant volume, a “typical” synthesis was placed inside placed inside a Teflon lined acid digestion bomb. The reaction solution was deoxygenated using N_2 bubbling for 15 minutes and was then placed inside a vacuum chamber for 12 hours to ensure removal of oxygen. The chamber was then flooded with nitrogen prior to opening and the container was sealed while in the nitrogen rich atmosphere. The bomb was placed inside an oven preheated to 205^0C (under vacuum) for a period of time. Following this, the bomb was carefully removed from the oven and placed in an isolated place to allow the container to cool. The dispersion was then washed and stabilised as described above. Two reaction times, 7 hours and 48 hours were chosen to investigate the effect of this approach on the formation of the nanoparticles. The microscopy results are shown below.

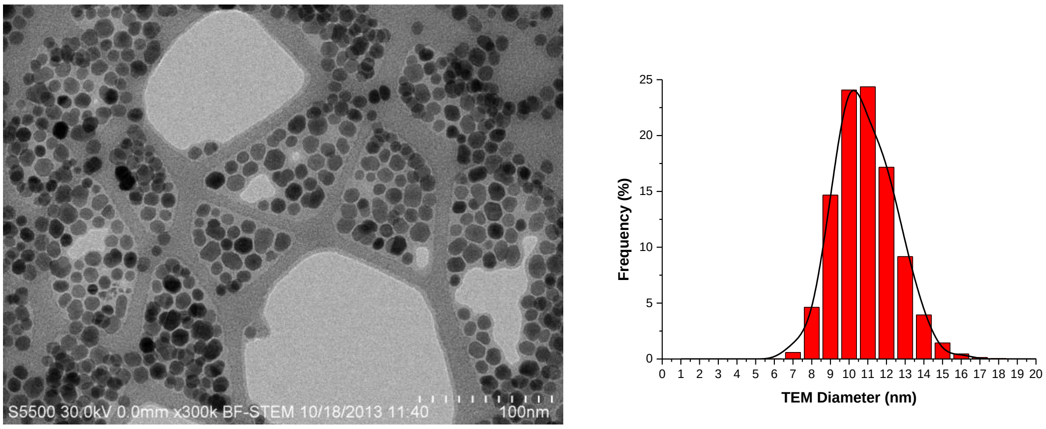

Figure 3-37 : Left - STEM micrograph for OA stabilised BA-NP synthesised in a bomb using 1 g of precursor and heating to 205^{0}C for 7 hours; Right - Experimental Particle Size distribution and log-normal fit to the experimental distribution

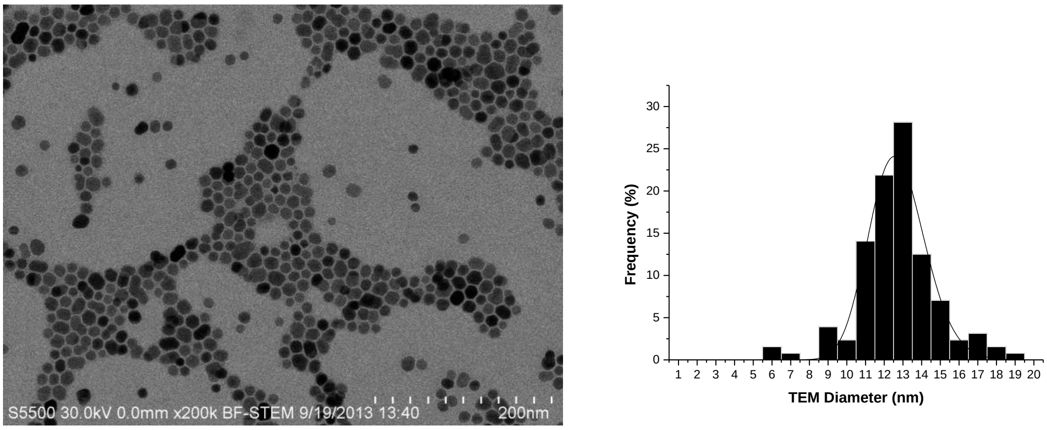

Figure 3-38 : Left - STEM micrograph for OA stabilised BA-NP synthesised in a bomb using 1 g of precursor and heating to 205^{0}C for 48 hours; Right - Experimental Particle Size distribution and log-normal fit to the experimental distribution

Table 3-12 : The statistical analysis of TEM images calculated using the log-normal model for OA stabilised BA-NP synthesised by heating 1 g of precursor to 205^{0}C for 48 hours at constant volume

Reaction Time (h)	# Particles Counted	d_{TEM}, Mean (nm)	d_{TEM}, Mode (nm)	σ (nm)	% σ (%)
7	301	10.9	10.5	1.6	14.4
48	150	12.7	12.5	1.4	10.8

From statistical analysis of the image, this method is shown to produce very uniform and monodisperse NP. For the 48 h reaction the % σ value is 10.8% is lower than the % σ (18%) obtained for the constant pressure synthesis. Typically % σ values in this range are associated with nanoparticles synthesised using the “hot injection” method, where the precursor is injected into a preheated solvent[50]. This is a remarkable result when compared to the quality of the nanoparticles produced in earlier work.

The constant volume approach has the effect of suppressing the boiling point and increasing the reaction temperature. Elevated reaction temperature extends the growth phase and the separation of this phase from nucleation may result in a lower %σ. Other factors that might improve the monodispersity include reduction of temperature gradients across the reaction space and potentially the homogenous nature of the solvent / N_2 atmosphere.

Increasing the reaction time from 7 to 48 h for the constant volume method results in an increased size (10.9 – 12.7 nm) and a decreased % σ (14.4 – 10.8). This is in contrast to the earlier results for the constant pressure experiments, in which case a decrease in size was observed when the reaction time was increased from 7 to 24 hours, an effect that was attributed to Ostwald ripening. In this case, considering the reaction time is increased to 48 h we would expect to see an even greater decrease in size. However, this is not what is observed. Upon examination of the micrographs we see some unusual shaped particles for the 48 h sample. The unusual NPs are cylindrical in shape as shown in Figure 3-39, suggesting the coalescence of spherical NPs. In particular in Figure 3-39-a) and e) we can see two striking examples, in a) it is clear due to the dimensions that this NP is formed by the merging of two spherical NP, in e) we can clearly see two particles partially merged with a clear interface between the two particles. From TEM analysis, the fraction of cylindrical particles was estimated to be 9%.

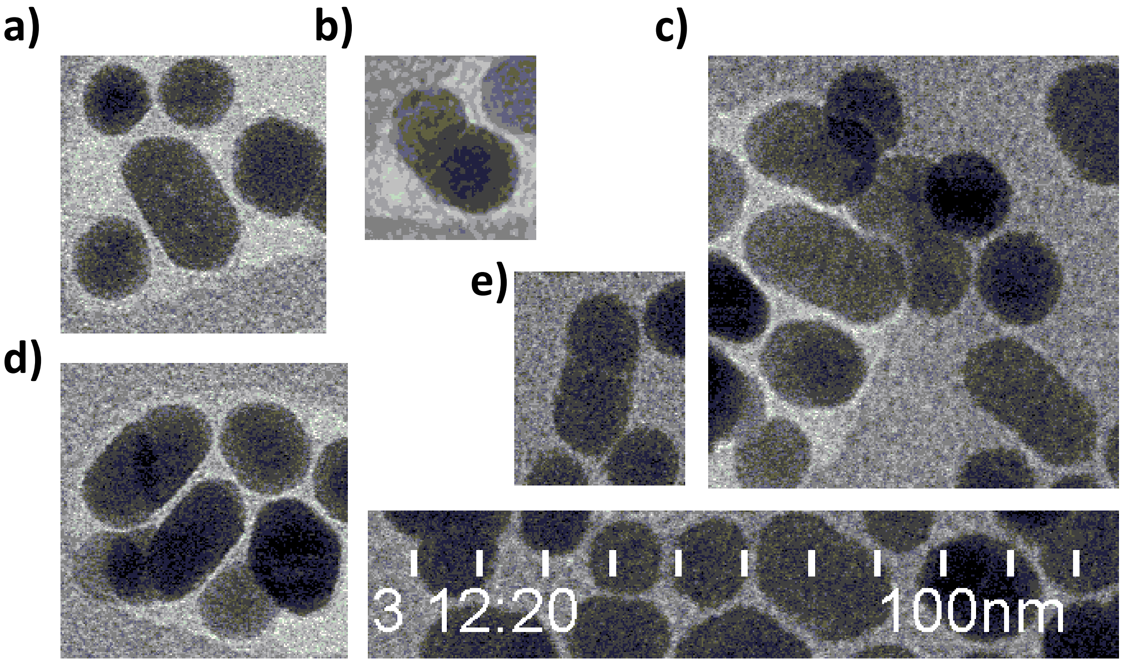

Figure 3-39 : Selected micrographs from the 48 h constant volume synthesis of OA stabilised BA-NP showing the coalescence of NP into cylinders

The DLS analysis shown in Table 3-13 and Figure 3-40 shows that a similar size trend to the microscopy analysis is again observed, the size increases as the reaction time is increased. The size distributions are monodisperse with very low PDI values.

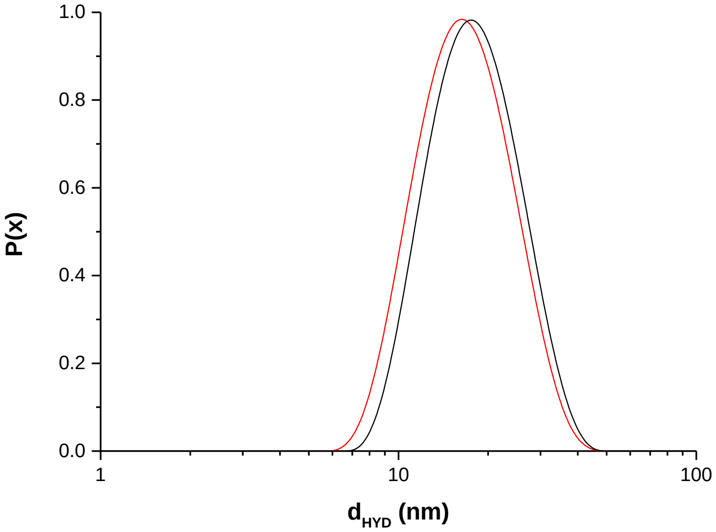

Figure 3-40 : OA stabilised BA-NP synthesised in a bomb using 1 g of precursor and heating to 205^{0}C for 48 hours, accompanied by the histogram and log normal fit

Table 3-13 : Probability hydrodynamic size distributions of for OA stabilised BA-NP in heptane synthesised in at constant volume using 1 g of precursor and heating to 205⁰C for varying time

Reaction Time (h)	d_{HYD} (nm)	PDI
7	15.51	0.09
48	16.90	0.09

The NMRD profiles are shown in Figure 3-41, with the usual superparamagnetic behaviour apparent as confirmed by the presence of the mid-frequency dip. The profiles were simulated using SPM theory and the simulations fit the data well. The ν_{max} value shifts to lower frequencies as the reaction time is increased. This suggests an increase in NP size as the reaction time is increased. The presence of cylindrical particles is not apparent from the NMRD profiles. It should be noted that by TEM the fraction of cylindrical particles was estimated to be 9%, there is no evidence of any interference with the NMRD curves.

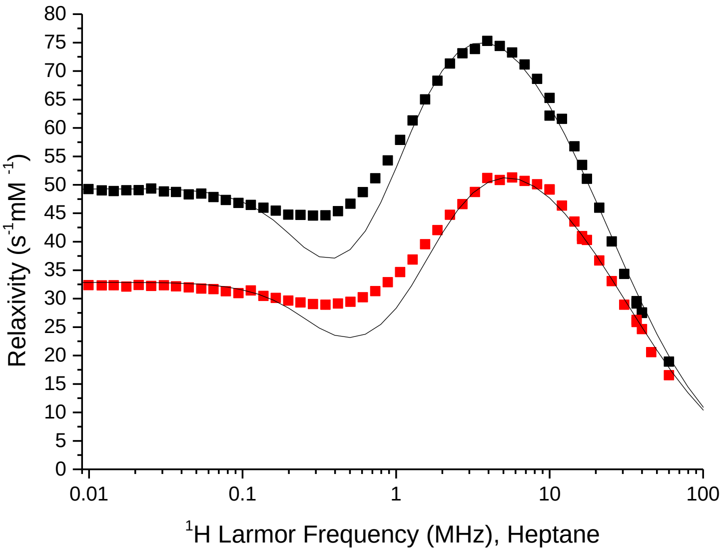

Figure 3-41 : NMRD profiles for OA stabilised BA-NP synthesised using constant volume using 1 g of precursor and heating to 205⁰C for 7 hours (🟥) and 48 hours (■), accompanied by the histogram and log normal fit

Table 3-14 : d_{NMRD}, the M_{NMR}, ΔE and τ_0 values obtained from SPM simulations developed by Muller et al [22, 23, 26] for OA stabilised BA-NP in heptane synthesised by heating 1 g of precursor to 200^{0}C using a constant volume for 7 hours using constant volume

Reaction Time (h)	d_{NMRD} (nm)	M_{NMR} (emu/g)	ΔE (GHz)	τ_0 (s)
7	11.5	57.0	0.35	2.6E-08
48	13.0	60.0	0.30	5.0E-08

From the NMRD simulations, a clear trend is evident; there is an increase in the d_{NMR}, as the reaction time increases. Furthermore, when these particles are compared to ones of a similar size, synthesised using the constant pressure reaction, we can see the new samples have a higher M_{NMR} value of 57 – 60 emu/g when compared to constant pressure values of 45.3 emu/g (Table 3-11).

3.3.6. Magnetic Properties as Extracted from Superparamagnetic Simulations

As discussed in Chapter 1 it is a commonly accepted that for SPM nanoparticles there are free or uncanted spins which are free to align with and against an externally applied magnetic field; and associated or canted spins in the outer layer[16, 64-68]. In this “dead layer” the spins are unable to align with or against an externally applied magnetic field. This phenomenon can reduce the magnetisable volume and thus reduces the saturation magnetisation; it is the reason why the saturation magnetisation of magnetic nanoparticles is lower than the bulk value. The thickness of the dead layer will largely determine the resulting magnetisation. There are many factors that can affect the thickness of this layer; some of these will be investigated in Chapter 4. In this case the dominant factor affecting t is probably the crystallinity of the particles. Tang et al.[64] used the relationship between the saturation magnetisation of the sample, $M_S(D)$, and the bulk saturation magnetisation of the material ($M_S(O)$) to develop an empirical relationship between the thickness of this magnetically dead layer (t) and the diameter of the nanoparticle which is shown in Equation 3-6. For maghemite, t was estimated at 0.57 nm[67] and 0.60 nm[68].

$$M_s(D) = M_s(O)\left(1 - \frac{6t}{D}\right)$$

Equation 3-6

This empirical relationship was extensively confirmed by Lu et al[65] and more recently by Meledandri et al.[1] using M_{NMR} values. The M_{NMR} value can be used to estimate the thickness of the dead layer and gain some insight into the crystallinity of the particles. In Figure 3-42 the M_{NMR} values from the different experimental sets are plotted as a function of d_{NMRD}. Using the Lu empirical model, t was fixed to the published figure of 0.6 nm and the result is overlaid below (black curve). It is evident that this approach doesn't fit the data, if we use an unconstrained approach and allow the free fitting of t; a value of t = 0.67 nm is obtained (red curve). However, this unconstrained approach does not fit the data. It should be noted that the effect of the ligands and the dead layer on the value obtained for M_{NMR}, as extracted from the SPM simulations, is not well understood. Additional magnetometry measurements are underway to investigate the dependence of M_s, as measured by traditional methods, on particle size

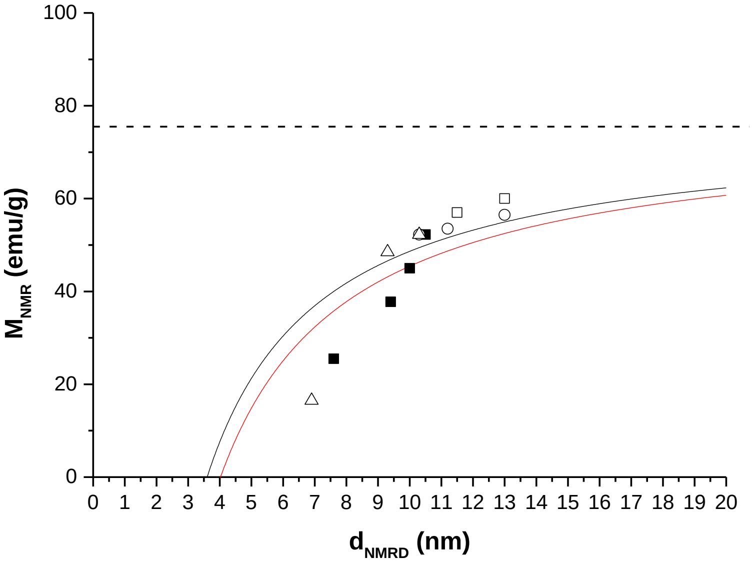

Figure 3-42 : M_{NMR} plotted against d_{NMRD}, the data is overlaid with the empirical model developed by Lu et al, — t = 0.6, — t = 0.67; Dashed line indicated bulk magnetism of Maghemite, ■ reaction temperature study, Δ reaction time study, □ closed volume study (bomb) and ○ precursor gram study

Upon re-examination of the data, the outliers are all samples synthesised at a reaction temperature other than 200⁰C (■) and BA-0.5H (Δ) which was identified earlier as having a very low M_{NMR} value. It this data is excluded and the unconstrained approach is repeated we obtain a good fit to the data ($R^2 = 0.98$), shown in Figure 3-43, with a t value extracted of 0.54 nm. This is 10% lower than what is reported by Lu, which suggests the NP synthesised at 200⁰C are more crystalline than other samples.

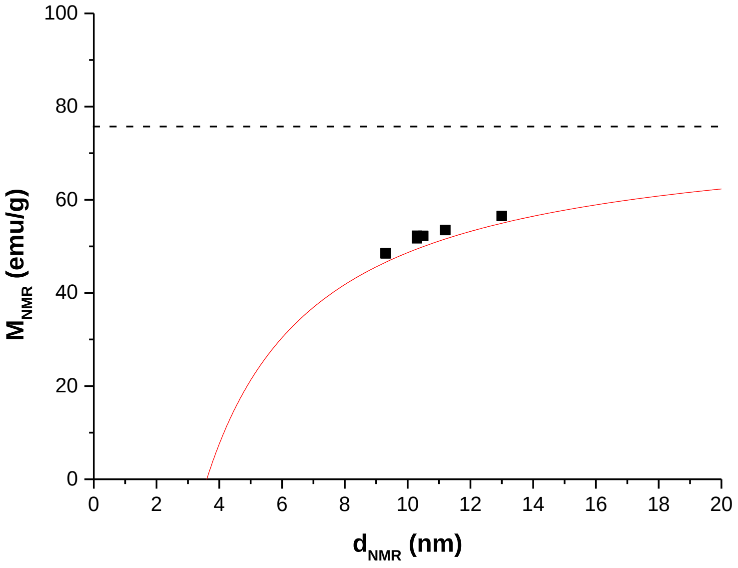

Figure 3-43 : M_{NMR} as extracted from SPM simulations plotted against d_{NMRD}, the data is overlaid with the empirical model developed by Lu et al, — t = 0.54; Dashed line indicated bulk magnetism of maghemite

Having shown that the Lu model can be applied to our materials, Equation 3-6 can now be used to calculate the thickness of the "dead layer" (t) for all the materials in the study which can then be used to judge the crystallinity of the materials. Figure 3-44 shows a clear negative correlation between t and reaction temperature. It was noted above that the relaxivity increased with temperature.

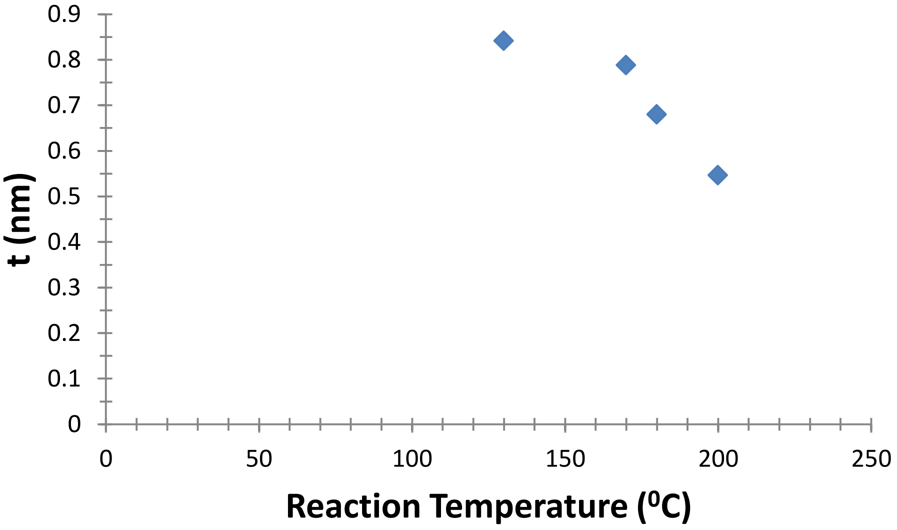

Figure 3-44 : t values calculated using the empirical developed by Lu et al. plotted against reaction temperature for samples synthesised using 1 g of precursor heated for 7 hours using different reaction temperatures

For the data shown in Figure 3-45, as the reaction time is increased from 0.5 hours a significant drop in t is observed. The thickness of the dead layer decreases significantly from 0.9 to 0.6 nm as the reaction time is increased from 0.5 – 3 hours. Following this, only a slight decrease in t (0.56 to 0.53 nm) is observed as the reaction time is extended further from 3 to 7 hours. Additionally there is a small increase in t (0.6 nm) as the reaction time is increased to 24 hours. This is a small change when compared to the change in t with reaction temperature, in which case t decreased from 0.8 to 0.55 nm on increase of the reaction temperature from 130 to 200^{0}C. This demonstrates that for the 1 g synthesis, there is little change in the crystallinity of the particles after the first 3 hours. However, temperature does play a significant role in determining the crystallinity of the particles, shown above.

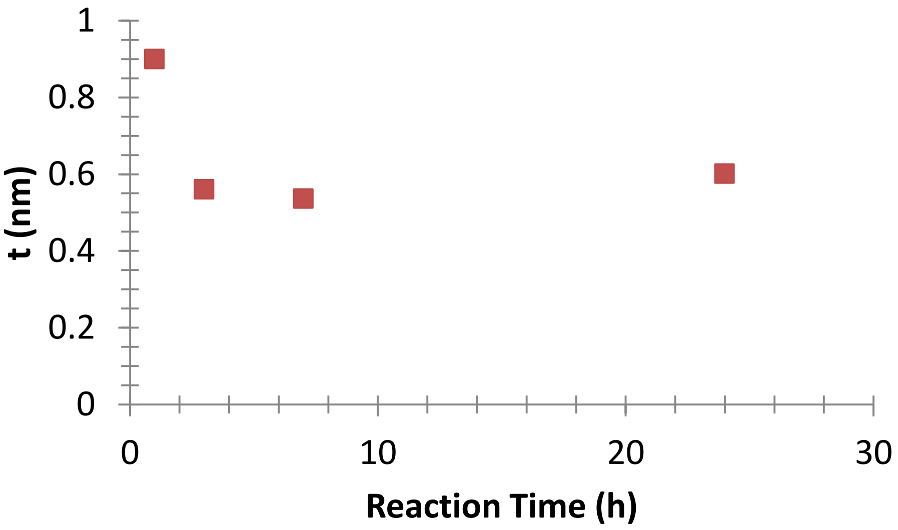

Figure 3-45 : t values calculated using the empirical developed by Lu et al. plotted against reaction time for particles synthesised using 1 g of precursor heated at 200⁰C using reaction times

From Figure 3-46, there is a trend with t, increasing the precursor quantity from 0.6 to 1 g results in a significant drop in t, following this there is change in t at the precursor quantity is increased to 8 g. However, for BA-12g and BA-16g the trend changes, we see an increase in the t value. This suggests a drop in crystallinity for these samples. The t values are of similar sizes to the BA-0.5H as shown in Figure 3-45, this similarity in t values ties in with our earlier observations that for these samples, there is remaining precursor following the reaction and the reaction has not gone to completion resulting in larger less crystalline NP. If future work were to be carried out, an experiment using the same increased precursor quantity as for BA-12g or BA-16g, but with an extended time could be attempted. This could result in larger and more crystalline NP.

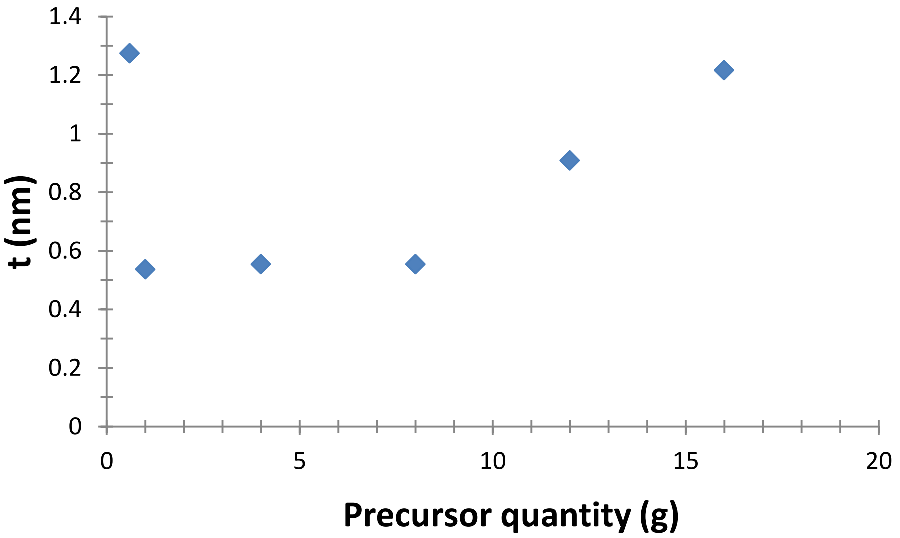

Figure 3-46 : t values calculated using the empirical model developed by Lu et al. plotted against precursor quantity for NP synthesised using varying amounts of precursor heated to 200^{0}C for 7 hours

Finally, the t values were calculated for the NPs synthesised under constant volume conditions using a solvothermal bomb. As we have shown that temperature appears to be the primary factor affecting the crystallinity, we would expect increased crystallinity for NPs synthesised using constant volume. From Table 3-15 we can see the NPs synthesised using constant volume have a much smaller t value. Previously, in this work the smallest t values we have calculated are ~ 0.53 nm, while for the bomb, the t value is ~ 14% smaller with a value of 0.46 nm. This is smaller than previously reported. This suggests that by synthesising NPs using a constant volume we can produce NPs of a very high crystallinity and monodispersity.

Table 3-15 : t values calculated for OA stabilised BA-NP synthesised using a bomb

Reaction Time (h)	t (nm)
7	0.479
24	0.456

3.4. **Conclusion**

A method to synthesise iron-oxide NPs of controlled size between the range of 6 to 13 nm through careful control of the reaction conditions was reported, (Figure 3-44). This control over size was confirmed using three different measurement techniques. The maximum M_{NMR} value (60 emu/g) was achieved for particles synthesised using 1 g of precursor dissolved in 20 ml of solvent heated for 48 hours at 200^{0}C prepared at a constant volume. This method also yielded the largest and most monodisperse NP, with a σ of 10% which is lower than previously reported for synthesises of this type. For future NP synthesis these conditions may represent the optimum. However, it may be that by increasing the precursor quantity extending the reaction time, larger particles could be produced, it is not clear at this point whether this would be at the expense of monodispersity.

It should be noted that the empirical approach of Lu et al. attributes all non-crystallinity to the outer layer. In an alternative interpretation it could be assumed that the thickness of the outer layer is always equivalent to one stoichiometric unit and by using the empirical relationship, the crystallinity of the core could be obtained in the form of a reduced magnetisation value. Nonetheless, it is very encouraging that the NMRD approach can produce semi-quantitative magnetometric data. There is some precedent for this finding [1, 24] but in this study we have extended the approach to a range of different NP sizes. A selection of the samples has been sent for detailed magnetometric analysis to further validate the interpretation presented here.

Chapter 4

Effect of Ligands on the Magnetic Resonance Properties of Nanoparticle Dispersions

4.1. **Introduction**

The excellent biocompatibility of iron oxide makes NPs especially interesting for biomedical applications, and when combined with their intrinsic superparamagnetism and relaxation enhancement properties they have great potential as theranostic agents. Upon administration the NP are transported around the body, reducing local concentrations to a point where relaxation rate enhancement of the surrounding molecules is lost. Doses can be increased, however; large doses of iron are toxic and can even be fatal. Currently it is estimated that doses above 60 mg iron per kg body weight display toxic effects[69]. Therefore, there is a clear need for contrast agents to be as efficient as possible in order to maximise the relaxation rate enhancement.

In Chapter 3, a method for the size controlled synthesis of γ-Fe_2O_3 NP in the nanometre size range was described, and using this method control over the relaxation properties was achieved. As previously discussed, NP in this size range introduce interesting properties resulting from surface area and volume considerations, particularly as the size decreases towards 10 nm. A number of studies describe the role of the surface ligand in altering the relaxation properties [70-73] assigning all relaxivity differences to the molecular nature and binding density of the stabilising ligand. However, these studies did not account for the polydispersity of the colloidal dispersion. It was described in Chapter 3 that the mono-dispersity of the colloidal dispersion has a huge effect on the magnetic properties. The method developed by Pinna et al. [50-52] produces NPs of good crystallinity, dispersions of good and reproducible mono-dispersity which can also be stabilised using a wide range of ligands. Hence, this method has been selected as it is an excellent platform to investigate the effects of ligands on the magnetic resonance properties of the dispersions.

This work comprises a study into the effect of chain length and head-group of stabilising ligand on relativities of γ-Fe_2O_3 nanoparticles. DLS was used to ensure that the samples were highly monodisperse. We have selected organic media for this study, as in our experience the colloidal control is better and the similarity between heptane and H_2O as a dispersing solvent from an NMRD perspective has been established[1]. The results of this study may be used as a guide in the design of aqueous γ-Fe_2O_3 NP suspensions with improved MRI and magnetic properties.

4.2. Experimental

4.2.1. Synthesis of Iron Oxide Nanoparticles

For the synthesis of iron oxide NP, Iron (III) acetylacetonate, Fe (III) $acac_3$ (purity ≥99.9%), oleic acid (≥99.0%) and benzyl alcohol, BA (purity ≥99.0%) were purchased from Sigma Aldrich. All reagents were used without further purification. For the washing and stabilisation of iron oxide NP reagent grade acetone was purchased from Labscan. Heptane (puriss), stearic acid, palmitic acid and lauric acid were purchased from Sigma Aldrich. All reagents were used as is.

Benzyl alcohol stabilised nanoparticles (BA-NP) were prepared as described in Chapter 3 using a modified surfactant free thermal decomposition of an organic iron precursor using 1 g of precursor refluxed at 200^0C for 7 hours.

4.2.2. Stabilisation of Benzyl Alcohol Nanoparticles

The NP in benzyl alcohol solution were stabilised using the procedure described in Chapter 3. As it was established that a PDI of < 0.1 is necessary to obtain reproducibility in the NMRD response, this criterion was applied to all samples, in this study in order to credibly investigate the effects of both ligand and head group. In Table 4-1 the ligands used are listed along with some relevant data. When referring to oleic acid nanoparticles, the label OA-NP will be used.

Table 4-1 : Characteristic details of the ligands used in the surface coating of NP

Name	Label	Head Group	Alkyl Group	M.W (g/mol)
Oleic acid	OA	R-COOH	C18:1 (cis-9)	282.46
Stearic acid	C18	R-COOH	C18:0	284.48
Palmitic acid	C16	R-COOH	C16:0	256.42
Lauric acid	C12	R-COOH	C12:0	200.32
Stearic dihydrogen phosphate	P18	R-O-POOOHH	C18:0	350.47
Palmitic dihydrogen phosphate	P16	R-O-POOOHH	C16:0	322.42
Lauric dihydrogen phosphate	P12	R-O-POOOHH	C12:0	266.31
Stearyl amine	N18	$-NH_2$	C18:0	269.51

4.2.3. Phosphorylation of Primary Alcohols

Phosphorus (V) oxychloride (puriss p.a., ≥99.0%), 1-octadecanol, 1-hexadecanol and 1-dodecanol were purchased from Sigma Aldrich. The alcohols were dried in a desiccator for 12 hours prior to reaction. Tetrahydrofuran (THF) and dichloromethane (DCM) were purchased from Labscan. The solvents were dried over 3Å molecular sieves before use. Deionised water was obtained from a Millipore water purification system with a resistivity of < 18.2 MΩ.cm.

A modified version of the method reported by Turro et al [74] was used. In a typical reaction 5 mmol of the primary alcohol was weighed out in a two-neck round-bottom flask. To this, 15 mL of THF was added to dissolve the alcohol. In all cases the alcohols dissolved completely in the 15 mL of THF. The two-neck round-bottom flask was equipped with a nitrogen flow system and a Teflon coated magnetic stirring bar. The solution was deoxygenated by N_2 bubbling for 15 minutes, and the nitrogen atmosphere was maintained for the duration of the reaction. Prior to reaction the solution was cooled in an ice bath then under vigorous stirring, 0.6 mL of $POCl_3$ was added drop wise. The reaction was allowed to proceed for 3 hours while stirring in an ice bath. The flask was then removed from the ice bath and the reaction was allowed to complete while stirring at room temperature for 1 hour. The reaction was finally quenched by adding 10 mL of water. The organic product was extracted using 4*15 mL aliquots of $CHCl_3$. The organic phase was collected and the $CHCl_3$ was removed using a rotary evaporator. The product was a slightly yellow power, which was stored in glass vials in a desiccator.

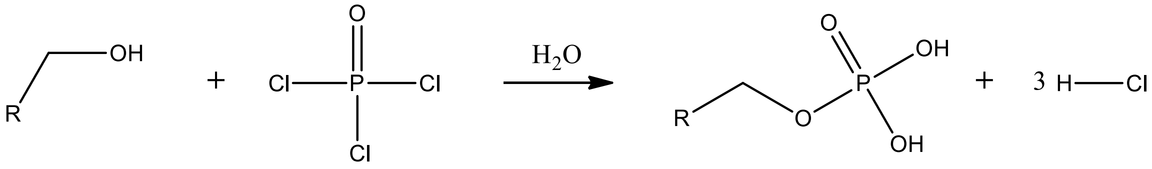

Figure 4-1: Reaction Scheme for the formation of alkyl phosphates using the reaction of $POCl_3$ with a primary alcohols and the subsequent quenching with water

The products of the phosphorylation reaction were analysed, using ATR-IR as described in Chapter 2. The data was smoothed using the in-built "data tune-up" post measurement routine contained within the Perkin-Elmer IR software. This tune-up consisted of a wavelength dependent absorption correction and a baseline correction routine the effects of which are shown in Chapter 2.

The ATR-IR spectra of the starting materials are overlaid in Figure 4-2. Broad features at 3325 cm^{-1} can be assigned to hydrogen bonding modes between alcohols, and the strong feature at 1064 cm^{-1} can be assigned to C-O stretching of a primary saturated alcohol, both features are indicative of primary alcohols. Hence the spectra confirm the presence of alcohols.

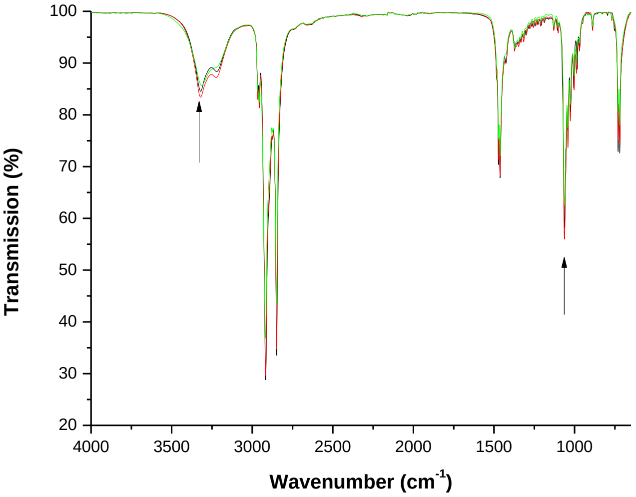

Figure 4-2: ATR-IR transmission spectra of primary alcohol precursors used to generate the phosphate products; — 1-octadecanol, — 1- hexadecanol and — 1-dodecanol, with the peaks assigned to alcohols identified

In Figure 4-3 the ATR-IR spectra of the products are overlaid. The broad peak at 3325 cm^{-1}, indicative of hydrogen bonded OH groups, has disappeared. Strong, sharp peaks in the region of 950 – 1150 cm^{-1} can be assigned to the stretching of the P-O of the phosphate[74]. The products were washed extensively and the presence of phosphate precursor can be ruled out. This confirms phosphorylation of the alcohol in all three of the products.

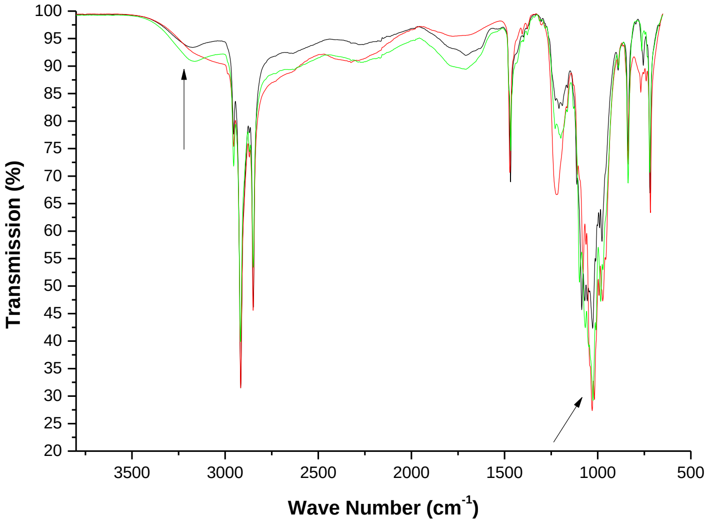

Figure 4-3: ATR IR transmission spectra of the phosphate products; — stearyl dihydrogen phosphate, — palmityl dihydrogen phosphate and — lauryl dihydrogen phosphate, note the significant difference in the spectrum as 1000 cm^{-1} when compared to Figure 4-2

4.2.4. Characterisation of Nanoparticle Dispersions

Eight dispersed NP samples, each with a different stabilising ligand (Table 4-1) were characterised using DLS and NMRD, as described in Chapter 2.

DLS measurements were performed at a stable temperature of 25°C ± 0.1°C. The concentration range used for DLS was between 1 – 5 mM. Each sample measurement consisted of an average of 3 measurements, each measurement was an average at least 10 sub runs each of a duration of 10 seconds in length. All sizes reported in this chapter are the z-average, derived from the cumulants analysis, and will be referred to as d_{HYD} unless stated otherwise. All size intensity distributions presented are derived from the intensity weighted distribution analysis.

The size and morphology of the particles were characterised as described in Chapter 2 using TEM. The solutions were diluted to approximately 0.2 – 1 mM with heptane. 5 μL of this solution was dropped onto a Formvar coated 400 mesh Copper grid (Agar Scientific, Essex, UK.) and allowed to evaporate prior to imaging.

The magnetic resonance properties of the suspensions were measured using NMRD, as described in Chapter 2 and Chapter 3. The profiles were recorded at 25°C ± 0.1°C. Each frequency reported consisted of an accumulation of at least 12 scans. In all cases the ^1H magnetisation recovery curves at different frequencies were successfully fitted to a mono exponential. The fitting error was < 2%, with the vast majority being < 1%, confirming that these dispersions have only a single T_1 and a single T_2 process. DLS Measurements were performed before and after NMRD analysis to assess aggregation due to exposure to the magnetic field. Unless otherwise stated, all samples showed no significant change in DLS response, indicating colloidal stability throughout the NMRD measurement.

The Fe concentrations of the different dispersions were measured using ICP-AES, as described in Chapter 3. The calibration curve was linear in the range 0.01 ppm to 10 ppm, in all cases $R^2 > 0.995$.

The dispersions were characterised using TGA as described in Chapter 2. In a typical experiment, stabilised nanoparticles were dried and the resulting power placed on a titanium TGA pan. The plan was placed inside a TGA furnace, under N_2 atmosphere and heated to 850^0C. The sample was heated to 100^0C at 10^0C/m, held isothermally for 30 minutes in order to remove any excess solvent; subsequently the sample was heated to 500^0C at a heating ramp of 2.5^0C/min to ensure maximum resolution between the different organic peaks. Finally the sample was heated to 850^0C at a ramp of 10^0C/min. The inter sample reproducibility was estimated to be between 5 to 10 % however, it was deemed necessary to have an initial sample mass of >10 mg to minimise the sample error and as such, all TGA experiments performed had an initial sample weight above 10 mg.

Selected samples were characterised by x-ray absorption spectroscopy (XAS), as described. These experiments were performed in collaboration with Miguel Angel Garcia, Instituto de Cerámica y Vidrio, Madrid.

4.3. **Results and Discussion**

4.3.1. Particle Size as determined by TEM

A typical TEM image of OA-NP is shown in Figure 4-4. The image shows very mono-disperse particles, with regular spherical shapes. Different batches of BA-NP are used throughout this work, however the reproducibility of the preparation method, as measured by DLS and NMRD, is demonstrated in Chapter 3.

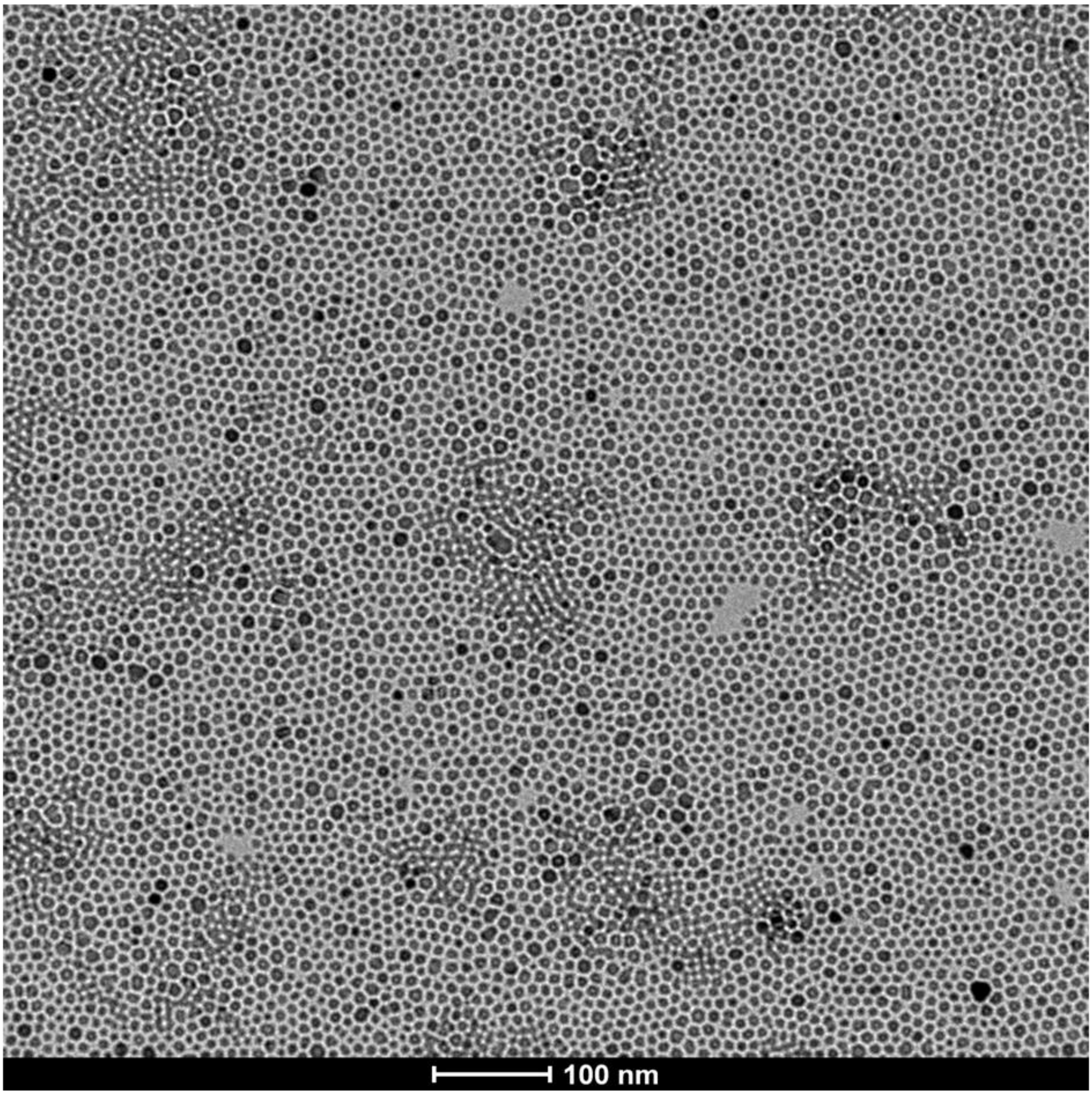

Figure 4-4: TEM image of monodisperse γ-Fe_2O_3 synthesised using surfactant free thermal decomposition nanoparticles synthesized (BA-NP) using 1 g of Fe(acac)$_3$ precursor refluxed in 20 mL of benzyl alcohol for 7 hours

Statistical analysis was performed on this image using ImageJ (National Institute of Health, US government) as described in Chapter 3. Figure 4-5 shows the overlay of the lognormal model with the experimental size distribution histogram constructed from a count of ~5000 particles. The R^2 value obtained was > 0.99 which shows the population conforms to this model. The mode size obtained from this analysis is 8.4 nm and a standard deviation of 1.6 nm (18%).

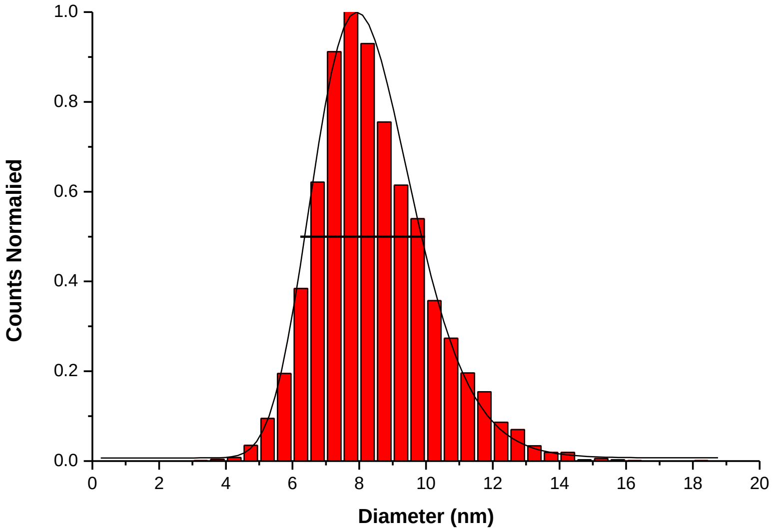

Figure 4-5: TEM Size distribution histogram of stabilised BA-NP, (Figure 4-4) with a DLS size of 14.8 nm and a PDI of 0.084; overlaid is the fitted lognormal distribution, ─, where the mode size is 8.4 nm and a standard deviation of 1.6 nm

4.3.2. Phase analysis by XAS

The normalised XAS spectra of NP samples stabilised with different ligands is presented in Figure 4-6. It is important to note the similarity in the shape of the spectra which suggests the same iron oxide phase present in all cases.

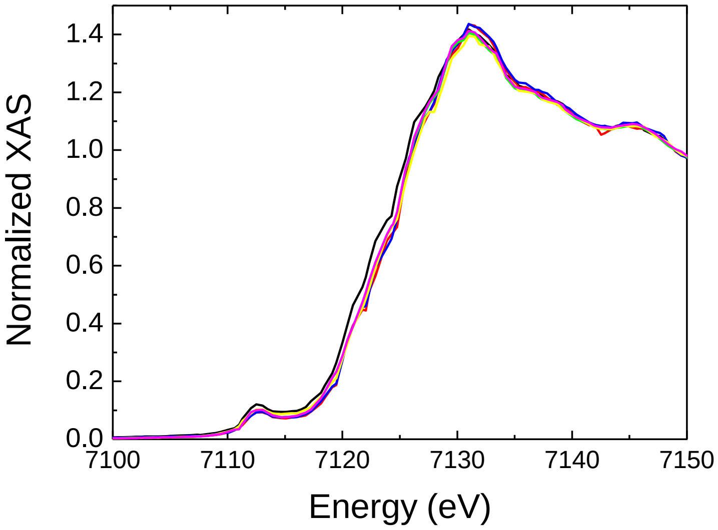

Figure 4-6 : Normalized XAS spectra of stabilised NP using different stabilising ligands; — Stearyl amine, (N18), — stearyl dihydrogen phosphate (P18), — palmityl dihydrogen phosphate (P16), — lauryl dihydrogen phosphate (P12), — stearic acid (C18), — lauric acid (C12)

Examining the XAS spectrum of the samples in Figure 4-6, it is clear there is little difference in the response of the NPs stabilised with different ligands. The variations present are about the same order of magnitude as measurement noise. Therefore, it can be said that changing the ligand has no measurable effect on the phase and electronic structure of NPs. It is also known that, the structure of the rising edge located between 7125 eV and 7140 eV, known as the X-ray Absorption Near Edge Structure (XANES), is highly sensitive to formal oxidation states and differences in the coordination sites [75] e.g. octahedral or tetrahedral sites. In the figure it is clear there is no significant difference in the near edge structure. This suggests that modifying the stabilising ligand had little to no effect on the oxidation state or coordination structure at the surface of the iron oxide particles.

In Figure 4-7 XAS spectra of different phases of iron oxide are overlaid with the spectrum of N18-NP. XAS suggests that our material is most similar to maghemite (γ-Fe_2O_3). There are small differences at higher energies; arising from self-absorption in the reference spectra due to a larger quantity of reference material used in the analysis.

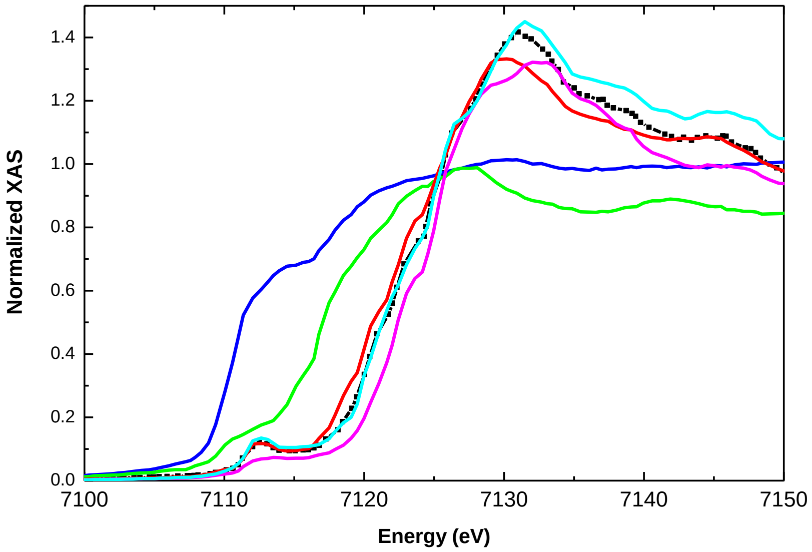

Figure 4-7 : Normalised reference XAS spectra of iron oxides of different phases; — Fe, — FeO, — Fe_3O_4, — α-Fe_2O_3, — γ-Fe_2O_3 and XAS spectrum of — NP-Stearyl amine, (NC18)

4.3.3. Investigation into the Effect of Chain Length on Particle Properties

Fatty acid stabilised nanoparticles

In Chapter 3 it was established that minor changes in PDI affected the NMRD response, in order to produce suspensions with reproducible NMRD response, the PDI value had to be <0.1. Preliminary experiments on alkyl-phosphate stabilised NP suspension confirmed that systematic and reproducible changes in r_1 and r_2 as the ligand was varied could not be obtained unless this criterion was met. Initially fatty acids were chosen due to the strong binding of the carboxylate group with iron-oxide [28]. In Figure 4-8, DLS data for fatty acid stabilised NP (FA-NP) suspensions in heptane are shown. The chain length was varied from C12:0 to C18:0. It is evident that by increasing the chain length of the stabilising ligand, d_{HYD} also increases slightly. This is to be expected as there is a longer alkyl chain extending from the surface. On the basis of a rudimentary calculation using ChemDraw, extending the chain length from C12:0 to C18:0 is expected to add 1.41 nm to the diameter. The observed size increase was 2.3 nm. The slight discrepancy can be attributed to two things; firstly the DLS size will include any associated solvent molecules, as the NPs are highly dispersible in the solvent it may be that the longer alkyl chain is associated with more solvent molecules. Secondly, the DLS scattering intensity scales with the sixth power of particle size. This is a key aspect of DLS as the measurement is extremely sensitive to larger particles. The strong weighting usually leads to higher DLS sizes.

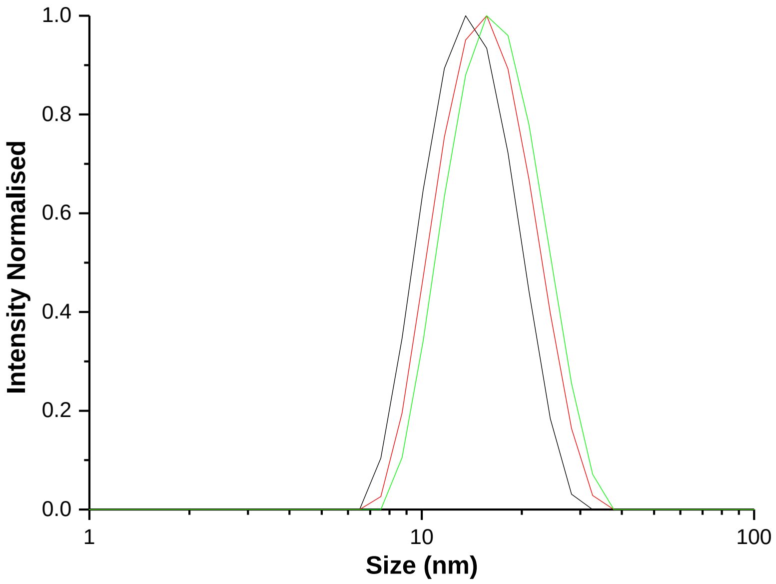

Figure 4-8: Intensity weighted DLS data for FA-NP with alkyl chains of differing length, it can be seen that the size increases as the chain length increases; d_{HYD} and PDI for the presented samples are — C12-NP 13.5 nm, PDI:0.06, — C16-NP 14.8 nm, PDI:0.08, — C18-NP 15.8 nm, PDI:0.07

The NMRD data for the heptane suspensions of iron oxide NP are shown in Figure 4-9; it was found there was little change in the d_{HYD} following NMRD confirming dispersion stability. The superparamagnetic response is confirmed by the presence of the mid-frequency dip. The frequency of the maximum (ν_{max}), which is very sensitive by the particle size, does not change; it lies at 8.3 MHz for all preparations. This indicates a fixed particle diameter, as sensed by the ^1H relaxation of the solvent molecules. However, the relaxivity is found to decrease with increasing chain length; the r_1 value at ν_{max} decreases from 33.4 to 32.7 to

31.7 $s^{-1}mM^{-1}$ as the chain length increases from C12:0 to C16:0 to C18:0. This corresponds to a decrease of 5%. SPM theory suggests the change in r_1 arises due to the changes in either diffusion coefficient, D, or M_S. As the ligand is in very low concentrations (~ 0.02 %w/v) it is not expected that D would be altered, therefore any changes in r_1 should arise from a change in M_s and hence from any effect of the ligand on magnetic properties of the particles.

The value of r_1 in the lower frequency plateau is largely determined by the Neel correlation time (τ_n) and the anisotropy energy (ΔE_{anis}). The r_1 value at the plateau also decreases from 21.1 to 17.4 to 16.3 $s^{-1}mM^{-1}$ as the chain length increases from C12:0 to C16:0 to C18:0. This corresponds to an increase of 23%. The different NMRD curves are overlaid with SPM simulations in Figure 4-9; the agreement of the simulations with the NMRD profiles is comparably good in all cases.

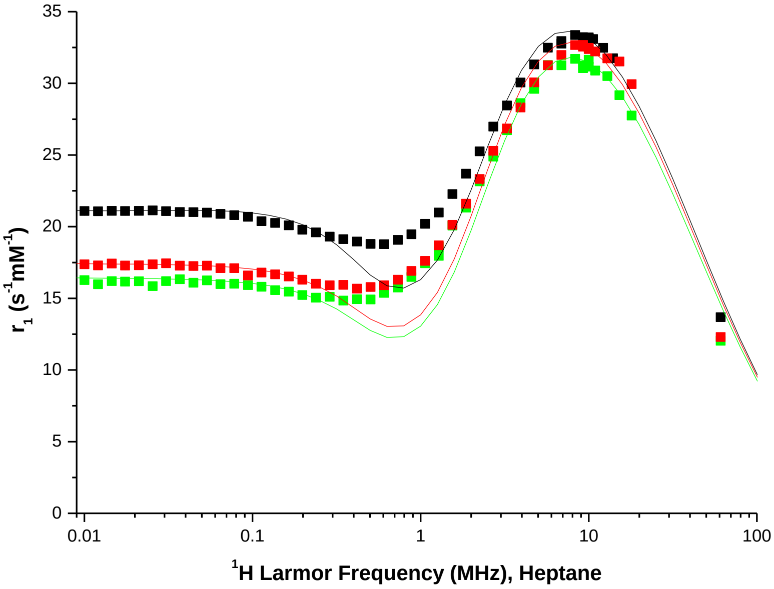

Figure 4-9: NMRD profiles (squares) FA-NP with alkyl chains of differing length overlaid with the simulated profiles (solid lines) using SPM theory, with d_{HYD} and PDI before and after NMRD respectively; ■ C12-NP; before 13.5 nm, PDI: 0.06, after 13.5 nm PDI: 0.07, 🟥 C16-NP; before 14.8 nm, PDI: 0.08, after 14.7 nm, PDI: 0.09, 🟩 C18-NP; before 15.8 nm, PDI: 0.07, after 15.6 nm, PDI: 0.09

Table 4-2: The parameters used in the simulated profiles of different preparations FA-NP with alkyl chains of varying length with d_{TEM} of 8.2 nm

	d_{HYD} (nm)	PDI	d_{NMR} (nm)	M_{NMR} (emu / g)	ΔE_{anis} (GHz)	τ_0 (s)
■ C12	13.5	0.09	10.3	54.25	0.6	20E-9
🟥 C16	14.8	0.06	10.3	53.75	0.6	9 E-9
🟩 C18	15.8	0.07	10.3	53	0.6	8 E-9

When examining the parameters used in the simulations, Table 4-2, the d_{NMR} value is 10.3 nm and remains unchanged for all the FA-NP suspensions, as expected as the ligand shell is permeable to the diffusing solvent molecules. This suggests that the length of the chain does not limit the diffusion of the solvent despite the change in d_{HYD}. The saturation magnetisation value, as extracted from the SPM model, hereby known as M_{NMR} was found to decrease slightly as chain length increased. The major change was a decrease in τ_0 with increasing chain length and increasing d_{HYD}.

Table 4-3: Relaxivity data for FA-NP suspensions with alkyl chains of varying length measured at 9.25 MHz (upper table), 61 MHz (lower table)

Chain Length	r_2 (s^{-1} mM^{-1})	Change (%)*	r_1 (s^{-1} mM^{-1})	Change (%)*	r_2/r_1
12	53.8	-	33.2	-	1.6
16	53.1	1	32.7	2	1.6
18	52.9	2	31.1	7	1.7

Chain Length	r_2 (s^{-1} mM^{-1})	Change (%)*	r_1 (s^{-1} mM^{-1})	Change (%)*	r_2/r_1
12	54.9	-	13.7	-	4.0
16	54.4	1	12.3	10	4.4
18	54.4	1	12.0	12	4.5

Note: * % change versus C12

The r_2, r_1 values and the r_2/r_1 ratios, obtained at the measurement frequencies of 9.25 and 61 MHz are presented in Table 4-3 and in all cases r_2 and r_1 decrease with increasing alkyl chain length. The decrease in r_2 is very small, ~1%. As r_2 is very sensitive to aggregation [47] this suggests that there is no change in aggregation on increasing chain length. Thus any effects observed for the FA-NP suspensions are a result of the different stabilising ligands used and not inter-particle interactions. Secondly there is a moderate decrease in the r_1 as the chain increases. At 61 MHz, the decrease in r_1 is 12%. This results in an increase of 12% in the r_2/r_1 ratio with increasing chain length.

For the FA-NP, as the chain length increases from C12:0 to C18:0, the d_{HYD} value increases by 17%. At 60 MHz, there is a small increase, of 1%, in r_2 suggesting that there is no aggregation. As noted above, DLS following NMRD confirmed colloidal stability. Hence, it appears that the size increase is a result of only the ligand coating. The d_{HYD} increase is similar to that the expected from molecular modelling. Secondly, as chain length increases, the r_1 value decreases by 5%, at $\nu_{max,}$ and by 23% at the plateau. Using SPM theory, this corresponds to a marginal decrease of 2% in the M_{NMR} value and a significant decrease of 60% in τ_0, indicating that a faster reorientation of the magnetic moments is a key change. Although the decrease of 2% in magnetisation is small, when the relaxation enhancement is examined, there is a significance decrease of 12% in r_1 at clinical fields (60 MHz).

Alkyl phosphate stabilised nanoparticles

The study was extended to AP stabilising ligands with alkyl chains of differing length in order to see if the trends observed for FA-NPs also held for AP-NP. The phosphate head group was chosen due to its strong affinity for iron-oxide. In Figure 4-10, the intensity weighted DLS data for AP-NP are shown and a trend similar to that observed for FA-NP is evident, the d_{HYD} value increases as the chain length increases from P12:0 to P18:0. The values of d_{HYD} are 12.8, 14.5 and 15.1 nm for P12, P16 and P18, respectively. This represents a d_{HYD} increase of 18% which compares to a 17% increase for the FA-NP suspensions.

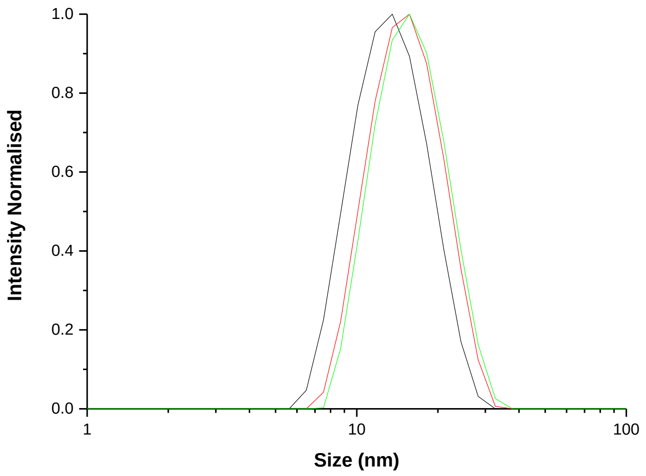

Figure 4-10: Intensity weighted DLS results for AP-NP with alkyl chains of differing length, it can be seen that the size increases as the chain length increases, note that as the chain length increases the size increases; d_{HYD} and PDI for the presented samples are — P12-NP 12.78 nm, PDI: 0.06, — P16-NP 14.48 nm, PDI: 0.07, — P18-NP 15.05 nm, PDI: 0.07

In Figure 4-11, the NMRD profiles of the AP-NP suspensions are shown. The dispersions were shown to be stable following the measurement by DLS. Again the shape of the profiles and the presence of a mid-frequency dip confirm that the presence of superparamagnetic nanoparticles. The ν_{max} value was 9.3 MHz for all chain lengths, as compared to a value of 8.3 MHz observed for the FA-NP suspensions. Systematic changes in r_1 with chain length, similar to those observed the FA-NP are evident in the profiles. The r_1 at ν_{max} decreased from 31.0 to 26.2 to 25.5 $s^{-1}mM^{-1}$ as the chain length increased from C12:0 to C16:0 to C18:0, a decrease of 30%. The r_1 value of the plateau also decreased from 19.5 to 17.1 to 15.1 s^{-1} mM^{-1} as the chain length increased, corresponding to a total decrease of 19%. Interestingly there is a sizable decrease in r_1 at ν_{max} between from P12-NP to P16-NP as compared to the FA-NP equivalents, Table 4-3.

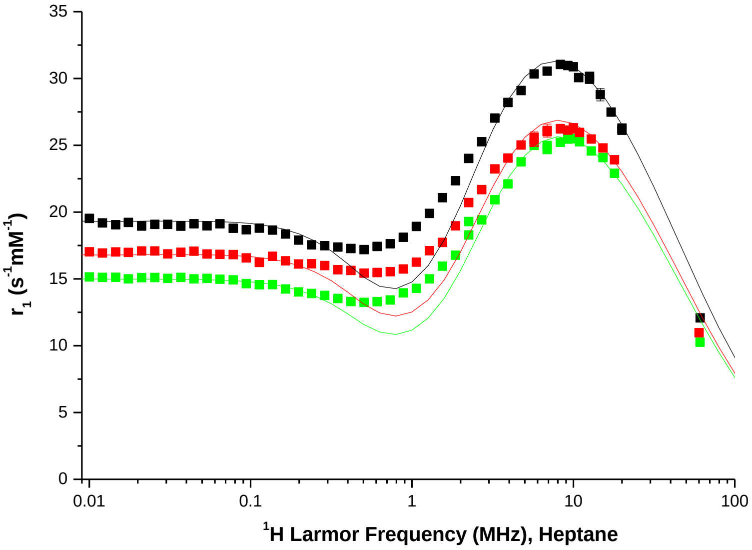

Figure 4-11 : NMRD profiles (squares) AP-NP with alkyl chains of differing length overlaid with the simulated profiles (solid lines) using SPM theory, with d_{HYD} and PDI before and after NMRD respectively; ■ P12-NP; before 12.8 nm, PDI: 0.06, after 12.9 nm PDI: 0.04, 🟥 P16-NP; before 14.5 nm, PDI: 0.07, after 14.5 nm, PDI: 0.06, 🟩 P18-NP; before 15.1 nm, PDI: 0.07, after 15.1 nm, PDI: 0.05

Due to the large decrease in relaxivity between P12 and P16, as seen in Figure 4-11, a new batch of BA-NP was synthesised and an aliquot was stabilised with lauric dihydrogen phosphate, generating a repeat of P12. In Figure 4-12 it can be seen there is little difference (<6%) between the two samples. This result further demonstrates the reproducibility of the synthesis, stabilisation and measurement, and confirms the findings for P12.

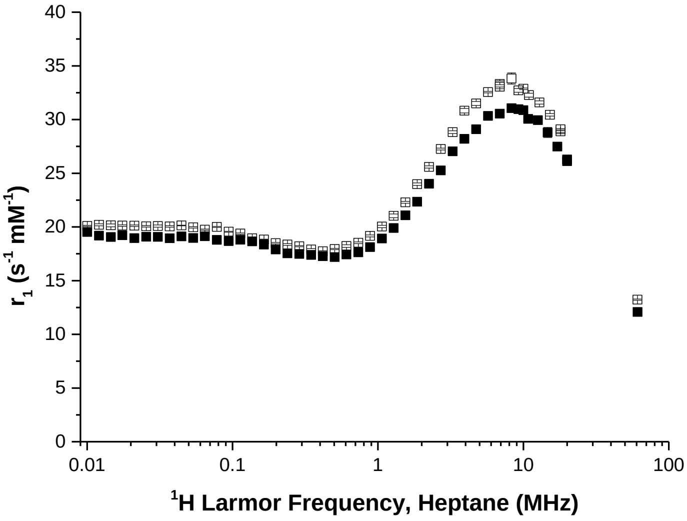

Figure 4-12 : NMRD profiles (squares) AP-12 stabilised Ba-NP synthesised using 1 g of precursor synthesised at 200^{0}C for 7 hours including analysis of a repeat preparation

In Figure 4-11, NMRD profiles of different preparations of AP-NPs (PDI< 0.1) with alkyl chains of differing length are shown. Overlaid on these profiles are simulations using SPM theory. The simulations fit well at both low and higher frequency with the expected difference in the mid frequency range present.

Table 4-4: The parameters used in the simulated profiles of different preparations of AP- NP with alkyl chains of varying length with a d_{TEM} of 8.2 nm

Sample	d_{HYD} (nm)	PDI	d_{NMR} (nm)	M_{NMR} (emu/g)	ΔE_{anis} (GHz)	τ_0 (s)
■ P12	12.8	0.06	10.3	52.5	0.6	17.7E-9
🟥 P16	14.7	0.07	10.3	49	0.6	17.7E-9
🟩 P18	15.1	0.07	10.3	48	0.6	13E-9

When examining the parameters extracted from the simulations for AP-NP, Table 4-4, the d_{NMR} value is identical to that obtained for FA-NP stabilised suspensions and it doesn't change with chain length. It seems that the change in the ligand from FA to AP does not alter the size of the core of the NP, as sensed by the diffusing solvent molecules, despite changes in d_{HYD}. As with FA-NP, M_{NMR} decreases slightly and τ_0 decreases as chain length is increased.

Table 4-5: Relaxivity data for AP-NP suspensions with alkyl chains of varying length measured; Upper table measurements performed at 9.25 MHz, Lower tables measurements performed at 61 MHz

Chain Length	r_2 (s^{-1} mM^{-1})	Change* (%)	r_1 (s^{-1} mM^{-1})	Change* (%)	r_2/r_1
12	44.3	-	30.9	-	1.6
16	43.7	1	26.1	16	1.7
18	41.0	7	25.5	18	1.7

Chain Length	r_2 (s^{-1} mM^{-1})	Change* (%)	r_1 (s^{-1} mM^{-1})	Change* (%)	r_2/r_1
12	44.3	-	12.1	-	4.0
16	43.9	1	10.9	9	4.2
18	42.6	4	10.3	15	4.2

Note: % change relative to P12

In Table 4-5 the r_2, r_1 values and the r_2/r_1 ratios of the AP-NP stabilised suspensions are shown for measurement frequencies of 9.25 and 61 MHz. Similar to the FA-NP case, the r_2 and r_1 values decrease with increasing alkyl chain length and the change in r_2 is very small. It should also be noted that the r_2 values for AP-NP are lower than for FA-NP, Table 4-3. Finally the change in r_1 across the series is significantly greater than the change in r_2, thus any changes in the r_2/r_1 ratio arise primarily due to changes in r_1.

For AP-NPs as the chain length is increased from C12:0 to C18:0 d_{HYD} increases by 16%. This is very similar to the observed increase in d_{HYD} for the FA-NP (17% increase). However, examination of the r_2 values at 60 MHz shows a 4% decrease in the r_2 data from P12 to P18 suggesting no significant aggregation present within the dispersions. The 15% decrease in r_1 at ν_{max}, and the 12 % decrease at the plateau, with increasing chain length, mirrors the observations for FA-NP. The simulations suggest that for AP-NP the key factors are a decrease of 4% in r_1 or 2% in M_{NMR} and a significant increase of 27% in τ_0.

For both head groups we find that as the chain length is increased, the ν_{max} value does not change. For FA-NP ν_{max} is at 8.3 MHz for all chain lengths while for AP-NP the ν_{max} is at 9.3MHz for all chain lengths. Despite the frequency difference the simulations give the same d_{NMRD} value for both FA-NP and AP-NP. This suggests that there is no significant difference in particle size as sensed by the diffusing solvent molecules. That interpretation makes the observation of a change in relaxivity more interesting. For the two cases, as the chain length increases, the relaxivity decreases; at the ν_{max} for FA-NP there is a 5% decrease in relaxivity, while for AP-NP there is a 30% decrease. When comparing the r_1 values at clinical fields (60 MHz), in both cases, as the chain length increases, the relaxivity decreases, FA-NP ~12%, AP-NP ~15%. Detailed analysis of differences in relaxation properties between different head groups is described below in section 4.3.4

A similar trend in magnetometry data obtained for alkylsulphate stabilised magnetite nanoparticles has been reported [71]. Yee et al observed a ~40% decrease in M_S as the chain length of the stabilising ligand was increased from C12:0 to C18:0 (hereby referred to as S12 to S18). Using IR evidence they suggested higher ligand packing density for S18 and that the sulphate head groups reduced the magnetisation by direct interaction with the Fe atoms on the nanoparticles surface. However TGA data reported in the paper was not fully analysed. Analysis of that data shows that the ligand packing density is slightly reduced for longer chain lengths; S12 has a binding density of 15 ligands/nm^2 and S18 a binding density of 13 ligands/nm^2. A similar trend in ligand binding density for alkylphosphate stabilised maghemite particles has been established by Sahoo et al[70] suggesting steric interactions limit the surface ligand density. For P12 stabilised NP a greater weight loss was observed, as compared to P18 NP stabilised in the same way. This suggests higher packing density for P12-NP, although again these details were not noted in the paper.

TGA analysis of FA-NPs (C12, C16 and C18) is presented in Figure 4-13, with the weight loss curves normalised so the inorganic weight fractions are equal to one. During these TGA measurements, the sample was heated to 100^0C and held for thirty minutes in order to remove all volatiles. Three features can be identified in the figure below; the first is attributed to unbound ligand decomposing at the lowest temperature. The second loss can be attributed to a small portion of ligand physisorbed as a partial bilayer [70] while the final feature, at the highest temperature (as indicated in the figure) can be attributed to decomposition of the chemisorbed ligand directly bound to the iron oxide surface, interestingly these features occur within 20^0C of the reported decomposition temperatures of the free ligands. The remaining weight fraction arises from iron oxide which decomposes above 800^0C. Using the weight of iron oxide, assuming spherical particles with a d_{TEM} of 8.4 nm, the weight of one particle was calculated, then from the weight fraction, the total number of particles and the total surface area of iron oxide nanoparticles was calculated. Using the weight fraction of chemisorbed ligand, the footprint of each ligand was calculated. Table 4-6 shows an increase in ligand footprint (decrease in binding density) of 15.3, 30.5 and 38.1 $Å^2$ as chain length increases from C12 – C16 – C18 respectively. These footprints are similar to, but smaller than the reported value for oleic acid of 38 $Å^2$ [60].

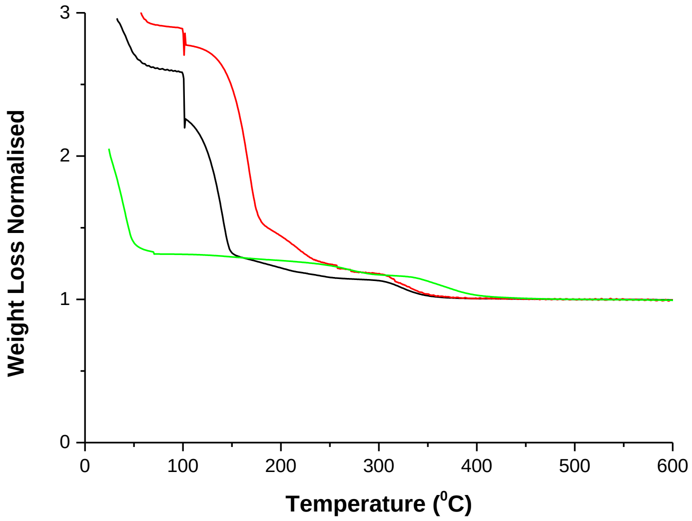

Figure 4-13 : TGA weight loss curve normalised to weight of iron oxide for BA-NP stabilised using fatty acids of varying chain length; — C12, — C16 and — C18

Table 4-6 : TGA analysis of FA-NP assuming a spherical core size of 8.4 nm (d_{TEM})

Sample	Decomposition Temperature (⁰C)	Footprint (Å²)
C18	360	38.1
C16	320	30.5
C12	323	15.3

As discussed in Chapter 3, it is a commonly accepted that in an oxide core of superparamagnetic nanoparticles there are two distinct regions; an inner region composed of free or uncanted spins which are free to align with an externally applied magnetic field; and an outer region with associated or canted spins, Figure 4-14 [16, 64-68]. This schematic representation of the spin orientations is commonly used in the literature, interestingly it does suggest ferromagnetic coupling in the outer layer, as opposed to disorder, although this is rarely commented on. There are several factors that can affect the thickness of this layer which are relevant to this study, including the binding density and binding strength of the ligand to the surface of the NP.

By keeping the ligand head group constant we have effectively kept the binding strength constant in an attempt to elucidate the effect binding density has on the magnetic resonance properties. For a reduced binding density a picture emerges of a patchy ligand coverage which gives rise to a patchy distribution of canted spins. We suggest that this results in multiple shallow minima that allow fast re-orientation of the moment. In contrast, for a higher binding density, the ligand coverage will be more conformal and the canted layer will follow the particle shape, in which case re-orientation dynamics are determined by the magnetocrystalline anisotropy of the core, which is on average identical for all samples.

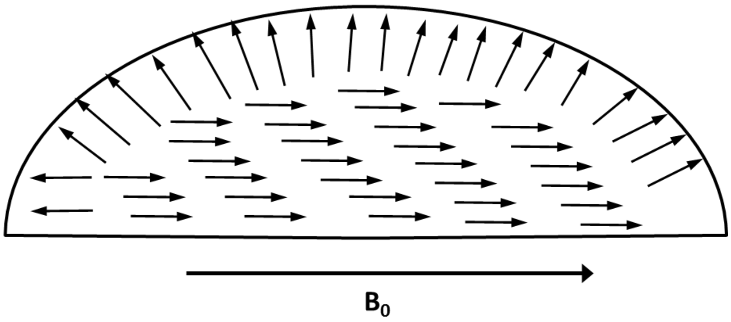

Figure 4-14: Schematic representation of spin canting of the surface of a nanoparticle

The NMRD study discussed in 4.3.2 and 4.3.3 shows that for both FA-NP and AP-NPs over the same range of chain lengths, we observe a marginal decrease in M_{NMR}. The key finding is a decrease in τ_0 which suggests a decrease in anisotropy for both head groups as chain length increases. This is interesting, and is to the best of our knowledge without precedent in magnetometric analysis of NP dispersions. We tentatively attribute this to the change in ligand binding density which affects the spin canting of the surface. However, further tests including field cooled and zero field cooled magnetometry are being carried out to investigate the effect of the ligand on the magnetic properties.

4.3.4. The Effect of Head Group on Magnetic Resonance Properties

To further examine the effect of the head group on the properties of NPs, the study was expanded to include alkyl amines with a C18:0 alkyl chain of (AA-NP). In Figure 4-15 the intensity weighted DLS results for the different preparations of NPs with a C18:0 chain lengths are shown. There is a slight difference in d_{HYD} between the three suspensions with sizes of 14.4, 15.8 and 15.1 nm obtained for AA-NP, FA-NP and AP-NP, respectively.

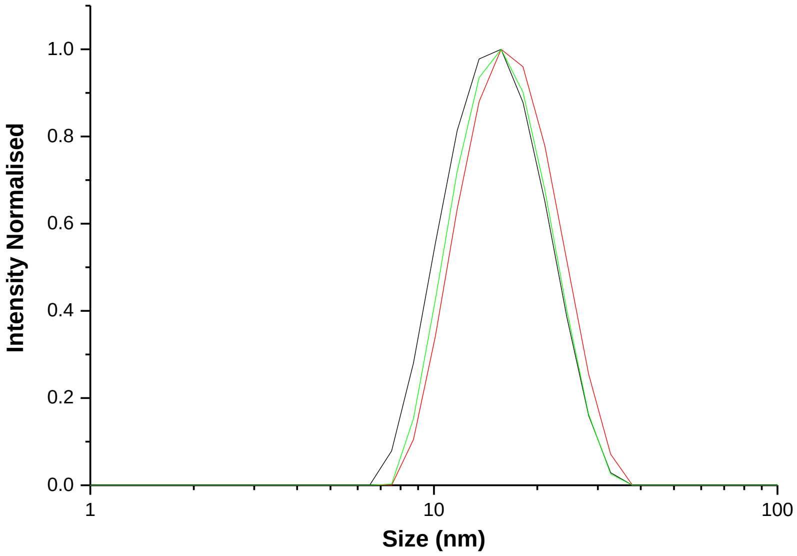

Figure 4-15: Intensity weighted DLS data for AA-NP —, FA-NP — and AP-NP — with a fixed alkyl chain length of C18:0; d_{HYD} and PDI for the presented samples are — N18-NP 14.4 nm, PDI: 0.08, — C18-NP 15.8 nm, PDI: 0.07, — P18-NP 15.1 nm, PDI: 0.08

Examining the NMRD data in Figure 4-16, once again the suspensions are shown to be stable and superparamagnetic. The frequency of the maximum varies, for AA-NP ν_{max} is at 8.5 MHz, as compared to 8.3 MHz for FA-NP and 9.3 MHz for AP-NP. The r_1 of the maximum decreases from 35.0 to 31.8 to 25.5 $s^{-1}mM^{-1}$ as the head group changes from amine to carboxylate to phosphate. This corresponds to a decrease of 26%, a sizable change in relaxivity. The r_1 of the plateau also decreases from 21.8 to 16.3 to 15.2 $s^{-1}mM^{-1}$ as the head group changes from amine to carboxylate to phosphate. This corresponds to a decrease of 30 %.

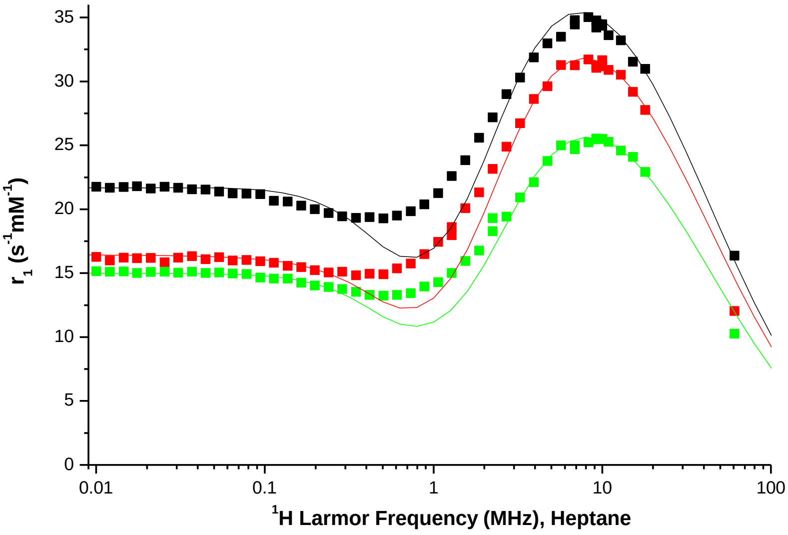

Figure 4-16: NMRD profiles (squares) and simulated profiles using SPM theory (solid lines) of C18:0 stabilised suspensions with varying head groups; AA-NP ■ (before 14.4 nm PDI: 0.08, after 14.7 nm PDI: 0.06), FA-NP 🟥 (before 15.8 nm PDI: 0.07, after 15.6 nm PDI: 0.09) and AP-NP 🟩 (before 15.1 nm PDI: 0.08, after 15.1 nm PDI: 0.05)

In Figure 4-16, NMRD profiles of N18, C18 and P18-NP are shown. Overlaid on these profiles are simulations using SPM theory. The simulations agree comparably well with the data in all cases and the parameters are shown in Table 4-7 below.

Table 4-7: The parameters obtained from simulated profiles of AA-NP ■, FA-NP 🟥 and AP-NP 🟩 each with a fixed alkyl chain length of C18:0 with a d_{TEM} of 8.4 nm

	d_{HYD} (nm)	PDI	d_{NMRD} (nm)	M_{NMR} (emu/g)	ΔE_{anis} (GHz)	τ_0 (s)
N18 ■	14.4	0.08	10.3	55.5	0.6	18E-9
C18 🟥	15.8	0.07	10.3	53.5	0.6	8E-9
P18 🟩	15.1	0.08	10.3	48.3	0.6	13E-9

Examination of Table 4-7 shows that there is no change in d_{NMRD} across the series suggesting that the different head groups do not limit the diffusion of the solvent molecules about the core. There is a moderate (12%) decrease in M_{NMR} as the head group changes from amine, to carboxylate and to phosphate.

Table 4-8: Relaxivity data for different NP suspensions each with varying head group with a fixed alkyl chain length of C18:0; Upper table, measured at 9.25 MHz, lower table measured at 61 MHz

Head Group	r_2 (s^{-1} mM^{-1})	Change (%)*	r_1 (s^{-1} mM^{-1})	Change (%)*	r_2/r_1
N18	56.7	-	34.8	-	1.63
C18	52.9	7	31.1	11	1.70
P18	43.9	22	25.5	27	1.72

Head Group	r_2 (s^{-1} mM^{-1})	Change (%)*	r_1 (s^{-1} mM^{-1})	Change (%)*	r_2/r_1
N18	56.7	-	16.4	-	3.46
C18	54.4	4	12.0	26	4.52
P18	42.6	25	10.3	37	4.16

Note:* % change when compared to N18

The r_2, r_1 values and the r_2/r_1 ratios for C18:0 stabilised NP with different head groups, measured at 9.25 and 61 MHz, are presented in Table 4-8. It is interesting to note that there is a significant change in both r_2 and r_1 as the head group changes from N18 to C18 to P18. It should be noted that the possibility of differences in head group mobility across the surface could affect r_1, but this is a difficult phenomenon to assess.

As discussed in Chapter 3, Tang et al.[64] developed a relationship (Equation 3-6), which has been confirmed empirically, [1, 65] between saturation magnetisation of the sample, $M_S(d)$, the bulk saturation magnetisation of the material ($M_S(O)$), the depth of the magnetically dead layer (t) and the diameter of the nanoparticle (d). Previously, for maghemite NP, t has been estimated at between 0.57 and 0.60 nm [67, 68].

$$\frac{M_s(d)}{M_s(O)} = 1 - \frac{6t}{d} \qquad \textbf{Equation 4-1}$$

In previous studies where the effect of ligands and surface coating on the magnetic properties was investigated [76, 77] a change in the M_s value was observed. From the data presented here, there is evidence to suggest that a similar effect is at work. We suggest that it is possible to use the empirical model developed by Lu et al. to quantify the change of the thickness of the dead layer as a function of the head group using the M_{NMR} values. As noted in Chapter 3.4, an alternative interpretation is that there is a fixed thickness of the spin canted layer and variable core crystallinity. Detailed magnetometric analysis is underway to refine the interpretation.

Before discussing the analysis of the MNMR values it is necessary to examine the binding mechanisms of alkyl amines, alkyl carboxylates and alkyl phosphates. It is believed that alkyl amines bind to the Fe centre through donation of the lone pair on the nitrogen, while alkyl carboxylates [78-80] and alkyl phosphates [71] are both conjugate bases, and thus bind through the similar binding mechanisms where by the negatively charged oxygen binds to the Fe centre. Alkylamines have been shown to have a lower binding strength to iron oxide compared to carboxylates and have been shown to be displaced by carboxylates[81]. Alkylphosphates have a similar binding mechanism to carboxylates [70, 71, 82] but the interaction is stronger as phosphates have empty d-orbitals and so a binding mechanism of pπ-dπ O-Fe electron donation, and dπ-dπ Fe-P electron accepting has been proposed [71]. It has been shown that alkylphosphates and phospholipids readily displace carboxylates [83].

TGA analysis of the three different head group samples are shown in Figure 4-17. Again, the curves have three distinct features. The first weight loss feature arises due to unbound ligand decomposing, the second arises from a physisorbed partial second layer, and the third high temperature feature can be assigned to decomposition of surface bound ligand. A similar approach to the previous TGA analysis was adopted which allows calculation of the footprints, Table 4-9. The data shows that P18 has a higher decomposition temperature than C18, as expected, and a higher binding density when compared to carboxylates. It should be noted that for these samples, there is little change in the footprint between iron oxide NP stabilised using different head groups. This is in contrast to the observations from the chain length study, and it strongly suggests that the footprint is determined by the alkyl chain length and not the head group, i.e. lateral interactions dominate.

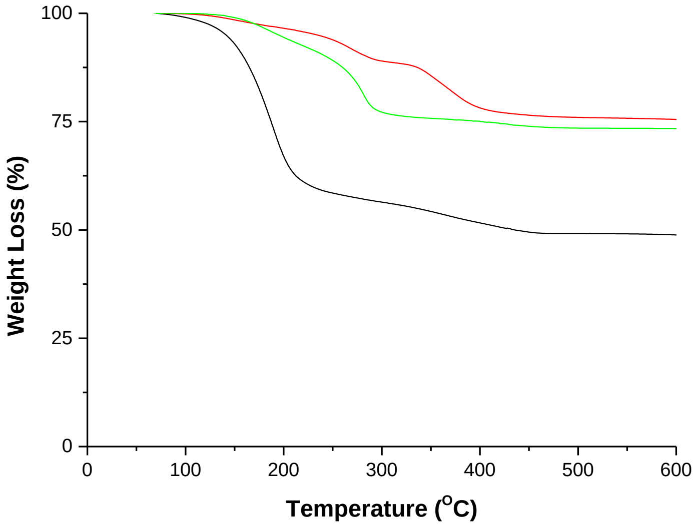

Figure 4-17: % Weight loss curves derived from TGA for — N18-NP, — C18-NP and — P18-NP

Table 4-9 : Decomposition temperature of different ligands bound to Ba-NP

Sample	Decomposition Temperature (^{0}C)	Footprint (Å^2)	Binding Density (ligand/nm^2)	M_{NMR} (emu/g)	t (nm)
P18	408	38.9	2.57	48.3	0.50
C18	363	40.4	2.47	53.5	0.41
N18	352	38.4	2.60	55.5	0.37

Returning to the M_{NMR} values, they are found to decrease as the head group changes from N18-NP to C18-NP to P18-NP, Table 4-9. We suggest that change in binding strength, associated with the different head group, results in a change in the thickness of the canted "dead" layer. When the empirical relationship developed by Tang et al., Equation 3-6 is applied to our figures, an increase in the thickness of the canted dead layer when moving from N18 (0.37 nm) to C18 (0.41 nm) to P18 (0.50 nm) is found. This trend fits the order of binding strength of the ligands, discussed above, and explains the decrease in magnetisation we observe. Furthermore NMRD studies show that AP has a larger τ_0 indicating greater anisotropy. We suggest this arises from the increased "dead" layer thickness which acts as a greater energy barrier resulting in slower dynamics.

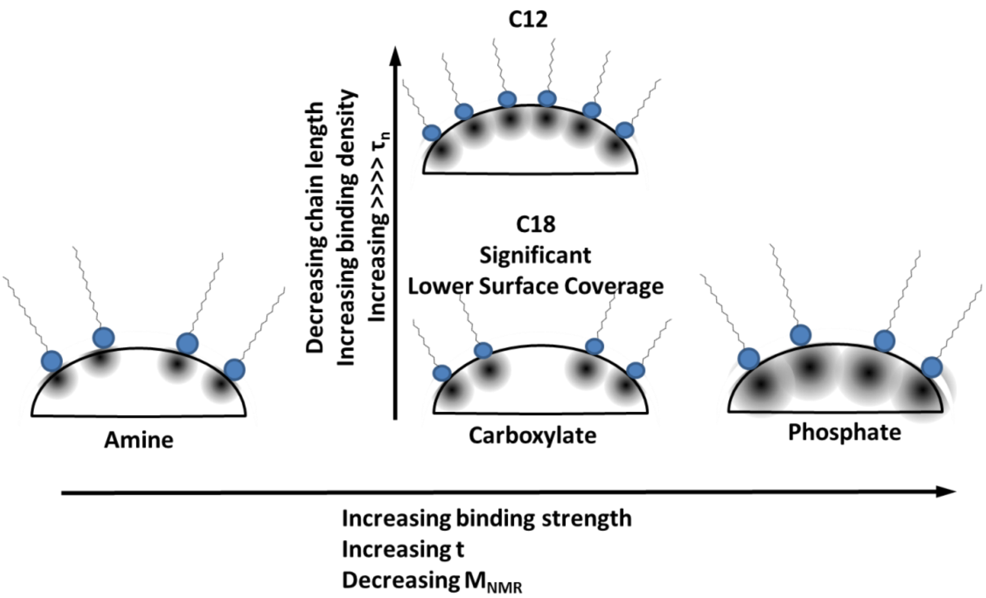

Figure 4-18: Schematic diagram of the canting effects of surface Fe atoms as chain length and of head group varies for alkyl head groups

The findings of the study are summarised in schematic form in Figure 4-18. It was found that as the chain length was decreased the binding density increased which resulted in a significant increase in τ_n due to slower reorientations dynamics. Additionally as the head group was changed from alkylamines to fatty acids to alkylphosphates, the binding strength was increased which resulted in a decrease in M_{NMR} which was due to an increases thickness of the canted spin layer.

4.4. **Conclusion**

In conclusion, NMRD can provide information on the magnetic resonance and magnetic properties of NPs in suspension. The effect of chain length on r_1 is moderate (12 – 15 %) in the clinical frequency range, while the effect on r_1 in the low frequency range dominated by the Néel relaxation process is substantial (22-25 %). It was tentatively proposed that this arises from a change in binding density due to varying chain length. This change in binding density results in areas of variable spin canting on the surface of the NP which in turn affect τ_n.

The effect of head group on r_1 is more significant, with changes of ~37 % in r_1 in the clinical frequency range which are attributed to a change in M_{NMR}. It seemed that this arises due to differences in the binding strength of the ligand to the surface of the iron oxide NP. Increased binding strength results in a thicker layer of canted spins which cannot contribute to the magnetic moment.

This work provides some hints as to how relaxivity could be optimised for aqueous suspensions; a change in τ_0 of up to 60 % can be achieved by using a shorter chain length stabilising ligand e.g., a shorter polymer chain, while for M_s an increase of ~ 15 % can be achieved by selecting head groups with a weaker binding strength e.g. water soluble amines such as polyethyleneimines. For MRI applications this potentially represents an increase of 37 to 52% in r_1 values at clinical fields. These choices need to be balanced against the requirement for colloidal stability.

In on-going work we are undertaking detailed magnetometry analysis in collaboration with Miguel Angel Garcia, Instituto de Cerámica y Vidrio, Madrid to verify our magnetic resonance interpretation. The study could be expanded to incorporate other head groups to try to design the optimum stabilising ligand. Work that is on-going in the group includes the development of water dispersible NP to confirm that the observations made in organic media apply in that case.

Chapter 5

Solvent Interface Mediated Assembly of Magnetic Nanoparticles using Competitive Stabiliser Desorption

5.1. **Introduction**

In Chapter 3 the effect of the synthetic conditions on magnetic properties of suspensions produced by surfactant free thermal decomposition nanoparticle synthesis was described. Building on this, in Chapter 4 we investigated the effect of stabilising ligand on the magnetic resonance properties of the NPs. Dispersed NPs described in Chapter 3 and 4 have the capacity to be applied as T_1 agents in MRI, however; there are limitations associated with their size. Firstly, as the magnetic moment of a particle is proportional to its volume, small NPs have a small magnetic moment per particle. Secondly, it has been shown, that in vivo, that small nanoparticles are usually identified rapidly and transported to the kidneys where they are rapidly excreted, this rapid identification results in a short half-life inside the body [11, 84, 85]. In Chapter 3 it was shown that it is possible to increase the NP size and thus the magnetisation of the particle to overcome some of these obstacles. However, as described in Chapter 1, there is a limit to how much the NP size can be increased as it would quickly exceed the superparamagnetic size limit. Once the particle size increases beyond this limit, the presence of multiple magnetic domains becomes favoured which means the particles would behave ferromagnetically, which can trigger magnetic agglomeration. One method to maximise the magnetic moment while avoiding the problems associated with larger NP is to assemble the NP to form nanoparticle clusters (NPCs). A further advantage of assembling NPs into NPCs is that it can allow for passive targeting of the clusters through control of the hydrodynamic size. It has been shown that the body treats different sized particles in different ways, for example 150 nm clusters tend to travel to the liver and spleen while 30 nm clusters end up in the kidneys[84]. This transport phenomenon is useful as this introduces a passive targeting to NPCs.

Currently there are several approaches to preparing stable NPC dispersions. These include the emulsion/solvent evaporation [46, 86, 87] method, or using polymers to form clusters of particles [88-90]. The former approach involves mixing two phases, typically one organic, containing the nanoparticles, and one aqueous containing the cluster stabilising ligand. Over time, the organic solvent evaporates and the nanoparticles are forced into contact with each other and the cluster stabilising ligand. Qiu et al [86] formed a dispersion of hydrophobic iron oxide NP and mixed an aliquot with a quantity of hydrophilic ligand solubilised in water. Following mixing and sonication to remove the organic solvent water soluble NPCs were generated. The latter approach involves the reaction of primary nanoparticles with polymers, or the incorporation of nanoparticles into a polymer matrix. Sondjaja et al. [88] formed NPC of iron oxide by including a large di-block polymer during the synthesis of the particles. In both these examples, polydisperse clusters were generated and a further size selection step was required for size control. These methods will be investigated in Chapter 6, however, in general polymer mediated assembly methods usually offer little control over cluster size and often the polydispersity of the clusters is low.

The work in this chapter describes an extension of a method known as competitive stabiliser desorption (CSD) which was developed within the Brougham group [27, 28, 91, 92] for the formation of NPCs. CSD can be used for the assembly of NPs that are stabilised in organic solvents with fatty acids, such as oleic acid (OA). The fatty acid molecules are adsorbed onto the surface of the NP but there exists an equilibrium between unbound oleic acid (i.e. free OA) and NP bound OA. The equilibrium lies heavily towards the bound OA, meaning there is a small amount of free oleic acid. When the free OA is removed, some bound OA desorbs from the surface to maintain the equilibrium. If enough free OA is removed, the NP can be destabilised and clustering is induced in a controlled manner. In CSD a quantity of the dispersed nanoparticles is placed over a thin layer of polar cyanopropyl modified silica beads. The carboxylate head group of the free OA is attracted to the highly polar silica beads, so OA adsorbs to the surface of the silica, which in turn causes some NP bound oleic acid to desorb into the solvent in order to maintain the equilibrium Desorption creates what is referred to as an activated nanoparticle, NP*. When two NP* collide, they bind to form a dimer/cluster of nanoparticles. As the experiment continues further free OA is adsorbed onto the silica, this creates an activated nanoparticle cluster, NPC* and if this collides with another NP* or NPC*, a larger NPC is generated, Figure 5-1. One important aspect of CSD is that the monodispersity of the size dispersion is maintained throughout the experiment, which along with the temporal control over the assembly offers advantages over other clustering techniques. It should be noted that to date CSD has been reported in organic solvents only.

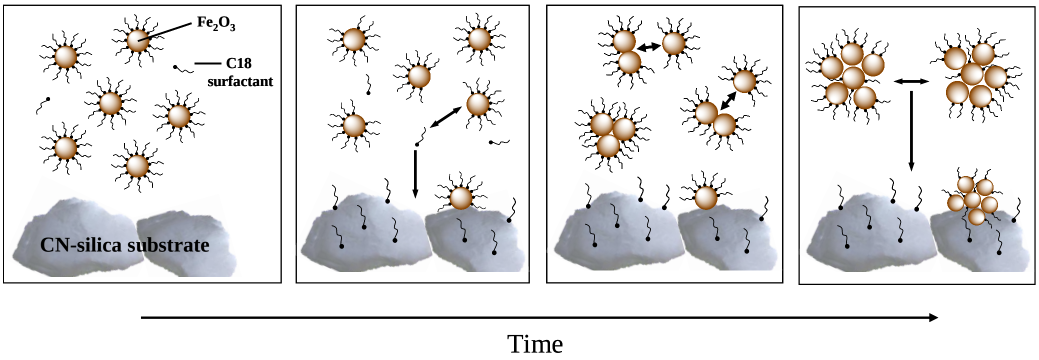

Figure 5-1 : Schematic representation of the proposed mechanism occurring during CSD, showing the desorption of stabilising oleic acid (C18) to generate NP*, and the subsequent collisions to generate NPC

A related process has been reported before for aqueous particle dispersions [93-98], although in this case, desalting as opposed to desorption modifies the interparticle interaction potentials. In this method, nanoparticles electrostatically stabilised in water with their charges shielded by salts, are mixed with a block polymer, in which one block consisting of a neutral polymer and the second consisting of an ionic polymer oppositely charged to the surface of the nanoparticle. The salts are removed in a range of ways and the oppositely charged nanoparticles and polymers interact forming clusters. This method does produce size controlled clusters, with the resultant size being very sensitive to the method of desalting. Furthermore, the desalting method requires the presence of a charged diblock polymer for assembly, with the charged portion in contact with the iron oxide. The CSD method allows for the formation of clusters over a wide size range. These clusters, although assembled in organic solvents, can be phase transferred into water, using a wide range of chemistries that are biocompatible [24, 30, 43, 46, 47]. Furthermore, the phase transfer chemistries can introduce further targeting moieties to widen the biomedical applications.

However, the silica assisted CSD approach is not without its experimental difficulties. The assembly process occurs after the dispersed nanoparticles are introduced to a cuvette with a thin layer of silica beads already on the floor of the cuvette. It is difficult to avoid disturbing the layer during the introduction of the NP suspension. Hence, there is variability of the silica surface area accessible to the suspension from experiment to experiment. The disturbance of the layer introduces silica particles into the suspension and while these do quickly settle, this can lead to additional reproducibility problems, as it alters the surface area accessible to the suspension. Another issue with the use of silica is NP* and the NPC* bind to the silica particles and over time the suspension reduces in concentration. This becomes evident during the experiment as the silica layer becomes stained brown throughout the experiment and progressively darkens over time. Finally, for controlled assembly to occur the concentration of the dispersed particles must be sufficiently low, typically < 1.5 mM [Fe]. Due to these problems, it can be difficult to obtain good reproducibility unless great care is taken. Furthermore, the process is costly as the cyanopropyl silica particles necessary for the assembly are expensive and cannot be reused. Therefore it would be advantageous to use the principles underlying the silica CSD experiment, in a more robust format.

The system developed here is a CSD approach, but instead of using silica as the competitor for OA, the NPs, dispersed in chloroform, are placed into a vessel and water is introduced onto the solution. As water is immiscible with chloroform it forms a stable, reproducible solvent-solvent interface at which the free surfactant accumulates, resulting in controlled particle assembly in the organic phase.

5.2. **Experimental**

5.2.1. Synthesis of Iron Oxide Nanoparticles

Iron (III) acetylacetonate, Fe(III)(acac)$_3$ (purity ≥99.9%) , oleic acid (OA) (≥99.0%) and benzyl alcohol, BA (≥99.0%) were purchased from Sigma Aldrich. All reagents were used without further purification. Reagent grade chloroform was purchased from Labscan and dried over freshly regenerated molecular sieves. De-ionised water was obtained from a Millipore MilliQ system and had a resistivity of < 16 MΩ.cm prior to use. Throughout this chapter de-ionised water will be referred to as water.

The synthetic protocol used to synthesis the nanoparticles in this work is a modified protocol similar to the one described in Chapter 3, using surfactant free thermal decomposition of an organic iron precursor [50-52]. In a typical synthesis 1.00 g (2.832 mmol) of Fe(III)(acac)$_3$ was weighed into a glass vial and then transferred to a three neck round bottom flask. 20 mL (0.193 mol) of benzyl alcohol was transferred to the round bottom flask with a nitrogen flow system, a water cooled condenser and a high temperature thermometer (>300^{0}C) attached. The mixture was de-oxygenated at room temperature by purging with N$_2$ for 15 minutes. A nitrogen atmosphere was maintained for the duration of the reaction. The heating mantle was turned to its highest settling and in all cases the reaction reached reflux at ~195^{0}C within 15 minutes. The reaction was allowed to reflux for 7 hours without stirring.

During the reaction, a colour change from red to black was observed. This suggests the formation of iron oxide nanoparticles. Following the reaction, the heating mantle was turned off and the reaction vessel was allowed to cool to room temperature gradually, while still under a N$_2$ atmosphere. The synthesised particles are known as benzyl alcohol stabilised iron oxide nanoparticles and hereby referred to as BA-NPs. The suspensions were stored in a sealed container and had a concentration of ~10.5 mg/mL of Fe$_2$O$_3$, as determined gravimetrically.

5.2.2. Stabilisation of Benzyl Alcohol Nanoparticles

The mother liquor was washed and prepared for stabilisation as described in Chapter 3 and 4. In short 1.5 mL of concentrated BA-NP suspension was precipitated out using centrifugation and washed twice with chloroform as opposed to acetone, as in Chapter 3. OA was dissolved in chloroform at a concentration of 10 mg/mL. A pre-calculated quantity of this stock solution (typically 0.18 mL) was added to the washed BA-NPs. This quantity is equivalent to a 0.75 fold equivalent of ligand needed to form a monolayer on the surface of the nanoparticles (assuming spherical NP with a core size obtained from TEM of 8.2 nm and a footprint of 38 Å^2 [60]). This mixture was shaken using a vortex mixer, transferred to a glass vial and the final volume was made up to 1.5 mL using chloroform. The vial was shaken overnight to allow for the complete surface coating of the nanoparticles. The stabilised nanoparticles were centrifuged for 10 minutes at 13,200 rpm in order to remove aggregates. This is known as the concentrated stabilised NP solution and was dark brown in colour; it is typically in the concentration range of 140 - 150 mM of Fe and is stable for extended periods of time (years) as measured by DLS.

5.2.3. Assembly of OA-NP using Solvent Interface Mediated Assembly

For the assembly stage, 50 μL of the concentrated stabilised NP solution and 1.4 mL of chloroform were placed into a 1.5 mL Eppendorf™ tube. The mixture was centrifuged for 10 minutes at 13200 rpm in order to remove any aggregates present, thereafter the precipitate was discarded. From this, 1.2 mL of the centrifuged solution was added to a standard 1cm^2 glass/quartz cuvette and its size was analysed by DLS using a Malvern™ NanoZS. Typically, at this point the suspension has a concentration of ~ 2.2mM [Fe]. To initiate assembly, 0.6 mL of de-ionised water (here after referred to as water) was placed carefully over the solution, ensuring the water formed a uniform layer with a clear solvent-solvent boundary. This method is hereby known as interfacial CSD.

5.2.4. Characterisation of Nanoparticle Dispersions

The size of the particles in solution were characterised by DLS as described in Chapter 2. The concentration range used was 1 – 5 mM [Fe], the measurement temperature was set to 25 ^{0}C and the sample was allowed to stabilise for 1 minute prior to measurement. The particles size and morphology were characterised as described in Chapter 2 using TEM. The solutions were diluted to approximately 0.2 – 1 mM (0.0035 – 0.0179 mg/L Fe) with $CHCl_3$ and 5 μL of this solution was dropped onto a Formvar coated 400 mesh Copper grid (Agar Scientific, Essex, UK.) and allowed to evaporate gradually prior to imaging.

The magnetic resonance properties of the suspensions were measured as described in Chapter 1 using NMRD. The NMRD measurement temperature was set to 25 ^{0}C. DLS Measurements were performed before and after NMRD to assess aggregation due to exposure to the magnetic field. Immediately after NMRD, a precise aliquot (typically 50-100 μL) of the dispersion was removed for Fe analysis.

The Fe concentrations of the different suspensions were measured using ICP-AES, as described in Chapter 3.

5.3. **Results & Discussion**

5.3.1. Size and Stability of Primary Nanoparticles

The core size of the primary nanoparticle was measured using TEM. In Figure 5-2, a typical micrograph is shown and the size and morphology of OA-NP can be seen. The particles are uniform with a quasi-spherical shape and have a narrow size distribution.

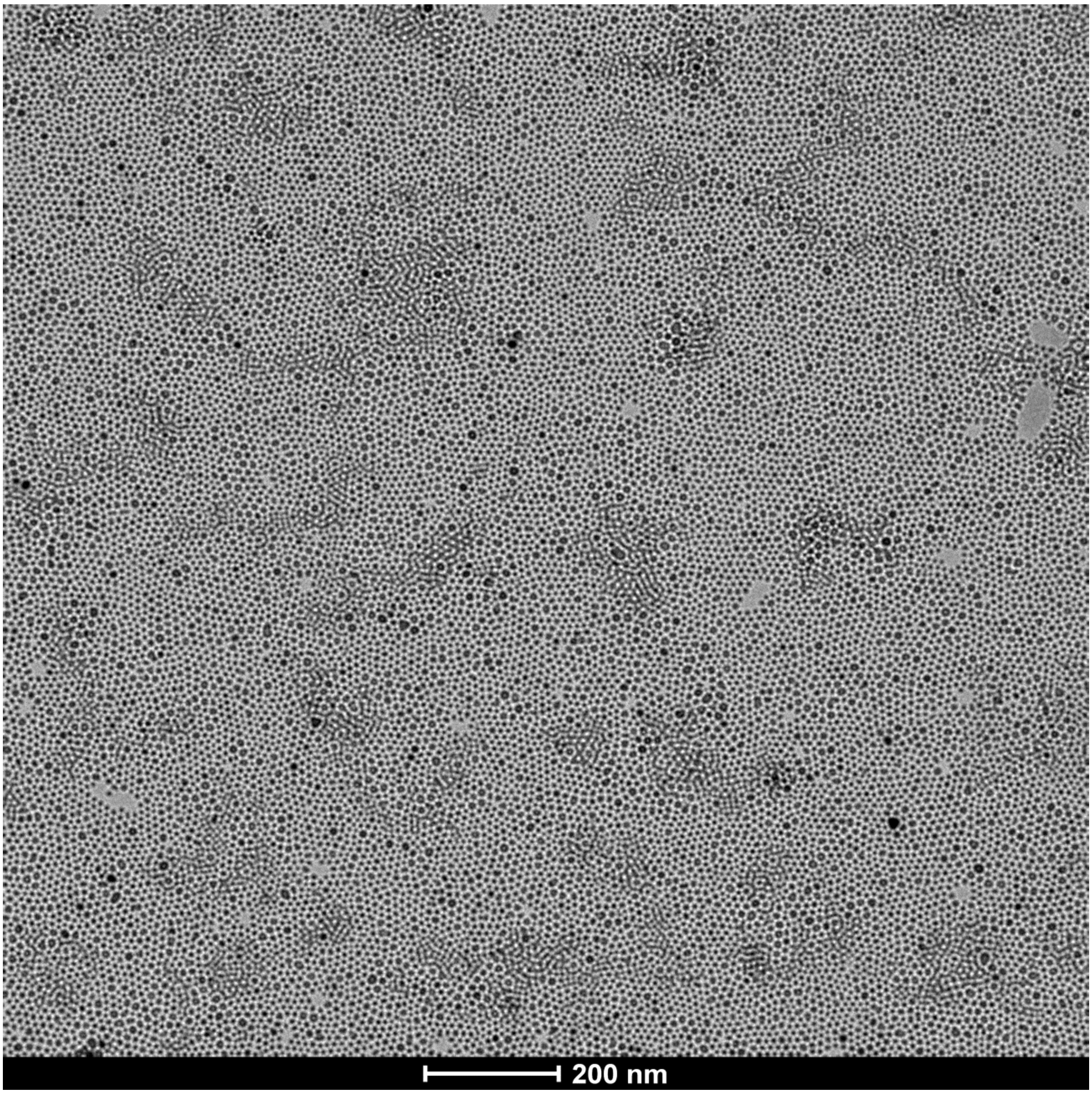

Figure 5-2 : TEM of oleic acid stabilised γ-Fe_2O_3 synthesised using the surfactant free thermal decomposition of $Fe(acac)_3$ in benzyl alcohol, the reaction parameters were 1 g of $Fe(acac)_3$ dissolved in 20 mL of benzyl alcohol, refluxed for 7 hours

Statistical analysis was performed on this image using ImageJ (National Institute of Health, US government). Over 5000 particles were analysed and from this, a size distribution histogram was constructed. The distributions were fitted to a log-normal particle size distribution, as described in Chapter 3. Figure 4-5 shows the overlay of the lognormal model with the experimental size distribution histogram. The R^2 is > 0.99 which shows the population conforms to this model. The mode size obtained from this analysis is 8.2 nm and a standard deviation of 1.6 nm (19%).

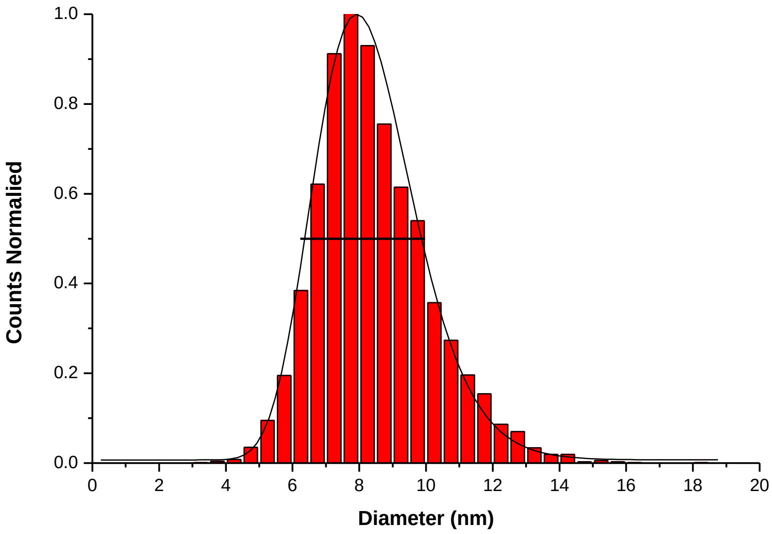

Figure 5-3: TEM Size distribution histogram of stabilised BA-NP, with a DLS size of 14.8 nm and a PDI of 0.084; overlaid is the fitted lognormal distribution, —, where the mode size is 8.2 nm and a standard deviation of 1.6 nm

A typical intensity weighted hydrodynamic size distribution as measured by DLS is shown in Figure 5-4. As discussed in Chapter 1, the intensity weighted data is particularly sensitive to larger particles and thus the absence of any larger particles in the size distribution shows that the particles are fully dispersed with an absence of larger particles and/or aggregates. The z-average size is 15.5 nm (σ=0.16) with a PDI of 0.14 (σ=0.03)

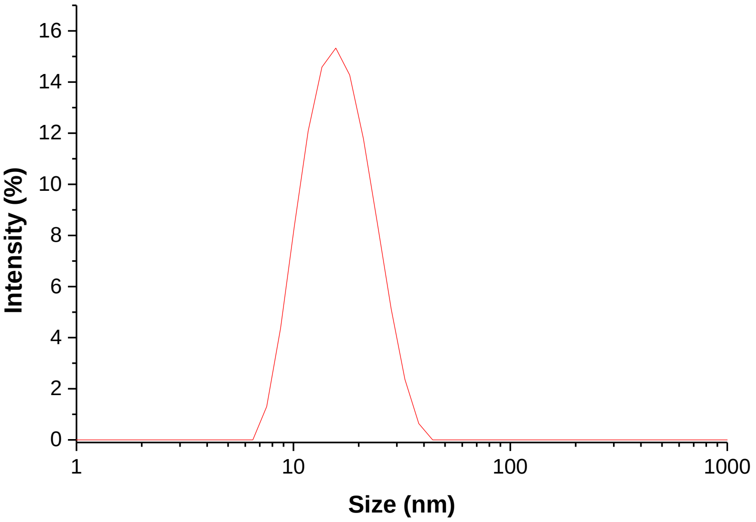

Figure 5-4: The intensity weighted hydrodynamic size distribution, as measured by DLS, of OA-NP (d_{TEM} 8.4 nm) dispersed in chloroform, — size, 15.5 nm, PDI 0.14.

Before any assembly experiments were undertaken, the stability of the suspensions was investigated. This was achieved by preparing a suspension of OA-NP at a concentration appropriate for assembly and monitoring d_{HYD} over time, by DLS. In Figure 5-5 it can be seen that the OA-NP suspension has excellent stability, the z-average (15.5 nm) remains unchanged over 65 hours and the derived count rate (which is particularly sensitive to any aggregation) also remains unchanged.

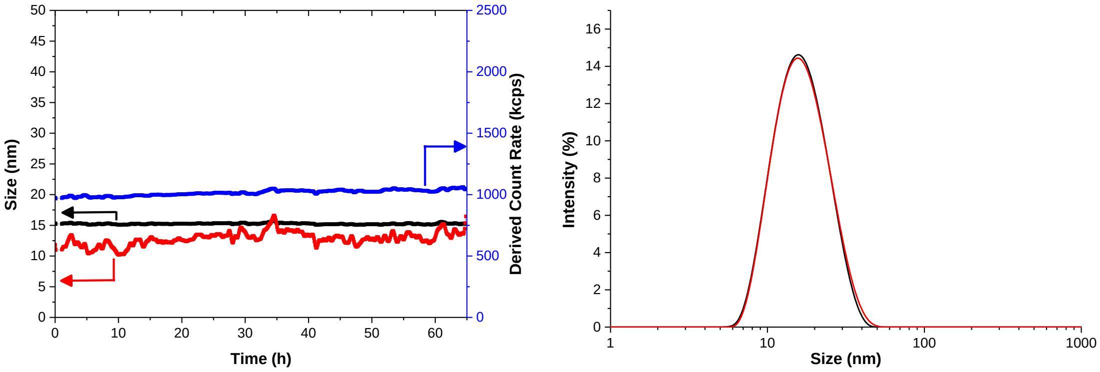

Figure 5-5 : Left - Graph of size of OA-NP dispersed in chloroform versus time; ■ z-average (nm), ■ PDI *100 and ■ derived count rate (kcps); Right, DLS Intensity weighted size distribution of OA-NP dispersed in chloroform at — 0 hours and at — 65 hours

5.3.2. Controlled Assembly of Nanoparticles

The careful addition of water to the dispersed OA-NP suspension resulted in the formation of an interface between chloroform and water, with water (the less dense) on top. A clear and reproducible interface could be achieved with practice, Figure 5-6. From this image it can be seen that the boundary between the two solvents is uniform with no defects associated with adhesion to the defects on the glass, this was found to be critical for reproducibility of the process.

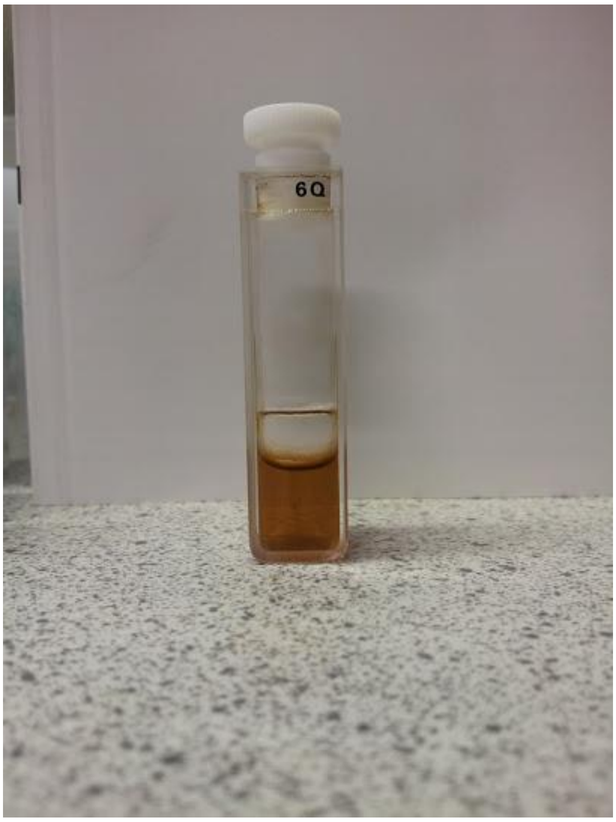

Figure 5-6: Standard 1 cm^2 quartz cuvette containing a bi-layer system, the lower layer containing OA-NP dispersed in chloroform, the upper containing water

Immediately following the addition of water it was observed, by DLS analysis of the $CHCl_3$ suspension, that the nanoparticles appeared to assemble into clusters. A typical result is shown in Figure 5-7, where the d_{HYD} value is seen to increase over time while still retaining a good PDI (<0.17). Control over PDI shows that this is a process where the quality of the size dispersion is maintained throughout. It should be noted that the derived count rate also increases as the size increases, which is as expected as larger particles scatter light more intensively. From the two graphs presented in Figure 5-7, it can be seen that there are two distinct assembly phases present. During the earlier times there is a rapid, exponential like increase in size, while at later times this slows and behaves in a more linear fashion.

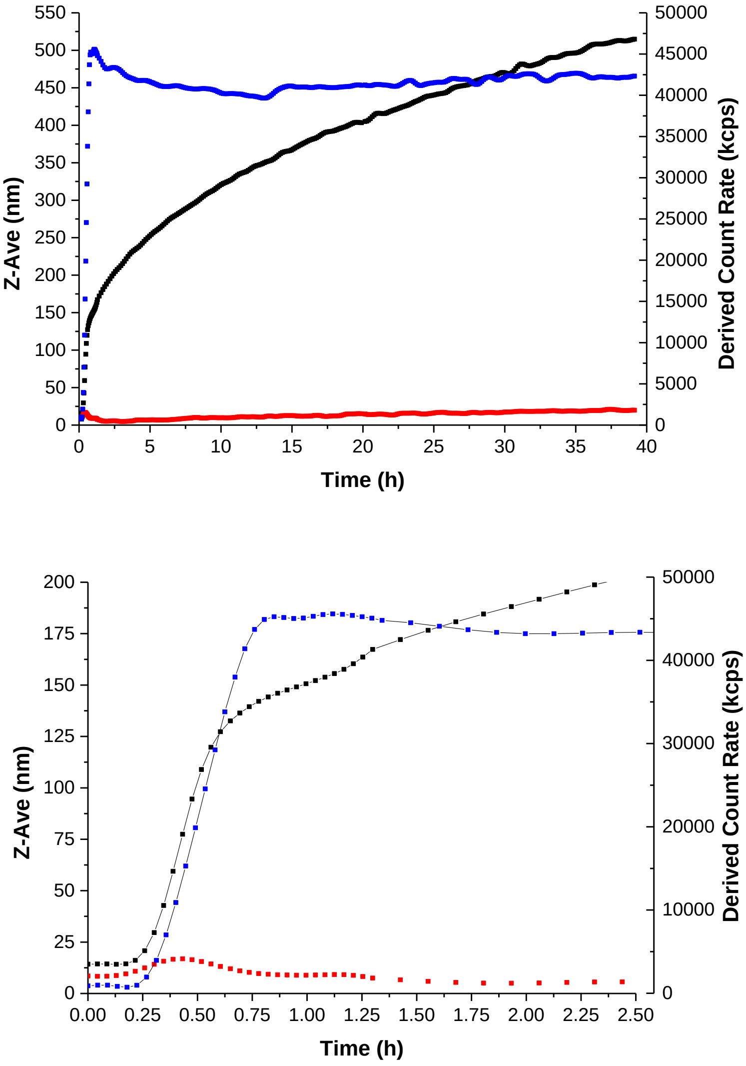

Figure 5-7 : Size of OA-NP dispersed in chloroform over time following the addition of water; ■ z-average (nm), ■ PDI *100 (left hand axis) and ■ derived count rate (kcps); Top graph the evolution of size over a long period of time, bottom graph showing the early time points expanded.

One of the most interesting aspects of interfacial CSD is that the size distribution remains narrow throughout the assembly process, i.e. there is not a loss in monodispersity. Nanoparticles and small clusters have a high surface energy due a high surface area to volume ratio. The thermodynamic driving forces must preferentially prefer the clustering of the smaller, higher energy particles and clusters in order to lower the energy of the system, which works to maintain the monodispersity. This is a highly unusual observation in the field of nanoparticle assembly and is one of the reasons the group are actively pursuing CSD for NP assembly.

5.3.3. Investigation into the role of water during competitive stabiliser desorption

It is clear that the addition of water induces assembly of the nanoparticles; the first issue is to elucidate the role of the water. Firstly, the interface between two solvent of different phases may result in the formation of micelles. This is unlikely as water only has a solubility of ~0.07% [99] (at 25^{0}C) in chloroform, but it is necessary to eliminate the possibility. Dispersed NPs were assembled into NPC and during the assembly phase 1 mL of THF was added to the system. This quantity of THF was sufficient to solubilise both layers completely, breaking the interface, THF is expected to change the polarity of the medium and thus disrupt any micelles. The effect of the addition of THF (marked by the arrow), and the solubilisation of the two layers is shown in Figure 5-8. Following the addition, assembly immediately stops, and NPCs remain stable for an extended amount of time (10 days). It should be noted that there is a slight increase in size following the addition of 1 mL THF to 1.2 mL of chloroform. This arises due to a change in viscosity, as the viscosity value used to calculate hydrodynamic size is fixed for the duration of the experiment. Additionally, by adding THF the system is diluted which, as expected, results in a drop in count rates apparent in Figure 5-8.

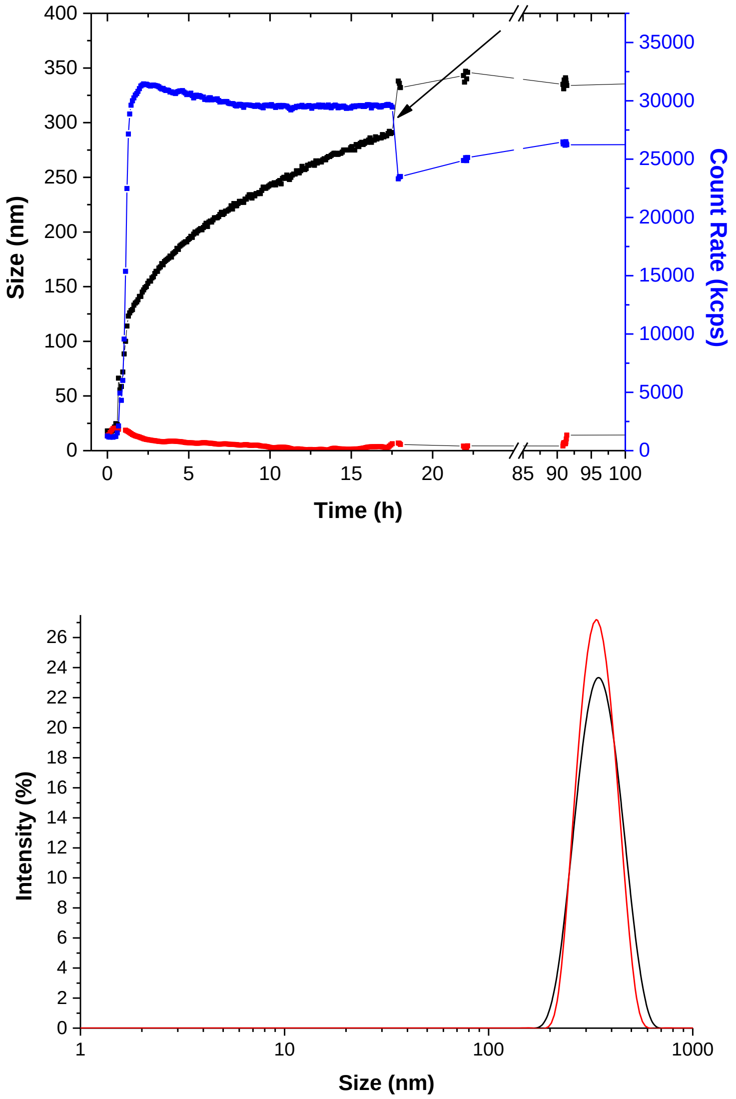

Figure 5-8 : Size of OA-NP dispersed in chloroform over time following addition of water, ■ z-average (nm), ■ PDI *100 (left axis) and ■ derived count rate (kcps), the arrow indicates the point at which 1 mL of THF was added to the solution in order to solubilise the chloroform and water; Bottom graph shows intensity weighted size distribution of the dispersed NPC following the addition of THF at — T=0 days and at — T=10 days.

Having established that the larger objects are not micelles, it is important to elucidate the role of the water layer in the assembly process. In Figure 5-9 an experiment is shown, where dispersed NPs were assembled by adding water. Most of the water layer was then removed using a pipette, and of the remaining $CHCl_3$ suspension, the majority was transferred from under the interface and placed into a second cuvette and observed over time. Typically, 100 μL of solution was left behind to ensure no remnant water was transferred to the second cuvette (Figure 5-9, arrow 1). Removal of the water layer in this way stopped the assembly, as is evident from the plateau between 5 and 22 hours, the assembly was reinitiated by adding a fresh layer (Figure 5-9, arrow 2). This confirms that the on-going presence of the interface is needed for the process to continue. This experiment demonstrates the process is controllable and that clusters of any size can be produced through the timing of the intervention.

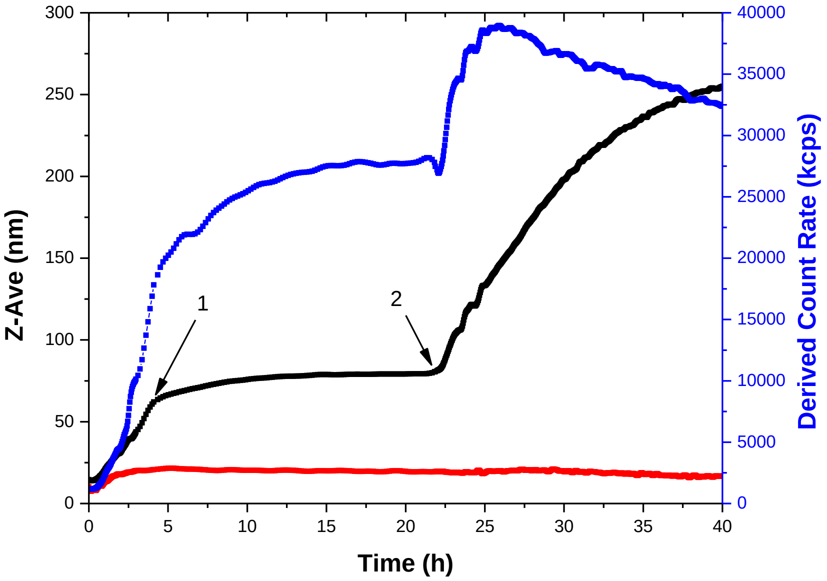

Figure 5-9 : Size of OA-NP dispersed in chloroform over time following addition of water, ■ z-average (nm), ■ PDI *100 (left axis) and ■ derived count rate (kcps), 1) water is removed and assembly stops, 2) fresh water is added and assembly restarts

It is also necessary to assess the role of the water layer and the interface in the assembly process. There are at least two possible mechanisms; the OA may cross the solvent boundary and transfer into the water, or it may remain at the interface. NPs were assembled to large sizes into the phase when the assembly rate is linear and slow, at which time the quantity of water was doubled by adding 600 µL of water. If the OA is transferring into the water, adding water should increase the assembly rate. DLS data for the 15 hours prior to the second addition of water, and for the 15 hours following the second addition of water is shown In Figure 5-10. The two data sets can be fitted independently to a linear model, with R^2 of 0.985 and 0.973 for the earlier and later phase, respectively. Although the R^2 values are lower than ideal, the linear models fit well with the observed trend. For the data prior to the second addition of water the data has a slope (assembly rate) of 1.3 ± 0.04 nm/hour (green line) and after the second addition of water the assembly rate was found to be 1.6 ± 0.03 nm/hour (yellow line). This is a very slight increase, within 1σ and not the expected jump in assembly rate expected. Therefore, increasing the water volume has a very small if any effect on the assembly rate and so is a minor contribution to OA desorption. In fact, the solubility of OA in water at 25^0C is 11.5 µg/L [100, 101]. This equates to the 600 µL of water having a capacity for 6.9 x 10^{-3} µg of OA. When this is compared to the total amount of OA present prior to assembly, 68.7 µg, it is likely that the quantity of OA that dissolves into the water layer is negligible.

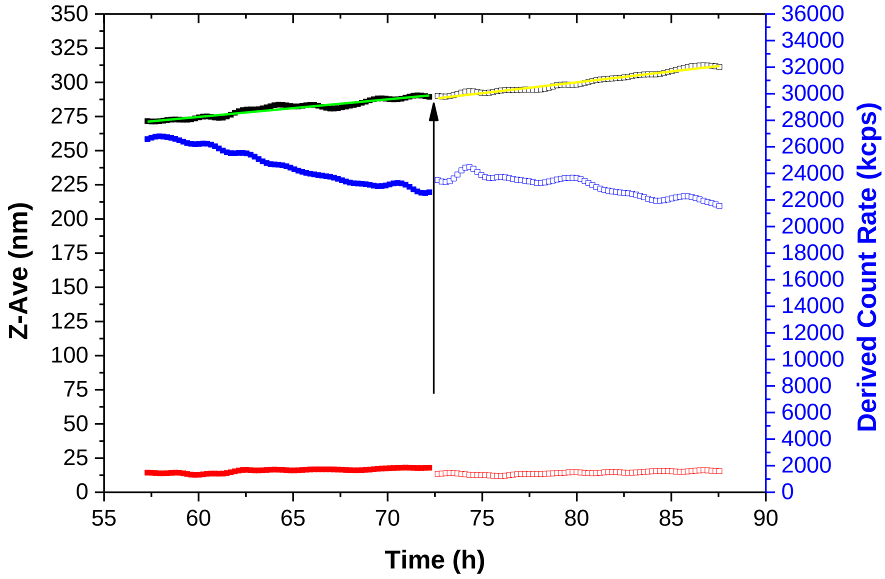

Figure 5-10: Size of OA-NP dispersed in chloroform overs time following the second addition of water layer, ■ z-average (nm), ■ PDI *100 (left axis) and ■ derived count rate (kcps), following 72.5 hours (indicated by the arrow) 600 µL of fresh water was added to the existing water layer, — linear fit of data prior to addition of water (slope =1.3, r^2 = 0.985) and — linear fit of data following the addition of water (slope =1.6, r^2 = 0.973).

As OA does not solubilise into the water layer in significant quantities, and it doesn't form reverse micelles, it must bind to the interface between the $CHCl_3$ and the water, with the carboxylate head solubilised in the water layer and the long aliphatic chain solubilised in the chloroform layer, Figure 5-11. Ellipsometry experiments to quantify the OA at the interface are currently being planned.

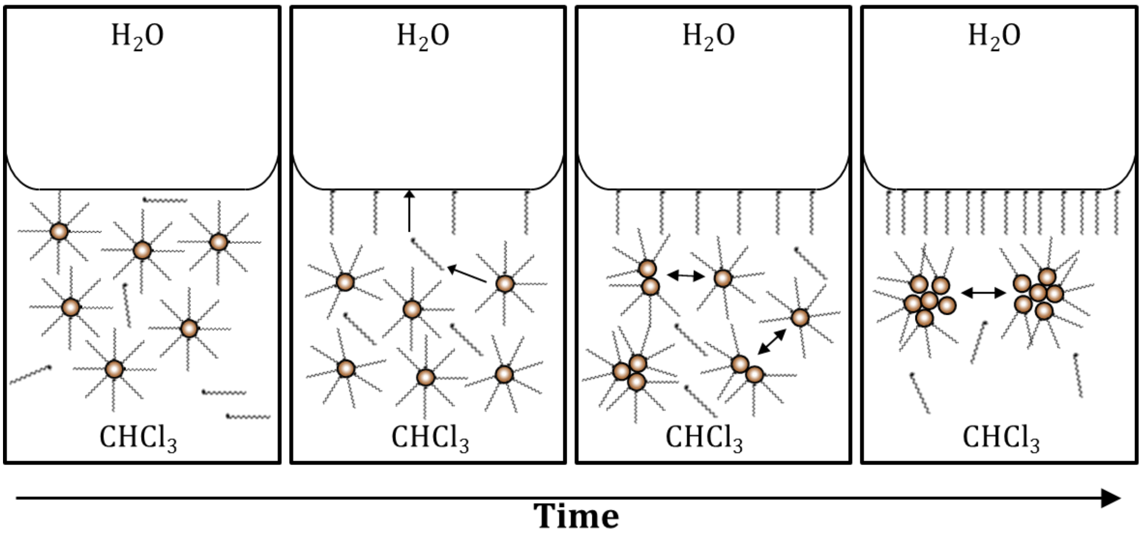

Figure 5-11: Proposed mechanism for the assembly of OA stabilised iron oxide dispersed in chloroform following the addition of a water layer

Assuming a flat interface measuring 0.01 m * 0.01 m (1×10^{-4} m^2) and assuming a footprint for OA of 3.8×10^{-19} m^2 [60], the interface has a capacity of 1.23×10^{-1} µg. This is approximately 18 times the OA capacity of the water fraction. This calculation is based on the assumption of a flat interface of 1×10^{-4} m^2, but it can be seen in Figure 5-6, that the interface is concave, so a greater surface area is available. Additionally there is also a thin layer of $CHCl_3$ between the water and the cuvette which is accessible to the dispersion. Factoring this into the area calculations a more realistic estimate of the interface area is 3.10×10^{-4} m^2. This puts the capacity for OA at the interface at 3.83×10^{-1} µg, ~55 times greater than the capacity of the water fraction. Additionally this geometry may allow for capillary effect at the quartz interface. In a typical assembly experiment 68 µg of OA are present, hence the interface could adsorb no more than 0.56% of the total OA. This represents a very small fraction of the total OA removed from the solution, which is consistent with a very low concentration of NP* as expected for a controlled and slow CSD assembly process.

To further investigate the role of the interface on the assembly process it would be ideal to change the surface area of the interface while keeping the volume and concentrations of the NP suspension and OA constant, thus in effect changing the ratio of OA to surface area of the interface. This is difficult as the experiment is performed inside a cuvette. A simple alternative is to keep the volume of water, the surface area of the interface and the concentration of dispersed NP/OA constant but to change the volume of NP suspension. This experiment allows us to change the ratio of OA to the surface area of the interface, a typical result is shown in Figure 5-12 where the volume of NP suspension was increased from 1200 µL to 3000 µL This, when expressed as a ratio of OA (µg) to surface area (cm^2) of interface, corresponds to a ratio of 22:1 to 43:1 µg/cm^2 of interface, as compared to 22:1 as in previous experiments. When Figure 5-12 is examined it can be see that as the ratio of OA to surface area increases, the assembly rate decreases and secondly, the size at which the assembly rate transitions from the exponential phase to the linear phase decreases. This is consistent with the interface having a fixed capacity for OA. As the volume of the NP suspension is increased there is a greater quantity of free OA present in solution. This free OA must bind to the interface before any bound OA can desorb (generating NP*). When the volume of dispersed NP and thus the amount of free OA is increased, the interfaces capacity for desorbed OA is reduced, resulting in a slower assembly rate. It should be noted that periodically there is a slight increase in size; this is a result of automatic changes in the DLS measurement parameters (attenuator setting) in order to optimise the count rate.

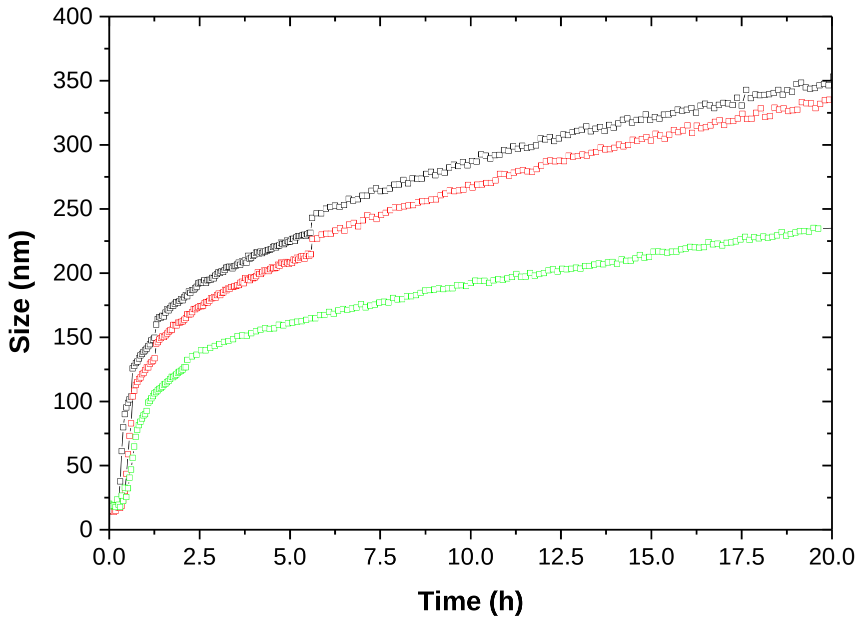

Figure 5-12 : Assembly curves for varying volumes of OA-NP dispersed in chloroform at a fixed concentration with a fixed (600 µL) volume of water; ■ 1200 µL dispersed NP (22:1 µg/cm^2), 🟥 1800 µL(32:1 µg/cm^2), 🟩 2400 µL(43:1 µg/cm^2)

The experiments presented here establish that the liquid-liquid interface plays a role equivalent to that of silica in the earlier versions of CSD.

5.3.4. Morphology of Clusters

A dispersed NPC sample was prepared for TEM as described previously is shown in Figure 5-13. The clusters are quasi spherical in shape and have a size of 222 nm (σ = 18%). This compares favourably with the hydrodynamic size of 269 nm, suggesting that the clusters are rigid and hold their shape and size well upon drying which is in contrast with observations for clusters assembled by other methods, which often lose their shape and morphology upon drying [28].

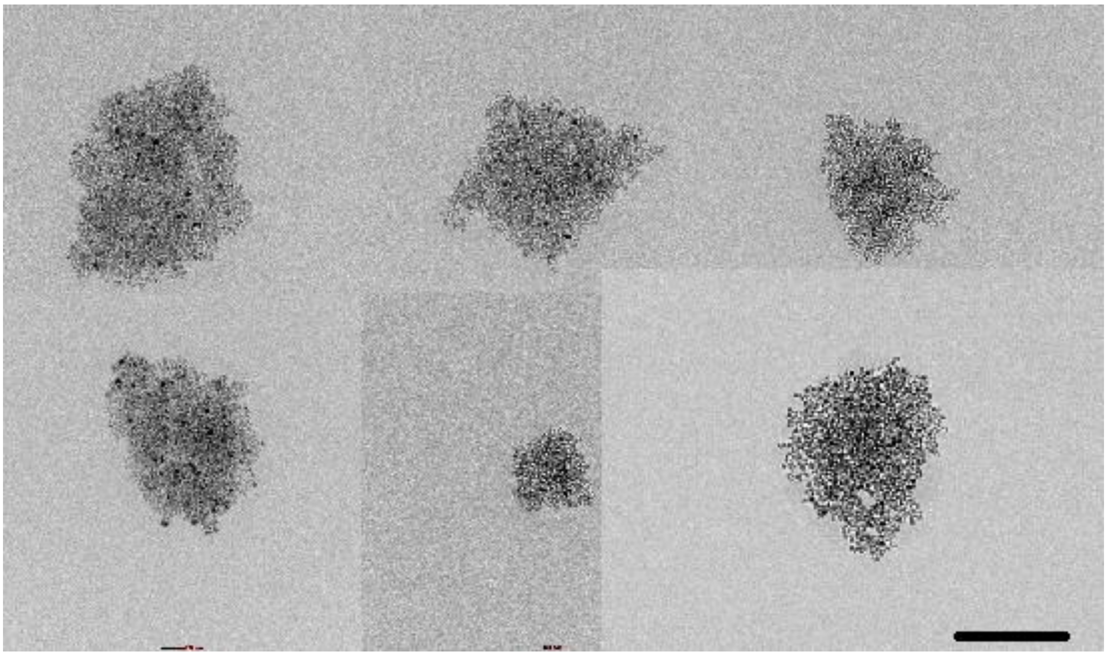

Figure 5-13 : TEM image of OA-NPC clustered (d_{HYD} = 259 nm) using the interfacial competitive stabiliser desorption method, inset scale bar represents 200 nm

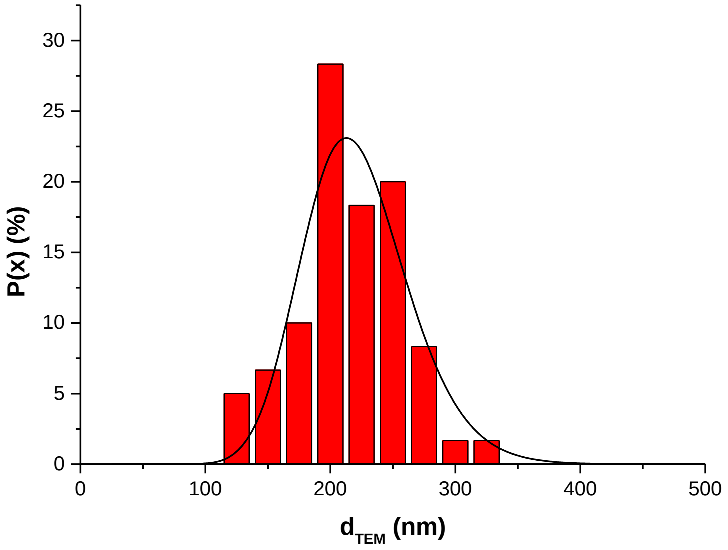

Figure 5-14 : Frequency histogram for OA-NPC assembled using interfacial competitive stabiliser desorption; overlaid is log-normal probability distribution

Table 5-1 : Comparision of OA-NPC size as measured by DLS and TEM

Measurement Technique	Size (nm)	# Particles Counted	PDI	% σ
DLS	259	-	0.06	-
TEM	222	60	-	18.0

5.3.5. Reproducibility of the Assembly Process

In order to investigate the robustness of the method, a series of reproducibility tests were performed. In the first study, from a single suspension of dispersed OA-NP, multiple individual assembly experiments were performed. The results are shown in Figure 5-15 . The process only has a < 4% variation which, for a dynamic process spanning a 300 nm size range over a 20 hour time scale, demonstrates remarkable reproducibility. All the suspensions were monodisperse with a PDI < 0.15, and in the majority of cases < 0.12.

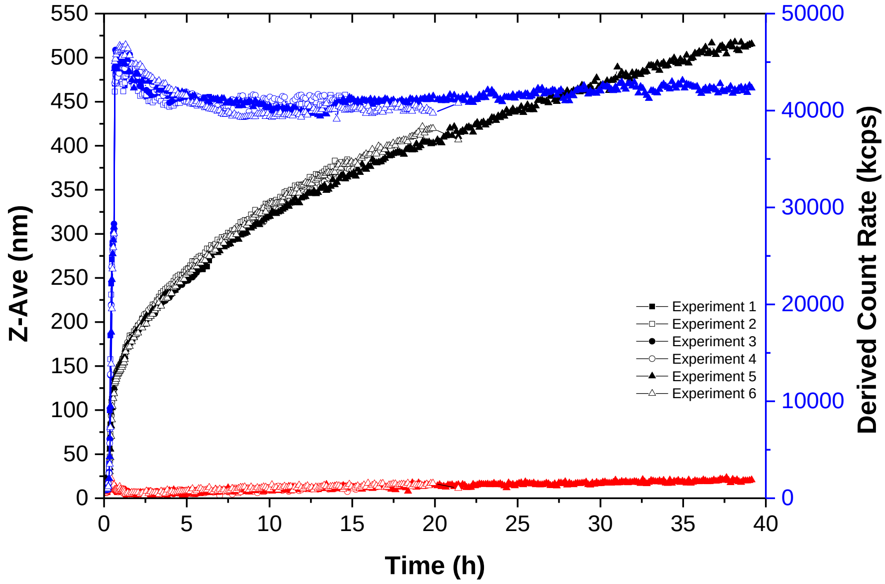

Figure 5-15 : Size of OA-NP dispersed in chloroform (1.2 mL, ~2.5 mM [FE]) over time following addition of water (0.6 mL), ■ z-average (nm), 🟥 PDI *100 and 🟦 derived count rate (kcps), contained above are 6 repetitions

In the second test, suspensions of primary NP from two different syntheses were stabilised with care taken to use the same Fe concentration and same equivalents of OA. Individual aliquots of these nanoparticles were dispersed in chloroform and assembled under identical conditions; the results are shown in Figure 5-16. The variation between the experiments is ≤ 5 %, which further demonstrate that the process and the rate of assembly can be reproduced. It should be noted that there is a variation in the count rates observed between the two measurement positions; this is a result of using of two different DLS instruments for this experiment. These results establish that the process can be reproduced.

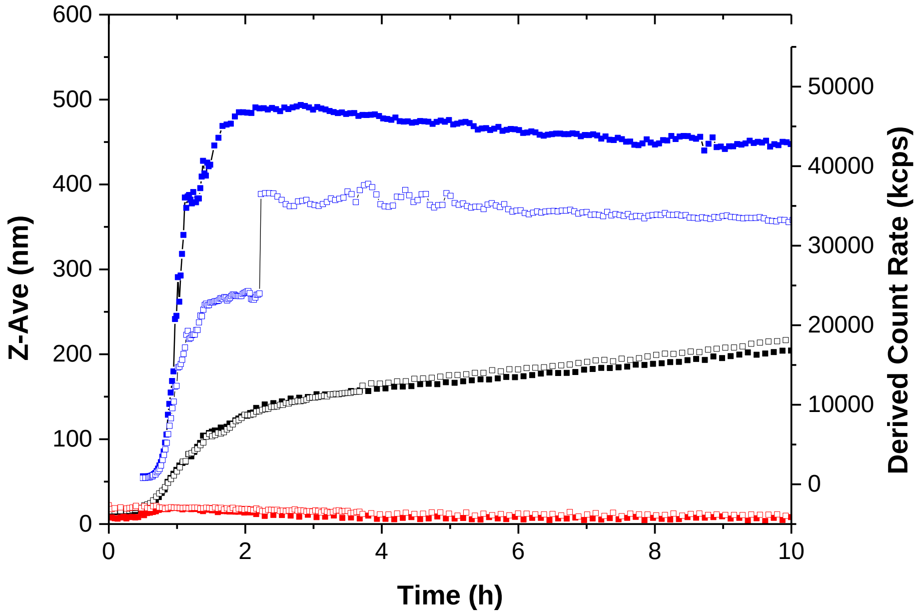

Figure 5-16 : Size of OA-NP dispersed in chloroform (1.2 mL, ~2.5 mM [FE]) over time following addition of water (0.6 mL) following the addition of 75 µL 10 mg/mL oleic acid in chloroform solution, ■ d_{HYD} (nm), 🟥 PDI *100 and 🟦 derived count rate (kcps), contained above is 2 repeats

5.3.6. Kinetics of Assembly by Competitive Stabiliser Desorption at the Solvent Interface

To analyse the kinetics of the assembly process, typical curves such as those shown in Figure 5-17 were fitted to a three stage model. The earlier, rapid assembly phase was fitted to an exponential function, while the latter, slower assembly phase was fitted to a linear function. Fits were performed and the coefficient of determination (R^2) was calculated. For the earlier assembly phase the exponential model shown in Equation 5-1 was used, where y_0 is the y offset, A is the amplitude, t_0 is the time offset and τ_{exp} is the characteristic time associated with the exponential assembly phase. In order to maximise the amount of data included in this model, t = 0 was used as the initial time and time points were added sequentially while maintaining a good fit, $R^2 > 0.990$. For the later assembly phase a linear model was used, Equation 5-3, where m_{lin} is the linear slope and c is the intercept. In order to maximise the amount of data included, progressively earlier time points were added sequentially while maintaining a good fit, $R^2 > 0.995$. This method allowed the maximum amount of data to be fitted, while also ensuring the mathematical models still applied. As this approach did not fit all the data, the remaining data was deemed to be an intermediate or transition between the two defined assembly phases. This data was fitted using a power law, Equation 5-2, where A is the amplitude, t_o is the time offset and τ_{pow} is the characteristic power associated with the intermediate phase. The power law model fitted the intermediate phase data well, with $R^2 > 0.990$. A typical assembly curve and its corresponding fits are overlaid in Figure 5-17.

$$y = y_0 + A.e^{\frac{t-t_0}{\tau_{exp}}} \quad \textbf{Equation 5-1}$$

$$y = A.|t - t_0|^{\tau_{pow}} \quad \textbf{Equation 5-2}$$

$$y = m_{lin}.t + c \quad \textbf{Equation 5-3}$$

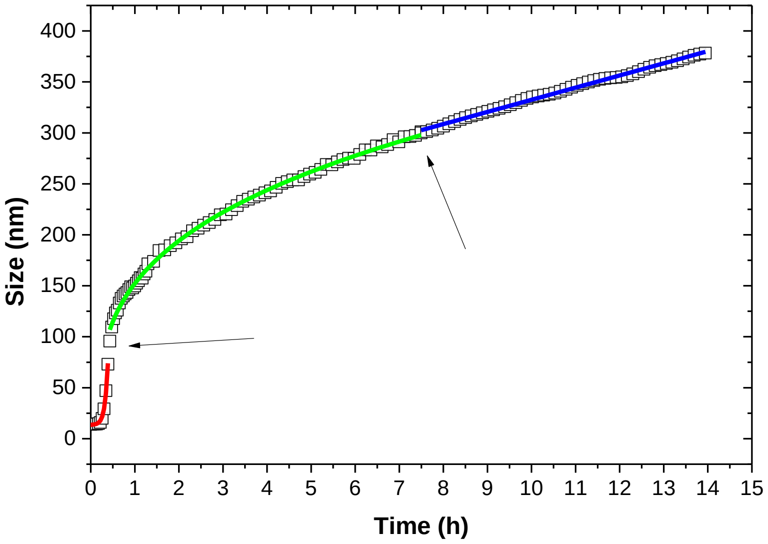

Figure 5-17 : Size of OA-NP dispersed in chloroform stabilised using a 0.75 surface equivalence over time following addition of water layer, ■ z-average; overlaid on this graph are the three mathematical models used to fit the data, — exponential fit (Equation 5-1), — power fit (Equation 5-2) and — linear fit (Equation 5-3); the arrows indicate the transitions between fits.

The different assembly phases can be rationalised when the mechanism for the adsorption of surfactants to a liquid interface is considered. In a two phase system where an interface exists, the work required to create a unit area of interface is given by $W = \gamma.\Delta A$ where γ is the interfacial tension. If one phase contains an amphilphilic surfactant (the bulk); over time the surfactant is transported to the interface. Classically it is thought there are two steps in adsorption; diffusion and transfer [102]. In the transfer step, the surfactant is transferred to the interface from a region known as the subsurface layer. Surfactants undergo this process due to free energy differences between the two phases which results in interfacial/surface tension. In the diffusion step, due to concentration gradients between the subsurface layer and the bulk, surfactant molecules diffuse to the subsurface layer. In the experiments presented here, when the water layer is introduced, free OA molecules in solution transfer to the interface in order to reduce the interfacial tension. Transfer depletes the local concentration of the OA in the subsurface layer resulting in diffusion of OA from the bulk to the subsurface layer. In the bulk, this depletion of free OA perturbs the equilibrium between free OA and NP bound OA, so NP bound OA desorbs from the particle surface to re-establish the equilibrium. This creates activated sites on the surface of the nanoparticles resulting in NP*. As more free OA binds to the interface, more and NP* are created and, as discussed previously, this leads to cluster formation. During later stages of the assembly process, if further free OA is removed, the replacement OA must come from NPC, generating activated clusters (NPC*) which leads to NPC assembling with NPC whose net effect will be an accelerated assembly rate.

It should be noted that for the experiments shown here the rate of adsorption is not directly monitored, but in effect it is measured through the continuous monitoring of d_{HYD} using DLS. In the early stages the rate of adsorption of surfactant to the interface is fast, indeed for processes obeying Langmuir kinetics, the rate of change of surface concentration is reported as exponential [103] (first order process), at least initially. In any case for our experiments the number of NP* generated per unit time is high which results in a high assembly rate, Figure 5-17. As the interface fills close to saturation, there is now steric hindrance at the interface due to interface bound OA. There is still a driving force for the OA to bind to the interface, but the rate of adsorption is reduced. However, when examining the kinetics; as the interface fills further, hindrance increases and results in the adsorption rate of free OA to the interface to decrease significantly over time which eventually should be close to zero. In fact we never see the assembly stop.

This may be due to the OA creeping up the wall of the cuvette through capillary action. This may provide an additional sink for OA at the $CHCl_3$/air interface.

There are several possible causes of the transition from exponential to linear assembly kinetics. Firstly, it may arise due to the decreased rate of adsorption of surfactant to the interface; the kinetics of this process could conceivably be second order; although we can find no literature on this topic. Alternatively, it could arise due to changes in the mechanism of particle assembly. Initially one could imagine that the kinetics of assembly should be dominated by NP* to NP* collisions which would result in an exponential increase in size with time [104]. In a subsequent phase the kinetics of assembly would be expected to be $NPC_n^* + NP^* \rightarrow NPC_{n+1}$, in which case geometric considerations for monodisperse particles suggest a $\sqrt[3]{t}$ (cube root of time) dependence of cluster size [104]. At later phases, the kinetics should be driven by a $NPC_n^* + NPC_m^* \rightarrow NPC_{n+m}$ process which would again result in an exponential increase of size with time. These considerations suggest that the early exponential like behaviour observed can be attributed to the first kinetic regime. The exponential behaviour is similar to that reported in previous studies of colloidal aggregation, this and the fact that the assemblies are non-fractal, suggests that the assembly process is a reaction-, as opposed to diffusion- limited [105].

However, it should be noted that the real situation is not as simple as that outlined above; the rate of desorption of NP bound OA may not be constant. It may be that the rate of desorption from particles decreases over time; perhaps due to initial OA loss arising from molecules bound to surface defects which may desorb more rapidly. Over time the fraction of readily desorbable OA may reduce so that the rate of desorption reduces accordingly. It should also be noted that in Figure 5-9, following the removal of water, the assembly process doesn't immediately stop, therefore stabilisation of NP* or NPC* must still be on going. This suggests that at this point in the process, desorption of OA from the NP is a slower process supporting the idea that the rate of desorption of NP bound OA may reduce over time. It seems more likely that the transition to the linear assembly phase is due to a reduction in the rate of OA adsorption.

In reality, detailed kinetic modelling of the assembly process must also consider the distribution of particles and cluster sizes and the fact that DLS measures the scattering intensity weighted population distribution. The appropriate methodology is described by the Einstein-Smoluchowski approach, which describes the probability of NP* and NPC* collisions resulting in an increase in cluster size as determined by the reaction kernel where NPC formation can be modelled by either the population balance equation [106] or by Brownian dynamics simulations [107]. Collaborative work is underway to apply these methods to model kinetics of NP assembly in a realistic way, e.g. Figure 5-18. The anticipated outcome is the time dependence of the OA coverage, information which could be used to implement CSD for other suspensions in a designed way. Other critical parameters, including temperature, could be varied to generate useable data. That work is ongoing

5.3.7. Effect of Oleic acid on the Kinetics of Assembly

To further investigate the mechanism of assembly the kinetics of the process were modified by varying the amount of free OA (dissolved in chloroform) added to the initial dispersed NP suspension. DLS data for the different suspensions is shown in Figure 5-18. In most cases the PDI value was < 0.15, with the exception of the assembly where 100 μg of OA was added. In this case the PDI value was slightly higher (~0.18), but in all cases the DLS data was checked to confirm that the dispersions had a unimodal size distribution. This result shows that the process can be controlled from very fast (150 nm/hour) to very slow (10 nm/hour) by simple addition of OA immediately prior to assembly. This is very useful, especially in experiments that are carried out offline, and it makes it easier to stop the assembly at selected sizes

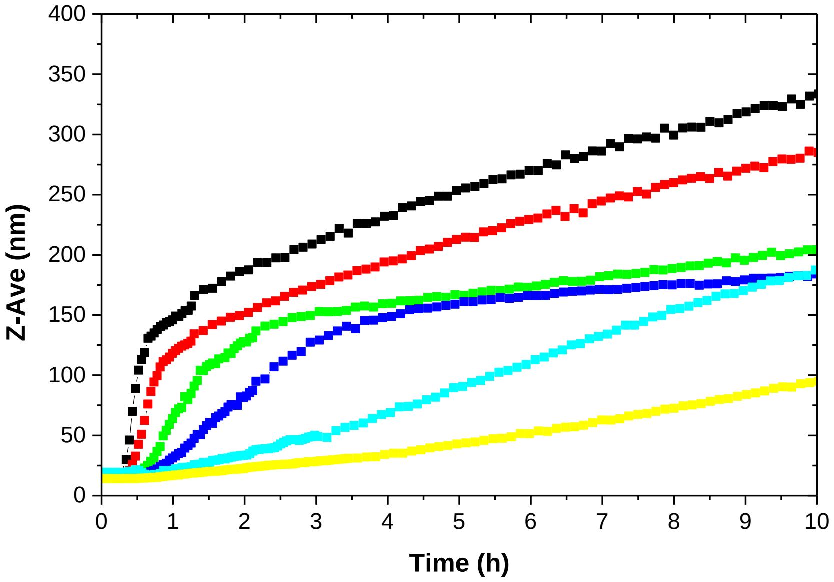

Figure 5-18 : Assembly curves for OA-NP dispersed in chloroform with ■ 0 µg OA added, 🟥 25 µg OA added, 🟩 50 µg OA added, 🟦 75 µg OA added, 🟦 100 µg OA added and 🟨 125 µg OA added

The different experiments shown in Figure 5-18, were modelled using the previously described procedure. The initial time points of the experiment were successfully fitted to the exponential model as shown by the R^2 value, the details are given in Table 5-2.

Table 5-2 : Extracted parameters from only the exponential fitting for different assemblies with varying amounts of added free OA. The oleic acid per area interface is calculated using the surface area calculated above, 1.47 cm^2

Oleic acid added (µg)	Oleic acid per area interface (µg / cm^2)	y_0 (nm)	A	t_o (hour)	Characteristic time, τ_{exp} (hour/nm)	Growth rate, τ_{exp}^{-1} (nm/hour)	R^2
0	22.2	13.83	0.44	0.13	0.06	15.56	0.996
25	30.2	13.21	1.22	0.17	0.11	8.98	0.990
50	38.4	13.07	1.48	0.26	0.19	5.32	0.997
75	46.4	12.50	3.32	0.35	0.40	2.50	0.988
100	54.4	12.50	4.22	0.47	0.70	1.43	0.983

When the extracted parameters are examined several trends become clear. The induction time (t_0) increases significantly as the ratio of oleic acid to area of interface increases. Further analysis of Figure 5-19-A demonstrates that the dependence is exponential, ($R^2 = 0.998$). At the start of the experiment, there is an excess of free OA in solution which must be adsorbed before any NP* can be generated. As the amount of free oleic acid is increased prior to the addition of the water, more oleic acid must bind to the interface before any bound OA can desorb thus increasing the induction time before assembly begins. It is found that during the exponential assembly phase, the assembly rate decreases exponentially with increasing added oleic acid, Figure 5-19 B ($R^2 = 0.998$). This is partially due to the adsorption of OA onto the interface; as the interface fills the rate at which OA adsorbs onto it will decrease, so the rate of generation of NP* will be reduced.

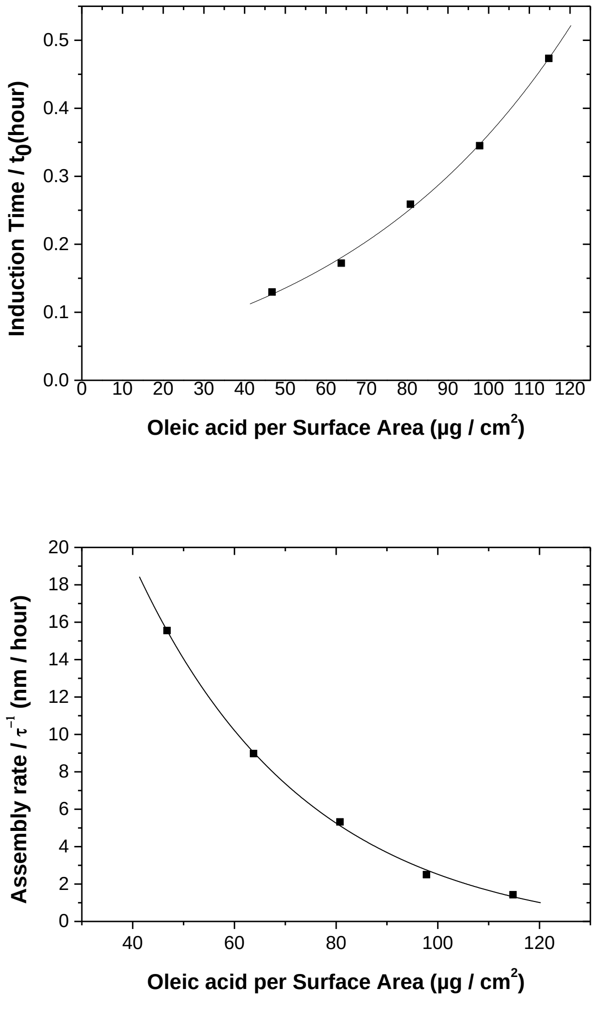

Figure 5-19 : Relationship between extracted parameters and OA per surface area of interface (ug / cm^2); Top - ■ induction time / OA per surface area interface (ug / cm^2), ─ exponential fit where y0 = -0.038 hour, amplitude = 0.075 and characteristic exponent time = -59.929 (µg / cm^2),

Bottom- - ■ assembly rate / OA per surface area interface (ug / cm^2), ─ exponential fit where y0 = -0.844 nm / hour, amplitude = 65.870 and characteristic exponent time = 33.622 (µg / cm^2) using the exponential relationship; $y = y_0 + A.e^{\frac{-t}{\tau_{exp}}}$.

This experiment has shown that by addition of surfactant prior to assembly, the kinetics of assembly can be readily modified. The approach allows the formation of NPC of any size at different rates. The effect of assembly rate on the magnetic resonance properties of the NPC suspensions is described below.

5.3.8. Scale Up Of Interfacial Competitive Stabiliser Desorption

Having demonstrated reproducibility of the method in section 5.3.5, a series of scale up experiments were performed to assess the viability of CSD at the solvent interface for NPC production at scale. Glass weigh boats (Sigma Aldrich) were chosen as they provide a vessel with a flat bottom and a crushed glass lid in order to provide a seal, as shown in Figure 5-20. During the experiment, care was taken to keep the ratio between the volume of suspension to surface area of the interface constant at a value of 1.2 $cm^3/1\ cm^2$ which is the ratio for assembly experiments using a cuvette.

Figure 5-20: Flat bottom crushed glass weighting vessels, 80 mL and 30 mL

However, during the experiment an issue arose when the volume of water was increased. The high surface tension of the water resulted in the water layer moving to one side of the vessel and displacing the suspension beneath, Figure 5-21, as opposed to forming a uniform layer.

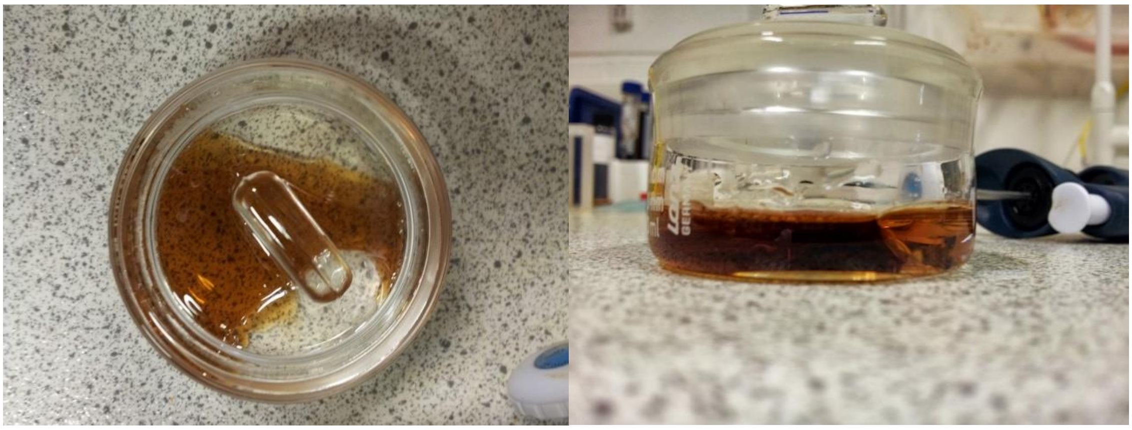

Figure 5-21: Initial attempt of scaling up the assembly resulted in a non-uniform water layer

A simple mesh was devised out of anodised aluminium wire which acted as a scaffold for the water layer to spread its weight, creating a uniform water layer and a stable interface, Figure 5-22 .

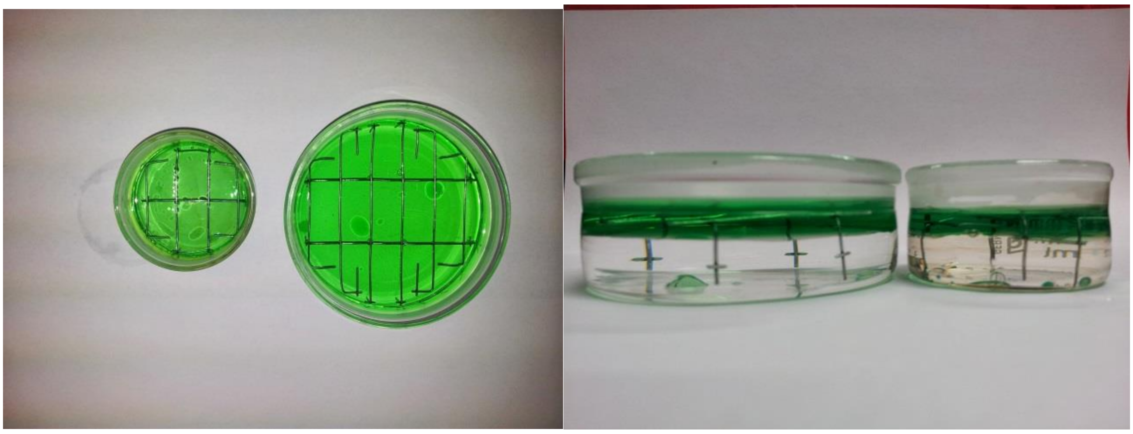

Figure 5-22: Design of a scaffold to support the water layer (highlighted using food colouring) over a chloroform layer

Following the addition of the scaffold, a scale up experiment was attempted and a stable interface between the dispersion and the water layer was achieved, Figure 5-23.

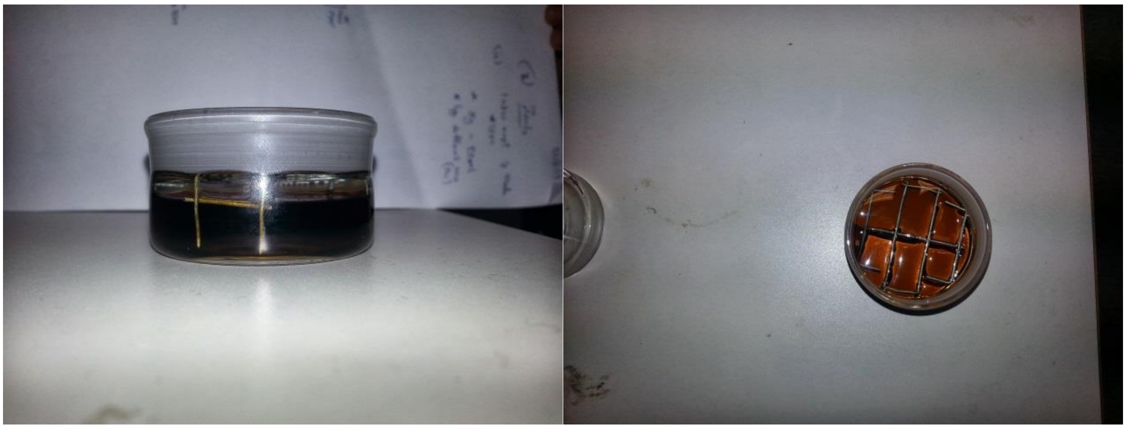

Figure 5-23: Scale up of assembly method to ~ 30 mL of OA-NP suspension

In Figure 5-24, the assembly curves for a typical inline 1.2 mL scale and for an offline 60 mL scale (x50 scale up) is shown. For the 60 mL assembly, aliquots were removed using a narrow bore needle and placed inside a low volume (100 µL) cuvette for analysis. Following analysis, the sample was discarded. There is good agreement between the two assembly curves. This result shows that this method can be scaled up by a factor of 50 while still retaining similar kinetics to the inline assembly; furthermore the monodispersity of the NPC dispersion is comparable (PDI < 0.15) to inline, small scale assembly.

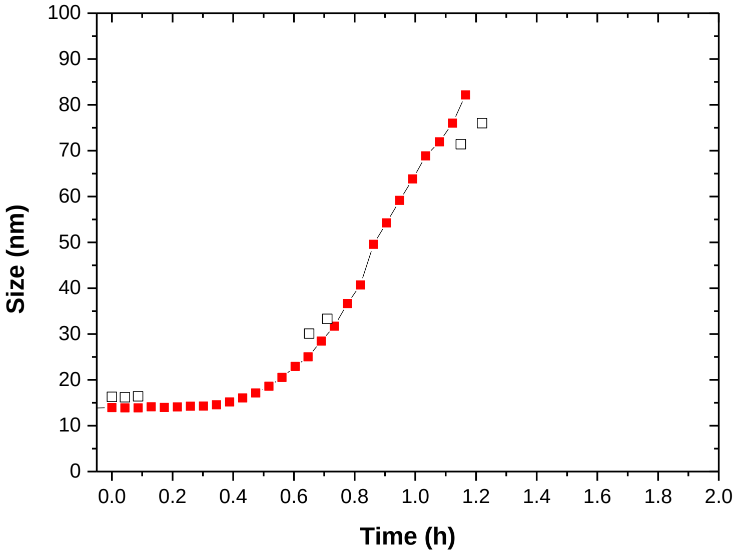

Figure 5-24 : Size of OA-NP dispersed in chloroform assembled using interfacial competitive stabiliser desorption plotted against time for 🟥 inline measurements for the 1.2 mL scale and ☐ offline measurements for 60 mL scale

It is surprising that the scale up by a factor of 50 produces such a similar result considering that transport is a significant kinetic factor. However, the long time-scale of CSD (hours) should be borne in mind. This experiment identifies the key parameters for further scale up; OA excess, volume to surface area ratio and concentration of NP. Another x50 scale up is planned, this would result in ~ 3 L of suspension corresponding to ~ 1 g of NPCs.

5.3.9. Effect of Assembly Rate on Nuclear Magnetic Resonance Properties of Nanoparticle Clusters Dispersions

The interfacial CSD approach has been shown to be a robust, reproducible and scalable assembly method; furthermore the exponential rate (τ_{exp}^{-1}) of assembly can be dramatically reduced from 15 to 1.4 nm/h, Table 5-2, by doping the NP suspension with small quantities of OA prior to assembly. This significant change in the assembly rate presents an opportunity to investigate whether the rate of assembly affects the magnetic resonance properties of the resulting suspensions. For this experiment, NPCs of comparable size were assembled using two different rates of 15 nm/h and 1.4nm/h. Assembly was stopped as described in 5.3.3, by removing the interface.

Table 5-3 : d_{HYD} and PDI values for different cluster sized assembled at different exponential assembly rates (τ_{exp}^{-1})

Quantity of OA added (µL)	τ_{exp}^{-1} (nm/h)	d_{HYD} (nm)	PDI
0	15.6	50.4	0.16
0	15.6	105	0.09
100	1.4	46.3	0.18
100	1.4	102	0.19

NMRD profiles for the NPC dispersions assembled using different assembly rates are shown in Figure 5-25, following the NMRD measurements each sample was analysed using DLS and in all cases there was no significant change demonstrating the clusters were stable to the magnetic fields of the measurement. The r_1

maximum is still evident demonstrating that the clusters still exhibit superparamagnetic behaviour It can be seen that the mid frequency minimum present in the profile of primary nanoparticles is suppressed upon clustering. This suppression of the minimum is expected [28], it arises due to interparticle interactions within the assemblies. For both slow and fast assemblies of NP, as NPC size increases there is a decrease in the r_1 response, arising presumably from a larger quantity of NP contained within the NPC that cannot contribute to the r_1 relaxation.

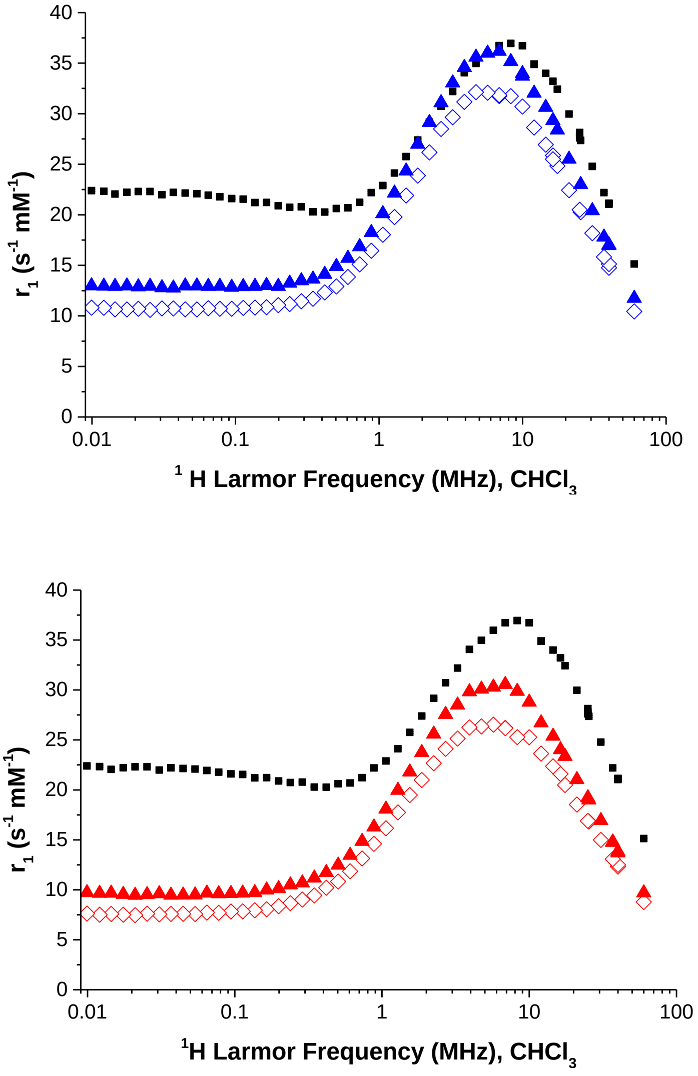

Figure 5-25 : NMRD profiles for clusters assembled using the interfacial CSD method using different assembly rates (■ dispersed OA-NP included as a comparison, 15.5 nm); Top graph showing ▲46.3 nm assembled at 1.4 nm/h ◊ 50.4 nm assembled at 15.6 nm/h; Bottom graph shows ▲101.9 nm assembled at 1.4 nm/h, ◊ 104.9 nm assembled at 15.6 nm/h

Examining the r_1 data in Figure 5-26, it can be seen that the change in assembly rate has a slight effect on the r_1 values. For all frequencies r_1 decreases with size, if we examine the r_1 values at 61 MHz, upon increasing the assembly rate (τ_{exp}^{-1}) from 1.4 to 15.6 nm/h, r_1 decreases by ~8 % for both 50 and 100 nm NPC. Having already discussed how NPs contained within the NPC do not contribute to the r_1 relaxation process, the observed decreased in r_1 is tentatively attributed to a higher packing density resulting from the faster assembly rate.

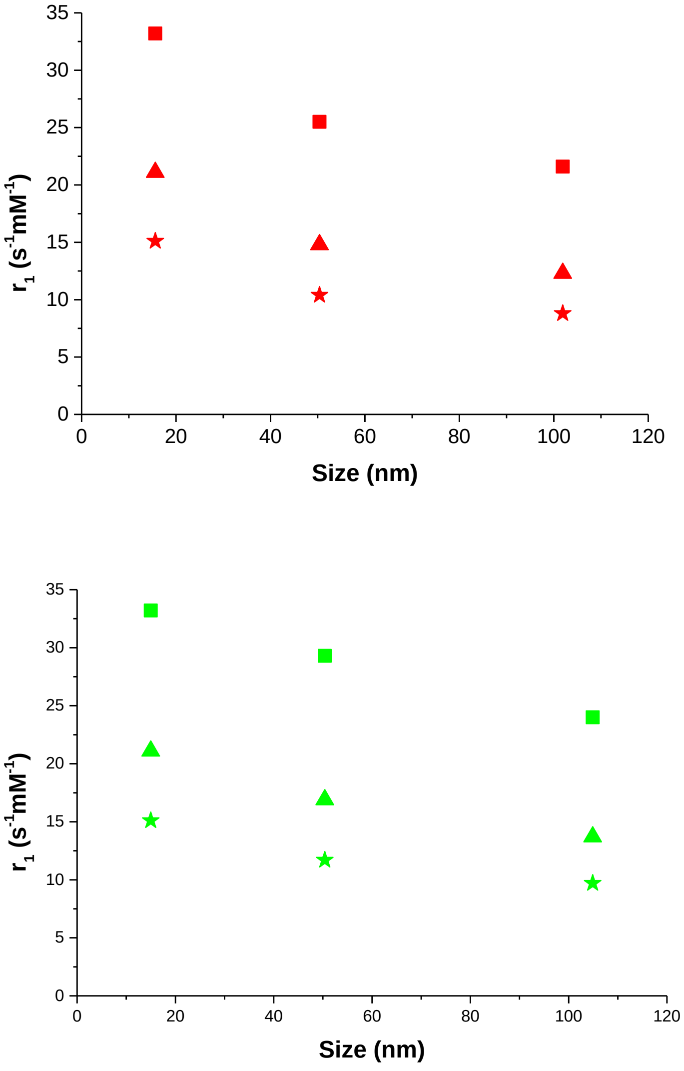

Figure 5-26 : r_1 of interfacial competitive stabiliser desorption plotted against size; Top graph shows red data that signifies clusters assembled at fast rate of τ_{exp}^{-1} of 15.6 nm/h; Bottom graph shows green data that signifies clusters assembled at slow rate τ_{exp}^{-1} of 1.4 nm/h; symbols indicate frequency of measurements, ■ 16.3 MHz, ▲40 MHz and ★ 60 MHz

Shown in Figure 5-27 are the r_2 values for NPCs assembled at varying rates. In all cases r_2 increases with size, however it is evident that r_2 increases with increasing assembly rate. For 50 nm NPC, r_2 increases by ~ 7 % at 60 (MHz) while for the 100 nm NPC, r_2 increases by 39 % at 60 MHz. The increase in r_2 can be attributed to the faster assembled NPC having a larger magnetic moment. This observation is consistent with a higher packing density arising from a faster assembly rate.

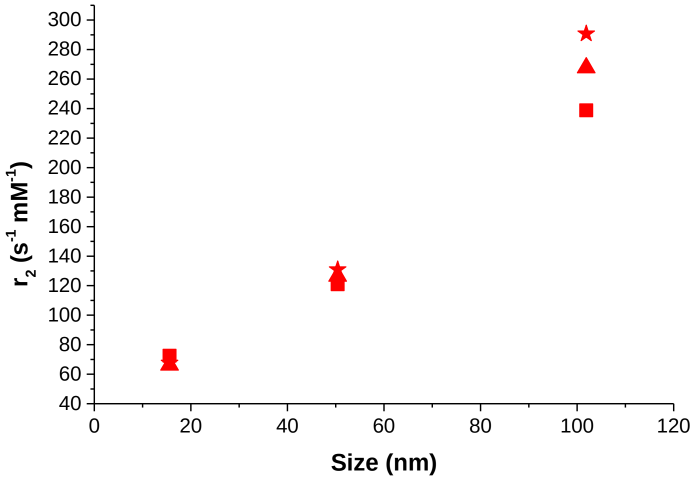

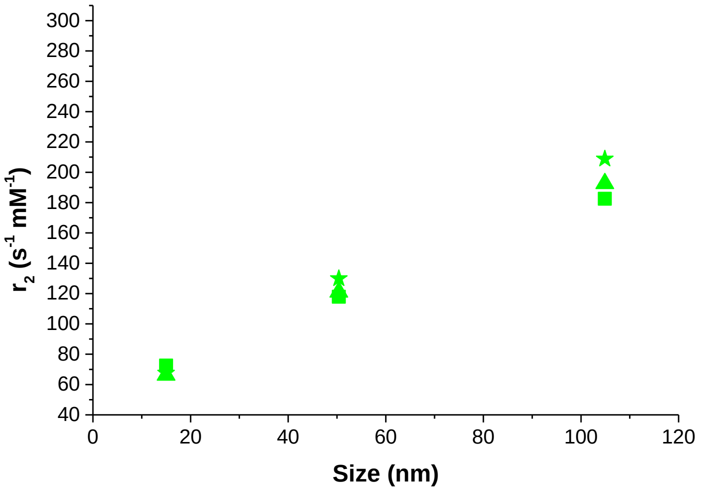

Figure 5-27 : r_2 of interfacial competitive stabiliser desorption plotted against size; Top graph shows red data that signifies clusters assembled at fast rate of τ_{exp}^{-1} of 15.6 nm/h; Bottom graph shows green data that signifies clusters assembled at slow rate τ_{exp}^{-1} of 1.4 nm/h; symbols indicate frequency of measurements, ■ 16.3 MHz, ▲40 MHz and ★ 60 MHz

The size dependence of the relaxivity ratios (r_2/r_1) are shown in Figure 5-28, in all cases the ratio increases with increasing size, however for the NPC assembled at a faster rate the increase in ratio is greater; for 50 nm NPS, there is a 11% increase of the ratio at 60 MHz and for the 100 nm NPS there is a 57 % increase in ratio. This is expected considering our findings for r_1 and r_2.

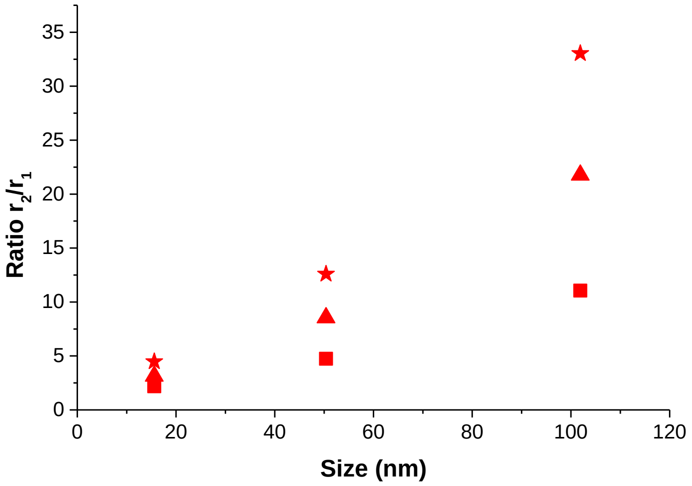

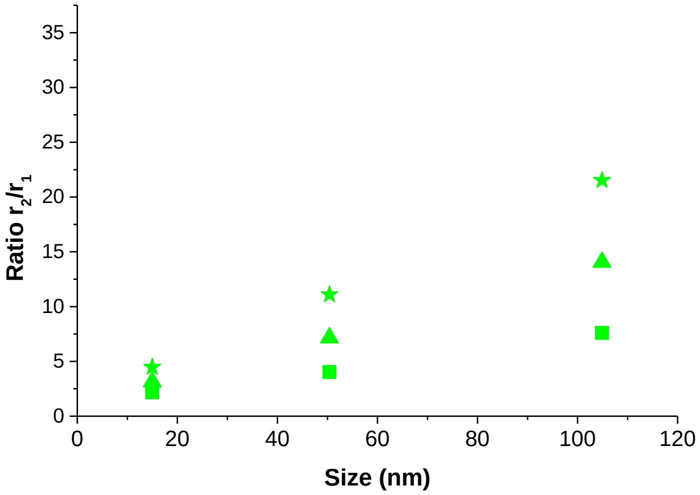

Figure 5-28 : Ratio of r_2/r_1 of interfacial competitive stabiliser desorption plotted against size; Top graph shows red data that signifies clusters assembled at fast rate of τ_{exp}^{-1} of 15.6 nm/h; Bottom graph shows green data that signifies clusters assembled at slow rate τ_{exp}^{-1} of 1.4 nm/h; symbols indicate frequency of measurements, ■ 16.3 MHz, ▲40 MHz and ★ 60 MHz

If an NPC is considered to be a dense NP assembly, NPs at the centre of the cluster would be shielded from interactions with the diffusing solvent molecules by the NPs in the outer layers of the NPC. This shielding has the effect of reducing the r_1 efficiency of the NPs, as fewer of them will contribute to the r_1 relaxation. If we assume that for a faster assembly rate, multiple activated sites are generated on each nanoparticle, then it is likely that denser clusters with multiple interparticle interactions will be formed. Hence, it is expected that suspensions produced using faster assembly rates will have reduced r_1 values due to increased shielding.

Considering the r_2 values, the increased interparticle interactions will result in a higher total moment and hence higher r_2 relaxivity as is observed from the NMRD measurements, Figure 5-27.

5.4. Conclusion

A novel method for the assembly of iron oxide NP into NPC of controlled size and of excellent monodispersity was successfully developed. The NPC produced are well defined dense NP assemblies. This interfacial method of CSD is highly reproducible which allows the method to be readily scaled up. To date this method has been scaled up to 50 times with further larger scale up experiments planned, which may allow for the assembly of gram quantities of monodisperse iron oxide NPCs.

The kinetics of assembly using the interfacial CSD process can be controlled by careful control over a few key parameters; primarily the quantity of excess OA, OA per unit area of interface area and NP concentration. This control over kinetics of assembly allows interfacial CSD to be used to acquire kinetic data that will be used for the development of mechanistic models of interactions between NP* and NPC*. This work is underway in collaboration with partners in LMU, Munich. Finally, through control over the assembly rate, the spin-spin (r_2) relaxivity of the cluster suspension can be increased by 40%, for a given hydrodynamic size. We suggest that this arises from a change in the particle packing density within the clusters.

Chapter 6

Effects of Cluster Architecture on the Relaxation Rate Enhancement of Water Suspensions

6.1. **Introduction**

In Chapter 5 a method to produce assemblies of NPs was described and the emergent magnetic resonance properties of NPC were examined. In that instance, data showed that rate of assembly of NP into NPC had a significant effect on the relativities. These observations raise the interesting question as to what role cluster architecture has in determining the magnetic resonance properties of NPC. A clearer understanding of the effect of cluster architecture may allow for better design of NPCs with a view to an enhanced r_1 or r_2 effects.

Theoretical studies have shown that for superparamagnetic assemblies, there exist three regions; the motional averaged region (MAR), the static dephasing regime (SDR) and the echo-limiting regime (ELR). In the MAR, the size of the NP/NPC are sufficiently small that all diffusing water molecules experience a changing magnetic field during their brief encounter with the particle[108], which dephases the ^1H moments of the water. In this region, as NPC size increases, the r_2 enhancement increases due to the increased magnetic moments. As NPC size increases further, the particles are said to be in the SDR, here local diffusing water molecules will experience a constant field resulting in no increased dephasing of the water molecules. In this region r_2 does not increase with increasing size. Typically, a maximum r_2 enhancement is seen in this region. As size of the particle increases into the ELR region, the magnetic moment of the NPC becomes so large that any water molecules located close to the NPC are completely dephased resulting in a reduction in r_2. Whether the particles behaviours places it in within the MAR or SDR is determined Redfield condition which is a relationship between the frequency shift experienced by a proton at the equator of the particle ($\Delta\omega$) and the translation diffusional time of protons relative to the diameter of the particle (τ_D), Equation 6-1.

$$\Delta\omega \,.\, \tau_D < 1$$

Equation 6-1

If the product of the two factors is greater than 1, the particle is considered to be in the SDR, while if the product is less than 1, the particle is considered to be in the MAR.

Recently, a universal scaling law has been developed to explain the r_2 of particles in the MAR [108] and has been shown to match a wide range of experimental data. For nanoparticles that are in the MAR, transverse relaxation mechanisms are proportional to the molar volume of the magnetic material (v_{mat}), the saturation magnetisation of the material expressed as A/m (M_v) and the diameter of the particle (d) according to Equation 6-2:

$$r_2 = \frac{R_2}{[Fe]} = \frac{4\gamma^2\mu_0^2 v_{mat} M_v^2 d^2}{405D}$$ **Equation 6-2**

where γ is the gyromagnetic ratio of the proton, μ_0 is the magnetic permeability of a vacuum and D being the diffusion coefficient of water. For maghemite, v_{mat} is known as 1.5×10^{-5} m^3/mol, allowing Equation 6-2 to be simplified to Equation 6-3. This shows that r_2 is theoretically proportional to the square of the saturation magnetisation and the diameter.

$$\frac{r_2}{M_v^2} = a_{theo} d^2 = 5.9\ x\ 10^{-12} d^2$$ **Equation 6-3**

Vuong et al.[108] calculated the reduced relaxivities for a wide range of published materials and by taking φ_{intra}, the volume fraction of magnetic material, into account they found a strong correlation between the reduced relaxivity with size. The empirical evidence fitted the theoretical results well, considering the theoretical model assumes one size for the particles distributions, while in reality there is a size distribution of nanoparticles which will affect the relaxation properties.

$$\frac{r_2 \cdot \varphi_{intra}}{M_v^2} = a_{exp} d^2 = 11.6\ x\ 10^{-12} d^2 \qquad \textbf{Equation 6-4}$$

By using this model, if one knows the M_v value and the size, it is possible to predict the r_2 of a material. Alternatively, if one knows the r_2, the size and the M_s value one can predict the NP loading density.

In this chapter NMRD results for a range of different cluster suspensions will be compared. The first cluster type examined is clusters formed using a polymer mediated assembly method. Organic dispersions of NP are mixed with a water solubilised triblock polymer. Through removal of the solvent, the organic stabilised NP interacts with the polymer forming assemblies, hereby referred to as PMA-NPC. Cluster size is controlled by careful control of the iron concentration to polymer content. The second cluster type is formed by mixing ascorbic acid with iron salts and heating. Water soluble clusters are formed that are stabilised with dehydroascorbic acid and are known as DHAA-NPC, with size control achieved through centrifugation [21]. Finally, allyl-PEG stabilised NPs are prepared by covalently attaching particles to pH responsive 2-vinylpyridine-co-divinylbenzene polymer beads through a one-step surfactant-free emulsion polymerisation. The size of the resulting assemblies can be controlled after synthesis by modifying the pH[30]. These “nanogels” will be known as NG-NPC.

6.2. **Experimental**

6.2.1. Polymer Mediated Assembly of Nanoparticles

Iron (III) acetylacetonate, Fe (III) $acac_3$ (purity ≥99.9%), oleic acid (≥99.0%), heptane (puriss) and benzyl alcohol, BA (purity ≥99.0%) were purchased from Sigma Aldrich. All reagents were used without further purification. Reagent grade chloroform was purchased from Labscan and was dried over 4Å molecular sieves prior to use. Reagent grade acetone and methanol was purchased from Labscan and was used without any further purification.

The synthetic protocol used is the same as in previous chapters [50-52], briefly; the synthetic parameters used were 1 g of precursor dissolved in 20 mL of benzyl alcohol heated to reflux (200^0C) for 7 hours. This was performed under fixed pressure. 5 mL of the resultant NP reaction solution were washed as described previously and stabilised in 2 mL of $CHCl_3$ using 70 μL of oleic acid (OA). Following this, the concentrated solution was centrifuged for 10 minutes to remove any larger aggregates. The dispersed NPs are referred to as OA-NP.

Pluronic® -F127 a tri-block polymer consisting of poly (propylene oxide) – poly (ethylene oxide) – poly (propylene oxide) (PPO-PEO-PPO) was purchased from Sigma Aldrich and used without any further purification. Reagent grade acetone and THF was purchased from Labscan and was used without any further purification. De-ionised water was obtained from a Millipore MilliQ system and had a resistivity of < 16 MΩ.cm prior to use.

In a typical coupling experiment 2 mL of a concentrated OA-NP solution (~10 mg/mL) were precipitated from solution using excess acetone and captured magnetically. The resulting precipitate was washed twice more with acetone. The washed NPs were dispersed using 10 mL of THF and had a concentration of ~ 130 mM [Fe]. Simultaneously, an 800 mg/L solution of F-127 was prepared and 2 mL aliquots were placed into 15 mL centrifuge tubes. To each centrifuge tube varying volumes of dispersed NP was placed and each tube was mixed using a vortex mixer for 1 minute. The tubes were left tumbling overnight; exposed to air to allow evaporation of THF, leaving water dispersed clusters of iron oxide NP (PMA-NPC).

6.2.2. Synthesis of Dehydroascorbic Acid Stabilised Nanoparticles

Dehydroascorbic acid stabilised nanoparticles (DHAA-NPC) were received from Lisong Xiao of the Sanjay Mathur group, Cologne. The particles were synthesised using a previously published method [21], which involved the use of ascorbic acid as a reducing agent and as a stabilising ligand to create highly water soluble clusters, upon receipt of the dispersions, the samples were analysed using DLS and NMRD. Following NMRD, the dispersions were reanalysed using DLS to confirm colloidal stability in the magnetic field. In all cases the samples showed no significant change in d_{HYD} confirming stability. TEM images presented below were recorded by Lisong Xiao and members of the Sanjay Mathur group, Cologne.

6.2.3. Synthesis of Decorated Stimulus Responsive Polymer Nanobeads

Stimuli responsive polymer nanobeads, decorated with iron oxide nanoparticles (nanogels) were received from Andreas Riedinger of the Teresa Pellegrino group, Genova. The nanogels (NG-NPC) were synthesised using a previously published method[30] where iron oxide NP were included in the polymerisation reaction to create pH responsive polymeric beads decorated with iron oxide NP. From the sample batch of NG-NPC, aliquots at three different pHs were analysed using DLS and NMRD. These NG-NPCs swelled at low pH due to protonation of the polymeric backbone resulting in a more hydrophobic structure. At different stages during NMRD experiment, the dispersions were reanalysed using DLS to check colloidal stability following exposure to the magnetic field. However, some of the NG-NPC samples showed signs of significant aggregation meaning the materials were not stable after exposure to high magnetic fields. This will be discussed below; however no NMRD data is included from materials which had shown aggregation. TEM images of the NG-NPC and DLS analysis of the primary iron oxide nanoparticles presented below were recorded by Alexander Riedinger and members of the Teresa Pellegrino group, Genova.

6.2.4. Characterisation of Nanoparticle Clusters

All dispersions were characterised using DLS, the magnetic resonance properties were measured using NMRD. Following NMRD analysis the dispersions were reanalysed using DLS to ensure colloidal stability throughout the measurements. In all cases presented there was no significant change in the DLS response. All measurements were carried out at 25^{0}C ± 0.1^{o}C. The clusters size and morphology was measured using TEM as described previously. The Fe concentrations were measured using ICP-AES as described previously. The calibration curve was linear -in the range 0.01 ppm to 10 ppm, in all cases $R^2 > 0.995$.

6.3. **Results and Discussion**

6.3.1. Polymer Mediated Assembly of Nanoparticles

DLS measurements of oleic acid stabilised iron oxide nanoparticles synthesised using the surfactant free thermal decomposition are presented in Figure 6-1. The particles d_{HYD} and PDI are shown in Table 6-1 and have a very narrow size distribution with a size of 14.9 nm in $CHCl_3$. The TEM results are previously reported in Chapter 4 and Chapter 5 and are summarised in Table 6-1.

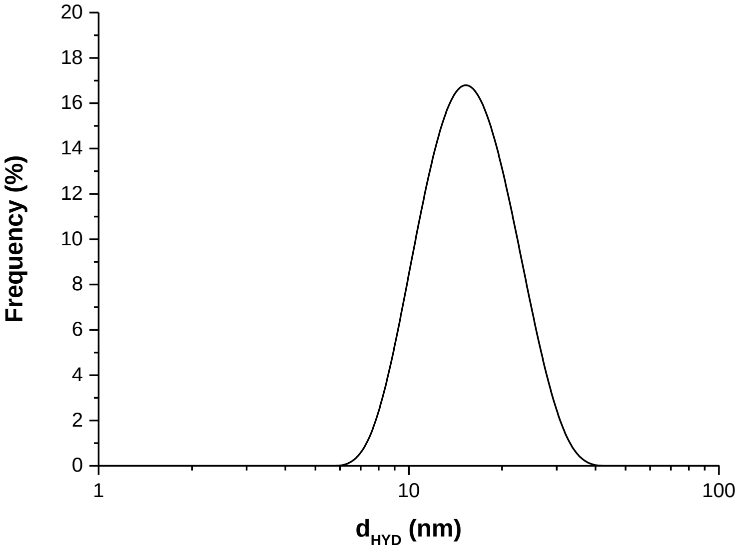

Figure 6-1 : Oleic acid nanoparticles dispersed in $CHCl_3$ synthesised using 1 g of precursor heated to 200°C for 7 hours

Table 6-1 : Size of dispersed oleic acid stabilised nanoparticles as measured by different techniques

Measurement Technique	Size (nm)	PDI	%σ
Light Scattering (d_{HYD})	14.9	0.09	-
Microscopy (d_{TEM})	8.8	-	18.4

Figure 6-2 shows the results of mixing pluronics, dissolved in water, with varying volumes of THF OA-NP dispersions. Following evaporation of the organic phase, clusters of NP have been generated, whose size varies with volume of THF OA-NP added. In Table 6-2, in all cases the PMA-NPC are well dispersed with low PDI values (<0.14), a size increases from 47 to 72 nm is seen as the volume of THF OA-NP is increased from 1.5 – 5 mL.

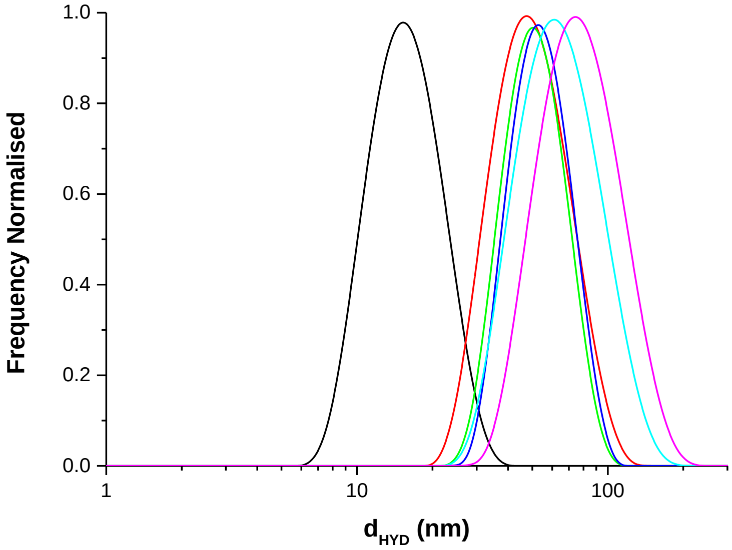

Figure 6-2 : DLS size distributions of — oleic acid stabilised nanoparticles dispersed in $CHCl_3$ and water dispersible PMA-NPC of varying size achieved by varying the amount of OA-NP added; — 1.5 mL OA-NP added, — 2 mL OA-NP added, — 3 mL OA-NP added, — 4 mL OA-NP added and — 5 mL OA-NP added

Table 6-2 : DLS data for different dispersions of PMA-NPC and starting $CHCl_3$ stabilised OA-NP

Fe added (mL)	d_{HYD} (nm)	PDI
Stock	14.9	0.09
1.5	47.1	0.14
2	49.6	0.04
3	51.6	0.06
4	59.6	0.12
5	71.7	0.12

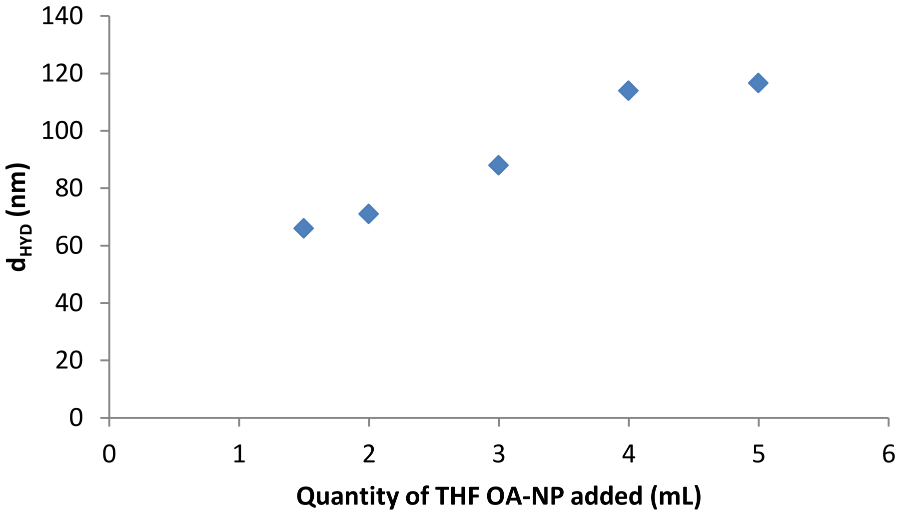

Figure 6-3 : Hydrodynamic size of PMA-NPCs as a function of the quantity of THF OA-NP added during the phase transfer

TEM analysis of PMA-NPC samples is shown below. Images of NPC with d_{HYD} of 59 nm and 78 nm are shown in Figure 6-5, respectively. In both cases very uniform clusters are formed with a low σ of 12 - 14%. The clusters appear to be very densely packed assemblies. In Figure 6-4, analysis of the images shows a significantly reduced size when compared to d_{HYD}, we see a similar trend in the sample with the larger d_{HYD}, (Figure 6-5), these results are summarised in Table 6-3. The discrepancy between d_{HYD} and d_{TEM} can be rationalised if the assumption is made that the cluster dries and shrinks upon preparing the material for TEM. This raises questions about the nature of particle packing in suspension. From TEM analysis the volume fraction ($f_{V(TEM)}$) of the non-collapsible component was estimated to be 0.16 and 0.14 for the 58.9 nm and 78 nm cluster, respectively.

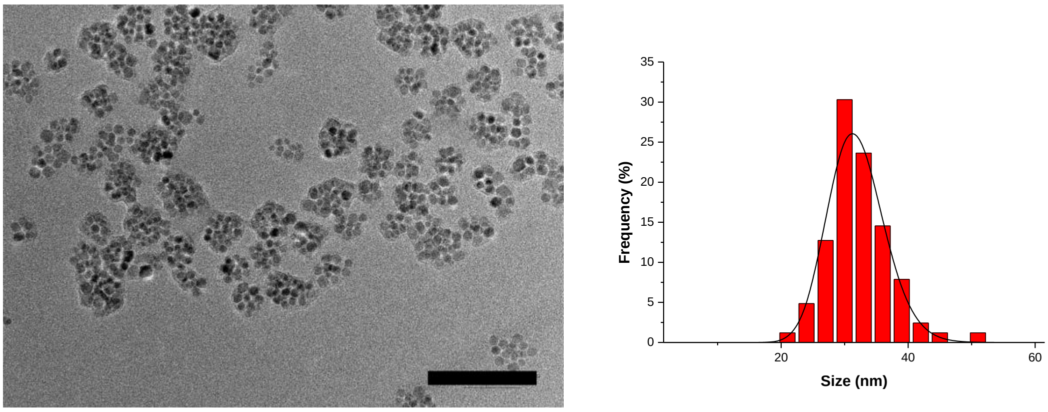

Figure 6-4 : Left: TEM micrograph of assemblies of OA-NP assembled using the polymer mediated assembly method; d_{HYD} – 56 nm, scale bar inset 100 nm, right: TEM analysis overlaid with a log normal model

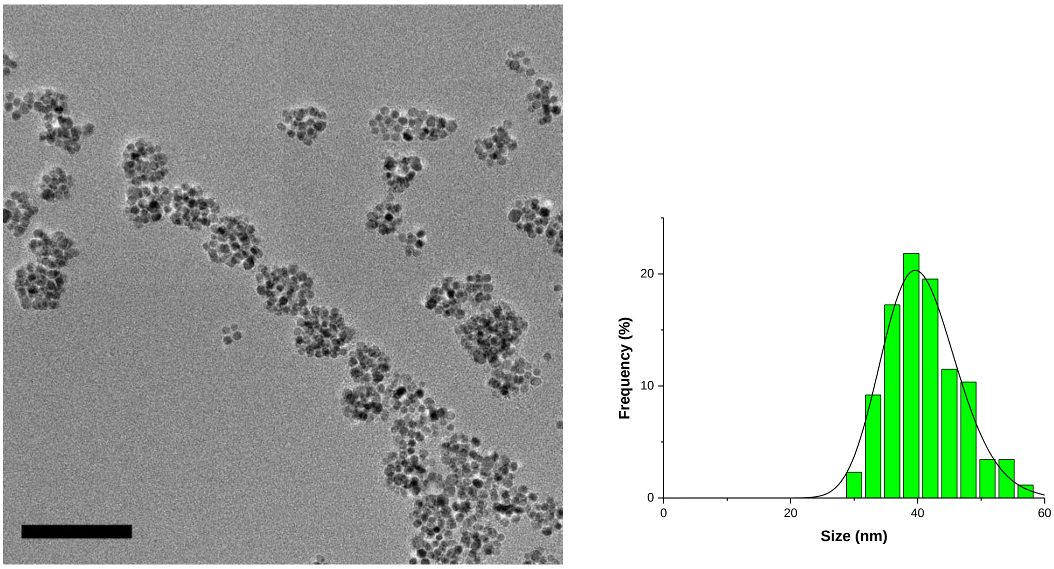

Figure 6-5 : Left: TEM micrograph of assemblies of OA-NP assembled using the polymer mediated assembly method; d_{HYD} – 78 nm, scale bar inset 100 nm, right: TEM analysis overlaid with a log normal model

Table 6-3 : Summary of PMA-NPC sizes as measured by different techniques

d_{HYD} (nm)	PDI	V_{HYD} (nm^3)	d_{TEM} (nm)	NPC counted	%σ (%)	V_{TEM} (nm^3)	$f_{V(TEM)}$
59	0.12	107536	31.9	164	12.8	16997	0.16
78	0.12	248475	40.72	101	14.0	35301	0.14

The NMRD profile for OA-NP dispersed in heptane is shown in Figure 6-6. The profile shows the characteristic features of superparamagnetic behaviour; a mid-frequency dip and a mid-frequency peak. The profile was modelled using SPM simulations based on theory developed by Muller et al.[23, 24], the simulations fit the profile well at low frequency and at high frequency except for a discrepancy at mid-frequency. This is expected as in this range the simulation provides an interpolation between the two different relaxation processes.

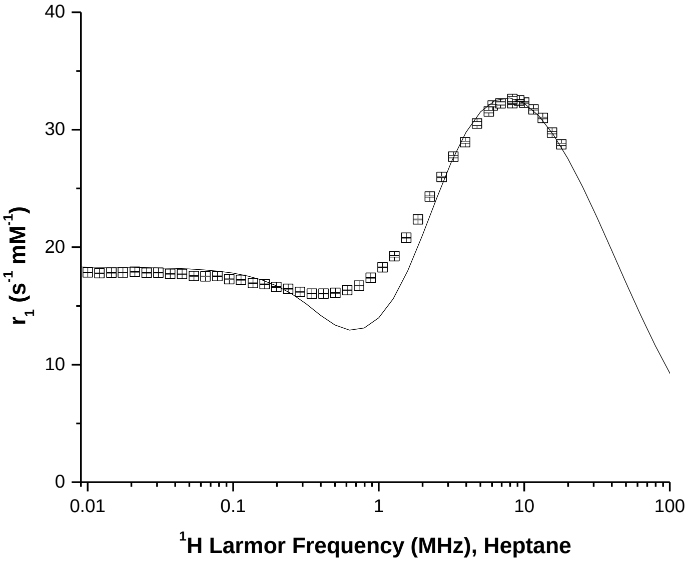

Figure 6-6 : NMRD profile of OA-NP stabilised in heptane prior to polymer mediated assembly with d_{HYD} of 14.9 nm and a PDI of 0.08

In Figure 6-7 the NMRD profiles of aqueous suspensions of PMA-NPC are shown. It can be seen that the mid frequency minimum, present in the NMRD profile of the primary nanoparticles shown in Figure 6-6, is suppressed. However, the peak is still evident demonstrating the clusters still exhibits superparamagnetic behaviour. The suppression of the minimum is expected [28] and can be attributed to interparticle interactions within the assembly. From the profiles it is evident that as size increases there is an increase in the r_1 value, while the position of ν_{max} moves slightly to lower frequencies. Additionally it should be noted that the presence of swollen polymer chains (PEO) inside the assembly, may slow down the diffusion of water molecules through the assembly, which would explain the increased r_1.

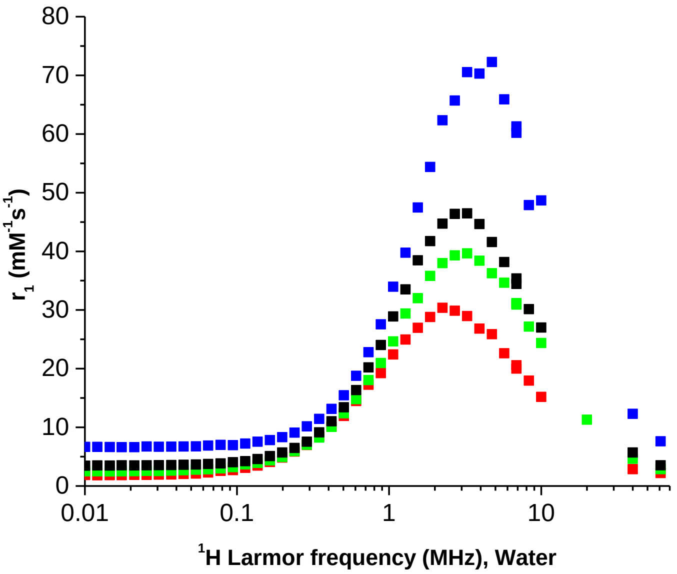

Figure 6-7 : NMRD profiles for clusters formed using polymer mediated assembly of different sizes; 🟦 60 nm , ■ 78 nm, 🟩 95 nm and 🟥 120 nm

Prior to the analysis of the r_2 values, for particles of this size it is important to assess if the particles are contained with the MAR or the SDR. This can evaluated by measuring r_2 using a series of differing echo delay values. For particles in the MAR there will be no significant echo delay dependence. The result shown in Figure 6-8 demonstrates that even the sample of the largest clusters in the study remains in the MAR.

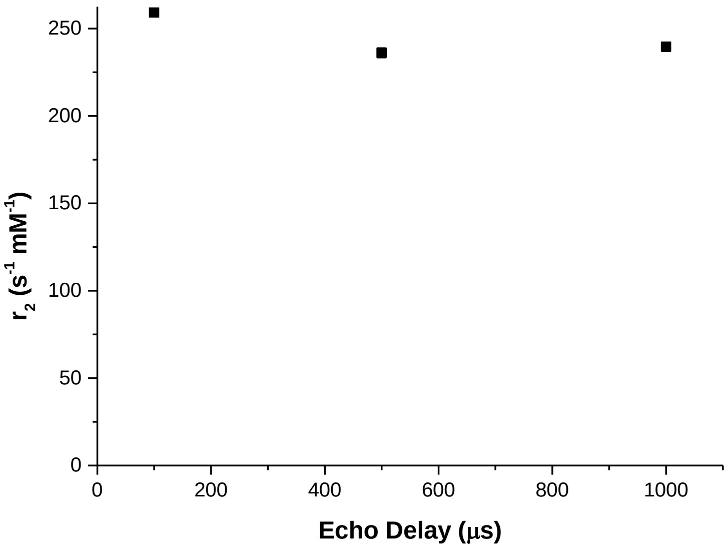

Figure 6-8 : Echo delay dependence study of polymer mediated assembly for clusters of d_{HYD} 129 nm

For all sized clusters, formed by PMA there is a decrease in r_1 with increasing size as shown in Figure 6-9.

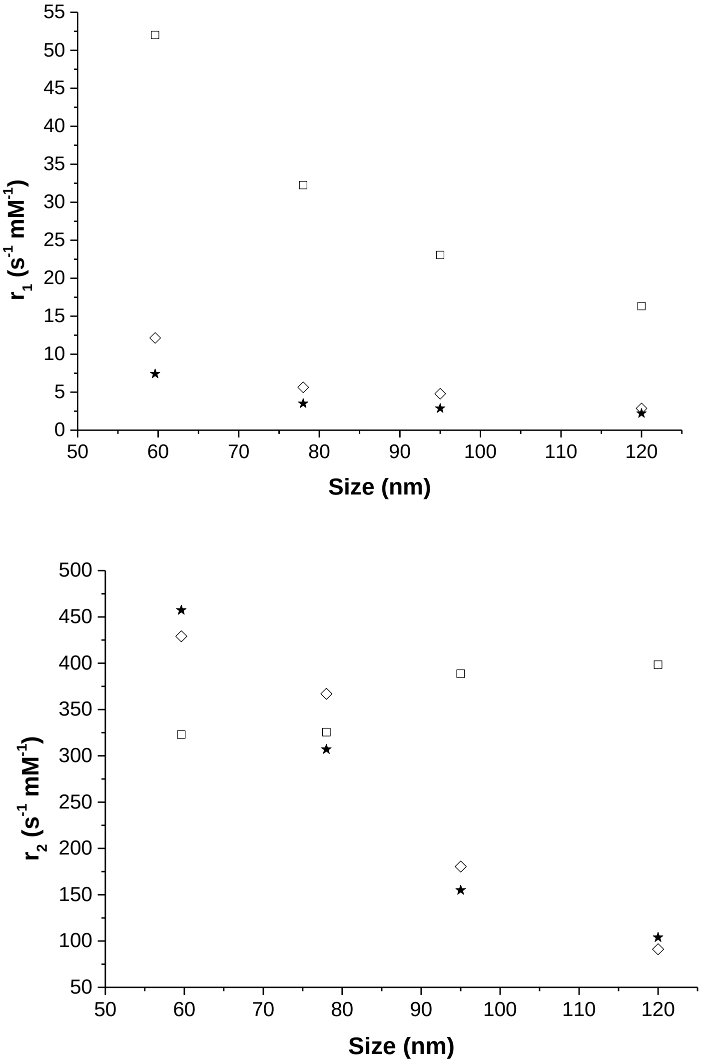

Figure 6-9 : Relativities of polymer mediated assembly clusters plotted against size for different NMRD frequencies; □ 9.25 MHz, ◊ 40 MHz and ★ 60 MHz; Top graph shows r_1 values; Bottom graph shows r_2 values

A trend in r_2, similar to that in r_1 is observed; r_2 decreases with increasing size, Figure 6-9. However, there is a contrary trend for r_2 measured at 9.25 MHz (□), with a moderate increase in r_2 apparent. This trend can perhaps be attributed to the incomplete locking of the moments at this field. When measured at 9.25 MHz, the PMA-NPCs lie on the field induced transition from the Neel to the Brownian relaxation mechanism. From Figure 6-7 it can be seen that the ν_{max} is changing over this frequency range and as a result discrepancies may arise during the transition from one relaxation mechanism to another. It should be noted that this result is in contrast with the results shown in Chapter 5. For densely packed clusters, as the size of the cluster increases, r_2 increases which is a result of decreased interparticle distances.

As identified above, both r_2 and r_1 (Figure 6-9) decrease with increasing size, the net effect is when the r_2/r_1 ratio is calculated there is a moderate decrease of ratio with increasing size, Figure 6-10. There is a discrepancy with the 79 nm sample which is currently under investigation. Detailed discussion of the relaxivity data for the range of different cluster types is provided below.

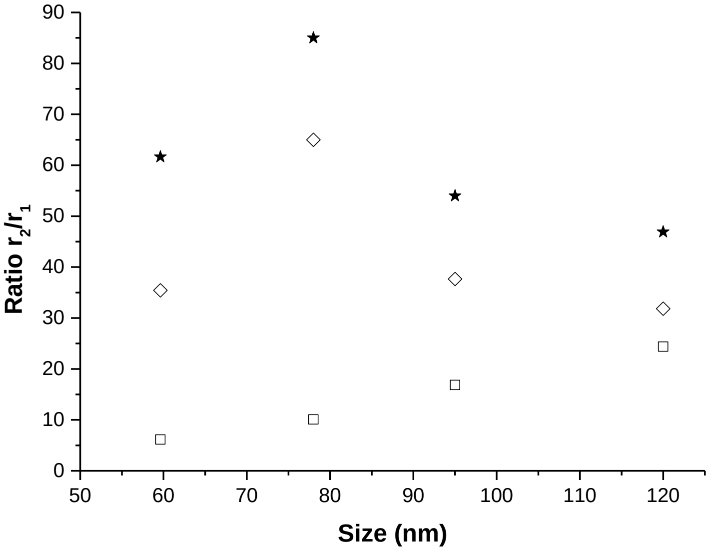

Figure 6-10 : Ratio r_2/r_1 of polymer mediated assembly clusters plotted against size for different NMRD frequencies; □ 9.25 MHz, ◊ 40 MHz and ★ 60 MHz

6.3.2. Dehydroascorbic Acid Stabilised Nanoparticles

The DLS size distributions of different size DHAA-NPC are shown in Figure 6-11. In all cases the clusters have a narrow size distribution (<0.15) and have sizes similar to those of the PMA-NPC (Table 6-4).

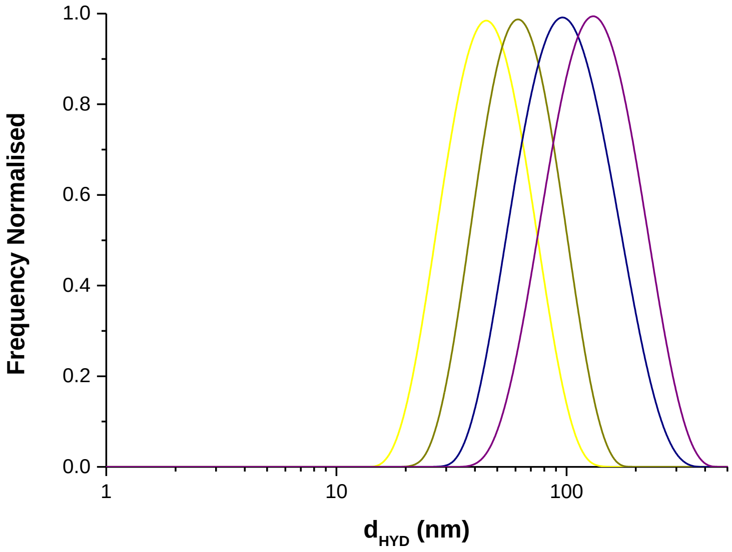

Figure 6-11 : DLS size distributions for DHAA-NPC of different size; — A1-D, — A1-C, — A1-B and — A1-A

Table 6-4 : DLS data for DHAA-NPC of different size

Sample Name	d_{HYD} (nm)	PDI
A1-A	119.7	0.14
A1-B	89.8	0.15
A1-C	58.1	0.11
A1-D	41.6	0.13

Representative TEM images of DHAA-NPC are shown below, and in all cases clusters of iron oxide nanoparticles are present. In all cases the structures appear to be loosely packed clusters, with a moderately NP packing density. Unfortunately, limited quantities of these samples were provided and as a result a comprehensive TEM characterisation was not undertaken. However, it appears that the samples do not survive drying intact.

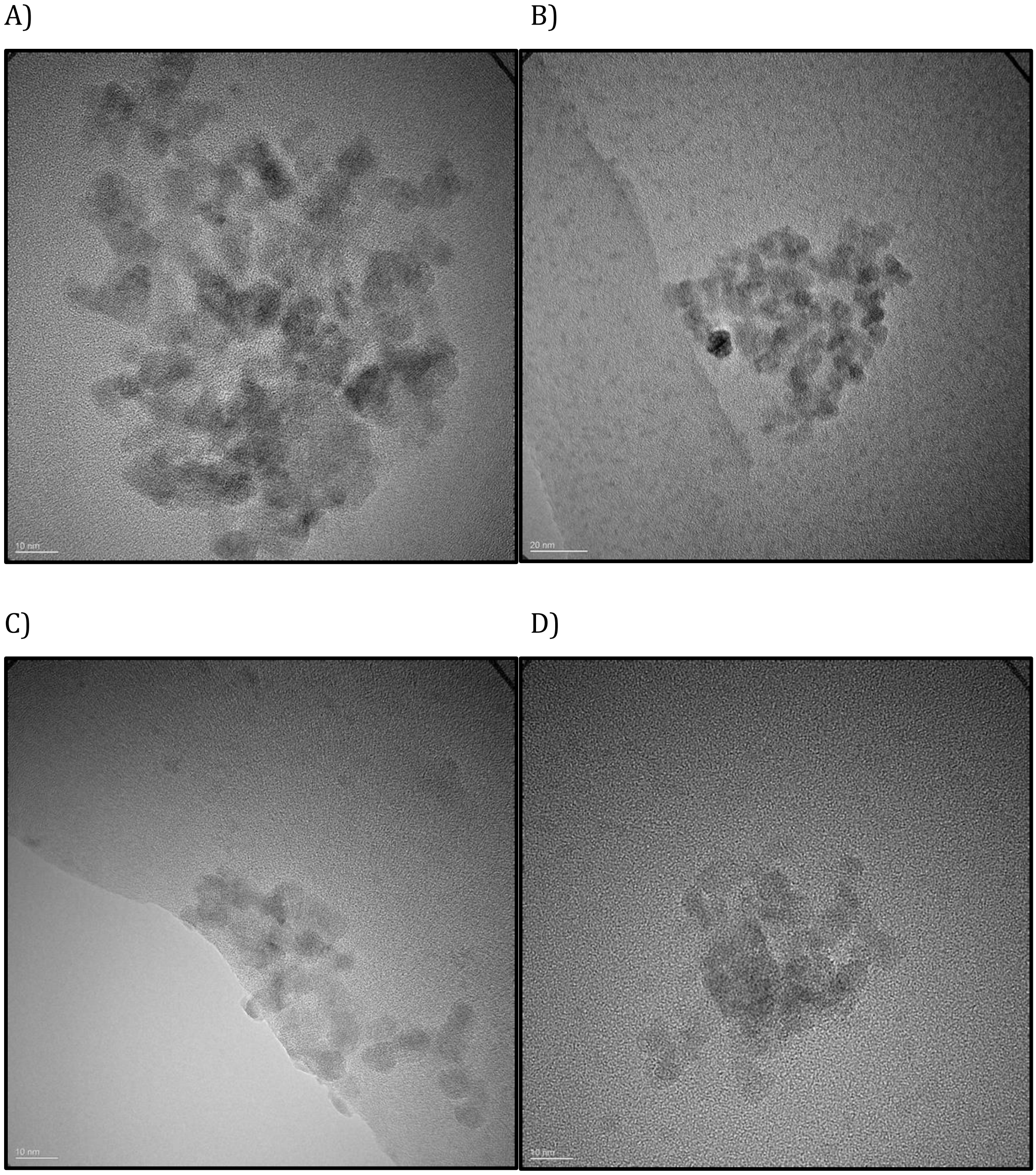

Figure 6-12 : Representative TEM micrograph of DHAA-NPC with a hydrodynamic size of A) 119 nm, B) 89 nm, C) 58 nm and D) 41 nm

NMRD profiles of aqueous dispersions containing DHAA-NPC of different sizes are shown in Figure 6-13. In all cases the clusters were found to be stable by DLS following the NMRD measurement. The profiles show superparamagnetic behaviour as characterised by the presence of a peak, ν_{max}, while the absence of a mid-frequency minimum is expected for clustered materials due to interparticle interactions. The ν_{max} value shifts to from 7.2 to 4.8 to 3.2 MHz as the size increases from 43 to 57 to 90 nm. It should be noted that as the size increases from 90 to 120 nm, there is no decrease in ν_{max}. From the NMRD profiles it can be seen that, particularly at low frequency, as size increases, r_1 increases; although this effect seems to reduce with increasing frequency. For the 90 – 120 nm clusters there is no significant increase in r_1 which is similar to the observed trend in ν_{max}.

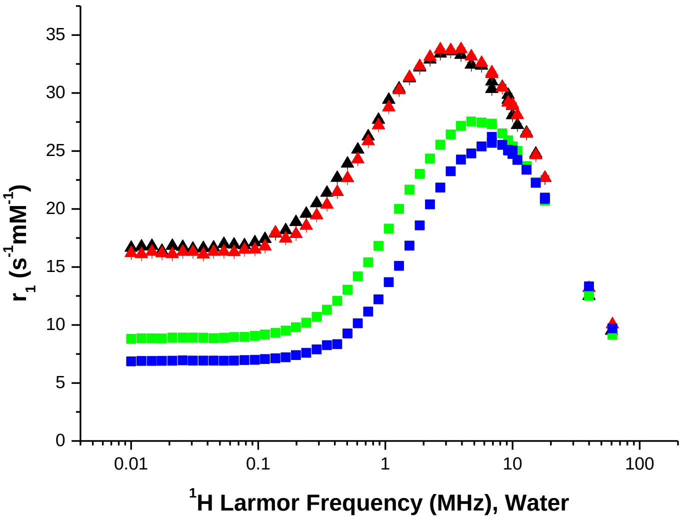

Figure 6-13 : NMRD profiles for DHAA-NPC of different sizes; ■ 42.8 nm , ■ 57.2 nm, ■ 89.9 nm and ■ 120.7 nm

Studies into the echo delay dependence of r_2 were carried out the largest DHAA-NPC, Figure 6-14. It was found there was no echo delay dependence, confirming that in this case the suspensions are also in the MAR.

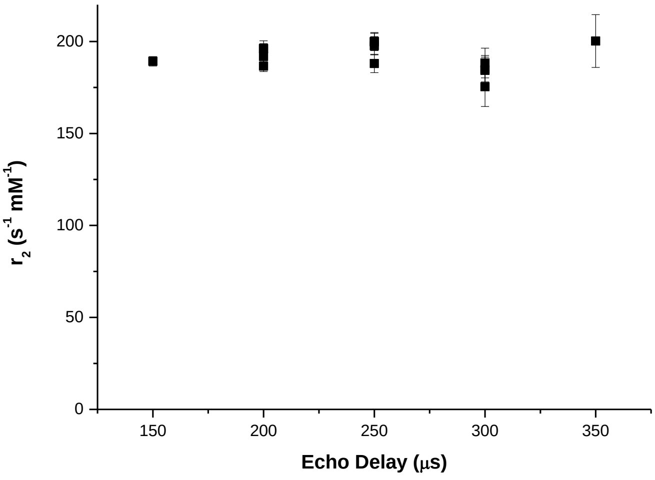

Figure 6-14 : Echo dependence study for DHAA-NPC with a d_{HYD} of 120 nm

Figure 6-15 shows how the r_1 values vary with size and is as expected; r_1 decreases with increasing field at 9.25 (■), 40 (▲) and 60 (★) MHz. However, it is interesting that there is little change in r_1 as size increases. In Figure 6-15 r_2 values for DHAA-NPC suspensions of varying sizes are also presented; as expected, r_2 is observed to increase with increasing frequency. Additionally it can be seen that r_2 increases with increasing size.

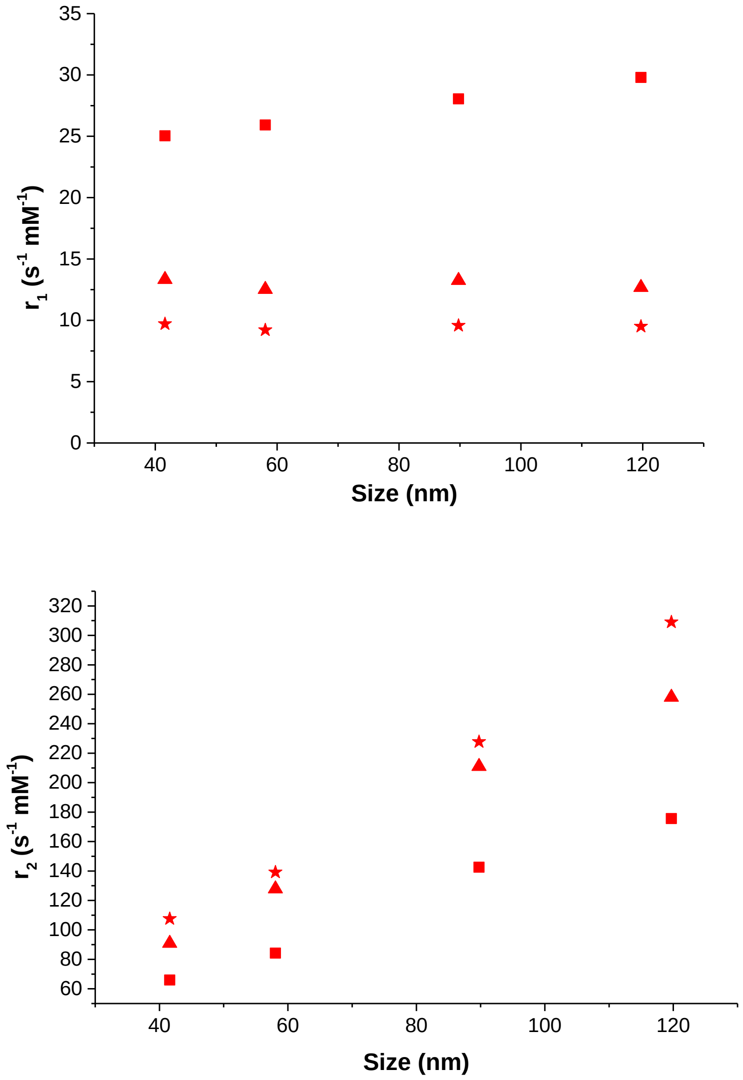

Figure 6-15 : Relativities of DHAA clusters plotted against size for different NMRD frequencies; ■ 9.25 MHz, ▲ 40 MHz and ★ 60 MHz; Top graph shows r_1; Bottom graph shows r_2

As a result of the observed trends in r_2 and r_1 (Figure 6-15), the increase in the r_2/r_1 ratio with increasing size (shown in Figure 6-16) can be attributed primarily to an increase in the r_2 value. This is consistent with the expectation for densely packed assemblies.

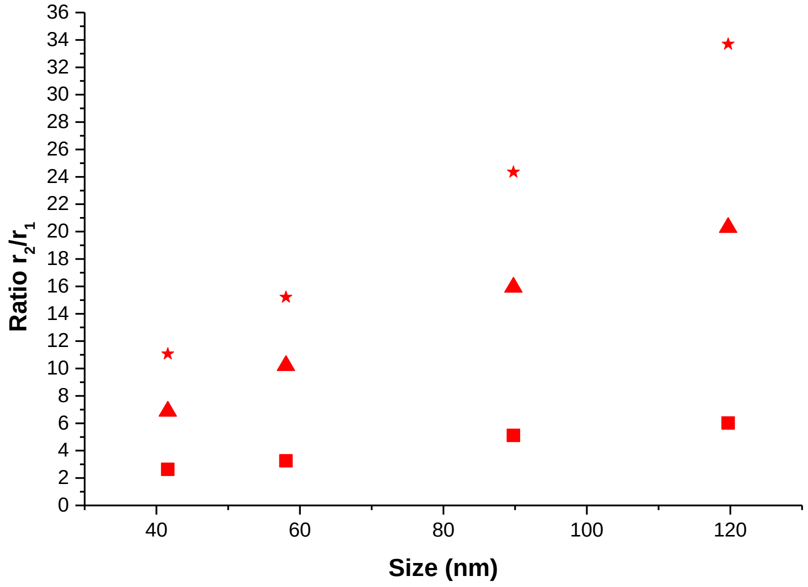

Figure 6-16 : Ratio of r_2/r_1 of DHAA clusters plotted against size for different NMRD frequencies; ■ 9.25 MHz, ▲ 40 MHz and ★ 60 MHz

6.3.3. Decorated Stimulus Responsive Polymer Nanobeads

Normalised DLS size distributions for dispersions of iron oxide nanoparticle decorated nanogels (NG-NPC) are shown in Figure 6-17. From this it can be seen the size increases with decreasing pH, and in all cases the size distributions exhibit reasonable PDI values (<0.19).

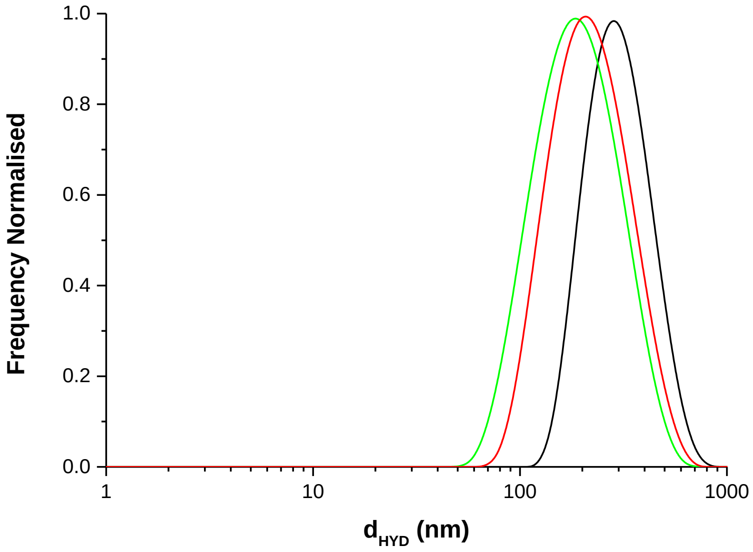

Figure 6-17 : DLS intensity weighted size distributions for NG-NPC of different sizes at different pHs

Table 6-5 : DLS values for nanogels of different sizes at different pHs

pH	d_{HYD} (nm)	PDI
6.2	169.9	0.15
4.2	198.0	0.14
3.2	297.2	0.19

In Figure 6-18 representative TEM images of NG-NPC at pH 6.2 are shown, from the image it can be seen that, on drying, the NP are decorated on the surface as opposed to embedded within the core of the polymer bead. The nanogel assemblies have a narrow distribution (%σ ~13) and conform to a log-normal fit (see Chapter 3). However, when the d_{TEM} value is compared to the d_{HYD} value it can be seen that there is a moderate decrease in size between the two measurements; this suggests some shrinking of the NPC following TEM sample preparation.

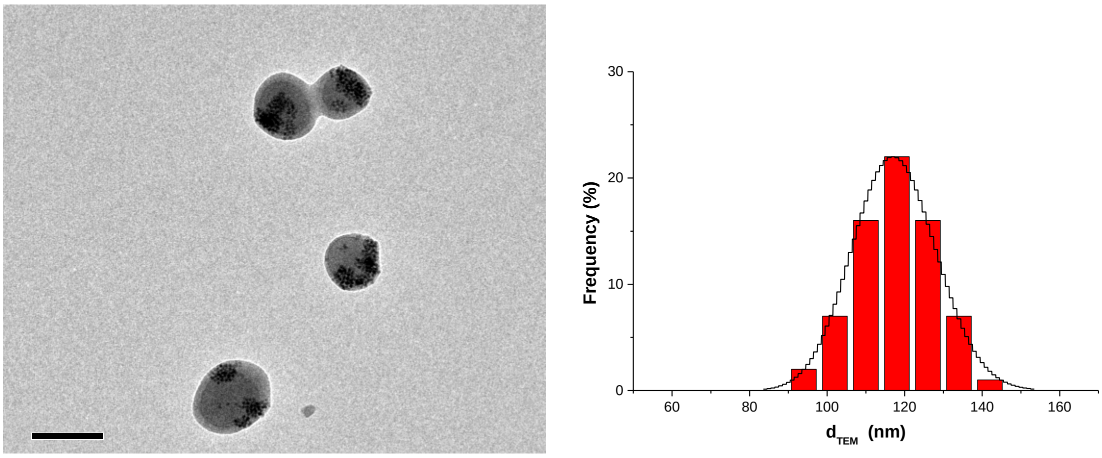

Figure 6-18: Left – TEM micrograph of decorated NG-NPC at pH 6.2, scale bar inset represents 100 nm; Right – Frequency distribution with overlaid log-normal fit; 90 NPC were counted

Table 6-6 : Sizes obtained from different sizing techniques for decorated nanogels at a pH of 6.2

Measurement Technique	Size (nm)	PDI	%σ
DLS (d_{HYD})	169.9	0.15	-
Microscopy (d_{TEM})	118.7	-	14.0

NMRD profiles for hybrid NG-NPC are shown in Figure 6-19 and again the profiles show the characteristic superparamagnetic shape with the expected absence of a mid-frequency dip. Following the NMRD measurements the NG-NPC were analysed using DLS to confirm colloidal stability. For the 170 nm sample (■) there was no significant change in DLS response, however for both the 199.5 nm (🟥) and the 312.0 nm (🟦) NG-NPC there was a significant change indicating that the sample was not stable throughout the measurement. In the case of these two unstable samples, only NMRD data is included for frequencies where colloidal stability was confirmed before and after NMRD measurements, hence for these two samples there is no high frequency data available. Using the available data it is clear there is little change in ν_{max} with increasing size. The NMRD profiles also show that r_1 decreases with increasing size. This is a similar observation to that for PMA-NPC, Figure 6-9.

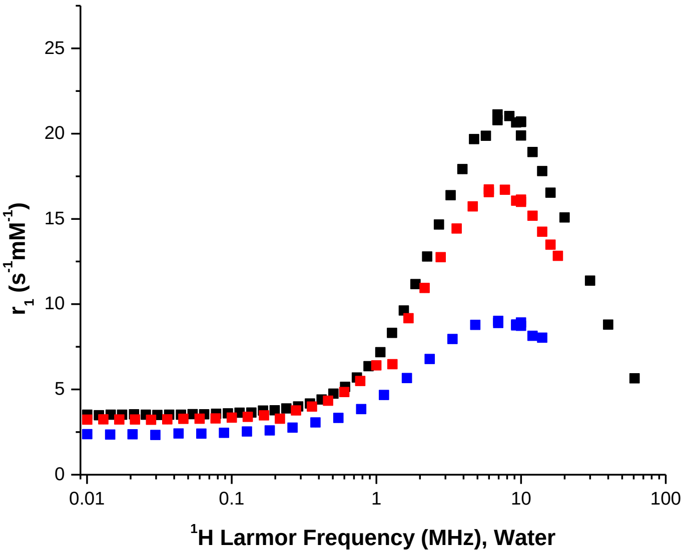

Figure 6-19 : NMRD profiles for hybrid NG-NPC of different sizes;, ■ 170.6 nm, ■ 199.5 nm and ■ 312.0 nm

Finally, echo delay dependence studies were carried out to assess if the NPC were in the MAR or the SDR. It is apparent from Figure 6-20 that there is a significant increase in r_2 with echo delay. It is questionable whether the 170.6 nm (■) samples show this effect but for the two larger clusters, a clear dependence is shows that these systems are not in the MAR.

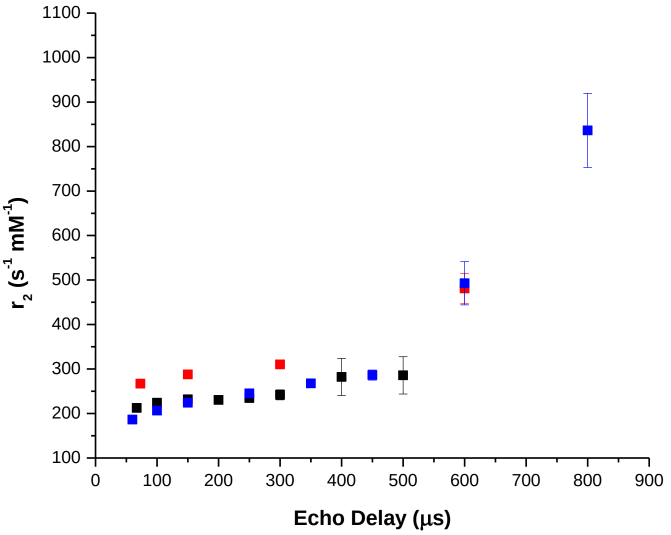

Figure 6-20 : Echo delay dependence of r_2 measured at 9.25 MHz for different sized clusters; d_{HYD}: ■ 170.6 nm, ■ 199.5 nm and ■ 312.0 nm

For the limited data presented in Figure 6-21, at 9.25 MHz the r_1 values decreases with size, which is a similar trend to that observed for the PMA assemblies. From r_2 data also shown in Figure 6-21, r_2 is shown to decrease with increasing size. Again this is a similar trend to the one observed in r_2 for PMA assemblies.

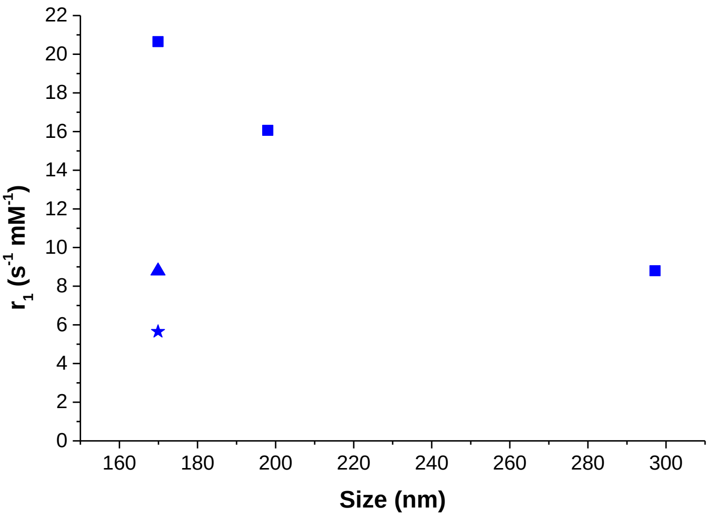

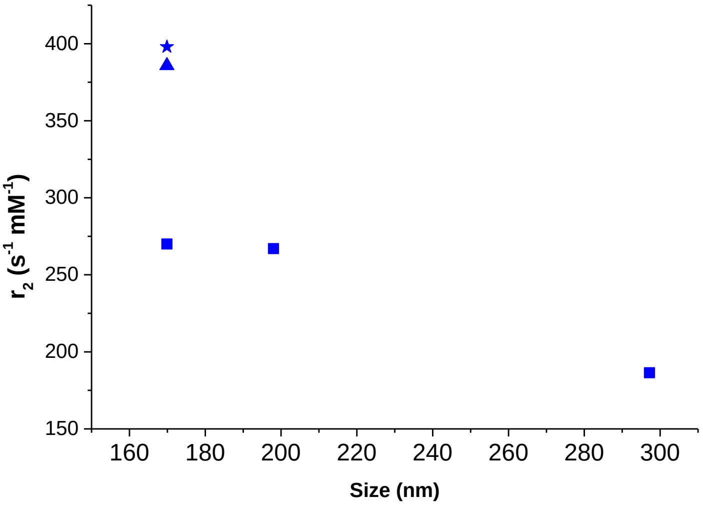

Figure 6-21: Relaxivity values of hybrid NG-NPC of different size plotted against size for different NMRD frequencies; ■ 9.25 MHz, ▲ 40 MHz and ★ 60 MHz; Top graph showing r_1 values; Bottom graph showing r_2 values

In Figure 6-22, the ratio of r_2/r_1 is shown, for the data available there is a moderate increase of ratio with increasing size (13 – 21) as the size increases from 170 to 300 nm. These results will be discussed fully below.

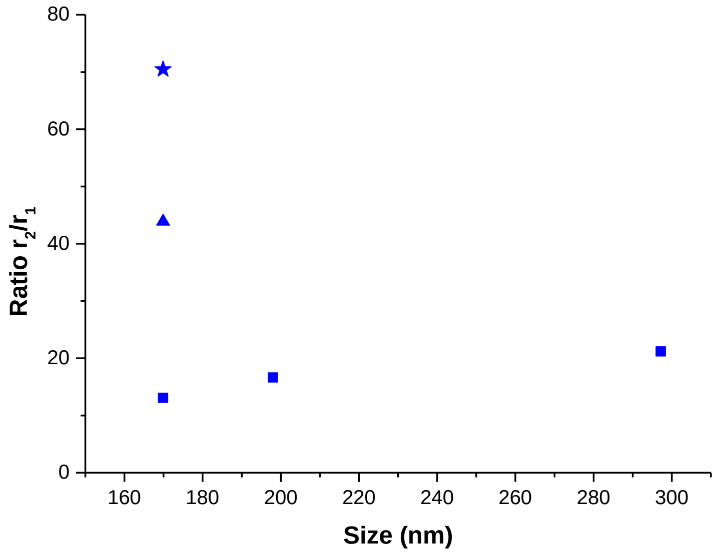

Figure 6-22 : Ratio of r_2/r_1 of NG assemblies of different size plotted against size for different NMRD frequencies; ■ 9.25 MHz, ▲ 40 MHz and ★ 60 MHz

6.3.4. Interpretation of NMR Data for Aqueous NPC Suspensions

For clusters of particles, it is expected for r_1 to decrease with increasing cluster size. This is as a result of particles in the centre of the cluster being shielded by the outer layers of particles, and so being unable to contribute to the relaxation of diffusing solvent molecules. Conversely, r_2 is expected to increase due to the increased magnetic moment of the assembly.

The changes in the relaxivity values with hydrodynamic size for the three types of assembly are summarised in Table 6-7. It can be seen that for all types the r_1 values decrease, although to different extends with increasing size. While for r_2 very different trends are observed.

Table 6-7 : Summary of different cluster types and their trends in r_1, r_2 and r_2/r_1 with respect to increasing size , measured at 61 MHz for DHAA-NPC and PMA-NPC, and at 9.25 MHz for NG-NPC

Cluster Type	Size Range (Δd_{HYD}) (nm)	% r_1 Change* $\left({}^{\Delta_{r_1}}/{}_{\Delta_{d_{HYD}}}\right)$	% r_2 Change* $\left({}^{\Delta_{r_2}}/{}_{\Delta_{d_{HYD}}}\right)$	% r_2/r_1 Change * $\left({}^{\Delta_{r_{ratio}}}/{}_{\Delta_{d_{HYD}}}\right)$
DHAA-NPC	41.6 - 119 (77.4)	-2.10 (-2.53E-3)	187 (2.56)	204 (2.92E-1)
NG-NPC	169 - 297 (128)	-57.5 (9.28E-2)	-31.1 (-6.55E-1)	66.4 (-2.43E-1)
PMA-NPC	59.6 - 120 (60.4)	-70.2 (8.61E-2)	-78.7 (-5.59)	-23.9 (-6.78E-2)

* Change in r_i is reported relative to the smaller sized cluster suspension

For DHAA there is small decrease in r_1 (2%) with increasing size, conversely r_2 increases significantly with size (187%). The latter is consistent with the expectations for a densely packed cluster; however the decrease in r_1 is quite small. For DHAA-NPC, the stabilising ligand is hydrophilic, a fact when combined with the observation from TEM of somewhat loosely packed clusters, suggests a loose assembly whose structure may allow diffusion of water molecules through it, so all particles contribute. The net effect is a significant increase in the r_2/r_1 ratio (204%) which arises from a strong increase in r_2.

For NG-NPC, r_1 is seen to decrease (58%) with increasing cluster size, and r_2 also decreases with increasing cluster size (31%). In this case the NPs are surface bound to polymer beads. The beads have hydrophobic components which should restrict or slow the diffusion of water through the matrix, resulting in decreased accessibility of water around the surface bound NPs, and so a decrease in r_1. As the pH is lowered, the polymer swells due to protonation of alcohol groups which increases the hydrophobicity, further reducing the accessibility of the water around the NPs thus further decreasing r_1. The increase in size is not associated with an increase in the number of particles in this case, but with swelling of polymer. From the TEM micrographs, the particles appear to be located in close proximity on the surface of the polymer bead. As the polymer swells the interparticle distance and the M_v value will decrease which may explain the observed reduction in r_2. These effects result in an increase in the r_2/r_1 ratio (66%), primarily due to a strong reduction in the r_1 values.

For PMA-NPC, r_1 was shown to decrease significantly (70%) with increasing cluster size, while r_2 is also shown to decrease (78%). In this case the expected decrease in r_1, for clustered NP, is observed. In fact the $\Delta r_1/\Delta d_{HYD}$ is very similar to the case of NG-NPCs, suggesting a non-permeable assembly in this case also. However, the decrease in r_2 for PMA-NPC with increasing cluster size is not consistent with the expectation for a densely packed assembly. The $\Delta r_2/\Delta d_{HYD}$ is of opposite sign to DHAA-NPCs and is negative but it is a stronger effect than in the case of NG-NPCs. For PMA-NPC, the clustering polymer is pluronic P127; a linear triblock polymer of PEO-PPO-PEO. For micelles of triblock polymers, the expectation is that the hydrophobic chain is sequestered at the centre of the construct surrounding a non-permeable core of particles with the two hydrophilic chains extended outwards. For this structure, an increase in cluster size should result in an increase in the M_v and thus r_2. However, we suggest that in the case of PMA-NPCs one chain points inwards to a polar core, the hydrophobic NPs and PPO occupy an intermediate space and the second PEO chain extends into the solvent.

This form of lower dimensional topology has been observed for nanoparticles using diblock copolymers [31]. This structure may result in a hydrophilic core surrounded by a hydrophobic layer through water cannot diffuse, which may result in a reduction of r_1. From analysis of TEM, the volume fraction of magnetic material ($f_{v(TEM)}$) for the two PMA-NPC samples analysed were calculated, it was found the $f_{v(TEM)}$ decreased with increasing hydrodynamic size which would result in a reduced M_v and reduced r_2 value. We suggest that this is a better representation of the structure and that these effects result in a decrease of the r_2/r_1 ratio (24%) with increasing size due to reductions in both r_1 and r_2. It should be noted that further structural analysis such as SANS, cryoTEM or depth of focus TEM would be required to fully elucidate the structure of PMA-NPC. The comparison with the materials reported by Hickey et al [31] needs to be considered in the light of the fact that those authors used PS-b-PAA which is known to be a more rigid polymer as compared to PEO-b-PPO-b-PEO used in PMA.

6.3.5. Spin-Spin Relaxivity Values of NPC Assemblies and the Universal Scaling Law

As mentioned in the introduction to this chapter, Vuong et al developed a universal scaling law which shows the relationship between a reduced r_2 (scaled using a combination of M_v and φ_{intra}). Using M_{NMR} values extracted from the simulation of the NMRD profiles shown above, the reduced r_2 values were calculated. For PMA and DHAA assemblies, where the volume or weight fraction is unknown, a hexagonal close packed (HCP) geometry was assumed. The volume fraction filled for HCP is 0.74. The key parameters are shown in Table 6-8.

The Redfield value, $\Delta\omega.\tau_D$ was calculated to assess whether the particles lay within the MAR or the SDR. These values obtained suggest that DHAA-NPC and PMA-NPC lie within the SDR while the NG-NPCs lie within the MAR. This is contrary to the experimental observation of the r_2 echo delay dependence, which shows that only the NG-NPCs lie in the SDR. This calls into question the assumption regarding the volume fraction for calculation of $\Delta\omega.\tau_D$. It should also be noted that these samples showed loose packed structures, on drying, by TEM.

Table 6-8 : Initial calculation, assuming a hexagonal close packed system for polymer mediated assembly (PMA) and DHAA clusters

Sample	d_{HYD} (nm)	M_v A/m	$\Delta\omega$	τ_D	$\Delta\omega.\tau_D$
Nanogel pH 3.2	297.0	27.4	3067.6	7.35E-06	0.023
Nanogel pH 4.2	198.0	127.3	14264.3	3.27E-06	0.047
Nanogel pH 6.2	169.9	224.2	25125.9	2.41E-06	0.060
DHAA-A1-A	119.7	113775	12749124.0	1.19E-06	15.2
DHAA-A1-B	89.76	111925	12541821.2	6.71E-07	8.4
DHAA-A1-C	58.06	126725	14200243.8	2.81E-07	3.9
DHAA-A1-D	41.6	144300	16169620.7	1.44E-07	2.3
PMA 4	120.0	95275	22596008.4	1.20E-06	12.8
PMA 3	98.0	120250	15547712.2	8.00E-07	10.8
PMA 2	78.0	138750	13474683.9	5.07E-07	7.9
PMA 1	120.0	201650	10676095.7	2.96E-07	6.7

In Figure 6-23 the reduced r_2 values are plotted on the published master curve and for both PMA-NPC and DHAA-NPCNPC they lie below the curve. It is interesting to note that NG-NPCs do not fit on the master curve either, and from Table 6-8, have an unusually low M_v. This suggests that the number of particles per polymer bead may be under estimated by TEM analysis. For surface decorated materials, it is necessary to perform a depth of field focus experiment in order to obtain a more accurate analysis of the number of particles bound to the 3D surface of the polymeric core. Furthermore, NG-NPCs may be particularly sensitive to drying.

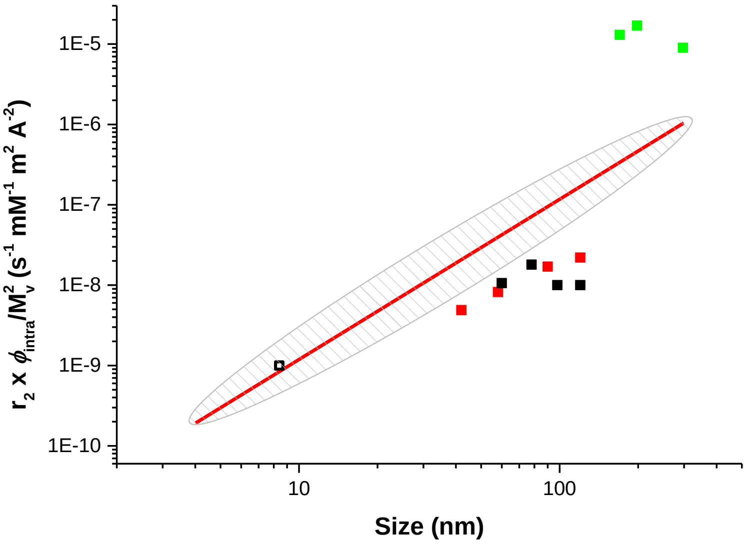

Figure 6-23 : r_2 scaled by the square of the material magnetisation weighted by the volume fraction of magnetic material plotted against size, adapted from [108]; 🟩 nanogel clusters 🟥 DHAA clusters ■ polymer mediated assembled clusters □ iron oxide nanoparticles with d_{HYD} 16 nm, d_{TEM} 8.4 nm fitted using this model. The oval indicates the approximate spread of reduced relaxivities reported in Vuong et al [108]

The evidence to date (TEM, NMR and the interpretation of r_2 using the master curve) suggests that DHAA and PMA clusters are not closely packed. A second approach was adopted whereby the volume fraction of magnetic material (f_v) was adjusted to fit the reduced relaxivity to the universal scaling law while keeping all other variables unchanged. Figure 6-24 shows the result of this approach which produces a revised estimate of the magnetic volume fraction, the values are summarised in Table 6-9.

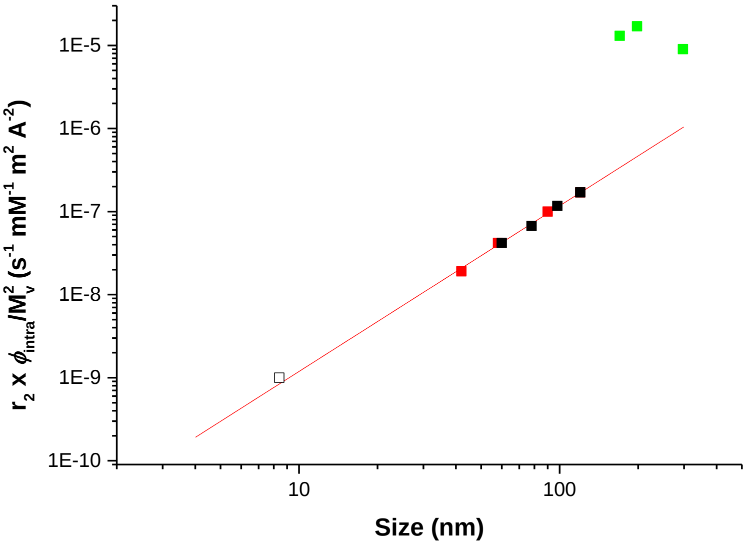

Figure 6-24 : r_2 normalised by the square of the material magnetisation weighted by the volume fraction of magnetic material plotted against size, the volume fraction of the magnetic material fitted was allowed to be free, results are shown in Table 6-9; 🟩 nanogel clusters 🟥 DHAA clusters ■ PMA clusters □ iron oxide nanoparticles with d_{HYD} 16 nm, d_{TEM} 8.4 nm fitted using this model

Table 6-9 : Revised calculations includingVolume fraction (f_v) and updated weight fraction (f_{wt}) of DHAA and PMA samples as extracted from an unconstrained fit using the universal scaling law

Cluster Type	Size (nm)	$f_{v,HCP}$	$f_{v,\ U.Scaling}$ [a]	$f_{wt,}$ [b]	$\Delta\omega.\tau_D$ First calculation	$\Delta\omega.\tau D,$ revised
DHAA	119.7	0.74	0.10	0.36	15.2	2.1
DHAA	89.8	0.74	0.12	0.42	8.4	1.4
DHAA	58.1	0.74	0.15	0.46	3.9	0.8
DHAA	41.6	0.74	0.19	0.54	2.3	0.6
PMA	120.0	0.74	0.05	0.19	12.8	0.8
PMA	98.0	0.74	0.06	0.25	10.8	0.9
PMA	78.0	0.74	0.20	0.56	7.9	2.2
PMA	59.6	0.74	0.19	0.53	6.7	1.7

[a] $f_{v,\ U.Scaling}$ derived from unconstrained fit of r_2 to the published master curve

[b] $f_{wt,}$ updated using the updated volume fraction

Volume fractions fitted using the universal scaling law are shown in Table 6-9 along with the corresponding values ($\Delta\omega.\tau_D$). For DHAA-NPC and PMA-NPC the result is significantly closer to 1. This is consistent with the r_2 echo delay dependence which shows the NPC suspensions lie in the MAR.

For DHAA-NPC the volume fraction decreases with increasing cluster size indicating that larger clusters are more loosely packed. The revised lower volume fraction is now consistent with the NRMD and TEM observations. Looser clusters should be more permeable to diffusing water, which results in the observed invariance in the r_1 values. It should be noted that this behaviour is unusual for clusters of iron oxide nanoparticles.

In the case of PMA-NPC the volume fraction also decreases with increasing size which is consistent with the structure of a decorated arrangement of particles with a polymeric core that is not readily accessible to the diffusing water molecules. The fitted f_v values of 0.19 and 0.20 are of a similar order to the values estimated from TEM, analysis for 59.6 and 78.0 nm clusters, of 0.16 and 0.14, respectively. However, when compared to NG-NPC, there is a larger decrease in $\Delta r_1/\Delta d_{HYD}$ size for PMA-NPC which suggests a similar partial inaccessibility of diffusing solvent through the assembly.

For the NG-NPC, the NMRD and TEM observations suggest the nanoparticles adopt a decorated arrangement on a polymeric bead. Similar to PMA-NPC, there is a decrease in the r_1 and r_2 values with increasing cluster size. This is primarily due to the partial inaccessibility of diffusing water molecules through the polymer bead. For materials of this type, it is difficult to obtain an accurate number of particles per cluster from traditional microscopy due to planar focus limitations. For a more accurate count of particles per polymer bead, depth of field focus TEM coupled with TGA should be performed. In addition, the NG-NPCs are not in the MAR, hence they are not expected to conform to the master curve.

6.4. **Conclusion**

In this chapter we have used both experimental evidence and theoretical relationships to investigate the effect of cluster architecture on both r_1 and r_2 relaxation processes. In the case of DHAA-NPC, the inclusion of hydrophilic ligands inside the cluster helped maintain high r_1 values while still enhancing r_2 values. Additionally, adopting a surface decorated approach by attaching NP to polymeric beads resulted in reduced r_1 and r_2 values with increasing cluster size for both NG-NPC and PMA-NPC. However, the reduction in r_1 is significant, which in turn results in a high r_2/r_1 ratio, > 80. PMA-NPCs are shown to behave similarly to NG-NPC; displaying comparable trends in both r_1 and r_2 values. It is suggested that this is again caused by a partial inaccessibility of water molecules through the core of the structure.

This work highlights the importance of careful consideration of the role of architecture in determining the relaxation properties of nanostructures. With recent developments in NP preparation [109, 110] and assembly methods [31, 47] it will be possible to improve control over the composition, size and spatial arrangement of particles within an assembly. In that context, methodologies that combine an experimental and theoretical understanding of cluster architecture may, in time, be used to rationally design next generation nanoparticles assemblies with improved magnetic, magnetic resonance and hyperthermic properties.

Thesis Conclusions

During this work with magnetic nanoparticle dispersions, in organic solvents, the size controlled synthesis of maghemite nanoparticle has been demonstrated. It was found that in general, the magnetic relaxation enhancement as measured by ^1H NMRD increased with increasing size. Superparamagnetic models were successfully used to extract the magnetic properties of the suspensions. From these models the saturation magnetisation, as extracted from ^1H NMRD profiles, was shown to increase with size similar to previously published empirical relationships and the crystallinity, as estimated by this relationship was shown to be lower than for other previously reported comparable materials.

Additionally for dispersions of maghemite nanoparticles in organic solvents, a study was carried out into the effect of stabilising ligand composition on the magnetic resonance properties. It was found that chain length of the ligand predominantly affected the reorientation dynamics of the magnetic moments which was attributed to a change in binding density of the ligand due to lateral interaction between the stabilising chains. Furthermore, the choice of head group was found have a significant effect on the magnetic resonance properties of nanoparticle suspensions. This was attributed to a difference in binding strength with the increased binding strength of the ligand resulting in an increased thickness of the surface canted spin layer which in turn reduced the total magnetic moment as measured by ^1H NMRD. This work, although carried out in organic suspensions the organic, is useful as it provides a guide for the potential optimisation of aqueous nanoparticle dispersions, which is on-going within the group.

A new method for the assembly of nanoparticles into nanoparticles clusters of controlled size and excellent monodispersity was developed. This interfacial assembly method, based on competitive stabiliser desorption, is highly reproducible which allows scale up and to date has been scaled up by a factor of 50 with further scale up plan experiments planned within the group. Through control over the assembly parameters the kinetics of assembly can be modified. It was found that the rate of assembly affected the magnetic resonance properties which we attributed to a change in the packing density of particles within the cluster.

Finally the role of structure in determining the magnetic resonance properties of different types of magnetic nanoparticle assemblies, in aqueous solvent was investigated. It was found that the cluster structure had a large impact in determining the resultant magnetic resonance properties. This is attributed to the accessibility of diffusing water through the nanoparticle assembly. These observation may, in time allow for the design assemblies with improved magnetic resonance properties.

Appendix A

Published Work

A.1 List of papers

1. XIAO, L., LI, J., BROUGHAM, D. F., **FOX, E. K.**, FELIU, N., BUSHMELEV, A., SCHMIDT, A., MERTENS, N., KIESSLING, F., VALLDOR, M., FADEEL, B. & MATHUR, S. 2011. Water-soluble superparamagnetic magnetite nanoparticles with biocompatible coating for enhanced magnetic resonance imaging. *Acs Nano,* 5, 6315-24.
2. KHAN, A. A., **FOX, E. K.,** GORZNY, M. L., NIKULINA, E., BROUGHAM, D. F., WEGE, C. & BITTNER, A. M. 2013. pH Control of the Electrostatic Binding of Gold and Iron Oxide Nanoparticles to Tobacco Mosaic Virus. *Langmuir,* 29, 2094-2098.

Contribution of the Author

1. Performed Fast Field Cycling NMR measurement of samples and contributed to the interpretation of the results
2. Synthesised and characterised electrostatically stabilised water dispersed iron oxide nanoparticles used in this paper

A.2 Conference Proceedings

1. Poster presentation: Fox, E. K., Ninjbadgar, T. , Brougham, D. F., "Controlled assembly of superparamagnetic iron-oxide nanoparticles" , 64th Irish Universities Chemistry Research Colloquium, University Limerick, 14 – 15 June 2012
2. Poster presentation: Fox, E. K., Brougham, D. F., "The effects of surface stabilisers on the magnetic properties of Superparamagnetic iron-oxide nanoparticles" , 63rd Irish Universities Chemistry Research Colloquium, University City Dublin, 23 – 24 June 2011
3. Oral presentation: Fox, E. K., Degenhard, S., Bittner, A. M., Wege C., Brougham D. F., "Towards Stable Magnetization of Plant Viral Nanorods via

Covalent Coupling" of Metal Oxide Particles", 21st Annual Meeting of the Society for Virology, Friburg, 23 – 26 March 2011

4. Poster presentation: Fox, E. K., Brougham, D. F., "Phase transfer of Magnetic Iron-Oxide Nano-Particles and subsequent surface polymerisation" 8th International Conference on the Scientific and Clinical Applications of Magnetic Carriers, Rostock, 25 - 27 May 2010

References

1. Meledandri, C.J., J.K. Stolarczyk, S. Ghosh, and D.F. Brougham, *Nonaqueous Magnetic Nanoparticle Suspensions with Controlled Particle Size and Nuclear Magnetic Resonance Properties.* Langmuir, 2008. **24**(24): p. 14159-14165.
2. Sun, S., H. Zeng, D.B. Robinson, S. Raoux, P.M. Rice, S.X. Wang, and G. Li, *Monodisperse MFe2O4 (M = Fe, Co, Mn) nanoparticles.* Journal of the American Chemical Society, 2004. **126**(1): p. 273-9.
3. Dai, Q., J. Frommer, D. Berman, K. Virwani, B. Davis, J.Y. Cheng, and A. Nelson, *High-Throughput Directed Self-Assembly of Core–Shell Ferrimagnetic Nanoparticle Arrays.* Langmuir, 2013. **29**(24): p. 7472-7477.
4. Lu, A.-H., W. Schmidt, N. Matoussevitch, H. Bönnemann, B. Spliethoff, B. Tesche, E. Bill, W. Kiefer, and F. Schüth, *Nanoengineering of a Magnetically Separable Hydrogenation Catalyst.* Angewandte Chemie International Edition, 2004. **43**(33): p. 4303-4306.
5. Weissleder, R., A. Bogdanov, E.A. Neuwelt, and M. Papisov, *Long-Circulating Iron-Oxides for Mr-Imaging.* Advanced Drug Delivery Reviews, 1995. **16**(2-3): p. 321-334.
6. Gleich, B. and J. Weizenecker, *Tomographic imaging using the nonlinear response of magnetic particles.* Nature, 2005. **435**(7046): p. 1214-1217.
7. Sanson, C., O. Diou, J. Thevenot, E. Ibarboure, A. Soum, A. Brulet, S. Miraux, E. Thiaudiere, S. Tan, A. Brisson, V. Dupuis, O. Sandre, and S. Lecommandoux, *Doxorubicin Loaded Magnetic Polymersomes: Theranostic Nanocarriers for MR Imaging and Magneto-Chemotherapy.* Acs Nano, 2011. **5**(2): p. 1122-1140.
8. Arruebo, M., R. Fernandez-Pacheco, M.R. Ibarra, and J. Santamaria, *Magnetic nanoparticles for drug delivery.* Nano Today, 2007. **2**(3): p. 22-32.
9. Martinez-Boubeta, C., K. Simeonidis, A. Makridis, M. Angelakeris, O. Iglesias, P. Guardia, A. Cabot, L. Yedra, S. Estrade, F. Peiro, Z. Saghi, P.A. Midgley, I. Conde-Leboran, D. Serantes, and D. Baldomir, *Learning from Nature to Improve the Heat Generation of Iron-Oxide Nanoparticles for Magnetic Hyperthermia Applications.* Scientific Reports, 2013. **3**.
10. Bruns, O.T., H. Ittrich, K. Peldschus, M.G. Kaul, U.I. Tromsdorf, J. Lauterwasser, M.S. Nikolic, B. Mollwitz, M. Merkel, N.C. Bigall, S. Sapra, R. Reimer, H. Hohenberg, H. Weller, A. Eychmuller, G. Adam, U. Beisiegel, and J. Heeren, *Real-time magnetic resonance imaging and quantification of lipoprotein metabolism in vivo using nanocrystals.* Nature Nanotechnology, 2009. **4**(3): p. 193-201.
11. Ito, A., M. Shinkai, H. Honda, and T. Kobayashi, *Medical application of functionalized magnetic nanoparticles.* Journal of Bioscience and Bioengineering, 2005. **100**(1): p. 1-11.
12. Cho, N.H., T.C. Cheong, J.H. Min, J.H. Wu, S.J. Lee, D. Kim, J.S. Yang, S. Kim, Y.K. Kim, and S.Y. Seong, *A multifunctional core-shell nanoparticle for dendritic cell-based cancer immunotherapy.* Nature Nanotechnology, 2011. **6**(10): p. 675-82.
13. *NIST Reference on Constants, Units, and Uncertaint.* National Institute of Standards and Technology (NIST), U.S. Department of Commerce.
14. Coey, J.M.D. and Knovel (Firm), *Magnetism and magnetic materials*. 2009, Cambridge University Press,: Cambridge ; New York. p. xiii, 628 p.

15. Furlani, E.P., *Magnetic Biotransport: Analysis and Applications.* Materials, 2010. **3**(4): p. 2412-2446.
16. Lu, A.H., E.L. Salabas, and F. Schuth, *Magnetic nanoparticles: Synthesis, protection, functionalization, and application.* Angewandte Chemie-International Edition, 2007. **46**(8): p. 1222-1244.
17. Getzlaff, M., *Fundamentals of magnetism*. 2008, Berlin ; New York: Springer. xiv, 387 p.
18. Roch, A., Y. Gossuin, R.N. Muller, and P. Gillis, *Superparamagnetic colloid suspensions: Water magnetic relaxation and clustering.* Journal of Magnetism and Magnetic Materials, 2005. **293**(1): p. 532-539.
19. Vuong, Q.L., P. Gillis, and Y. Gossuin, *Monte Carlo simulation and theory of proton NMR transverse relaxation induced by aggregation of magnetic particles used as MRI contrast agents.* Journal of Magnetic Resonance, 2011. **212**(1): p. 139-148.
20. Bloch, F., *Nuclear Induction.* Physical Review, 1946. **70**(7-8): p. 460-474.
21. Xiao, L., J. Li, D.F. Brougham, E.K. Fox, N. Feliu, A. Bushmelev, A. Schmidt, N. Mertens, F. Kiessling, M. Valldor, B. Fadeel, and S. Mathur, *Water-soluble superparamagnetic magnetite nanoparticles with biocompatible coating for enhanced magnetic resonance imaging.* Acs Nano, 2011. **5**(8): p. 6315-24.
22. Laurent, S., D. Forge, M. Port, A. Roch, C. Robic, L. Vander Elst, and R.N. Muller, *Magnetic iron oxide nanoparticles: synthesis, stabilization, vectorization, physicochemical characterizations, and biological applications.* Chemical Reviews, 2008. **108**(6): p. 2064-110.
23. Roch, A., R.N. Muller, and P. Gillis, *Theory of proton relaxation induced by superparamagnetic particles.* Journal of Chemical Physics, 1999. **110**(11): p. 5403-5411.
24. Taboada, E., E. Rodríguez, A. Roig, J. Oró, A. Roch, and R.N. Muller, *Relaxometric and Magnetic Characterization of Ultrasmall Iron Oxide Nanoparticles with High Magnetization. Evaluation as Potential T1 Magnetic Resonance Imaging Contrast Agents for Molecular Imaging.* Langmuir, 2007. **23**(8): p. 4583-4588.
25. Forge, D., A. Roch, S. Laurent, H. Tellez, Y. Gossuin, F. Renaux, L. Vander Elst, and R.N. Muller, *Optimization of the Synthesis of Superparamagnetic Contrast Agents by the Design of Experiments Method.* The Journal of Physical Chemistry C, 2008. **112**(49): p. 19178-19185.
26. Roch, A., P. Gillis, A. Ouakssim, and R.N. Muller, *Proton magnetic relaxation in superparamagnetic aqueous colloids: a new tool for the investigation of ferrite crystal anisotropy.* Journal of Magnetism and Magnetic Materials, 1999. **201**: p. 77-79.
27. Meledandri, C.J., J.K. Stolarczyk, and D.F. Brougham, *Hierarchical Gold-Decorated Magnetic Nanoparticle Clusters with Controlled Size.* Acs Nano, 2011. **5**(3): p. 1747-1755.
28. Stolarczyk, J.K., S. Ghosh, and D.F. Brougham, *Controlled Growth of Nanoparticle Clusters through Competitive Stabilizer Desorption.* Angewandte Chemie-International Edition, 2009. **48**(1): p. 175-178.
29. Fresnais, J., J.F. Berret, B. Frka-Petesic, O. Sandre, and R. Perzynski, *Electrostatic Co-Assembly of Iron Oxide Nanoparticles and Polymers: Towards the Generation of Highly Persistent Superparamagnetic Nanorods.* Advanced Materials, 2008. **20**(20): p. 3877-+.
30. Riedinger, A., M. Pernia Leal, S.R. Deka, C. George, I.R. Franchini, A. Falqui, R. Cingolani, and T. Pellegrino, *"Nanohybrids" Based on pH-Responsive*

Hydrogels and Inorganic Nanoparticles for Drug Delivery and Sensor Applications. Nano Letters, 2011. **11**(8): p. 3136-3141.

31. Hickey, R.J., X. Meng, P. Zhang, and S.-J. Park, *Low-Dimensional Nanoparticle Clustering in Polymer Micelles and Their Transverse Relaxivity Rates.* ACS Nano, 2013. **7**(7): p. 5824-5833.
32. Aryal, S., J. Key, C. Stigliano, J.S. Ananta, M. Zhong, and P. Decuzzi, *Engineered magnetic hybrid nanoparticles with enhanced relaxivity for tumor imaging.* Biomaterials, 2013. **34**(31): p. 7725-7732.
33. Chen, Y., G. Nurumbetov, R. Chen, N. Ballard, and S.A.F. Bon, *Multicompartmental Janus Microbeads from Branched Polymers by Single-Emulsion Droplet Microfluidics.* Langmuir, 2013. **29**(41): p. 12657-12662.
34. Gao, X., C. He, C. Xiao, X. Zhuang, and X. Chen, *Biodegradable pH-responsive polyacrylic acid derivative hydrogels with tunable swelling behavior for oral delivery of insulin.* Polymer, 2013. **54**(7): p. 1786-1793.
35. Kimmich, R. and E. Anoardo, *Field-cycling NMR relaxometry.* Progress in Nuclear Magnetic Resonance Spectroscopy, 2004. **44**(3-4): p. 257-320.
36. *Dynamic Light Scattering: An Introduction in 30min*, in *Technical Notes*. Malvern Instruments.
37. Kaszuba, M., *A lecture on DLS.* Malvern Technical notes.
38. Kaszuba, M., D. McKnight, M.T. Connah, F.K. McNeil-Watson, and U. Nobbmann, *Measuring sub nanometre sizes using dynamic light scattering.* Journal of Nanoparticle Research, 2008. **10**(5): p. 823-829.
39. *Stanford University, http://em-1.stanford.edu/Schedule/ICP/abouticp.htm, Accessed on 10/11/2010*.
40. *Creative Commons Attribution-ShareAlike 3.0 Unported License*.
41. Habault, D., A. Dery, J. Leng, S. Lecommandoux, J.F. Le Meins, and O. Sandre, *Droplet Microfluidics to Prepare Magnetic Polymer Vesicles and to Confine the Heat in Magnetic Hyperthermia.* Ieee Transactions on Magnetics, 2013. **49**(1): p. 182-190.
42. Tromsdorf, U.I., N.C. Bigall, M.G. Kaul, O.T. Bruns, M.S. Nikolic, B. Mollwitz, R.A. Sperling, R. Reimer, H. Hohenberg, W.J. Parak, S. Forster, U. Beisiegel, G. Adam, and H. Weller, *Size and surface effects on the MRI relaxivity of manganese ferrite nanoparticle contrast agents.* Nano Letters, 2007. **7**(8): p. 2422-2427.
43. Tromsdorf, U.I., O.T. Bruns, S.C. Salmen, U. Beisiegel, and H. Weller, *A Highly Effective, Nontoxic T(1) MR Contrast Agent Based on Ultrasmall PEGylated Iron Oxide Nanoparticles.* Nano Letters, 2009. **9**(12): p. 4434-4440.
44. Shen, L.F., P.E. Laibinis, and T.A. Hatton, *Bilayer surfactant stabilized magnetic fluids: Synthesis and interactions at interfaces.* Langmuir, 1999. **15**(2): p. 447-453.
45. Daou, T.J., G. Pourroy, S. Begin-Colin, J.M. Greneche, C. Ulhaq-Bouillet, P. Legare, P. Bernhardt, C. Leuvrey, and G. Rogez, *Hydrothermal synthesis of monodisperse magnetite nanoparticles.* Chemistry of Materials, 2006. **18**(18): p. 4399-4404.
46. Lai, S.M., J.K. Hsiao, H.P. Yu, C.W. Lu, C.C. Huang, M.J. Shieh, and P.S. Lai, *Polyethylene glycol-based biocompatible and highly stable superparamagnetic iron oxide nanoclusters for magnetic resonance imaging.* Journal of Materials Chemistry, 2012. **22**(30): p. 15160-15167.
47. Poselt, E., H. Kloust, U. Tromsdorf, M. Janschel, C. Hahn, C. Masslo, and H. Weller, *Relaxivity Optimization of a PEGylated Iron-Oxide-Based Negative*

Magnetic Resonance Contrast Agent for T-2-Weighted Spin-Echo Imaging. Acs Nano, 2012. **6**(2): p. 1619-1624.

48. Levy, M., A. Quarta, A. Espinosa, A. Figuerola, C. Wilhelm, M. Garcia-Hernandez, A. Genovese, A. Falqui, D. Alloyeau, R. Buonsanti, P.D. Cozzoli, M.A. Garcia, F. Gazeau, and T. Pellegrino, *Correlating Magneto-Structural Properties to Hyperthermia Performance of Highly Monodisperse Iron Oxide Nanoparticles Prepared by a Seeded-Growth Route.* Chemistry of Materials, 2011. **23**(18): p. 4170-4180.
49. Park, J., J. Joo, S.G. Kwon, Y. Jang, and T. Hyeon, *Synthesis of Monodisperse Spherical Nanocrystals.* Angewandte Chemie International Edition, 2007. **46**(25): p. 4630-4660.
50. Niederberger, M., N. Pinna, and SpringerLink (Online service), *Metal oxide nanoparticles in organic solvents synthesis, formation, assembly and application*, in *Engineering materials and processes,*. 2009, Springer,: Heidelberg. p. xiii, 215 p.
51. Pinna, N., S. Grancharov, P. Beato, P. Bonville, M. Antonietti, and M. Niederberger, *Magnetite nanocrystals: Nonaqueous synthesis, characterization, and solubility.* Chemistry of Materials, 2005. **17**(11): p. 3044-3049.
52. Pinna, N. and M. Niederberger, *Surfactant-free nonaqueous synthesis of metal oxide nanostructures.* Angewandte Chemie-International Edition, 2008. **47**(29): p. 5292-5304.
53. LaMer, V.K. and R.H. Dinegar, *Theory, Production and Mechanism of Formation of Monodispersed Hydrosols.* Journal of the American Chemical Society, 1950. **72**(11): p. 4847-4854.
54. Nanda, K.K., A. Maisels, F.E. Kruis, H. Fissan, and S. Stappert, *Higher Surface Energy of Free Nanoparticles.* Physical Review Letters, 2003. **91**(10): p. 106102.
55. Lifshitz, I.M. and V.V. Slyozov, *The kinetics of precipitation from supersaturated solid solutions.* Journal of Physics and Chemistry of Solids, 1961. **19**(1–2): p. 35-50.
56. Tiemann, M., F. Marlow, J. Hartikainen, O. Weiss, and M. Linden, *Ripening Effects in ZnS Nanoparticle Growth.* The Journal of Physical Chemistry C, 2008. **112**(5): p. 1463-1467.
57. Vengrenovitch, R.D., *On the ostwald ripening theory.* Acta Metallurgica, 1982. **30**(6): p. 1079-1086.
58. Layek, A., G. Mishra, A. Sharma, M. Spasova, S. Dhar, A. Chowdhury, and R. Bandyopadhyaya, *A Generalized Three-Stage Mechanism of ZnO Nanoparticle Formation in Homogeneous Liquid Medium.* The Journal of Physical Chemistry C, 2012. **116**(46): p. 24757-24769.
59. Schwertmann, U. and R.M. Cornell, *Iron oxides in the laboratory : preparation and characterization*. 1991, Weinheim ; New York: VCH. xiv, 137 p.
60. Wooding, A., M. Kilner, and D.B. Lambrick, *Studies of the Double Surfactant Layer Stabilization of Water-Based Magnetic Fluids.* Journal of Colloid and Interface Science, 1991. **144**(1): p. 236-242.
61. Maher, S., *4th year project.* DCU, 2010.
62. Feltin, N. and M.P. Pileni, *New Technique for Synthesizing Iron Ferrite Magnetic Nanosized Particles.* Langmuir, 1997. **13**(15): p. 3927-3933.
63. Popplewell, J. and L. Sakhnini, *The dependence of the physical and magnetic properties of magnetic fluids on particle size.* Journal of Magnetism and Magnetic Materials, 1995. **149**(1–2): p. 72-78.

64. Tang, Z.X., C.M. Sorensen, K.J. Klabunde, and G.C. Hadjipanayis, *Size-dependent Curie temperature in nanoscale MnFe_{2}O_{4} particles.* Physical Review Letters, 1991. **67**(25): p. 3602-3605.
65. Lu, H.M., W.T. Zheng, and Q. Jiang, *Saturation magnetization of ferromagnetic and ferrimagnetic nanocrystals at room temperature.* Journal of Physics D: Applied Physics, 2007. **40**(2): p. 320.
66. Hendriksen, P.V., S. Linderoth, C.A. Oxborrow, and S. Morup, *Ultrafine maghemite particles. II. The spin-canting effect revisited.* Journal of Physics: Condensed Matter, 1994. **6**(16): p. 3091.
67. Berkowitz, A.E., W.J. Schuele, and P.J. Flanders, *Influence of Crystallite Size on the Magnetic Properties of Acicular gamma-Fe[sub 2]O[sub 3] Particles.* Journal of Applied Physics, 1968. **39**(2): p. 1261-1263.
68. Martínez, B., X. Obradors, L. Balcells, A. Rouanet, and C. Monty, *Low Temperature Surface Spin-Glass Transition in γ- Fe_{2}O_{3} Nanoparticles.* Physical Review Letters, 1998. **80**(1): p. 181-184.
69. Baranwal, A.K. and S.C. Singhi, *Acute iron poisoning: management guidelines.* (0019-6061 (Print)).
70. Sahoo, Y., H. Pizem, T. Fried, D. Golodnitsky, L. Burstein, C.N. Sukenik, and G. Markovich, *Alkyl phosphonate/phosphate coating on magnetite nanoparticles: A comparison with fatty acids.* Langmuir, 2001. **17**(25): p. 7907-7911.
71. Yee, C., G. Kataby, A. Ulman, T. Prozorov, H. White, A. King, M. Rafailovich, J. Sokolov, and A. Gedanken, *Self-assembled monolayers of alkanesulfonic and -phosphonic acids on amorphous iron oxide nanoparticles.* Langmuir, 1999. **15**(21): p. 7111-7115.
72. Peddis, D., C. Cannas, A. Musinu, A. Ardu, F. Orru, D. Fiorani, S. Laureti, D. Rinaldi, G. Muscas, G. Concas, and G. Piccaluga, *Beyond the Effect of Particle Size: Influence of CoFe2O4 Nanoparticle Arrangements on Magnetic Properties.* Chemistry of Materials, 2013. **25**(10): p. 2005-2013.
73. Peddis, D., F. Orru, A. Ardu, C. Cannas, A. Musinu, and G. Piccaluga, *Interparticle Interactions and Magnetic Anisotropy in Cobalt Ferrite Nanoparticles: Influence of Molecular Coating.* Chemistry of Materials, 2012. **24**(6): p. 1062-1071.
74. Turro, N.J., M.A. White, J.A. Johnson, and J.T. Koberstein, *Toward the syntheses of universal ligands for metal oxide surfaces: Controlling surface functionality through click chemistry.* Journal of the American Chemical Society, 2006. **128**(35): p. 11356-11357.
75. Newville, M., *Fundamentals of XAFS*. Revision 1.7 ed. 2004: Consortium for Advanced Radiation Sources, University of Chicago.
76. Paulus, P.M., H. Bönnemann, A.M. van der Kraan, F. Luis, J. Sinzig, and L.J. de Jongh, *Magnetic properties of nanosized transition metal colloids: the influence of noble metal coating.* The European Physical Journal D - Atomic, Molecular, Optical and Plasma Physics, 1999. **9**(1): p. 501-504.
77. van Leeuwen, D.A., J.M. van Ruitenbeek, L.J. de Jongh, A. Ceriotti, G. Pacchioni, O.D. Häberlen, and N. Rösch, *Quenching of Magnetic Moments by Ligand-Metal Interactions in Nanosized Magnetic Metal Clusters.* Physical Review Letters, 1994. **73**(10): p. 1432-1435.
78. Salafranca, J., J. Gazquez, N. Pérez, A. Labarta, S.T. Pantelides, S.J. Pennycook, X. Batlle, and M. Varela, *Surfactant Organic Molecules Restore Magnetism in Metal-Oxide Nanoparticle Surfaces.* Nano Letters, 2012. **12**(5): p. 2499-2503.

79. Nagesha, D.K., B.D. Plouffe, M. Phan, L.H. Lewis, S. Sridhar, and S.K. Murthy, *Functionalization-induced improvement in magnetic properties of Fe3O4 nanoparticles for biomedical applications.* Journal of Applied Physics, 2009. **105**(7): p. -.
80. Chen, L.X., T. Liu, M.C. Thurnauer, R. Csencsits, and T. Rajh, *Fe2O3 Nanoparticle Structures Investigated by X-ray Absorption Near-Edge Structure, Surface Modifications, and Model Calculations.* The Journal of Physical Chemistry B, 2002. **106**(34): p. 8539-8546.
81. Klokkenburg, M., J. Hilhorst, and B.H. Erné, *Surface analysis of magnetite nanoparticles in cyclohexane solutions of oleic acid and oleylamine.* Vibrational Spectroscopy, 2007. **43**(1): p. 243-248.
82. Daou, T.J., J.M. Greneche, G. Pourroy, S. Buathong, A. Derory, C. Ulhaq-Bouillet, B. Donnio, D. Guillon, and S. Begin-Colin, *Coupling agent effect on magnetic properties of functionalized magnetite-based nanoparticles.* Chemistry of Materials, 2008. **20**(18): p. 5869-5875.
83. Meledandri, C.J., T. Ninjbadgar, and D.F. Brougham, *Size-controlled magnetoliposomes with tunable magnetic resonance relaxation enhancements.* Journal of Materials Chemistry, 2011. **21**(1): p. 214-222.
84. Gaumet, M., A. Vargas, R. Gurny, and F. Delie, *Nanoparticles for drug delivery: The need for precision in reporting particle size parameters.* European Journal of Pharmaceutics and Biopharmaceutics, 2008. **69**(1): p. 1-9.
85. Minchin, R., *Sizing up targets with nanoparticles.* Nature Nanotechnology, 2008. **3**(1): p. 12-13.
86. Qiu, P.H., C. Jensen, N. Charity, R. Towner, and C.B. Mao, *Oil Phase Evaporation-Induced Self-Assembly of Hydrophobic Nanoparticles into Spherical Clusters with Controlled Surface Chemistry in an Oil-in-Water Dispersion and Comparison of Behaviors of Individual and Clustered Iron Oxide Nanoparticles.* Journal of the American Chemical Society, 2010. **132**(50): p. 17724-17732.
87. Xu, F.H., C.M. Cheng, F.J. Xu, C.F. Zhang, H. Xu, X. Xie, D.Z. Yin, and H.C. Gu, *Superparamagnetic magnetite nanocrystal clusters: a sensitive tool for MR cellular imaging.* Nanotechnology, 2009. **20**(40).
88. Sondjaja, R., T.A. Hatton, and M.K.C. Tam, *Clustering of magnetic nanoparticles using a double hydrophilic block copolymer, poly(ethylene oxide)-b-poly(acrylic acid).* Journal of Magnetism and Magnetic Materials, 2009. **321**(16): p. 2393-2397.
89. Ma, W.F., S.A. Xu, J.M. Li, J. Guo, Y. Lin, and C.C. Wang, *Hydrophilic Dual-Responsive Magnetite/PMAA Core/Shell Microspheres with High Magnetic Susceptibility and pH Sensitivity via Distillation-Precipitation Polymerization.* Journal of Polymer Science Part a-Polymer Chemistry, 2011. **49**(12): p. 2725-2733.
90. Yoon, K.Y., C. Kotsmar, D.R. Ingram, C. Huh, S.L. Bryant, T.E. Milner, and K.P. Johnston, *Stabilization of Superparamagnetic Iron Oxide Nanoclusters in Concentrated Brine with Cross-Linked Polymer Shells.* Langmuir, 2011. **27**(17): p. 10962-10969.
91. Ghosh, S.K., *The Preparation of Magnetic Nanoparticle Assemblies for Biomedical Applications.* Ph.D Thesis, Dublin City University, 2006.
92. Meledandri, C.J., *NMR Studies of Membrane-Bound Nanoparticles and Nanoparticle Assemblies.* Ph.D Thesis, Dublin City University, 2008.

93. Fresnais, J., C. Lavelle, and J.F. Berret, *Nanoparticle Aggregation Controlled by Desalting Kinetics.* Journal of Physical Chemistry C, 2009. **113**(37): p. 16371-16379.
94. Yan, M., J. Fresnais, S. Sekar, J.P. Chapel, and J.F. Berret, *Magnetic Nanowires Generated via the Waterborne Desalting Transition Pathway.* Acs Applied Materials & Interfaces, 2011. **3**(4): p. 1049-1054.
95. Frka-Petesic, B., J. Fresnais, J.F. Berret, V. Dupuis, R. Perzynski, and O. Sandre, *Stabilization and controlled association of superparamagnetic nanoparticles using block copolymers.* Journal of Magnetism and Magnetic Materials, 2009. **321**(7): p. 667-670.
96. Qi, L., J. Fresnais, J.F. Berret, J.C. Castaing, F. Destremaut, J.B. Salmon, F. Cousin, and J.P. Chapel, *Influence of the Formulation Process in Electrostatic Assembly of Nanoparticles and Macromolecules in Aqueous Solution: The Interaction Pathway.* Journal of Physical Chemistry C, 2010. **114**(39): p. 16373-16381.
97. Qi, L., J. Fresnais, J.F. Berret, J.C. Castaing, I. Grillo, and J.P. Chapel, *Influence of the Formulation Process in Electrostatic Assembly of Nanoparticles and Macromolecules in Aqueous Solution: The Mixing Pathway.* Journal of Physical Chemistry C, 2010. **114**(30): p. 12870-12877.
98. Yan, M., J. Fresnais, and J.F. Berret, *Growth mechanism of nanostructured superparamagnetic rods obtained by electrostatic co-assembly.* Soft Matter, 2010. **6**(9): p. 1997-2005.
99. Gibby, W.C., Hall, J., *XCIV.—The system water–chloroform.* Journal of the Chemical Society, 1931(0): p. 691-693.
100. Voss, L.F., C.M. Hadad, and H.C. Allen, *Competition between atmospherically relevant fatty acid monolayers at the air/water interface.* Journal of Physical Chemistry B, 2006. **110**(39): p. 19487-19490.
101. Howard, P.H., Meylan, William M., *Handbook of physical properties of organic chemicals*. 1 ed. 1997: Lewis Publishers.
102. Miller, R. and G. Kretzschmar, *Adsorption kinetics of surfactants at fluid interfaces.* Advances in Colloid and Interface Science, 1991. **37**(1–2): p. 97-121.
103. Tomoaia, G., A. Tomoaia-Cotisel, M. Tomoaia-Cotisel, and A. Mocanu, *Kinetic study of adsorption of some biocompounds at the oil/water interface.* Central European Journal of Chemistry, 2005. **3**(2): p. 347-360.
104. Stolarczyk, J.K., *Private communication*.
105. Lin, M.Y., H.M. Lindsay, D.A. Weitz, R.C. Ball, R. Klein, and P. Meakin, *Universal reaction-limited colloid aggregation.* Physical Review A, 1990. **41**(4): p. 2005-2020.
106. Khan, S.J., F. Pierce, C.M. Sorensen, and A. Chakrabarti, *Self-Assembly of Ligated Gold Nanoparticles: Phenomenological Modeling and Computer Simulations†.* Langmuir, 2009. **25**(24): p. 13861-13868.
107. Lattuada, M., H. Wu, J. Sefcik, and M. Morbidelli, *Detailed Model of the Aggregation Event between Two Fractal Clusters.* The Journal of Physical Chemistry B, 2006. **110**(13): p. 6574-6586.
108. Vuong, Q.L., J.F. Berret, J. Fresnais, Y. Gossuin, and O. Sandre, *A Universal Scaling Law to Predict the Efficiency of Magnetic Nanoparticles as MRI T2-Contrast Agents.* Advanced Healthcare Materials, 2012. **1**(4): p. 502-512.
109. Lee, J.-H., J.-t. Jang, J.-s. Choi, S.H. Moon, S.-h. Noh, J.-w. Kim, J.-G. Kim, I.-S. Kim, K.I. Park, and J. Cheon, *Exchange-coupled magnetic nanoparticles for efficient heat induction.* Nat Nano, 2011. **6**(7): p. 418-422.

110. Lartigue, L., P. Hugounenq, D. Alloyeau, S.P. Clarke, M. Lévy, J.-C. Bacri, R. Bazzi, D.F. Brougham, C. Wilhelm, and F. Gazeau, *Cooperative Organization in Iron Oxide Multi-Core Nanoparticles Potentiates Their Efficiency as Heating Mediators and MRI Contrast Agents.* ACS Nano, 2012. **6**(12): p. 10935-10949.